

**Evolution of the Western Cordillera  
and Coastal Margin of Peru:  
Evidence from low-temperature Thermochronology  
and Geomorphology**

**Martin Wipf**

DISS. ETH NO. 16383

**Evolution of the Western Cordillera and Coastal Margin of Peru:  
Evidence from low-temperature Thermochronology and  
Geomorphology**

A dissertation submitted to the

**SWISS FEDERAL INSTITUTE OF TECHNOLOGY ZÜRICH**

For the degree of

**DOCTOR OF NATURAL SCIENCES**

Presented by

**MARTIN ANDREAS WIPF**

Dipl. Natw. ETH Zürich

Born February 2<sup>nd</sup>, 1974

Citizen of Switzerland

Accepted on the recommendation of

Prof. Dr. Jean-Pierre Burg  
Dr. Diane Seward  
Prof. Dr. Rainer Wieler  
Prof. Dr. Fritz Schlunegger

ETH Zürich  
ETH Zürich  
ETH Zürich  
University of Berne

Referee  
Co-referee  
Co-referee  
Co-referee

Zürich, February 2006

Front cover: "The Bird; Nazca Lines;"

Back cover: "The Paracas Cathedral" near Pisco

*"We shall not cease from exploration and  
the end of all our exploring will be to  
arrive where we started and know the  
place for the first time."*

T.S. Eliot

"Little Gidding"



# Table of Contents

<b>Abstract</b>	<b>1</b>
<b>Zusammenfassung</b>	<b>3</b>
<b>1 Introduction</b>	<b>5</b>
<b>1.1 Aims and Project Backgrounds</b>	<b>5</b>
1.1.1 Development of the (U-Th)/He dating technique	5
1.1.2 The field study	5
1.1.2.1 <i>The Peruvian Coastal margin</i>	6
<b>1.2 Outline of the Thesis</b>	<b>7</b>
<b>1.3 References cited</b>	<b>8</b>
<b>2 Regional Background</b>	<b>9</b>
<b>2.1 The Andes</b>	<b>9</b>
<b>2.2 Plate setting</b>	<b>11</b>
<b>2.3 Overview of the regional Geology of Peru</b>	<b>14</b>
<b>2.3.1 Regional subdivision</b>	<b>14</b>
2.3.1.1 <i>The Andean Forearc</i>	14
2.3.1.2 <i>The High Andes</i>	17
2.3.1.3 <i>The Subandean Lowlands</i>	18
<b>2.3.2 Radiometric Geochronology</b>	<b>18</b>
2.3.2.1 <i>Arequipa Massif and San Nicolás Batholith</i>	20
2.3.2.2 <i>The Coastal Batholith</i>	21
<b>2.3.3 Late Mesozoic – Cenozoic events</b>	<b>22</b>
2.3.3.1 <i>The Mochica phase</i>	24
2.3.3.2 <i>The Peruvian Phase</i>	24
2.3.3.3 <i>The Incaic Phase</i>	24
2.3.3.4 <i>The Aymara Phas</i>	25
2.3.3.5 <i>The Quechua Phases</i>	28
2.3.3.6 <i>The Pliocene Phase</i>	29
2.3.4. Recent morphology and landscape evolution	29

---

<b>2.4 Climate of western margin</b>	<b>30</b>
<b>2.5 References cited</b>	<b>31</b>
<b>3 The subducting Nazca Ridge:</b>	
<b>Impact on the Geomorphology in South-Central Peru</b>	<b>41</b>
<b>ABSTRACT</b>	<b>41</b>
<b>KEYWORDS</b>	<b>42</b>
<b>INTRODUCTION</b>	<b>42</b>
<i>Background</i>	<i>42</i>
<b>METHODS</b>	<b>45</b>
<b>RESULTS</b>	<b>46</b>
<b>South</b>	<b>46</b>
<b>Centre</b>	<b>46</b>
<b>North</b>	<b>47</b>
<b>DISCUSSION</b>	<b>48</b>
<b>CONCLUSIONS</b>	<b>49</b>
<b>ACKNOWLEDGEMENTS</b>	<b>49</b>
<b>REFERENCES CITED</b>	<b>50</b>
<b>4 (U-Th)/He dating on apatite:</b>	
<b>using laser heating and MC-ICPMS</b>	<b>53</b>
<b>ABSTRACT</b>	<b>53</b>
<b>INTRODUCTION</b>	<b>54</b>
<i>Historical background</i>	<i>55</i>
<i>Technical Background</i>	<i>56</i>
<b>APATITE GRAIN SELECTION AND PREPARATION</b>	<b>57</b>
<b>IR LASER EXTRACTION OF HELIUM AND MEASURING</b>	
<b>HELIUM VOLUMES</b>	<b>58</b>
<i>Blanks</i>	<i>60</i>
<i>Calibrations and determination of helium concentration and uncertainties</i>	<i>61</i>
<b>URANIUM AND THORIUM ANALYSIS</b>	<b>62</b>
<i>Sample preparation</i>	<i>62</i>

---

<i>Mass spectrometry</i>	63
<i>Determination of the ion counters' relative gains</i>	64
<i>Determinations of Uranium and Thorium concentrations in apatites</i>	66
<i>Uncertainties</i>	66
<b>RESULTS</b>	<b>67</b>
<i>Durango</i>	68
<i>Lim t3</i>	68
<b>DISCUSSION</b>	<b>71</b>
<b>CONCLUSIONS</b>	<b>72</b>
<b>ACKNOWLEDGEMENTS</b>	<b>73</b>
<b>REFERENCES CITED</b>	<b>74</b>
<b>5 Thermochronology of the Coastal Margin of Peru</b>	<b>79</b>
<b>5.1 Introduction</b>	<b>79</b>
<b>5.2 Methods</b>	<b>81</b>
<b>5.3 Results</b>	<b>82</b>
<b>5.3.1 Zircon fission track</b>	<b>82</b>
<b>5.3.2 Apatite fission track</b>	<b>88</b>
<b>5.3.3 Apatite (U-Th)/He</b>	<b>96</b>
<b>5.3.4 Data breakdown into regions</b>	<b>97</b>
<b>5.3.5 Low temperature modelling</b>	<b>105</b>
<i>5.3.5.1 Talara-Chiclayo</i>	<i>107</i>
<i>5.3.5.2 Chiclayo-Huacho</i>	<i>107</i>
<i>5.3.5.3 Lima -Lunahuana</i>	<i>110</i>
<i>5.3.5.4 Nazca Ridge area- trailing edge</i>	<i>110</i>
<i>5.3.5.5 Nazca Ridge area- leading edge</i>	<i>112</i>
<i>5.3.5.6 Chala-Tacna</i>	<i>112</i>
<b>5.4 Interpretation and Discussion</b>	<b>112</b>
<b>5.4.1 Zircon fission track</b>	<b>112</b>
<b>5.4.2 Apatite fission track</b>	<b>116</b>
<b>5.4.3 (U/Th)/He</b>	<b>116</b>
<b>5.4.4 Cooling histories of different regions</b>	<b>116</b>

---

5.4.4.1 Talara – Chiclayo	117
5.4.4.2. Chiclayo-Huacho	118
5.4.4.3 Lima - Lunahuana	120
5.4.4.4 Nazca Ridge area- trailing edge	121
5.4.4.5 Nazca Ridge area- leading edge	123
5.4.4.6. Chala-Tacna	123
<b>5.4.5 Impact of the Nazca Ridge</b>	<b>125</b>
5.4.5.1 Evidence from fission-track and (U/Th)/He ages	125
5.4.5.2 Evidence from thermal modelling	126
<b>5.5 Conclusions</b>	<b>127</b>
<b>5.5.1 Meaning of the cooling ages</b>	<b>127</b>
5.5.1.1 Precambrian and Palaeozoic suites	127
5.5.1.2 Coastal Batholith	128
<b>5.5.2 Identification of tectonic events</b>	<b>129</b>
<b>5.5.3 Erosion</b>	<b>129</b>
<b>5.6 References cited</b>	<b>130</b>
<b>6 Summary and outlook</b>	<b>135</b>
<b>6.1 Development of the (U-Th)/He method</b>	<b>135</b>
<b>6.2 The Peruvian coastal margin</b>	<b>135</b>
<b>6.3 Outlook</b>	<b>137</b>
6.3.1 (U-Th)/He	137
6.3.2 The Peruvian coastal margin	138
<b>6.4 References cited</b>	<b>139</b>
<b>7 Appendix</b>	<b>141</b>
<b>7.1 Curriculum Vitae</b>	<b>142</b>
<b>7.2 <math>\zeta</math>-calibration factor used for apatite fission-track analysis</b>	<b>145</b>
<b>7.3 Radial plots</b>	<b>146</b>
<b>7.4 Acknowledgments</b>	<b>151</b>

# Abstract

In this thesis the thermotectonic and geomorphological history of the Peruvian coastal margin is described. The influence of the subducting Nazca Ridge on the evolution of this margin in particular is revealed and discussed in detail. To constrain the low temperature cooling history an integrated approach combining various methodologies was applied. These included geomorphological investigations, as well as apatite and zircon fission-track analysis and in order to include the lower temperature range of the cooling paths the (U-Th)/He technique.

A major part of this thesis was therefore dedicated to the development of the (U-Th)/He method at the ETH in Zürich by applying a new combination of analytical procedures. The radiogenic helium was extracted through laser heating from carefully chosen apatite crystals and subsequently analysed on a sector type mass spectrometer. Afterwards the degassed grains were recovered and their uranium and thorium contents were determined on a Multiple-Collector Inductively Coupled Plasma Mass Spectrometer (MC-ICPMS). This approach allowed the determination of very precise (U-Th)/He ages.

The Peruvian coastal margin consists mainly of Precambrian to Palaeozoic rocks and the Jurassic to Cretaceous Coastal Batholith. The Precambrian to Palaeozoic rocks yield zircon fission-track ages that range from 530-121 Ma. Since they are significantly younger than their crystallisation ages they are believed to represent the slow cooling of these “old” rock bodies. The zircon fission-track ages from the Jurassic to Cretaceous age range Coastal Batholith on the other hand suggest that these later intrusives cooled rapidly. Apatite fission-track ages are younger and range from 124-23 Ma for all samples which is consistent with the lower closure temperature. The cooling histories based on the modelling of the apatite fission-track data suggest for the majority of the samples a long period of stability following the initial rapid cooling, with a renewed and final cooling in the late Neogene. When the period of quiescence is greater than 20 myrs the associated apatite helium ages display a broad intra-sample spread. The meaning of such a spread is open yet to interpretation but it is remarkable that in all cases the helium ages fall onto the modelled paths of the apatite fission-track data.

Based on the data obtained in this study it is concluded that there has been very little exhumation along the Peruvian coastal margin. In the south, which has not yet been affected by the subduction of the Nazca Ridge erosion rates are  $<0.05$  mm/yr. An estimated rate of erosion based on geomorphological data from areas above the Nazca Ridge yields a value of  $\sim 0.3$  mm/yr. Interpretation of the (U-Th)/He results from the trailing edge and immediately to the north of the Ridge indicate that a total of 2-3 km of overburden have been removed corresponding to erosion rates of the order of  $\sim 1$  mm/yr. Hence it is concluded that the subduction of the Nazca Ridge has influenced the evolution of the Peruvian coastal margin by causing surface uplift which generated variations in the rate of erosion that can be quantified by combining the results obtained with different methodologies.

# Zusammenfassung

Im Rahmen dieser Dissertation wurden die thermotektonische und geomorphologische Geschichte des peruanischen Küstenstreifens untersucht. Insbesondere der Einfluss der Subduktion des Nazca Rückens auf die Entwicklung dieser Küstenregion wird ausführlich analysiert und diskutiert. Um die Abkühlungsgeschichte bis zu niedrigen Temperaturen rekonstruieren zu können, wurden verschiedenen Verfahren angewendet und kombiniert. Dazu gehören sowohl geomorphologische Untersuchungen als auch Spaltspurdaterungen an Apatiten und Zirkonen und aufgrund ihrer niedrigen Schliesstemperatur auch die (U-Th)/He Datierungsmethode.

Ein grosser Teil dieser Arbeit diente folglich der Entwicklung und Anwendung der (U-Th)/He Methode an der ETH in Zürich. Zu diesem Zweck wurde eine neue Kombination von analytischen Techniken verwendet. Das radiogene Helium wurde durch Heizen mit Hilfe eines Lasers, aus sorgfältig ausgewählten Apatitkristallen extrahiert, und anschliessend mit einem Sektorfeld-Massenspektrometer gemessen. Anschliessend wurde der Uran- und Thoriuminhalt mit einem induktiv gekoppelten Plasma-Massenspektrometer mit mehrfach-Kollektor (MC-ICPMS) bestimmt. Diese Messmethode erlaubte die Ermittlung von sehr präzisen (U-Th)/He Altern.

Der peruanische Küstenrand besteht hauptsächlich aus praekambrischen bis palaeozoischen Gesteinen und aus dem Küstenbatholithen mit jurassischen bis kretazischen Intrusionsaltern. Die Zirkon Spaltspurdaterungen der praekambrischen bis palaeozoischen Gesteinen ergaben Alter welche von 530-121 Ma reichen. Diese Alter sind erheblich jünger als die Kristallisationsalter der Gesteine und werden deshalb als Folge der langsamen Abkühlung interpretiert. Andererseits deuten die Zirkon Spaltspurdaterungen des jurassische bis kretazischen Küstenbatholithen daraufhin, dass diese jüngeren Intrusionen schnell abkühlten. Die Apatit Spaltspurdaterungen für alle Proben ergaben Alter welche von 124-23 Ma reichen. Diese jüngeren Alter lassen sich gut mit der tieferen Schliesstemperatur erklären. Die Mehrheit der modellierten Abkühlungsgeschichten, welche auf den Daten der Apatit Spaltspurdaterungen basieren, schlagen eine lange Periode der Stabilität vor, welche der schnellen ersten Abkühlung folgte. Diese Periode war gefolgt von einer erneuten Abkühlung im Neogen. Wenn die Länge dieser Ruheperiode mehr als 20 Ma beträgt,

zeigen die Heliumalter eine beträchtliche Streuung innerhalb einer Probe. Die Bedeutung solcher Streuungen ist noch nicht geklärt, es ist jedoch bemerkenswert, dass alle Heliumalter mit den modellierten Abkühlungsgeschichten übereinstimmen. Basierend auf diesen Daten der Studie wird deshalb gefolgert, dass nur eine sehr geringe Exhumation entlang des peruanischen Küstenstreifens stattgefunden hat. Im Süden welcher noch nicht durch die Subduktion des Nazca Rückens beeinflusst wurde, beträgt die Rate  $<0.05$  mm/J. Aufgrund von geomorphologischen Daten im Bereich über dem Nazca Rücken kann eine Exhumationsrate von  $\sim 0.3$  mm/J abgeschätzt werden. Die Interpretation der (U-Th)/He Resultate von Gebieten über dem nördlichen Bereich des Nazca Rücken lassen eine maximale Abtragung von 2-3 Kilometern vermuten. Dies entspricht einer Rate von  $\sim 1$ mm/J. Die Subduktion des Nazca Rückens hat dementsprechend die Entwicklung der Peruanischen Küstenregion beeinflusst da durch das Heben der Oberfläche Schwankungen in der Exhumationsrate verursacht wurden. Durch die Kombination der Resultate der verschiedenen Methoden konnten diese Schwankungen quantifiziert werden.

# Chapter 1

## Introduction

### 1.1 Aims and Project Backgrounds

This thesis is part of the research project # 21-63410.00 supported by the Swiss National Science Foundation (SNCF). The project was a four year investigation that included a technical part, i.e. the development of a new dating technique and a fieldwork orientated part i.e. the application of the developed technique in combination with other methods such as fission-track and geomorphological analysis in a field study.

#### 1.1.1 Development of the (U-Th)/He dating technique

The goal of the technical part was to develop and implement the recently rediscovered (U-Th)/He technique at the ETH Zürich. This method is based on the  $\alpha$ -decay of uranium and thorium and was proposed by Rutherford (1905) as the first scheme to date minerals radiometrically, but technical problems and difficulties in interpreting the results prevented the wide utilisation of the technique until recently. Since its development as low temperature thermochronometer in the last few years (Farley, 2000; House et al., 1997; Warnock et al., 1997; Wolf et al., 1995, 1997; Zeitler et al., 1987) the (U-Th)/He technique has become a widely used tool to reveal the low temperature thermal history of earth's upper crust. The uniquely low closure temperature for the (U-Th)/He system in apatite of  $\sim 68^{\circ}\text{C}$  offers a great opportunity to detect shorter term morphological changes.

The development of this method at the ETH in Zürich included a new combination of equipment previously not applied for this technique. The degassing of the helium was done through laser heating and the released gas was analysed on a sector type mass spectrometer. Uranium and thorium were analysed with a multi collector inductively coupled plasma mass spectrometer (MC-ICPMS).

#### 1.1.2 The field study

The availability of increasingly accurate information on the exhumation paths experienced by rock bodies constrains the rates and timing of landscape evolution with respect to the tectonic

and climatic forces controlling them. The low-temperature geochronometers, such as zircon and apatite fission-track analysis and the (U-Th)/He method provide such important means to reveal rates of cooling. By combining these low temperature geochronometers the time can be extended backwards to longer term cooling histories. By including geomorphological analysis the shorter term changes in the evolution of the landscape can also be quantified.

### 1.1.2.1 The Peruvian Coastal margin

The coastal margin of Peru is the focus of this study (Fig. 1.1). This area represents part of the upper plate of the South American continent. Along the western length of Peru there is reasonable constancy in rock type as well as in climate, both of which may influence the rates of exhumation. By eliminating these two parameters the importance of other factors which may have exerted influence on the regional exhumation may be brought to light.

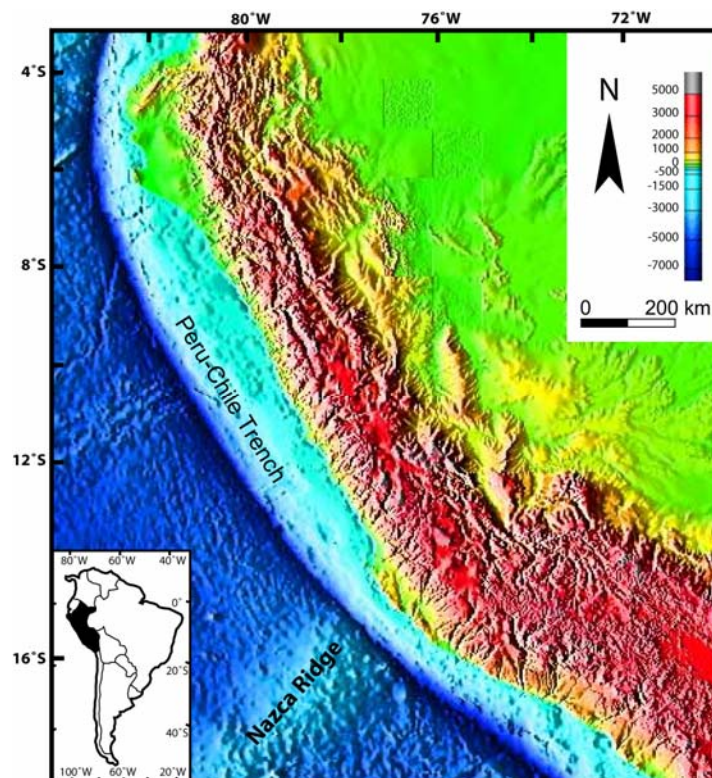


Figure 1.1: The Peruvian Coastal margin with the subducting aseismic Nazca Ridge

Of particular interest in this study is the influence on the exhumation of the coastal margin and the Western Cordillera, by the subducting Nazca Ridge and the “Lost Inca Plateau”. The Nazca Ridge, *per se*, is thought to have begun subducting at  $\sim 11^\circ\text{S}$  at  $\sim 11$  Ma (Hampel, 2002). The present leading edge lies at  $\sim 16^\circ\text{S}$ . Thus any effects that the Ridge may have had

on the surface uplift and/or exhumation of the Andean margin might be expected from latitudes 11°-16°S (Fig. 1.1).

Thus by combining the various low temperature thermochronometers with geomorphological analysis, the main goal of this thesis was to quantify the thermal evolution and exhumation of the coastal margin of Peru.

## 1.2 Outline of the Thesis

Following this introduction, in chapter 2 the geological setting and the tectonic background of the Andes with special emphasis on the Peruvian coastal margin is presented. Chapters 3 to 5 form the core of this thesis.

Chapter 3 addresses the geomorphology north, over and south of the Nazca Ridge. It explains the possible effects caused by the subduction of the ridge with the help of topographic profiles and dispersal directions of rivers. The necessary data was generated from newly available digital elevation models (SRTM 90 DEM). This chapter will be submitted to *Geology*.

Chapter 4 explains the development of the (U-Th)/He method at the ETH Zürich. The implementation of this technology was one of the main topics of this thesis. A new combination of mass spectrometric technologies was applied in order to reduce errors on single grain analysis. These techniques include degassing of the helium from analysed apatite grains through laser heating and its measurement on a sector type mass spectrometer with subsequent uranium and thorium analysis performed on a multiple collector ionisation mass spectrometer (MC-ICPMS). This chapter will be submitted to the *International Journal of Mass Spectrometry*.

Chapter 5 discusses the results of the apatite and zircon fission-track analysis as well as the (U-Th)/He data obtained from the samples of the Peruvian coastal margin. The thermochronological data reveal the exhumation history which is integrated with previously published tectonic studies, geomorphological analysis as well as previous radiometric dates. As a result of this multidisciplinary approach the exhumation history for the different areas from north to south is reconstructed. This chapter will be published as two independent papers in the near future.

Chapter 6 summarizes the results of this thesis and reveals that the work presented demonstrates that an integrated study can contribute significantly to the understanding of how tectonic processes interact with local surface processes along a subduction zone. Still open

geological problems are mentioned in a brief outlook and possible approaches to solve these questions are suggested.

### 1.3 References cited

- Farley, K.A., 2000, (U-Th)/ He dating; a review of the technique and current applications, Fission track 2000; 9th international conference on fission track dating and thermochronology, Volume 58;: Sydney, N.S.W., Australia, Geological Society of Australia, p. 77-79.
- Hampel, A., 2002, The migration history of the Nazca Ridge along the Peruvian active margin: a re-evaluation: *Earth and Planetary Science Letters*, v. 203, p. 665-679.
- House, M.A., Wernicke, B.P., and Farley, K.A., 1997, Estimation of paleorelief using (U-Th)/ He thermochronology; an example from the Sierra Nevada, California, Geological Society of America, 1997 annual meeting, Volume 29; 6: Boulder, CO, United States, Geological Society of America (GSA), p. 478.
- Rutherford, E., 1905, Present problems in radioactivity: *Popular Science Monthly*, p. 1-34.
- Warnock, A.C., Zeitler, P.K., Wolf, R.A., and Bergman, S.C., 1997, An evaluation of low-temperature apatite U-Th/ He thermochronometry: *Geochimica et Cosmochimica Acta*, v. 61, p. 5371-5377.
- Wolf, R.A., Farley, K.A., and Silver, L.T., 1995, (U-Th)/ He dating; diffusion studies and application to an uplifted mountain block in the Peninsular Ranges Batholith, California, Geological Society of America, 1995 annual meeting, Volume 27; 6: Boulder, CO, United States, Geological Society of America (GSA), p. 37.
- , 1997, Assessment of (U-Th)/ He thermochronometry; the low-temperature history of the San Jacinto Mountains, California: *Geology (Boulder)*, v. 25, p. 65-68.
- Zeitler, P.K., Herczeg, A.L., McDougall, I., and Honda, M., 1987, U-Th-He dating of apatite; a potential thermochronometer: *Geochimica et Cosmochimica Acta*, v. 51, p. 2865-2868.

# Chapter 2

## Regional background

### 2.1 The Andes

The Andes form an 8000 km long chain along the western edge of South America reaching a maximum width of 750 km (Fig. 2.1). The highest peak, the Aconcagua in Chile ( $32^{\circ} 38' / 70^{\circ} 01'$ ) reaches an altitude of 6960 m. Three segments of distinct orientation can be recognised. 1: The Colombian-Ecuadorian segment ( $12^{\circ}\text{N} - 5^{\circ}\text{S}$ ) is approximately 2000 km long and trends north-northeast to south-southwest. The Huancabamba bend (Megard, 1984) separates it from 2: The Peruvian segment ( $5^{\circ}\text{S} - 18^{\circ}\text{S}$ ) which extends approximately 2000 km following a northwest to southeast trend. 3: The Chilean segment is separated by the Arica Bend from the Peruvian segment to the north. It follows a north to south trend over a distance of 4000 km.

The Andean chain displays a highly asymmetric topography with a steep western slope and a wide eastern side. The western location of the Andes relative to the South American continent explains why the rivers flowing toward the Pacific Ocean do not exceed 300 km in length, whereas those flowing to the Atlantic reach 4000 km. In Peru the distance between the Peru-Chile trench and the drainage divide varies from 240 to 300 km, whereas the distance between the drainage divide and the 200 m contour line in the east ranges between 280 km ( $5^{\circ}\text{N}$ ) and about 1000 km ( $8^{\circ}\text{S} - 12^{\circ}\text{S}$ ).

Two drainage divides exist between  $13^{\circ}\text{S}$  and  $24^{\circ}\text{S}$  (southern Peru – Bolivia). They delimit a wide, flat, internally draining basin known as the Altiplano, which coincides with the zone of highest average elevation and largest width of the chain.

The highest peaks are formed by recent or active volcanoes situated on the deformed chain or on metamorphic or granitic slices uplifted by reverse faults. Among the highest volcanos are Cotopaxi (5897 m) and Chimborazo (6310 m) in Ecuador, the Coropuna (6425 m) and Ampato (6310 m) in Peru, the Sajama (6520 m) in Bolivia, the Aconcagua (6960 m) and the Bonete (6872 m) in Argentina, the Ojos del Salado (6880 m) and the Mercedario (6770 m) in Chile. Among the uplifted slices is the mainly granitic Cordillera Blanca in northern Peru culminating with the Nevado Huascarán (6768 m), and the metamorphic Eastern Cordillera of

southern Peru and northern Bolivia with the Nevado Illimani (6682 m) and the Nevado Illampu (6485 m). Deformed and uplifted sediments may however also form high summits such as Nevado Yerupajá (6632 m) in the Cordillera Huayhuash and Nevado Ausangate (6384 m) in southern Peru or the Nevado Cololo (5975 m) in Bolivia.

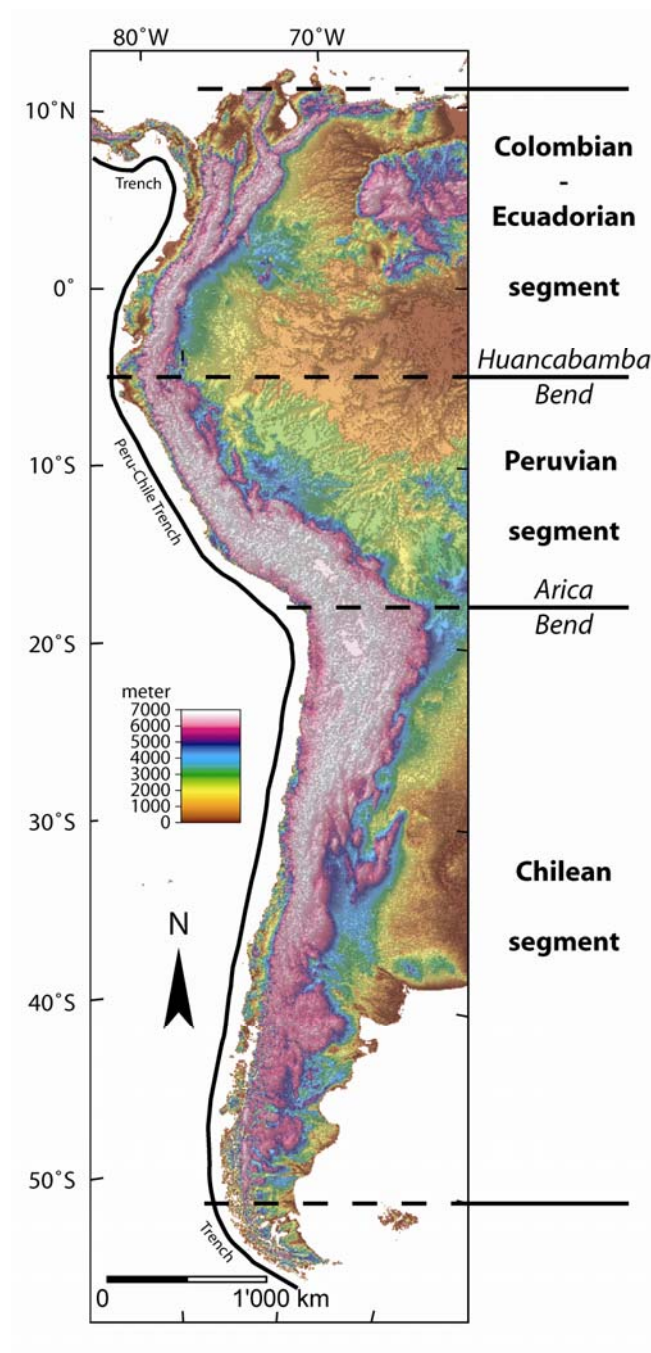


**Figure 2.1:** The west coast of South America with the segmentation of the Andes into the Colombian-Ecuadorian, Peruvian and Chilean segment. Resolution of the Digital Elevation Models is 920 m/pixel.

## 2.2 Plate setting

The Andean chain defines the boundary between the South American Plate and three oceanic plates. These plates are from north to south: the Cocos Plate, the Nazca Plate and the Antarctic Plate (Fig. 2.2). In the following only the parts of the Nazca Plate relevant to the study area in Peru affected by its subduction will be discussed in more detail.

The Nazca Plate is migrating to the east-northeast at a rate of 5 cm/yr while the South America continent migrates westwards at a rate of 3 cm/yr (Silver, 1998) resulting in a convergence rate between the two plates of around 6.1 cm/yr (Norabuena et al., 1998). As a result the oceanic Nazca Plate is consumed along the deep sea trench from Colombia in the north to southern Chile. The oceanic Nazca Plate is separated by age differences into two portions by the northeast trending Grijalva Fracture Zone (GFZ) located between 3°S and 5°S (Fig. 2.2). To the north of the GFZ, the currently subducting oceanic plate is of Miocene age and 2800 to 3500 m below sea level. Its subduction forms the mostly less than 4000 m deep Ecuadorian–Colombian trench. South of the GFZ, the oceanic plate is of Eocene to early Oligocene age and 4000 – 5600 m below sea level.

The depth of the Peru-Chile trench reaches 6600 m (11°S, 17°S) to 8055 m (23°S). Clear anomalies are apparent however, such as the Nazca Ridge colliding with the South American continent. Here the trench is diminished to a depth of 4800-5200 m. Trailing this collision zone northwards between 5°S and 14°S a 1500 km long segment of flat subduction (<30°) exists (Fig. 2.2). Within this zone recent volcanism is absent in spite of active subduction. Nonetheless the Cordillera Blanca forming some of the highest peaks in the Andes is located between 9°S and 11°S (Fig. 2.3). This mountain chain consists of a 120 km long linear batholith of Neogene age, i.e. 8 Ma (McNulty et al., 1998) and is believed to have started to exhume at approximately 6 Ma (Garver et al., 2005; McNulty and Farber, 2002; McNulty et al., 1998).

The association of flat slab subduction with areas of volcanic gaps have been a puzzling phenomenon ever since their discovery (Barazangi and Isacks, 1976; Hasegawa and Sacks, 1981; Pilger, 1981). The angle of subduction varies considerably along the western coast of South America. From north to south the Nazca Plate subducts at an angle of 19° - 35° to a depth which varies from 250 km to 650 km. Between 5°N and 2°S the subducting slab dips at 35° and represents a sector of “normal” subduction with active volcanism. At latitudes 5°S – 14°S seismic activity indicate that the Nazca Plate initially descends to a depth of 100 km at an angle of 30° before extending horizontally for several hundred km. Between 14°S and

16°S, where the angle of subduction abruptly increases to 30°, active volcanoes are observed again. Several explanations have been suggested to explain this unusual geometry of the Peruvian flat slab region. 1: Intraplate hydrostatic suction was proposed by (Jischke, 1975) 2: Subduction of young and therefore buoyant lithosphere was used to explain the flat subduction (Abbott et al., 1994; Cloos, 1993; Sacks, 1983; Vlaar, 1983; Vlaar and Wortel, 1976; Wortel and Vlaar, 1976) 3: Sacks (1983) and Pennington (1984) reasoned that delay in the transition of basalt to eclogite and hence less rapid increase of density would cause flat subduction. 4: Bevis (1986), Cahill and Isacks (1992) and Gephart (1994) argued that the gentle convex curvature of the Peruvian margin was the reason for the peculiar flat slab geometry. 5: The rapid absolute motion of the upper plate which overrides the oceanic lithosphere faster than the latter can sink (Cross and Pilger, 1982; Olbertz et al., 1997) has also been used to help explain flat subduction. While these hypotheses can explain some of the observations they do not all apply to all flat subduction areas worldwide. Nevertheless whilst a variety of factors are likely to contribute, one is present in nearly all cases of flat subduction, overthickened oceanic crust. While the southern portion of the flat slab segment correlates spatially and temporally with the subduction of the Nazca Ridge (Mcgeary et al., 1985; Nur and Benavraham, 1981, 1983; Pilger, 1981; von Huene et al., 1996) its vast extent to the north is less obvious. According to Gutscher (1999) it is caused by the completely subducted “Lost Inca Plateau”. Hence the Peru flat segment is the result of the combined buoyancy of the Nazca Ridge and the Lost Inca Plateau located under northern Peru (Fig. 2.2). It was further suggested that the pattern of seismicity and volcanic activity are related since volcanism seems to be controlled by the dip of the subducting slab and the amount of asthenospheric material between the slab and the overriding South American lithosphere (Barazangi and Isacks, 1976; Jordan et al., 1983; Nur and Benavraham, 1981, 1983; Pilger, 1981). This assumption is supported by the occurrence of similar volcanic gaps farther south, at the point where the Juan Fernandez Ridge collides with the Chilean coast and, although not as pronounced, south of the point where the Cocos Ridge meets the coast of Panama.

Regional earthquake focal mechanisms (Gutscher et al., 1999; Jordan et al., 1983; Suarez et al., 1983) are predominantly compressional (thrust type) to transcurrent (strike-slip) with p-axes typically aligned parallel to the plate motion (i.e. east-west). This suggests that the subduction boundary stresses are transmitted far (several hundred km) into the upper plate. Gutscher (2000) quantified seismic variation along the entire length of the subducting Nazca Plate. Seismic energy released in the upper plate above flat segments is on average 3-5 times

greater than in adjacent steep ( $>30^\circ$  dipping) slab segments. This increase is attributed to viscous coupling across the increased area of intraplate contact. Present day seismicity suggests that approximately 90% of interplate motion is taken up by slip on the subduction zone and only 10% by shortening and thickening in the overlying continental margin, (Dewey and Lamb 1992). Shortening directions are close to  $080^\circ$  indicating that little strain partitioning is taking place. Displacement of orogen parallel strike slip faults is less than 100km (Lamb, 1997).

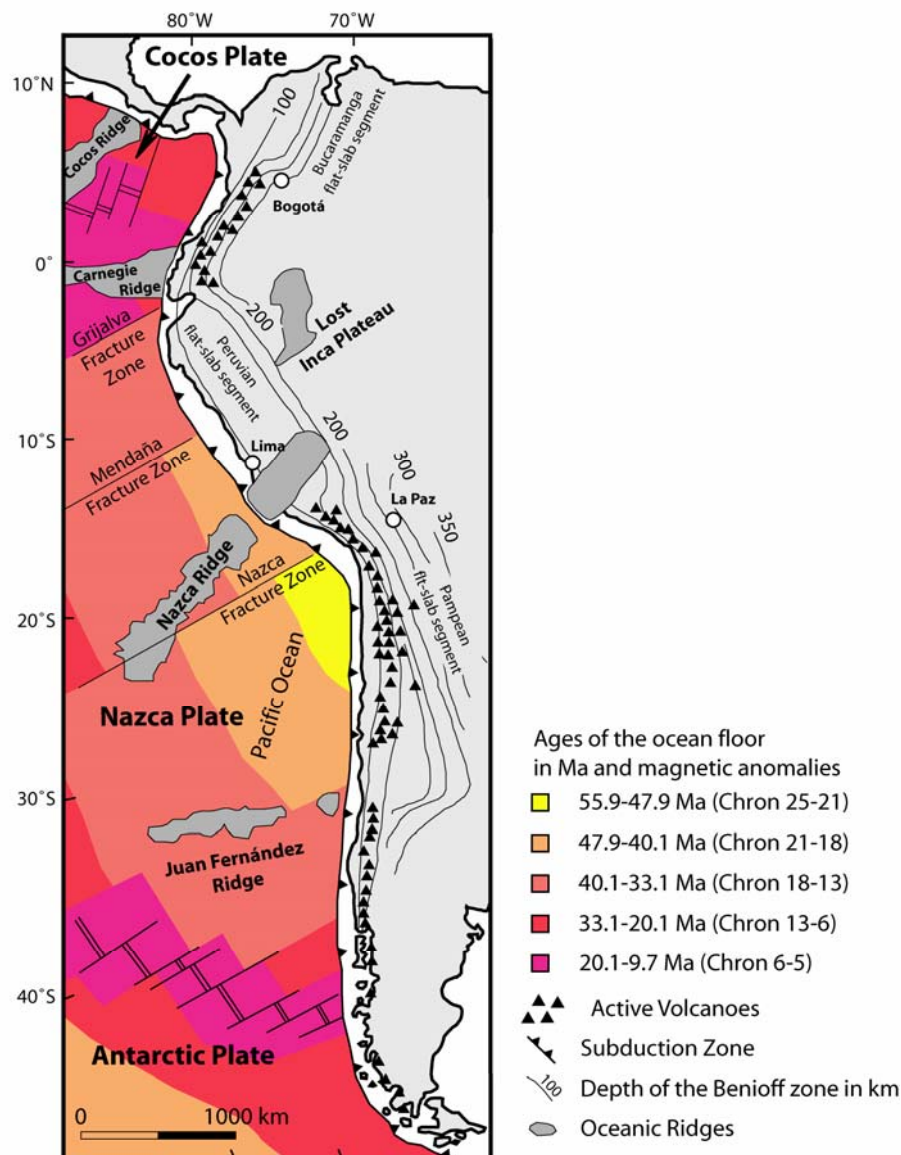


**Figure 2.2:** Plate setting of the west coast of South America. Plate boundaries, location of active volcanoes, and depth of the Wadatti-Benioff plane after Ramos and Aleman (2000); location of aseismic ridges including the “Lost Inca Plateau” after Gutscher et al. (1999; 2000), age of the oceanic plate after Muller et al. (1997).

## 2.3 Overview of the regional Geology of Peru

### 2.3.1 Regional subdivision

Both the present day topography and geological setting of the Andes in Peru from the Peru-Chile trench to the Brazilian Shield define three parallel major regions (Fig. 2.3).

All three of these morphostructural units formed during the Meso-Cenozoic evolution of the Central Andes. According to Jaillard et al. (2000) and Sebrier et al. (1988) they are defined as the Andean Forearc, the High Andes and the Andean Foreland.

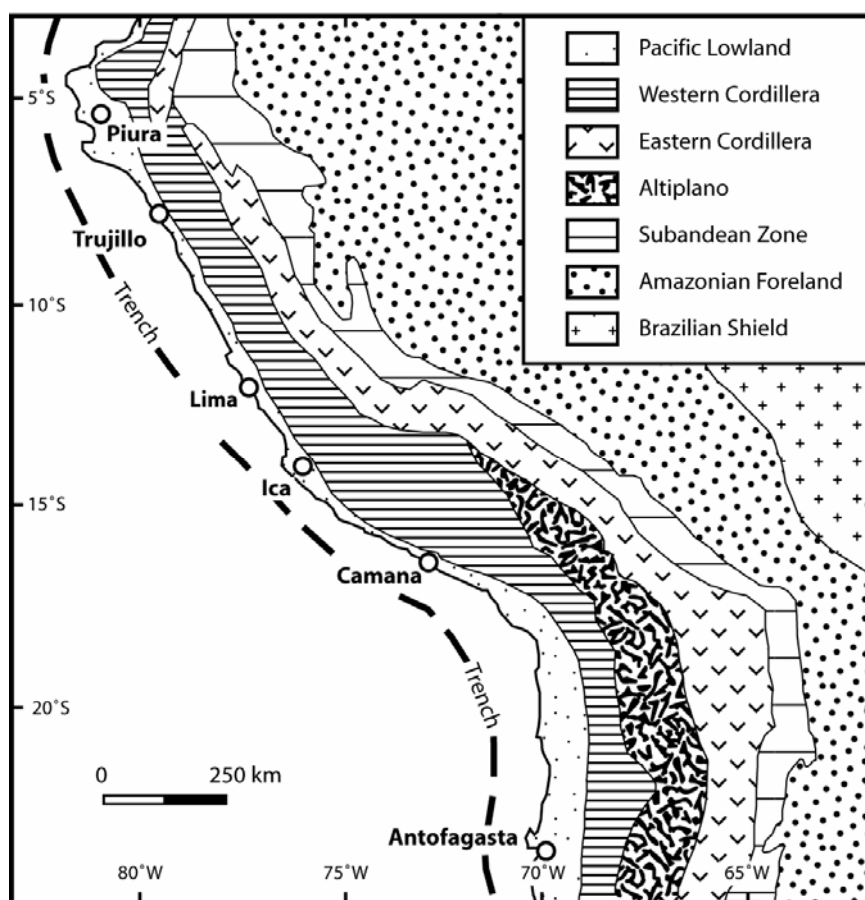


**Figure 2.3:** The morphostructural units of Peru, Bolivia and northern Chile after Jaillard et al. (2000) and Sebrier et al. (1988).

#### 2.3.1.1 The Andean Forearc

The Andean Forearc can be subdivided into the submerged Andean slope and the emerged Pacific Lowlands. They are bordered to the east by the Coastal Cordillera and to the west by the Peru-Chile trench.

Lying eastward of the trench, between depths of 7000 to 2000 m, the lower and middle slope is exempt of sediment and if an accretionary prism is present it is very small and restricted to the lowermost slope (Hampel, 2002; Hampel et al., 2004b; Kukowski and Pecher, 1999; Kukowski et al., 1994; von Huene et al., 1985). The upper slope, shallower than a depth of 2000 m, corresponds to the fore-arc basins (DeVries, 1998; Dunbar et al., 1990; Machare and Ortlieb, 1992). These include the Talara, Sechura, Trujillo, Yauquina, Salaverry, Lima, East Pisco, West Pisco, Caballas, Mollendo, and Moquegua Basin (Fig. 2.4). The emerged eastern edges of these basins which crop out along the Pacific Coast and in the Pacific Lowlands are discussed here. They are well documented and reveal the timing of events during the Cenozoic.

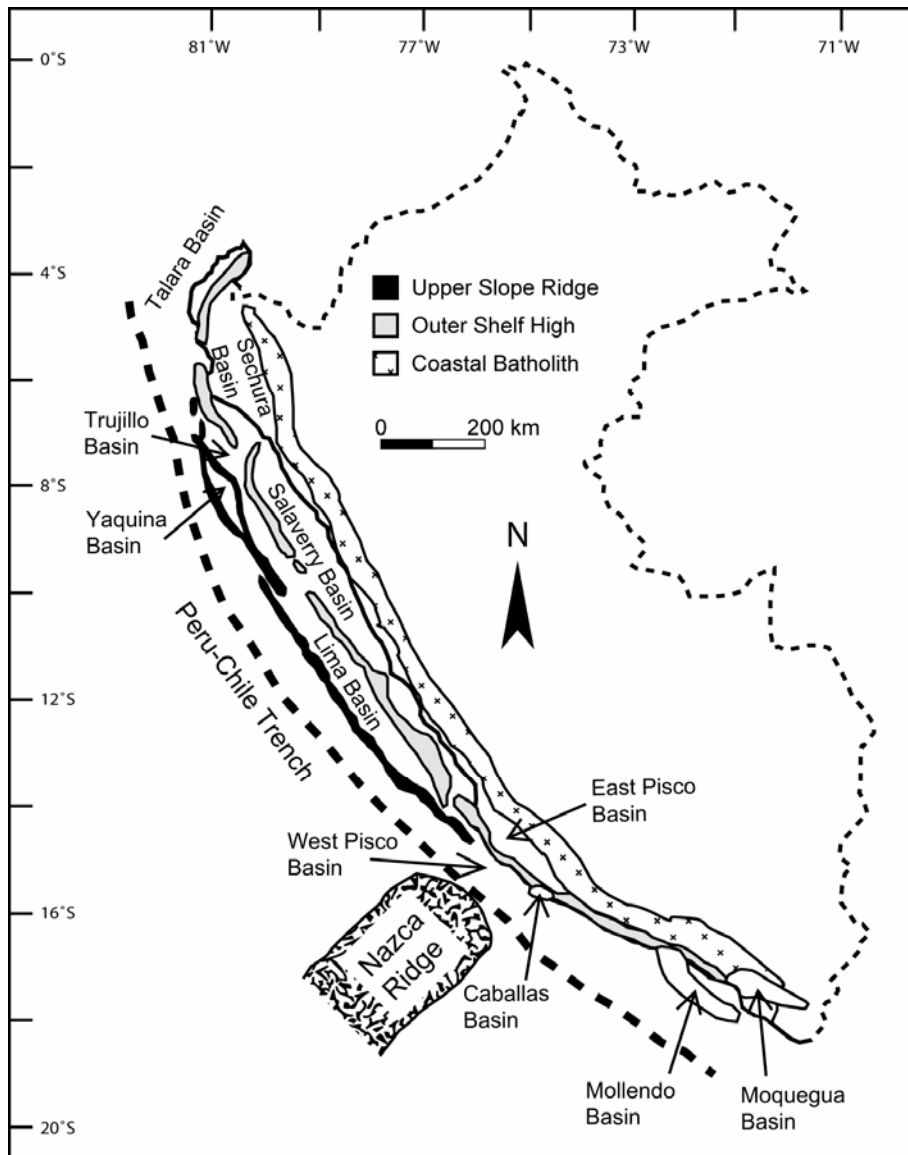


**Figure 2.4:** Map of the forearc basins of Coastal Peru, adapted from (Dunbar et al., 1990).

a) The Sechura basin of northern Peru is bounded to the west by the Precambrian and Palaeozoic rocks of the Cerros Illescas, an onshore extension of the Outer Shelf High, and to the east by the Western Cordillera. The Outer Shelf High is cored by metamorphic and crystalline rocks (Caldas et al., 1980). The sedimentary units in the Sechura Basin range from late Eocene to Pleistocene in age and were deposited during four major transgressive cycles (DeVries, 1988; Dunbar et al., 1990), upper Eocene (~35 Ma), lower Miocene (~20 Ma), mid- upper Miocene (~15-5 Ma) and upper Miocene (~5 Ma). The upper Miocene unit is unconformably overlain by continental Pliocene – Pleistocene deposits. Within the sedimentary deposits of the Sechura basin four major hiatuses are present which span the periods of before middle Eocene (>40 Ma), the early Eocene - Oligocene (i.e. ~37-24 Ma), early – mid Miocene (~18-15 Ma) and late Miocene (~8-7 Ma).

b) The East Pisco basin is bounded to the west by the Coastal Cordillera and to the east by the Coastal Batholith. The sedimentary units in the East Pisco Basin range in age from middle Eocene to the earliest Pleistocene. According to DeVries (1998) within these sedimentary sequences six hiatus recording major transgressions during the Cenozoic are present. These are middle Eocene (>41 Ma), early Oligocene (~34-31 Ma), late Oligocene (~28-25 Ma), middle Miocene (~16-14 Ma), late Miocene (~11-10 Ma), and early Pliocene (~5-4 Ma). Pleistocene marine terraces crop out along the coastal scarp. Their high elevations of up to 600 – 700 m are interpreted to result from uplift during the subduction of the Nazca Ridge beneath this part of the Peruvian fore-arc (Hampel et al., 2004a; Hampel et al., 2004b; Hsu, 1992; Hsu et al., 1989; Hsu, 1988; Machare and Ortlieb, 1992)

Also part of the Andean forearc is the Coastal Cordillera composed of the Precambrian Arequipa Massif which is believed to have affinities to Mesoproterozoic Grenvillian orogeny (Wasteneys et al., 1995). The Palaeozoic San Nicolas and Camaná-Atico batholith are also exposed.

c) The Moquega Basin is thought to have initiated sometime during late Paleocene - Eocene time. It is filled with unfossiliferous continental clastic deposits, interbedded with numerous ignimbritic tuffs. The lack of tuffs in the oldest layers makes it difficult to establish an exact initial timeframe. A major unconformity exists within these aggradational strata. Its age is uncertain but is believed to be middle Eocene (Noble et al., 1985) or late Eocene- early Oligocene (Tosdal et al., 1984). From upper Miocene to the present erosion prevails. The Pleistocene consists of three stepped fluvial terraces which were deposited while rivers were down-cutting present-day valleys (Tosdal et al., 1984).

### 2.3.1.2 *The High Andes*

The High Andes can be divided into three sections.

a) The up to 150 km wide Western Cordillera, which is the focus of this study, is made up of Mesozoic-Tertiary age rocks. It is dominated by the impressive Coastal Batholith, consisting of multiple intrusions, with ages ranging from Lower Jurassic to Upper Eocene extending for 1600 km, the length of Peru, subparallel to the coast (Fig. 2.3). It is up to 65 km across and extends through isolated plutons into Ecuador and Chile. More than a thousand plutons are involved with somewhat similar structure and overall petrology. Bussell and Pitcher (1985) described the different lithologies in detail and also suggested that the magmas rose everywhere to a similarly high subvolcanic level in the crust independent of the time of emplacement. Over vertical distances of as much as 4000 m there is no significant change in magma type or in mode of emplacement. Haederle and Atherton (2002) also suggested that the melts ascended to within 2 to 3 km of the surface up dyke-like conduits, then spread laterally to form tabular plutons.

Remnants of several units of Cenozoic volcanic and volcanoclastic rocks cap the Western Cordillera. These rocks range in age from at least Eocene to Quaternary and the older units show effects of compressive deformation.

b) The Altiplano is a high internally drained plain situated at a mean elevation of almost 4000 m, i.e. slightly below the average altitudes of the Western and Eastern Cordillera. It is 150 km wide and 1500 km long, extending southeast of 14°S to northern Argentina (27°S) (Fig. 2.5). The Altiplano is thus restricted to the central part of the Andes. During the Cenozoic the Altiplano was subsiding - the infill resulting from the erosion of the surrounding Cordilleras and from volcanic emissions. Lamb and Hoke (1997) reported a maximum thickness of up to 10'000 m from the Bolivia Altiplano. Cenozoic deposition was not continuous, however Sebrer et al. (1988) and Lamb and Hoke (1997) reported five main depositional periods which are separated by folding and related unconformities.

c) The Eastern Cordillera forms a 4000 m high and 150 km wide plateau. It corresponds to the locus of the "inner magmatic arc" (Clark and Farrar, 1983). During the Cenozoic era the arc has been uplifted forming the Eastern Cordillera. At the same time small intermontane basins were formed within the area. Their substratum in the south is composed of Palaeozoic black shale and quartzite assemblages, while in the north it comprises greenschist to amphibolite facies metamorphic rocks with Mesozoic and Cenozoic strata widely preserved

in thrust footwalls and synclinal cores. Since upper Oligocene time, it was characterised by the occurrence of both mantle and crustal derived magmatism.

### *2.3.1.3 The Subandean Lowlands*

The Subandean Lowlands correspond to the Amazonian piedmont of the Andes. They form a subsiding trough in which debris resulting from the erosion of the Andean Cordillera accumulate. These Andean Lowlands can be subdivided into two narrow zones: the approximately 50 km wide Subandean zone and the Amazonian Foreland plain. The Subandean zone is hilly, with elevations ranging between 400 and 1000 m that corresponds to a Cenozoic fold and thrust belt that was deformed mainly in the late Miocene (Sebrier et al., 1988). The Amazonian foreland plain corresponds to the present-day area of sedimentation and approximately to the easternmost front of the Andean deformation. Due to unfavourable field conditions, the Subandean geology is still poorly known. From Upper Cretaceous to Present it is characterised by five series. These series are of Upper Cretaceous, Palaeogene, Oligocene-Miocene, Neogene and Pleistocene to present age.

### **2.3.2 Radiometric Geochronology**

Numerous age determinations are available for the Western Cordillera and the coastal margin especially for the Coastal Batholith and Arequipa massif with associated intrusions. They have been obtained using various methods: K/Ar (Cobbing et al., 1977; Cobbing et al., 1981; Farrar and Noble, 1976; Giletti and Day, 1968; Laughlin et al., 1968; McBride, 1977; Mckee and Noble, 1982; Moore, 1984; Myers, 1976; Noble, 1978; Noble et al., 1979a; Noble et al., 1984a; Noble et al., 1974; Noble et al., 1978, 1979b; Noble et al., 1990; Noble et al., 1985; Sanchez, 1983; Soler and Bonhomme, 1987, 1988; Stewart et al., 1974; Tosdal et al., 1984; Tosdal et al., 1981; Vatin-Perignon et al., 1982; Vidal, 1987; Wilson, 1975); Ar/Ar (Clark et al., 1990a; Clark et al., 1990b; Quang et al., 2003; Quang et al., 2005); U/Pb (Dalmayrac et al., 1977; Mukasa, 1986; Mukasa and Henry, 1990; Polliand et al., 2005; Wasteneys et al., 1995); Rb-Sr (Beckinsale et al., 1985; Bellon and Lefevre, 1976; James et al., 1976; Shackleton et al., 1979; Stewart et al., 1974).

Ages pertinent to this study are discussed below.

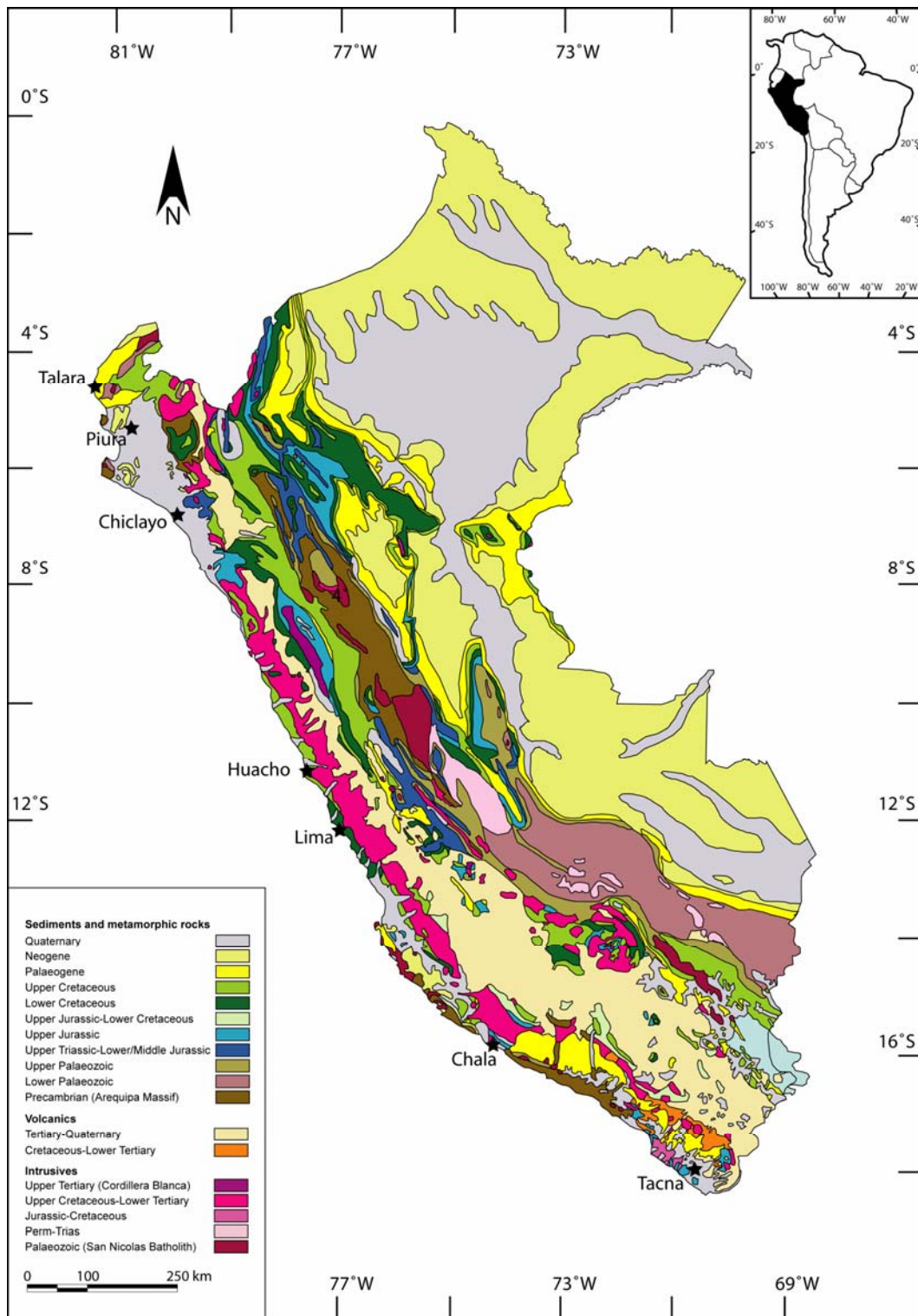


Figure 2.5: The geology of Peru

### 2.3.2.1 Arequipa Massif and San Nicolás Batholith

The Arequipa massif forms the western margin of southern Central Peru (Fig. 2.5). Its basement is composed of granulite facies paragneisses, dioritic gneisses, and migmatites and has a protolith age of ~1900 Ma (Dalmayrac et al., 1977; Shackleton et al., 1979; Wasteneys et al., 1995). It is thought to represent an exotic terrane that originated as the tip of a pre-Grenville Laurentian promontory, comprising Labrador, Greenland and Scotland that was embedded into the proto-Andean margin during the Grenville orogeny (Wasteneys et al., 1995). The Grenville orogen is thought to be the result of the collision between Laurentia and Amazonia in the Mesoproterozoic (Sadowski and Bettencourt, 1996; Vidal, 1987; Wasteneys et al., 1995). Peak metamorphic assemblages consisting of hypersthene-sillimanite-garnet indicate ~8.5-10 kb pressure at 900°C, which in places are extensively retrograded. U-Pb zircon geochronology indicates peak metamorphism for two granulite facies domains that took place at ~1198 Ma and ~970 Ma (Wasteneys et al., 1995). K/Ar ages on biotite have yielded ~675 and ~642 Ma (Stewart et al., 1974). These gneisses are unconformably overlain by greenschist tilloids, psammites, carbonates, phyllites and slates. Correlating the tilloids with the Port Askaig tillite in Scotland would imply that they are of Neoproterozoic age. The Arequipa Massif is truncated, either by tectonic erosion due to subduction (von Huene and Scholl, 1991), or by detachment of a large piece of basement, the Oaxaquia Terrane, as was proposed by Dalziel (1994).

The San Nicolás Batholith in southwestern Peru (Fig. 2.5) is interpreted as the root of the magmatic arc resulting from eastward subduction of oceanic crust along the active margin of Gondwana during the Palaeozoic (Mukasa and Henry, 1990). Ordovician – Devonian ages obtained for the lower intercepts in U/Pb geochronology of basement rocks along the western Arequipa-Antofalla Craton reflect thermal overprinting and Pb-loss coinciding with peaks of this Paleozoic magmatic activity (Damm et al., 1994; Damm et al., 1990; Mukasa and Henry, 1990; Mukasa et al., 1990; Shackleton et al., 1979; Tosdal, 1996). Deepening of the basin and increased subsidence rates broadly coincide in time with this Ordovician-Devonian peak of magmatic activity, and demonstrate the syntectonic character of deposition, in close relationship with tectonic piling and uplifting along the fold-thrust belt (Diaz Martinez, 1996; Sempere, 1995)

### 2.3.2.2 *The Coastal Batholith*

The Coastal Batholith, which constitutes the most intensively outcropping plutonic suite in Peru (Fig. 2.5), is a complex set of I-type medium to high-K granitoids that have been described in great detail by Pitcher (1985) and Cobbing et al. (1981) and references therein. In central Peru the Coastal Batholith predominantly intrudes rocks of the Albian - Cenomanian Casma Group. Numerous age determinations exist for the Coastal Batholith. They have been obtained primarily through K/Ar (McBride, 1977; Stewart et al., 1974; Wilson, 1975); Ar/Ar (Clark et al., 1990a; Noble et al., 1990), whole-rock Rb/Sr (Beckinsale et al., 1985; Stewart et al., 1974) and zircon U-Pb (Mukasa, 1986; Wasteneys et al., 1995). Direct comparison between these ages cannot be made, because the studies using these different isotopic systems were carried out during separate projects. Mukasa (1986) observed however that in central and southern Peru U/Pb ages are slightly older or statistically indistinguishable from the K/Ar ages. He concluded that these similarities were the result of rapid cooling and that any younger ages were due to loss of radiogenic argon resulting from younger intrusions or hydrothermal activity. In the easternmost part of the Coastal Batholith K/Ar ages have also been reported to be reset by Oligocene-Miocene tectonothermal effects due to loss of argon (Soler and Bonhomme, 1987). Clark et al. (1990a) reported Ar/Ar ages which are statistically identical to conventional K/Ar ages (Beckinsale et al., 1985; McBride, 1977) from the Ilo area in southern Peru. Uncertainties in Rb/Sr are generally high, probably due to Sr-heterogeneities of the magmas (Soler and Rotach-Toulhoat, 1990).

The radiochronological data suggest that the Batholith was emplaced in a series of magmatic episodes between late Albian and late Palaeocene (~102-59 Ma). The number of age determinations however is small in comparison with the numbers of individual plutons. The geographic stability of the magmatic front in central Peru suggests that the tectonic deformation in late Albian (105-100 Ma) did not significantly change the shape of the active margin (Jaillard et al., 1996; Megard, 1984; Soler and Rotach-Toulhoat, 1990). The plutonic belt was basically stable for more than 40 myrs (102-59 Ma) (Bussell and Pitcher, 1985), resulting in the whole Batholith being less than 60 km in width, with an average of 45 km. Nevertheless, in detail, the distribution of the successive superunits, at least in the Lima region (the area with the most complete field and radiochronological data set), suggests that the plutonic belt did migrate slightly eastward with time (Moore, 1984; Mukasa, 1986; Soler and Rotach-Toulhoat, 1990).

In central-southern Peru intrusions are dated at 101-94 Ma with K/Ar (Beckinsale et al., 1985; McBride, 1977) and Ar/Ar (Clark et al., 1990a) on hornblende and biotite. A magmatic pulse in Central Peru with high plutonic activity during Turonian time (94-90 Ma) has been shown to have occurred by Beckinsale et al. (1985) applying Rb/Sr and K/Ar by Mukasa (1986) using U/Pb.

During late Turonian-early Coniacian significant wrench movements associated with a variable compressional regime took place in the Coastal Batholith of Peru (Bussell and Pitcher, 1985). Plutonic intrusions are very scarce and volcanic activity is unknown between early Coniacian and Santonian (~90--~84 Ma) forming a magmatic gap (Soler and Bonhomme, 1987).

A major plutonic pulse in the Coastal Batholith of central Peru followed in the late Santonian – early Campanian, during which mainly granodioritic bodies were emplaced. Based on K/Ar ages and on radiometric data by several authors (Beckinsale et al., 1985; Cobbing et al., 1981; Moore, 1984; Mukasa, 1986; Mukasa et al., 1984; Soler and Bonhomme, 1987; Stewart et al., 1974) this episode lasted from 84-78 Ma. From 75-59 Ma there was more or less continuous magmatic activity during which the magmatic belt broadened less however than between 101-84 Ma (Soler and Bonhomme, 1990).

### 2.3.3 Late Mesozoic – Cenozoic events

The Andean genesis is characterised by relatively short tectonic phases that may have lasted a few hundred thousand years to a few million years (Jaillard et al., 1996; Megard, 1984) and by longer intervals of relative tectonic quiescence (Fig. 2.6).

The Pacific slope of the Western Cordillera displays a series of major pediments that are interpreted as regionally extensive erosional surfaces (McLaughlin, 1924; Quang et al., 2005; Sandeman et al., 1995; Steinmann, 1929; Tosdal et al., 1984; Tosdal et al., 1981). They are believed to have been rapidly generated by uplift and led to the recognition of important Mesozoic and Cenozoic events and subsequent erosion. The establishment of their ages by radiometric dating of overlying ash layers was first introduced by Hollingworth and Rutland (1968) and Rutland (1971) in northern Chile. Clark et al. (1967) and Mortimer (1973) extended the record of central Andean physiographic uplift back into the Miocene and Eocene, respectively. At the latitudes of Peru no landforms *per se* from the Palaeocene to early Eocene interval have survived. The Tertiary geomorphic features of the Eastern Cordillera are more complex and will not be discussed further here.

Below is listed a chronological sequence of tectonic phases taken from the various studies (Fig. 2.6). Many events have been identified by different authors but often there are regional differences and all events may not be recognised throughout Peru. The nomenclature originally defined by Steinmann (1929) and McLaughlin (1929) has subsequently been extended by various authors but is not clearly defined in some cases.

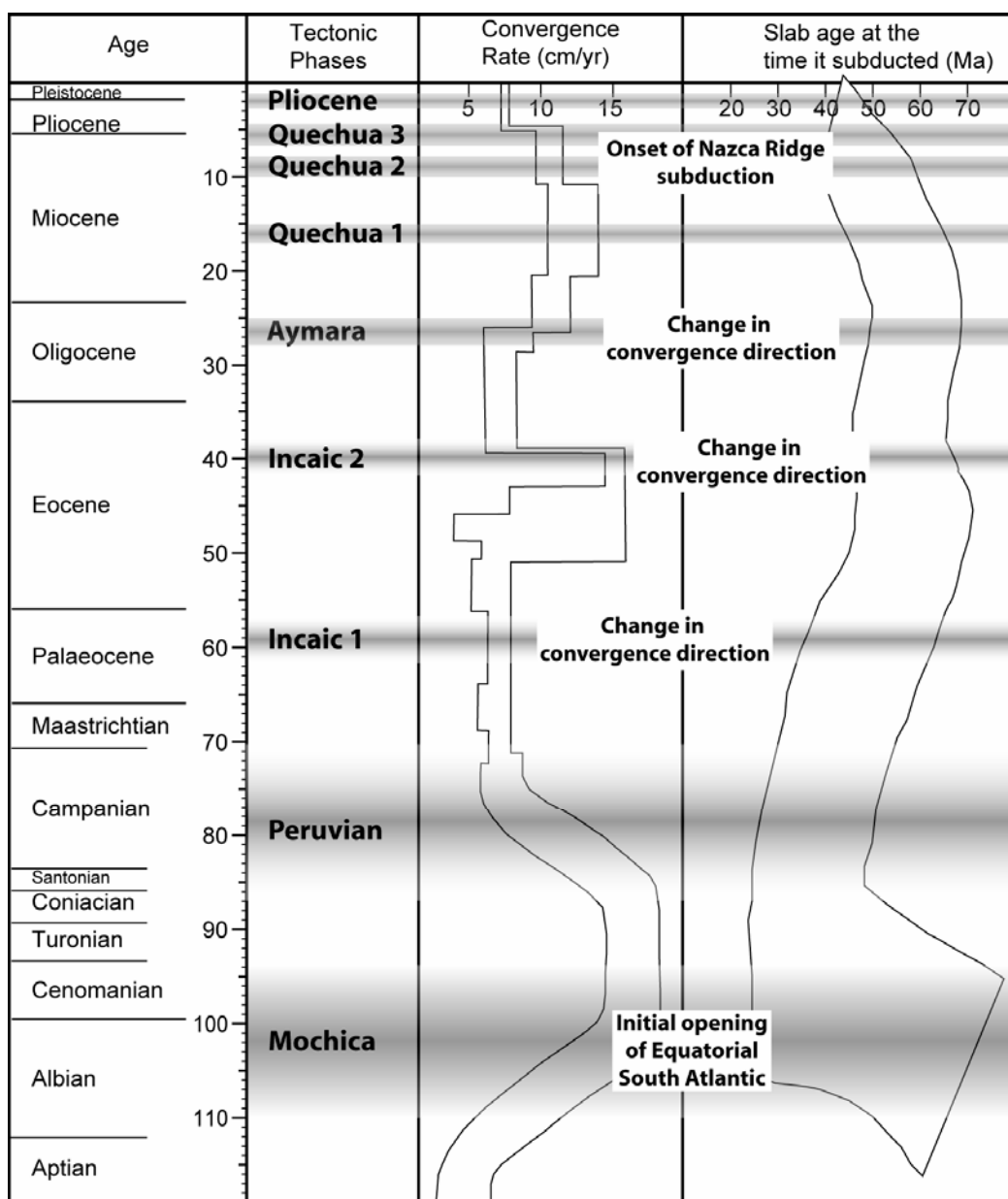


**Figure 2.6:** Relation between tectonic events, convergence rate and age of the slab during subduction. Tectonic events after Jaillard et al. (2000), Sandemann et al. (1995) and Sebrier et al. (1988); convergence rate after Norabuena et al. (1998) and Soler and Bonhomme (1990); age of the slab after Soler and Bonhomme (1990).

### 2.3.3.1 *The Mochica phase*

During late Aptian to early Albian the Peruvian margin underwent extensional tectonic activity (Jaillard, 1987). The westernmost part of the margin recorded the intense volcanic activity of a magmatic arc that formed the Casma Group (Atherton et al., 1985; Soler and Bonhomme, 1990) and the beginning of upper-crustal intrusions associated with the Coastal Batholith (Beckinsale et al., 1985; Soler and Bonhomme, 1990). The period of folding of the Casma Group was named the “Mochica Phase” by Megard (1984) and extended to various events recorded during the late Aptian–middle Cenomanian period by Jaillard (1994) (Fig. 2.6). Volcanic activity ceased by late Albian -early Cenomanian times, as the western part of the margin was deformed by these compressional events (Jaillard et al., 1996), which was probably associated with a strong dextral wrenching component (Bussell and Pitcher, 1985) and is recorded by extensional synsedimentary tectonic features (Jaillard, 1994).

### 2.3.3.2 *The Peruvian Phase*

The Peruvian tectonic phase of Late Cretaceous age (Fig. 2.6) is a widespread episode of deformation observed in the western Cordillera of the of Peruvian Andes (Jaillard et al., 1996; McLaughlin, 1929; Megard, 1978, 1984). In southern Peru the Peruvian Phase postdates Coniacian (~88 Ma) marine beds and predates red beds of Campanian (~72 Ma) and younger age (Vicente et al., 1979). In central and northern Peru the correlations are less clear. North of 13°S a major unconformity is observed; marine sedimentation is replaced by continental red bed deposits. Benavides (1956) considered the unconformity to be the result of the Late Cretaceous Peruvian orogenic phase. However based on K-Ar ages determined on plagioclase and sanidine, Noble et al. (1990) questioned the Cretaceous age of this observed major unconformity and assigned it to the Palaeocene Incaic I phase.

### 2.3.3.3 *The Incaic Phase*

The Incaic phase originally defined by McLaughlin (1929) and Steinmann (1929) is commonly considered to be the main phase of shortening in the Peruvian and Bolivian Andes (Fig. 2.6). The intensely deformed north-eastern belt of the Western Cordillera in central and northern Peru is a response of the Incaic phase. Erosional surfaces believed to have formed subsequent to uplift due to the Incaic phase have been reported by several authors (McLaughlin, 1929; Noble et al., 1974; Noble et al., 1979b; Noble et al., 1990; Noble et al., 1985; Quang et al., 2005; Steinmann, 1929; Tosdal et al., 1984; Tosdal et al., 1981). Based on

radiometric ages of volcanic rocks unconformably overlying these erosional surfaces the phase was divided into two discrete phases the Incaic 1 and 2 phases by Bussell (1983), McKee (1990) and Noble et al. (1985).

a.) The Incaic 1 pulse is poorly defined but Bussell (1983) and Noble et al. (1985) assigned it an early Tertiary age. A K-Ar age of a plagioclase from a fresh rhyolite located 500 m above the unconformity previously thought to be Late Cretaceous yielded an age of 54.8 Ma (Noble et al., 1990). The same author therefore suggested an age of ~60 Ma for the unconformity. This age frame is supported by Quang et al. (2003) and Quang et al. (2005) who report supergene modification of upper Palaeocene porphyry copper deposits in southern Peru and northern Chile during the Palaeocene. This phase is most likely caused by a change in the convergence direction of the South American and the Farallon plates from north and/or north-northeast to northeast (Pardocacas and Molnar, 1987).

b.) The Incaic 2 event was the result of intensified compressional tectonism (Farrar et al., 1988; Horton et al., 2001; McQuarrie and DeCelles, 2001). This phase produced isoclinal and locally recumbent folds and imbricate thrust faults (Megard, 1978, 1984) in central and northern Peru. In both areas plutons of Late Cretaceous or early Palaeogene age were unroofed (Noble et al., 1978, 1979b). The resulting major erosion surface is recognised on the Coastal Batholith, as well as on folded Mesozoic strata. On the Coastal Batholith it is today undeformed and nearly horizontal. To the east of the Coastal Batholith this erosion surface was strongly deformed during Neogene times by later pulses of compressive tectonics. Stratigraphic details and radiometric ages of volcanic rocks that overlie this Incaic 2 unconformity demonstrate that the deformation was essentially completed prior to 41 Ma (Noble et al., 1979b). Bussell (1983) assigned the Incaic 2 tectonism a Palaeocene or early Eocene age. It is likely that the Incaic 2 event is somehow linked to a major reorganisation of the motion of the Pacific plate which is recorded by the Hawaiian-Emperor Elbow (Gordon and Jurdy, 1986). The Incaic 2 phase is equivalent to the Incaic tectonic phase defined by McLaughlin (1929) and Steinmann (1929) in the Western Cordillera of central Peru at the latitude of Lima and with the “F1 Incaic event” described by Sebrier et al. (1988) and Sebrier and Soler (1991).

The post Incaic 2 erosional surface has been mapped as far south as 14° south (Noble et al., 1979a; Salazar, 1970). Based on further radiometric ages from central Peru and on coarse basal conglomerates which overlie the volcanics, Noble et al. (1979a) assumed that active volcanism was taking place prior to and during uplift related to the Incaic 2 phase. Small

volumes of volcanics are present above the dated horizons; and only few intrusive bodies with ages between ~35 and ~25 Ma are known from northern or central Peru (Cobbing et al., 1981; Noble et al., 1979a; Noble et al., 1990; Soler and Bonhomme, 1987, 1990) indicating that the interval between the late Eocene and the late Oligocene was a period of tectonic and magmatic quiescence (Baker and Francis, 1978; McKee et al., 1990; Petersen, 1958).

South of 14°S neither the post Incaic 1 or 2 can be identified through geomorphic expressions. Clark et al. (1990a; 1990b) state that the Incaic orogeny was represented by widespread but probably minor uplift, folding and erosion in the Western Cordillera in southern Peru. Supergene alunite from the Cerro Verde porphyry Cu-Mo cluster from Arequipa dated by Ar/Ar show maximum ages of 36.1 to 38.8 Ma (Quang et al., 2003; Quang et al., 2005), implying that the supergene activity was underway by the late Eocene. This activity was probably in response to the uplift and erosion during the Incaic 2 tectonism. Similar late-Eocene to early Oligocene ages for supergene activity are documented in northern Chile (Bouzari and Clark Alan, 2002; Rowland and Clark Alan, 2001; Sillitoe and McKee, 1996). Southern Peru was mostly close to sea level during the Oligocene which infers that any relief and erosional surfaces present in the early and middle Palaeogene were degraded by the Oligocene (Tosdal et al., 1984; Tosdal et al., 1981).

#### 2.3.3.4 *The Aymara Phase*

The Aymara phase of the middle to late Oligocene time (Fig. 2.6) is recognised by various authors throughout the central Andes. It is unclear however whether it occurred synchronously across the entire central Andes. The dominant physiographic feature in southern Peru extending to the Chilean border is an erosion surface which slopes regularly towards the coast and upon which thin to moderately thick sequences of Tertiary sedimentary rocks and silicic tuffs have been deposited. Tosdal et al. (1984) termed this surface Altos de Camilaca Plain and assigned it an Oligocene age. Biotite of ash flows yield K-Ar ages of 25.3 to 22.7 Ma (Tosdal et al., 1984; Tosdal et al., 1981). Quang et al. (2005) reported Ar/Ar ages on plagioclase, hornblende and biotite ranging from 25.5 to 23.1 Ma. The late Eocene supergene activity at Cerro Verde near Arequipa in southern Peru was overprinted at 28.0 to 24.4 Ma by renewed supergene activity, that also generated minor natroalunite veinlets (Quang et al., 2003). Equivalent ages of supergene activity are also documented for the Santa Rosa deposits also near Arequipa (Quang et al., 2003). The late Oligocene leaching, inferred

to have occurred, beneath the surface provides a minimum age for the final configuration of this landform.

These ages are similar to the K-Ar ages of 23.3-18.7 Ma reported by (Noble et al., 1979a) on biotite, sanidine and plagioclase for tuffs in the Nazca Formation in central Peru. It remains unclear however what the age of the underlying erosional surface is. Tosdal et al. (1984) proposed that the surface is the equivalent of the Altos the Camilace surface further south while Noble et al. (1979a) argued that the conglomerates underlying the ignimbrites might be of Eocene age. In this case the surface might be equivalent to the post Incaic 2 surface and subject to erosion and deposition from Eocene to early Miocene. Early Miocene volcanics of similar age are also found in northern Peru. They unconformably overlie formations of late Palaeogene age. Noble et al. (1990) reported a plagioclase K/Ar age of 23.2 Ma which is in excellent agreement with the 21.0 Ma determined by Laughlin et al. (1968) on hydrothermally altered rocks. Clark et al. (1990a) reported a 29.0 Ma year old ignimbrite that most likely predates the erosion event.

The precise age of the unconformity in north Peru remains uncertain however. Gaps in the sedimentary rocks in the Sechura- and East Pisco basin (Fig. 2.5) of 37-24 Ma (Dunbar et al., 1990) Ma and 28-24 Ma (DeVries, 1998) respectively, can tentatively be associated with these unconformities further inland. The time frame is in accord with the very broadly defined late Oligocene to Early Miocene “tectonic crisis” of Sempere et al. (1990) and Sempere et al. (1994), the “Quechua 1” event of Lavenu (1989), the “Ayamará (F2)” event of Sebrier et al. (1988) and Sebrier and Soler (1991), all of which are reported to be between 28 and 25 Ma in age. The activity is represented by a short-lived pulse of magmatism associated with largely transtensional stress regimes and probably crustal thickening. This late Oligocene event was important in southern Peru because it heralded the orogenesis that generated the modern Andes (Kennan, 2000). The coarse-grained fore-arc deposits indicate that the palaeo-Andes of southern Peru were more actively uplifted than those of the central Peru during Oligocene to early Miocene times (Jaillard et al., 2000). According to Sebrier and Soler (1991) this compressional event is associated with the beginning of the increase in Miocene Andean convergence (Fig. 2.6). The high convergence rate is thought to be caused by the break-up of the oceanic South Farallon plate into the Nazca- and the Cocos-Plates (Gordon and Jurdy, 1986). This break-up is also believed to have led to a nearly orthogonal convergence direction towards the Peru-Chile trench.

### 2.3.3.5 *The Quechua Phases*

The Miocene in southern Peru was punctuated by Quechuan tectonic events (Ellison, 1991; Mckee and Noble, 1982; Megard, 1984; Sebrier and Soler, 1991) resulting in major crustal thickening and uplift.

a) The “Quechua 1 (F3)” phase which lasted from ~17 to ~15 Ma (Sebrier et al., 1988; Sebrier and Soler, 1991) is poorly known and structures related to this tectonic pulse (monoclinical folds and reverse faults) appear to be few (Sebrier et al., 1988). Unconformably overlying formations are imprecisely dated or the unconformities are unclear. In the Western Cordillera of central Peru, middle – late Eocene Incaic structures were reactivated (Megard, 1984; Megard et al., 1984). This reactivation led to uplift of 400 m (Sebrier et al., 1988) and triggered large scale incision (Huaman, 1985; Sebrier et al., 1988; Sebrier et al., 1979; Tosdal et al., 1984; Tosdal et al., 1981). Valleys were cut to approximately their present depth in central Peru (Noble et al., 1990) as well as in southern Peru (Tosdal et al., 1981).

b) The “Quechua 2 (F4)” event lasted from ~10 to ~8 Ma (Megard et al., 1984; Sebrier and Soler, 1991). The phase is interpreted to be the result of the beginning of nearly “en bloc” eastward thrusting of the palaeo-Andes onto the Brazilian and Guiana shields. The movement resulted in crustal thickening and rapid uplift of the arc zones and palaeo-Andes, and the transfer of active deformation into the Subandean thrust and fold belts (Jaillard et al., 2000). Prior and contemporaneously to this phase palaeo-valleys were filled and mantled by sheets of ignimbrites. Their radiometric ages (K/Ar) range from 14.2 Ma to 8.9 Ma (Noble et al., 1990; Thouret et al., 2005; Tosdal et al., 1981) in the south and from 10.2 to 8 Ma (Farrar and Noble, 1976; McKee et al., 1986; Noble et al., 1984b; Petersen et al., 1977) in the north. In the Pacific Piedmont of southernmost Peru, the middle Miocene phase is coeval with an erosional period that formed stepped pediplains (Tosdal et al., 1984). The Quechua 2 (F4) is characterised by a period of uplift marked by erosion and depositional areas restricted to the fore-arc domains.

c) The contractional “Quechua 3 (F5)” phase which took place 7-4 Ma is the result of an east-west shortening (Megard, 1984; Sebrier et al., 1988). The event is well documented along the whole Andean chain. In the Western Cordillera the event is marked by strike-slip and reverse faulting as well as folding (Sebrier et al., 1988). The arc-zones of northern and central Peru are marked by an effusive pulse centred around 4-6 Ma of ignimbritic tuffs associated with rhyolitic dykes in the Western Cordillera (Soler and Bonhomme, 1990). In the Cordillera Negra tuffs, dated by K/Ar at about 6 Ma (Farrar and Noble, 1976; Myers, 1976) fill steep

canyons that are cut into the western slope. In southern Peru alkaline, peraluminous and shoshonitic suites were emplaced along major fault systems (Carlier et al., 1996).

#### *2.3.3.6 The Pliocene Phase*

The most recent event described is the “F6” phase that was proposed by Sebrier et al. (1988) and Sebrier and Soler (1991) at approximately 2 Ma. In the Western Cordillera it is however not yet clearly characterised (Sebrier et al., 1988; Sebrier and Soler, 1991). The effects of this latest Neogene compressional phase are locally recognisable reverse and strike slip faults as well as monoclinical folds. These kind of structures affect marine upper Pliocene sediments near Pisco and Camana (Sebrier et al., 1988).

#### **2.3.4. Recent morphology and landscape evolution**

Offshore the topography is dominated by the Peru-Chile trench and the bathymetry changes remarkably as the Nazca Ridge approaches the continental margin. Where the buoyant Nazca Ridge subducts, the depth of the trench decreases to 5200-4800 m (Fig. 2.2, Chapter 3). This submarine Ridge is almost 250 km wide and its crest rises 1600 m above the surrounding seafloor. It is interesting to note that the shoaling only exists where the ridge subducts today. Immediately to the north and south of the ridge the trench deepens again.

Like the bedrock geology, the large-scale topography today has also a strong northwest-southeast trend subparallel to the coast (Fig. 2.1).

The topography of the western margin (Western Cordillera) that is part of the proposed study area is dominated to the south of 16°S by the active volcanic arc. North of this latitude the arc does not exist and active volcanoes are absent. This limit coincides with the change in subduction angle that in turn might be related to the presence of the Nazca Ridge as previously discussed (Fig. 2.2). The westward drainage from the Cordillera into the Pacific is generally very simple. The rivers are mostly sourced in Mesozoic to Cenozoic sediments of the Western Cordillera and all cross the Coastal Batholith before reaching the coast. Above the present location of the subducting Nazca Ridge, rivers in the coastal area are rerouted (see Chapter 3).

The Altiplano is the northern extension of the “Bolivian Orocline“, which extends into southern Peru. A compound internal drainage system exists in this very flat region. The eastern side of the Eastern Cordillera has a somewhat complicated drainage system, directed

towards the Amazon with dispersion direction both orogen parallel and orogen normal. The drainage basins vary in size.

## 2.4 Climate of western margin

The present climatic zones of the Andes are also orogen parallel, (Fig. 2.7). Climate is a major parameter which has an influence on the development of the topography through erosion. The region of the Coastal and San Nicolas Batholiths and the Arequipa Massif is dominantly dry for the full length of Peru. The constancy of climate therefore reduces the parameters that may have had an impact on erosion seen through low temperature thermochronometry, assuming constancy over time.

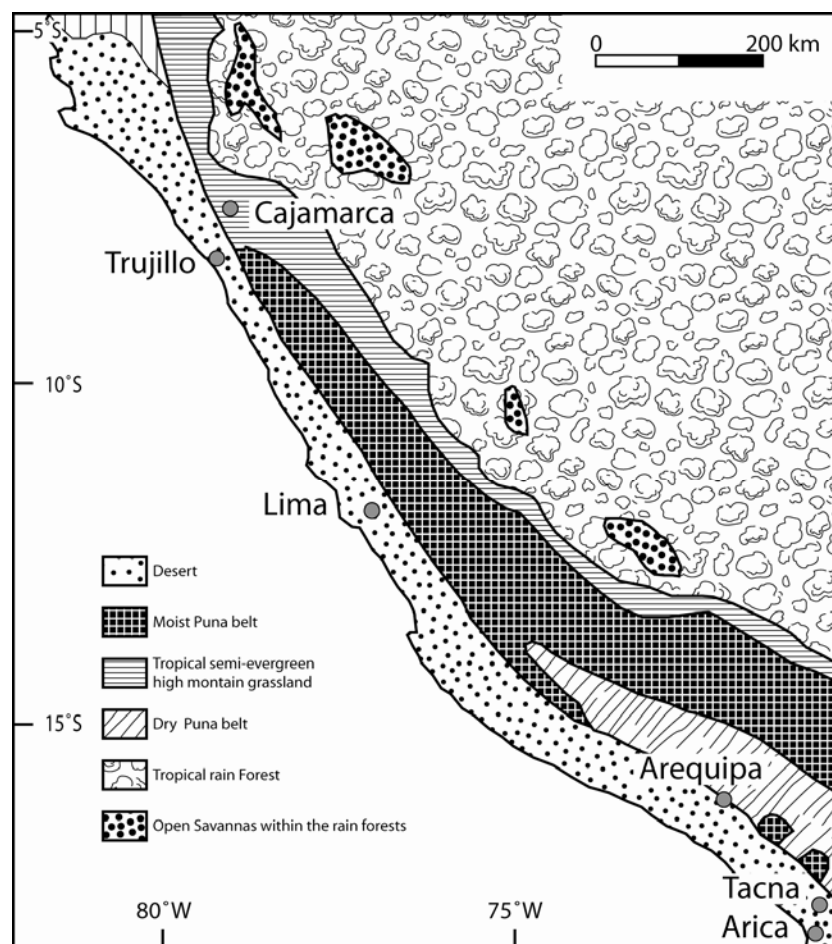


Figure 2.7: Climate zones of Peru, after Troll (1968)

## 2.5 References cited

- Abbott, D., Drury, R., and Smith, W.H., 1994, Flat to Steep Transition in Subduction Style: *Geology*, v. 22, p. 937-940.
- Atherton, M.P., Warden, V., and Sanderson, L.M., 1985, The Mesozoic marginal basin of Central Peru: A geochemical study of within-plate-edge volcanism, *in* Pitcher, W.S., Cobbing, E.J., and Beckinsale, R.D., eds., *Magmatism at a Plate Edge: The Peruvian Andes*: London, Blackie Halsted Press, p. 47-58.
- Baker, M.C.W., and Francis, P.W., 1978, Upper Cenozoic Volcanism in Central Andes - Ages and Volumes: *Earth and Planetary Science Letters*, v. 41, p. 175-187.
- Barazangi, M., and Isacks, B.L., 1976, Spatial-Distribution of Earthquakes and Subduction of Nazca Plate beneath South-America: *Geology*, v. 4, p. 686-692.
- Beckinsale, R.D., Sanchez-Fernandez, A.W., Brook, M., Cobbing, E.J., Taylor, W.P., and Moore, N.D., 1985, Rb-Sr whole-rock isochron and K-Ar age determinations for the Coastal Batholith of Peru, *in* Pitcher, W.S., and Atherton, M.P., eds., *Magmatism at a Plate Edge: The Peruvian Andes*: Glasgow, Blackie, p. 177-202.
- Bellon, H., and Lefevre, C., 1976, Geochronological Data on Andean Volcanism from Southern Peru - Volcano-Tectonic Implications: *Comptes Rendus Hebdomadaires Des Seances De L Academie Des Sciences Serie D*, v. 283, p. 1-4.
- Benavides, V., 1956, Cretaceous system in Northern Peru, *American Journal of Natural History Bulletin*, Volume 108: New York, p. 352-494.
- Bevis, M., 1986, The Curvature of Wadati-Benioff Zones and the Torsional Rigidity of Subducting Plates: *Nature*, v. 323, p. 52-53.
- Bouzari, F., and Clark Alan, H., 2002, Anatomy, evolution, and metallogenic significance of the supergene orebody of the Cerro Colorado porphyry copper deposit; I Region, northern Chile: *Economic Geology*, v. 97, p. 1701-1740.
- Bussell, M.A., 1983, Timing of tectonic and magmatic events in the Central Andes of Peru, v. 140, p. 279-286.
- Bussell, M.A., and Pitcher, W.S., 1985, The structural control of batholith emplacement, *in* Atherton, M.P., Cobbing, E.J., and Beckinsale, R.D., eds., *Magmatism at a Plate edge: The Peruvian Andes*: Glasgow, Blackie, p. 167-176.
- Cahill, T., and Isacks, B.L., 1992, Seismicity and Shape of the Subducted Nazca Plate: *Journal of Geophysical Research-Solid Earth*, v. 97, p. 17503-17529.
- Caldas, J., Palacios, O., Pecho, V., and Vela, C., 1980, Geologia de los Cuadrangulos de: Bayovar, Sechura, La Redonda, Pta. la Negra, Lobos de Tierra, Las Salinas y Morrope.: *Boletin de la sociedad Geologica del Peru*, v. Ser. A. 32, p. 78pp.
- Carlier, G., Lorand, J.-P., Bonhomme, M.G., and Carlotto, V., 1996, A reappraisal of the Cenozoic inner arc magmatism in Southern Peru: consequences for the evolution of the Central Andes for the past 50 Ma., 3rd. International Symposium on Andean Geodynamiques (ISAG 1996), Volume Extended Abstracts: St. Malo, p. 551-554.
- Clark, A.H., and Farrar, E., 1983, Evolution of the Central Andean magmatic arc: *EOS*, v. 18, p. 326.
- Clark, A.H., Farrar, E., Kontak, D.J., Langridge, R.J., Arenas, M.J., France, L.J., McBride, S.L., Woodman, P.L., Wasteneys, H.A., Sandeman, H.A., and Archibald, D.A., 1990a, Geologic and Geochronological Constraints on the Metallogenic Evolution of the Andes of Southeastern Peru: *Economic Geology and the Bulletin of the Society of Economic Geologists*, v. 85, p. 1520-1583.

- Clark, A.H., Mayer, A.E.S., Mortimer, C., Sillitoe, R.H., Cook, R.V., and Snelling, N.J., 1967, Implications of the isotopic ages of ignimbrite flows, southern Atacama Desert, Chile: *Nature*, v. 215, p. 723-724.
- Clark, A.H., Tosdal, R.M., Farrar, E., and Plazolles, A., 1990b, Geomorphologic Environment and Age of Supergene Enrichment of the Cuajone, Quellaveco, and Toquepala Porphyry Copper-Deposits, Southeastern Peru: *Economic Geology and the Bulletin of the Society of Economic Geologists*, v. 85, p. 1604-1628.
- Cloos, M., 1993, Lithospheric Buoyancy and Collisional Orogenesis - Subduction of Oceanic Plateaus, Continental Margins, Island Arcs, Spreading Ridges, and Seamounts: *Geological Society of America Bulletin*, v. 105, p. 715-737.
- Cobbing, E.J., Ozard, J.M., and Snelling, N.J., 1977, Reconnaissance Geochronology of Crystalline Basement Rocks of Coastal Cordillera of Southern Peru: *Geological Society of America Bulletin*, v. 88, p. 241-246.
- Cobbing, E.J., Pitcher, W.S., Wilson, J.J., Baldock, J.W., Taylor, W.P., McCourt, W., and Snelling, N.J., 1981, *The geology of the Western Cordillera of northern Peru*: London, Institute of Geological Sciences, 143 p.
- Cross, T.A., and Pilger, R.H., 1982, Controls of Subduction Geometry, Location of Magmatic Arcs, and Tectonics of Arc and Back-Arc Regions: *Geological Society of America Bulletin*, v. 93, p. 545-562.
- Dalmayrac, B., Lancelot, J.R., and Leyreloup, A., 1977, 2-Billion-Year Granulites in Late Precambrian Metamorphic Basement Along Southern Peruvian Coast: *Science*, v. 198, p. 49-51.
- Dalziel, I.W.D., 1994, Precambrian Scotland as a Laurentia-Gondwana Link - Origin and Significance of Cratonic Promontories: *Geology*, v. 22, p. 589-592.
- Damm, K.W., Harmon, R.S., and Kelley, S., 1994, Some isotopic and geochemical constraints on the origin and evolution of the Central Andean basement (19 - 24S), *in* Reutter, K.J., Scheuber, E., and P.J., W., eds., *Tectonics of the Southern Central Andes: Structure and Evolution of an Active Continental Margin*: Berlin, Springer, p. 263-276.
- Damm, K.W., Pichowiak, S., Harmon, R.S., Todt, W., Omarini, R., and Niemeyer, H., 1990, Pre-Mesozoic evolution of the Central Andes-the basement revisited: *Geological Society of America Special Paper*, v. 241, p. 101-126.
- DeVries, T.J., 1988, The geology of late Cenozoic marine terraces (tablazos) in northwestern Peru: *Journal of South American Earth Sciences*, v. 1, p. 121-136.
- , 1998, Oligocene deposition and Cenozoic sequence boundaries in the Pisco Basin (Peru): *Journal of South American Earth Sciences*, v. 11, p. 217-231.
- Diaz Martinez, E., 1996, Sintesis estratigráfica y geodinamica del Carbonifero de Bolivia, *Congreso Geologico de Bolivia*, Volume 1: Tarija, p. 355-367.
- Dunbar, R.B., Marty, R.C., and Baker, P.A., 1990, Cenozoic Marine Sedimentation in the Sechura and Pisco Basins, Peru: *Palaeogeography Palaeoclimatology Palaeoecology*, v. 77, p. 235-261.
- Ellison, R.A., 1991, The geology of the Western Cordillera and Altiplano west of Lake Titicaca, southern Peru: *Overseas Geology and Mineral Resources Series*, v. 65, p. 53.
- Farrar, E., Clark, A.H., Kontak, D.J., and Archibald, D.A., 1988, Zongo-San Gaban Zone - Eocene Foreland Boundary of the Central Andean Orogen, Northwest Bolivia and Southeast Peru: *Geology*, v. 16, p. 55-58.
- Farrar, E., and Noble, D.C., 1976, Timing of Late Tertiary Deformation in Andes of Peru: *Geological Society of America Bulletin*, v. 87, p. 1247-1250.

- Garver, J.I., Reiners, P.W., Walker, L.J., Ramage, J.M., and Perry, S.E., 2005, Implications for timing of Andean uplift from thermal resetting of radiation-damaged zircon in the Cordillera Huayhuash, northern Peru: *Journal of Geology*, v. 113, p. 117-138.
- Gephart, J.W., 1994, Topography and Subduction Geometry in the Central Andes - Clues to the Mechanics of a Noncollisional Orogen: *Journal of Geophysical Research-Solid Earth*, v. 99, p. 12279-12288.
- Giletti, B.J., and Day, H.W., 1968, Potassium-Argon Ages of Igneous Intrusive Rocks in Peru: *Nature*, v. 220, p. 570-&.
- Gordon, R.G., and Jurdy, D.M., 1986, Cenozoic global plate motions: *Journal of Geophysical Research*, v. 91, p. 12389-12406.
- Gutscher, M.A., Olivet, J.L., Aslanian, D., Eissen, J.P., and Maury, R., 1999, The "Lost Inca Plateau": cause of flat subduction beneath Peru?: *Earth and Planetary Science Letters*, v. 171, p. 335-341.
- Gutscher, M.A., Spakman, W., Bijwaard, H., and Engdahl, E.R., 2000, Geodynamics of flat subduction: Seismicity and tomographic constraints from the Andean margin: *Tectonics*, v. 19, p. 814-833.
- Haederle, M., and Atherton, M.P., 2002, Shape and intrusion style of the Coastal Batholith, Peru: *Tectonophysics*, v. 345, p. 17-28.
- Hampel, A., 2002, The migration history of the Nazca Ridge along the Peruvian active margin: a re-evaluation: *Earth and Planetary Science Letters*, v. 203, p. 665-679.
- Hampel, A., Adam, J., and Kukowski, N., 2004a, Response of the tectonically erosive south Peruvian forearc to subduction of the Nazca Ridge: Analysis of three-dimensional analogue experiments: *Tectonics*, v. 23, p. TC 5003, doi: 10.1029/2003TC001585.
- Hampel, A., Kukowski, N., Bialas, J., Huebscher, C., and Heinbockel, R., 2004b, Ridge subduction at an erosive margin: The collision zone of the Nazca Ridge in southern Peru: *Journal of Geophysical Research-Solid Earth*, v. 109, p. B02101, doi: 10.1029/2003JB002593.
- Hasegawa, A., and Sacks, I.S., 1981, Subduction of the Nazca Plate beneath Peru as Determined from Seismic Observations: *Journal of Geophysical Research*, v. 86, p. 4971-4980.
- Hollingworth, S.E., and Rutland, R.W.R., 1968, Studies of Andean uplift - Part I, Post-Cretaceous evolution of the San Bartolomea, north Chile.: *Geological Journal*, v. 6, p. 49-62.
- Horton, B.K., Hampton, B.A., and Waanders, G.L., 2001, Paleogene synorogenic sedimentation in the Altiplano plateau and implications for initial mountain building in the central Andes: *Geological Society of America Bulletin*, v. 113, p. 1387-1400.
- Hsu, J.T., 1992, Quaternary uplift of the Peruvian coast related to the subduction of the Nazca Ridge; 13.5 to 15.6 degrees south latitude., in Berryman-Kelvin-R., O.-Y.N.-A.-R., ed., *Impacts of tectonics on Quaternary coastal evolution.*, Volume Quaternary International: Oxford, Pergamon, p. 87-97.
- Hsu, J.T., Leonard, E.M., and Wehmiller, J.F., 1989, Aminostratigraphy of Peruvian and Chilean Quaternary Marine Terraces: *Quaternary Science Reviews*, v. 8, p. 255-262.
- Hsu, J.T.J., 1988, Emerged Quaternary marine terraces in southern Peru; sea level changes and continental margin tectonics over the subducting Nazca Ridge [Doctoral thesis]: Ithaca, NY, United States, Cornell University.
- Huaman, D., 1985, *Évolution tectonique cénozoïque et néotectonique du piémont pacifique dans la région d'Arequipa (Andes du Sud du Pérou)*: Orsay, Paris.

- Jaillard, E., 1987, Sedimentary evolution of an active margin during Middle and Upper Cretaceous times; the North Peruvian margin from late Aptian up to Senonian: *Geologische Rundschau*, v. 76, p. 677-697.
- , 1994, Kimmeridgian to Paleocene tectonic and Geodynamic evolution of the Peruvian (and Ecuadorian) margin., *in* Salfity, J.A., ed., *Cretaceous Tectonics in the Andes: Braunschweig/Wiesbaden, Earth Evolution sciences.*
- Jaillard, E., Herail, G., Monfret, T., and Diaz Martinez, E., 2000, Tectonic evolution of the Andes of Equador, Peru, Bolivia and northernmost Chile  
In: *Tectonic evolution of South America*, *in* Cordani Umberto, G., Milani Edison, J., and Thomaz Filho, A., eds., *Tectonic Evolution of South America*, In-Folo Producao Editorial Grafica e Programacao Visual. Rio de Janeiro Brazil. 2000., p. 481-559.
- Jaillard, E., Soler, P., Dewey John, F., and Lamb Simon, H., 1996, Cretaceous to early Paleogene tectonic evolution of the northern Central Andes (0-18 degrees S) and its relations to geodynamics  
In: *Geodynamics of the Andes: Tectonophysics*, v. 259, p. 41-53.
- James, D.E., Brooks, C., and Cuyubamba, A., 1976, Andean Cenozoic Volcanism - Magma Genesis in Light of Strontium Isotopic Composition and Trace-Element Geochemistry: *Geological Society of America Bulletin*, v. 87, p. 592-600.
- Jischke, M.C., 1975, Dynamics of Descending Lithospheric Plates and Slip Zones: *Journal of Geophysical Research*, v. 80, p. 4809-4813.
- Jordan, T.E., Isacks, B.L., Ramos, V.A., and Allmendinger, R.W., 1983, Mountain Building in the Central Andes: Episodes, p. 20-26.
- Kennan, L., 2000, Large-scale geomorphology of the Andes: interrelationships of tectonics, magmatism and climate, *in* Summerfield, M., ed., *Geomorphology and global Tectonics*, John Wiley and sons Ltd., p. 267-199.
- Kukowski, N., and Pecher, I., 1999, Thermo-hydraulics of the Peruvian accretionary complex at 12 degrees S: *Journal of Geodynamics*, v. 27, p. 373-402.
- Kukowski, N., Vonhuene, R., Malavieille, J., and Lallemand, S.E., 1994, Sediment Accretion against a Buttress beneath the Peruvian Continental-Margin at 120-Degrees-S as Simulated with Sandbox Modeling: *Geologische Rundschau*, v. 83, p. 822-831.
- Lamb, S., and Hoke, L., 1997, Origin of the high plateau in the Central Andes, Bolivia, South America: *Tectonics*, v. 16, p. 623-649.
- Laughlin, A.W., Damon, P.E., and Watson, B.N., 1968, Potassium-Argon Dates from Toquepala and Michiquillay Peru: *Economic Geology*, v. 63, p. 166-&.
- Machare, J., and Ortlieb, L., 1992, Plioquaternary Vertical Motions and the Subduction of the Nazca Ridge, Central Coast of Peru: *Tectonophysics*, v. 205, p. 97-108.
- McBride, S.L., 1977, A K-Ar study of the Cordillera Real Bolivia and its regional setting: Kingston, Canada, Queens University.
- Mcgeary, S., Nur, A., and Benavraham, Z., 1985, Spatial Gaps in Arc Volcanism - the Effect of Collision or Subduction of Oceanic Plateaus: *Tectonophysics*, v. 119, p. 195-221.
- Mckee, E.H., and Noble, D.C., 1982, Miocene Volcanism and Deformation in the Western Cordillera and High Plateaus of South-Central Peru: *Geological Society of America Bulletin*, v. 93, p. 657-662.
- McKee, E.H., Noble, D.C., Ericksen, G.E., Pinochet, M.T., and Reinemund, J.A., 1990, Cenozoic tectonic events, magmatic pulses, and base- and precious-metal mineralization in the Central Andes  
In: *Geology of the Andes and its relation to hydrocarbon and mineral resources*, Circum-Pacific Council for Energy and Mineral Resources. Houston TX United States. 1990.

- McKee, E.H., Noble, D.C., and Vidal, C., 1986, Timing of Volcanic and Hydrothermal Activity, Huancavelica Mercury District, Peru: *Economic Geology*, v. 81, p. 489-492.
- McLaughlin, D.H., 1924, Geology and physiography of the Peruvian cordillera, Departments of Junin and Lima: *Geological Society of America Bulletin*, v. 35, p. 591-632.
- , 1929, Review of Steinmann, G: *Geologie von Peru-Heidelberg*, Carl Winters Universitätsbuchhandlung, 448p.: *Economic Geology*, v. 24, p. 664-669.
- McNulty, B., and Farber, D., 2002, Active detachment faulting above the Peruvian flat slab: *Geology*, v. 30, p. 567-570.
- McNulty, B.A., Farber, D.L., Wallace, G.S., Lopez, R., and Palacios, O., 1998, Role of plate kinematics and plate-slip-vector partitioning in continental magmatic arcs: Evidence from the Cordillera Blanca, Peru: *Geology*, v. 26, p. 827-830.
- McQuarrie, N., and DeCelles, P., 2001, Geometry and structural evolution of the central Andean backthrust belt, Bolivia: *Tectonics*, v. 20, p. 669-692.
- Megard, F., 1978, Etude géologique des Andes du Pérou central: *Mémoires ORSTOM*, v. 86, p. 310.
- , 1984, The Andean Orogenic Period and Its Major Structures in Central and Northern Peru: *Journal of the Geological Society*, v. 141, p. 893-900.
- Megard, F., Noble, D.C., McKee, E.H., and Bellon, H., 1984, Multiple Pulses of Neogene Compressive Deformation in the Ayacucho Intermontane Basin, Andes of Central Peru: *Geological Society of America Bulletin*, v. 95, p. 1108-1117.
- Moore, N.D., 1984, Potassium-Argon Ages from the Arequipa Segment of the Coastal Batholith of Peru and Their Correlation with Regional Tectonic Events: *Journal of the Geological Society*, v. 141, p. 511-519.
- Mortimer, C., 1973, The Cenozoic history of the southern Atacama Desert, Chile: *Geological Society of London Journal*, v. 129, p. 505-526.
- Mukasa, S.B., 1986, Zircon U-Pb Ages of Super-Units in the Coastal Batholith, Peru - Implications for Magmatic and Tectonic Processes: *Geological Society of America Bulletin*, v. 97, p. 241-254.
- Mukasa, S.B., and Henry, D.J., 1990, The San-Nicolas Batholith of Coastal Peru - Early Paleozoic Continental Arc or Continental Rift Magmatism: *Journal of the Geological Society*, v. 147, p. 27-39.
- Mukasa, S.B., Tilton, G.R., Harmon, R.S., and Barreiro Barbara, A., 1984, Lead isotope systematics in batholithic rocks of the western and coastal cordilleras, Peru In: *Andean magmatism; chemical and isotopic constraints*, Shiva Publ., Nantwich United Kingdom. 1984.
- Mukasa, S.B., Vidal, C.E., and Injoqueespinoza, J., 1990, Pb Isotope Bearing on the Metallogenesis of Sulfide Ore-Deposits in Central and Southern Peru: *Economic Geology and the Bulletin of the Society of Economic Geologists*, v. 85, p. 1438-1446.
- Muller, R.D., Roest, W.R., Royer, J.Y., Gahagan, L.M., and Sclater, J.G., 1997, Digital isochrons of the world's ocean floor: *Journal of Geophysical Research-Solid Earth*, v. 102, p. 3211-3214.
- Myers, J.S., 1976, Erosion surfaces and ignimbrite eruption, measures of Andean uplift in northern Peru: *Journal of Geology*, v. 11, p. 29-44.
- Noble, D.C., 1978, Cenozoic Volcanic and Tectonic Evolution of Andes of Peru - Summary of on-Land Geologic Data: *Transactions-American Geophysical Union*, v. 59, p. 383-383.
- Noble, D.C., Farrar, E., and Cobbing, E.J., 1979a, Nazca Group of South-Central Peru - Age, Source, and Regional Volcanic and Tectonic Significance: *Earth and Planetary Science Letters*, v. 45, p. 80-86.

- Noble, D.C., McKee, E.H., Eyzaguirre, V.R., and Marocco, R., 1984a, Age and Regional Tectonic and Metallogenic Implications of Igneous Activity and Mineralization in the Andahuaylas-Yauri Belt of Southern Peru: *Economic Geology*, v. 79, p. 172-176.
- Noble, D.C., McKee, E.H., Farrar, E., and Petersen, U., 1974, Episodic Cenozoic Volcanism and Tectonism in Andes of Peru: *Earth and Planetary Science Letters*, v. 21, p. 213-220.
- Noble, D.C., McKee, E.H., and Megard, F., 1978, Eocene Uplift and Unroofing of Coastal Batholith near Lima, Central Peru: *Journal of Geology*, v. 86, p. 403-405.
- , 1979b, Early Tertiary Incaic Tectonism, Uplift, and Volcanic Activity, Andes of Central Peru: *Geological Society of America Bulletin*, v. 90, p. 903-907.
- Noble, D.C., McKee, E.H., Mourier, T., and Megard, F., 1990, Cenozoic Stratigraphy, Magmatic Activity, Compressive Deformation, and Uplift in Northern Peru: *Geological Society of America Bulletin*, v. 102, p. 1105-1113.
- Noble, D.C., Seabrier, M., Megard, F., and McKee, E.H., 1985, Demonstration of 2 Pulses of Paleogene Deformation in the Andes of Peru: *Earth and Planetary Science Letters*, v. 73, p. 345-349.
- Noble, D.C., Vogel, T.A., Peterson, P.S., Landis, G.P., Grant, N.K., Jezek, P.A., and McKee, E.H., 1984b, Rare-Element Enriched, S-Type Ash-Flow Tuffs Containing Phenocrysts of Muscovite, Andalusite, and Sillimanite, Southeastern Peru: *Geology*, v. 12, p. 35-39.
- Norabuena, E., Leffler-Griffin, L., Mao, A.L., Dixon, T., Stein, S., Sacks, I.S., Ocola, L., and Ellis, M., 1998, Space geodetic observations of Nazca-South America convergence across the central Andes: *Science*, v. 279, p. 358-362.
- Nur, A., and Benavraham, Z., 1981, Volcanic Gaps and the Consumption of Aseismic Ridges in South-America: *Geological Society of America Memoirs*, v. 154, p. 729-740.
- , 1983, Volcanic Gaps Due to Oblique Consumption of Aseismic Ridges: *Tectonophysics*, v. 99, p. 355-362.
- Olbertz, D., Wortel, M.J.R., and Hansen, U., 1997, Trench migration and subduction zone geometry: *Geophysical Research Letters*, v. 24, p. 221-224.
- Pardocasas, F., and Molnar, P., 1987, Relative Motion of the Nazca (Farallon) and South-American Plates since Late Cretaceous Time: *Tectonics*, v. 6, p. 233-248.
- Pennington, W.D., 1984, The Effect of Oceanic Crustal Structure on Phase-Changes and Subduction: *Tectonophysics*, v. 102, p. 377-398.
- Petersen, U., 1958, Structure and uplift of the Andes of Peru, Bolivia, Chile and adjacent Argentina: *Sociedad Geológica del Perú*, v. 33, p. 57-129.
- Petersen, U., Noble, D.C., Arenas, M.J., and Goodell, P.C., 1977, Geology of Julcani Mining District, Peru: *Economic Geology*, v. 72, p. 931-949.
- Pilger, R.H., 1981, Plate Reconstructions, Aseismic Ridges, and Low-Angle Subduction beneath the Andes: *Geological Society of America Bulletin*, v. 92, p. 448-456.
- Polliand, M., Schaltegger, U., Frank, M., and Fontbote, L., 2005, Formation of intra-arc volcanosedimentary basins in the western flank of the central Peruvian Andes during Late Cretaceous oblique subduction: field evidence and constraints from U-Pb ages and Hf isotopes: *International Journal of Earth Sciences*, v. 94, p. 231-242.
- Quang, C.X., Clark, A.H., Lee, J.K.W., and Guillen, J.B., 2003, Ar-40-Ar-39 ages of hypogene and supergene mineralization in the Cerro Verde-Santa Rosa porphyry Cu-Mo cluster, Arequipa, Peru: *Economic Geology and the Bulletin of the Society of Economic Geologists*, v. 98, p. 1683-1696.
- Quang, C.X., Clark, A.H., Lee, J.K.W., and Hawkes, N., 2005, Response of supergene processes to episodic Cenozoic uplift, pediment erosion, and ignimbrite eruption in the porphyry copper province of southern Peru: *Economic Geology*, v. 100, p. 87-114.

- Ramos, V., and Aleman, A., 2000, Tectonic Evolution of the Andes, *in* Cordani Umberto, G., Milani Edison, J., and Thomaz Filho, A., eds., Tectonic Evolution of South America, In-Folo Producao Editorial Grafica e Programacao Visual. Rio de Janeiro Brazil. 2000., p. 635-685.
- Rowland, M., and Clark Alan, H., 2001, Temporal overlap of supergene alteration and high-sulfidation mineralization in the Spence porphyry copper deposit, Il Región, Chile: Geological Society of America Abstracts, v. 33, p. A-358.
- Rutland, R.W.R., 1971, Andean orogeny and ocean floor spreading: *Nature*, v. 233, p. 252-255.
- Sacks, I.S., 1983, The Subduction of Young Lithosphere: *Journal of Geophysical Research*, v. 88, p. 3355-3366.
- Sadowski, G.R., and Bettencourt, J.S., 1996, Mesoproterozoic tectonic correlations between eastern Laurentia and the western border of the Amazon Craton: *Precambrian Research*, v. 76, p. 213-227.
- Salazar, H., 1970, Mapa geologico del Dpto. de Huancavelica; 1.250'000: Servicio Nacional de Geología y Minería del Perú.
- Sanchez, A.W., 1983, Edades K-Ar en rocas intrusivas del area de Ilo, Dpto. de Moqugua: Geological Society Perú, p. 183-192.
- Sandeman, H.A., Clark A., H., and Farrar, E., 1995, An Integrated Tectono-Magmatic Model for the Evolution of the Southern Peruvian Andes (13°-20°) since 55 Ma: *International Geology Review*, v. 37, p. 1039-1073.
- Sebrier, M., Lavenu, A., Fornari, M., and Soulas, J.-P., 1988, Tectonics and uplift in Central Andes (Peru, Bolivia, and Northern Chile) from Eocene to Present: *Géodynamique*, v. 3, p. 85-106.
- Sebrier, M., Marocco, R., Gross, J.J., Macedo, S., and Montoya, R., 1979, Evolución neógena del piedemonte Pacífico de los andes del sur del Perú, Segundo Congreso Geológico Chileno: Arica, p. 177-178.
- Sebrier, M., and Soler, P., 1991, Tectonics and magmatism in the Peruvian Andes from late Oligocene time to the present  
In: Andean magmatism and its tectonic setting: Geological Society of America Bulletin Special Paper, v. 265, p. 259-278.
- Sempere, T., 1995, Phanerozoic evolution of Bolivia and adjacent areas., *in* Tankard, A.J., Suarez, R., and Welsink, H.J., eds., Petroleum Basins of South America, Volume 62: AAPG Memoir, AAPG, p. 207-230.
- Sempere, T., Herail, G., Oller, J., and Bonhomme, M.G., 1990, Late Oligocene Early Miocene Major Tectonic Crisis and Related Basins in Bolivia: *Geology*, v. 18, p. 946-949.
- Sempere, T., Marshall, L.G., Rivano, S., and Godoy, E., 1994, Late Oligocene Early Miocene Compressional Tectosedimentary Episode and Associated Land-Mammal Faunas in the Andes of Central Chile and Adjacent Argentina (32-37-Degrees-S): *Tectonophysics*, v. 229, p. 251-264.
- Shackleton, R.M., Ries, A.C., M.P., C., and Cobbold, P.R., 1979, Structure, metamorphism and geochronology of the Arequipa Massif of coastal Peru: Geological Society of London, v. 136, p. 195-214.
- Sillitoe, R.H., and McKee, E.H., 1996, Age of supergene oxidation and enrichment in the Chilean porphyry copper province: *Economic Geology and the Bulletin of the Society of Economic Geologists*, v. 91, p. 164-179.
- Soler, P., and Bonhomme, M.G., 1987, K-Ar Radiochronological Data on the Granitoids of the Eastern Cordillera of Central Peruvian Andes - Tectonic Implications: *Comptes Rendus De L Academie Des Sciences Serie Ii*, v. 304, p. 841-845.

- , 1988, New K-Ar age determinations of intrusive rocks from the Cordillera Occidental and Altiplano of central Peru; identification of magmatic pulses and episodes of mineralization: *Journal of South American Earth Sciences*, v. 1, p. 169-177.
- , 1990, Relations of magmatic activity to Plate dynamics in Central Peru from Cretaceous to Present, *in* Kay, S.M., and C.W., R., eds., *Plutonism from Antarctica to Alaska*, Volume 241, Geological Society of America, p. 173-191.
- Soler, P., and Rotach-Toulhoat, N., 1990, Implications of the time-dependent evolution of Pb- and Sr-isotopic compositions of Cretaceous and Cenozoic granitoids from the coastal region and the lower Pacific slope of the Andes of central Peru  
In: *Plutonism from Antarctica to Alaska*, *in* M., K.S., and C.W., R., eds., *Plutonism from Antarctica to Alaska*, Volume 241: Boulder USA, Geological Society of America (GSA). Boulder CO United States. 1990., p. 161-171.
- Steinmann, G., 1929, *Geologie von Peru-Heidelberg*, Carl Winters Universitätsbuchhandlung, 448p. p.
- Stewart, J.W., Evernden, J.F., and Snelling, N.J., 1974, Age-Determinations from Andean Peru - Reconnaissance Survey: *Geological Society of America Bulletin*, v. 85, p. 1107-1116.
- Suarez, G., Molnar, P., and Burchfiel, B.C., 1983, Seismicity, Fault Plane Solutions, Depth of Faulting, and Active Tectonics of the Andes of Peru, Ecuador, and Southern Colombia: *Journal of Geophysical Research*, v. 88, p. 403-428.
- Thouret, J.-C., Wörner, G., Singer, B., and Finizola, A., 2005, The Central Andes in Peru: "Old" valleys in a "young" mountain range?, 6th. International Symposium on Andean Geodynamics (ISAG 2005), Volume Extended Abstracts: Barcelona, p. 726-729.
- Tosdal, R.M., 1996, The Amazon-Laurentian connection as viewed from the middle proterozoic rocks in the central Andes, western Bolivia and northern Chile: *Tectonics*, v. 15, p. 827-842.
- Tosdal, R.M., Clark, A.H., and Farrar, E., 1984, Cenozoic Polyphase Landscape and Tectonic Evolution of the Cordillera Occidental, Southernmost Peru: *Geological Society of America Bulletin*, v. 95, p. 1318-1332.
- Tosdal, R.M., Farrar, E., and Clark, A.H., 1981, K-Ar Geochronology of the Late Cenozoic Volcanic-Rocks of the Cordillera Occidental, Southernmost Peru: *Journal of Volcanology and Geothermal Research*, v. 10, p. 157-173.
- Troll, C., 1968, Geo-Ecology of the mountainous Regions of the tropical Americas, *in* Troll, C., Hahn, H., Kuls, W., and Lauer, W., eds., UNESCO Natural Resources Research Division, Volume 9: Mexico, *Colloquium Geographicum*, p. p. 37.
- Vatin-Perignon, N., Vivier, G., Sebrier, M., and Fornari, M., 1982, Les derniers événements andins marqués par le volcanisme cénozoïque de la cordillère occidentale sud-péruvienne et de son piémont pacifique entre 15°45 et 18°S: *Bulletin Société Géologique France*, v. 24, p. 649-650.
- Vicente, J.C., Sequeiros, F., Vladivía, M.A., and Zavala, J., 1979, El sobre-escurrimientode Cincha-Luta: elemento del accidente mayor andino al NW de Arequipa: *Boletín de la sociedad Geologica del Peru*, v. 61, p. 67-100.
- Vidal, C.E., 1987, Kuroko-Type Deposits in the Middle Cretaceous Marginal Basin of Central Peru: *Economic Geology*, v. 82, p. 1409-1430.
- Vlaar, N.J., 1983, Thermal Anomalies and Magmatism Due to Lithospheric Doubling and Shifting: *Earth and Planetary Science Letters*, v. 65, p. 322-330.
- Vlaar, N.J., and Wortel, M.J.R., 1976, Lithospheric Aging, Instability and Subduction: *Tectonophysics*, v. 32, p. 331-351.

- 
- von Huene, R., Kulm, L.D., and Miller, J., 1985, Structure of the Frontal Part of the Andean Convergent Margin: *Journal of Geophysical Research-Solid Earth and Planets*, v. 90, p. 5429-5442.
- von Huene, R., Pecher, I.A., and Gutscher, M.A., 1996, Development of the accretionary prism along Peru and material flux after subduction of Nazca Ridge: *Tectonics*, v. 15, p. 19-33.
- von Huene, R., and Scholl, D.W., 1991, Observations at Convergent Margins Concerning Sediment Subduction, Subduction Erosion, and the Growth of Continental-Crust: *Reviews of Geophysics*, v. 29, p. 279-316.
- Wasteneys, H.A., Clark, A.H., Farrar, E., and Langridge, R.J., 1995, Grenvillian Granulite-Facies Metamorphism in the Arequipa Massif, Peru - a Laurentia-Gondwana Link: *Earth and Planetary Science Letters*, v. 132, p. 63-73.
- Wilson, P.A., 1975, K-Ar studies in Peru with special reference to the emplacement of the Coastal Batholith [Ph.D. thesis]: Liverpool, University of Liverpool.
- Wortel, M.J.R., and Vlaar, N.J., 1976, Age-Dependent Subduction of Oceanic Lithosphere beneath Central and South-America: *Transactions-American Geophysical Union*, v. 57, p. 676-676.



# Chapter 3

## The subducting Nazca Ridge: Impact on the Geomorphology in South-Central Peru

(submitted to Geology)

M. Wipf<sup>1</sup>, G. Zeilinger<sup>2</sup>, D. Seward<sup>1</sup>, F. Schlunegger<sup>2</sup>

<sup>1</sup> Geological Institute, ETH-Zentrum, Sonneggstr. 5, 8092 Zürich, Switzerland

<sup>2</sup> Institute of Geological Sciences, University of Berne, 3012 Berne, Switzerland

### ABSTRACT

Over the past 10-12 million years the Nazca Ridge has migrated approximately 650 km southward along the Peruvian Coastal margin as it subducts south-eastwards under the South American continent. The relatively simple and uniform geology and climate make South-Central Peru a unique area to study the impact on geomorphology by the passage of a subducting aseismic ridge.

To study this issue, Digital Elevation Models (DEM) based on newly available data of the Peruvian coastal margin were used. Data extracted from these highlight several geomorphological effects. 1: Offshore the depth of the deep-sea trench decreases by 1200 m where the Nazca Ridge collides with the continental South American Plate. 2: Onshore the ridge causes a maximum uplift of almost 1800 m in the Coastal Cordillera forcing the coastline westwards resulting in an almost 100 km wide coastal plain. 3: At the trailing edge of the ridge the coastal plain subsides and the coastline retreats eastward, producing at least part of the indentation observed between Paita and Pisco. 4: The foothills of the Western Cordillera and the drainage divide recede eastwards.

In summary the Nazca Ridge acts like a wave uplifting the Andean margin as it traverses inland and southwards leaving a clear fingerprint in the topographic evolution of the western Peruvian Andes. It appears that no significant topographic effects are observable more than 250 km from the trench.

**KEYWORDS:** Nazca Ridge, Subduction, Exhumation, Digital Elevation Models, Geomorphology, Peru

## INTRODUCTION

The subduction of oceanic lithosphere with strong relief, such as ridges or seamounts, may induce superimposed tectonic effects on continental margins which are different to those effects caused by the subduction of the surrounding "normal" oceanic plate (von Huene and Scholl, 1991). These ridges and seamounts are generally believed to have been sourced at hotspots on or near a mid-ocean ridge and tend to be aseismic and more buoyant than the surrounding ocean floor. This buoyancy may therefore lead to low-angle subduction of less than 45° (Turcotte and Schubert, 2002). Importantly, the occurrence of low-angle subduction and the presence of a relatively buoyant ridge on the subducting slab may initiate a strong effect on the topography of the associated trench as well as on the overlying plate (von Huene and Lallemand, 1990). Further, it has been proposed that tectonic erosion, which exists normally in areas of active subduction, might actually increase with the presence of a subducting ridge (Clift et al., 2003; Hampel et al., 2004a; von Huene and Lallemand, 1990). According to Spence et al. (1999) the subducting Nazca Ridge should provide a continually refreshed topography over the shallow subduction zone as it causes surface uplift. As a consequence, change in base level will result in enhanced exhumation rates of the upper crustal section overlying the slab in comparison to the neighbouring areas. This implicitly states that the flow directions of the rivers, the location of the drainage divides and the magnitudes of the local relief are also likely to adjust in accordance with the rising landmass. We provide a quantitative test of this hypothesis.

### *Background*

The entire length of the Peruvian coastal region consists of the same major lithologies without significant tectonic disturbances and is subject to the same general climatic conditions (Gregory, 2000). The geology, both lithologically and structurally strikes parallel to the coast. The topography in different sections may therefore be relatively easily compared to each other. The Nazca Ridge, rising 1500–2000 m above the surrounding ocean floor, is located on the oceanic Nazca Plate which is being subducted in an essentially east-west (080°E) direction beneath the South American plate (Fig. 3.1). The ridge trends approximately 045° oblique to subduction, which results in a south-eastwards migration of the collision zone with the South American Plate through time. Hampel (2002) calculated that the Nazca Ridge initially collided with the upper plate of the South American continent at ~11° S at ~11Ma. This is synchronous with work describing the "Lost Inca Plateau" in northern Peru and its

subduction between 10 and 12 Myrs ago (Gutscher et al., 1999). It is estimated that 900-1100 km of the Nazca Ridge and the complete “Lost Inca Plateau” to the north have already been subducted and have caused subsequent modifications of the Peruvian coastal margin.

The first order observation of the coastal protrusion where the Nazca Ridge is currently subducting implies uplift of the margin in this region. Cenozoic marine sediments in the East Pisco Basin (Fig. 3.1) between the coastal batholith and the oceanic trench that have been uplifted above sea level (DeVries, 1998; Dunbar et al., 1990) support this interpretation. Precambrian and Palaeozoic strata crop out near Paita in the far north and between Pisco and San Juan. They have also been reported offshore (Kulm, 1982; Sosson et al., 1994) between Pisco and Paita paralleling the structural trend of the onland geology. Their presence suggests that a large component north of the position of the present Nazca Ridge has subsided. This implies downwarping of the coastal margin after the ridge has passed. This is emphasised by the fact that between Paita and the present position of the ridge the coastline is indented eastward. It is tentatively suggested that the indentation of this 1500 km coastline is due to erosion caused by surface uplift and enhanced by later subsidence, which has taken place as the “Lost Inca Plateau” and the Nazca Ridge were passing and subducting.

Further evidence for uplifted sequences related to the passage of the subducted ridge can be seen in late Pleistocene marine terraces that appear to have formed simultaneously along many parts of the South American west coast during sea level maxima (Hsu, 1992; Hsu et al., 1989; Machare and Ortlieb, 1992; Ortlieb et al., 1992). It has been suggested that raised marine terraces near Paita could be correlated with terraces in the Pisco area and regions further south in Peru and Chile (DeVries, 1988). Varying uplift rates of terraces of equal age might record the dynamic passage of the ridge. The region south of the present ridge position serves hereby as a proxy for areas unaffected by ridge subduction. Here marine terraces near Ilo, reach 350 m in altitude (Goy et al., 1990; Navarez, 1964). They have undergone only slow continuous uplift of 0.15 mm/yr (Hsu 1992) that is believed to represent the “background uplift” south of the ridge intersection with the trench. Overlying the Nazca Ridge, Broggi (1946) recognized several marine terraces up to 800 m high. Hsu (1992) determined surface uplift rates over the last 125,000 years of 0.5 mm/yr above the southern flank and of 0.3 mm/yr above the crest of the Nazca Ridge. Machare and Ortlieb (1992) estimated maximum uplift rates of 0.7 mm/yr and recognised that terraces north of the present ridge position, i.e. between Paita and Pisco are absent; presumably due to the subsidence following passage of the ridge. This observation provides further supporting evidence that the

coast subsides after the ridge has passed. It has been argued that enhanced tectonic erosion is at least partly responsible for the subsidence (Clift et al., 2003; Hampel et al., 2004b; Kulm, 1982; von Huene et al., 1996; von Huene et al., 2004).

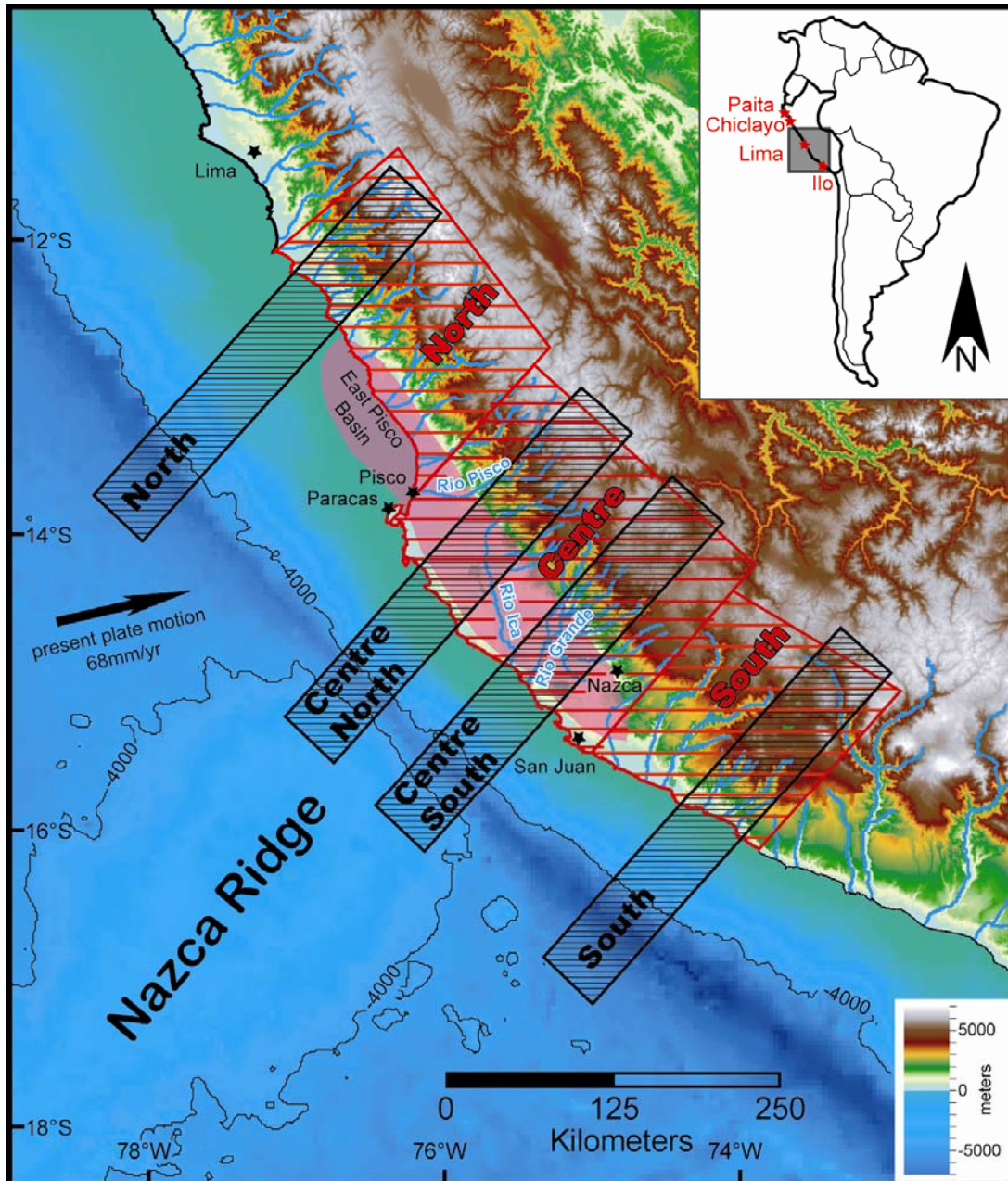


**Figure 3.1.** Digital Elevation Model of the Peruvian coastal margin from 10° to 18°S and from 72° to 82°W. The model was compiled using the SRTM-3 model and offshore data from Smith and Sandwell (1997). Hatched in black colour are the four swaths (North, Centre North, Centre South and South) chosen to extract the topography. Hatched in red colour are the three areas used to extract the river dispersal patterns.

The observed altitudes of the terraces over the Nazca Ridge are predicted by different models (Hampel et al., 2004b; Hsu, 1992). Hsu's model (1992) is a simplified 3-D model and suggests that any point at the coast needs 3.5 myrs to move from a position directly over the southern edge of the ridge to a position directly over the northern edge. Hampel et al. (2004b) using a sandbox model estimated an uplift rate of 0.9 mm/yr reaching a maximum surface uplift of 900 m. Both models predict that maximum uplift would occur, as is observed, above the southern edge and that the maximum altitude is reached within approximately 1 myrs.

In this contribution the models and assumptions mentioned above are tested. The analysis of Digital Elevation Models (DEM's) provides an ideal tool to identify and quantify ridge-induced changes in the topography and to constrain the effects in detail.

## **METHODS**

The influence of the subducting Nazca ridge on the morphometry of the overlying crust is quantified here by using the SRTM-3 DEM which was supplemented by adding offshore data from Smith and Sandwell (1997). The model covers the Peruvian coastal margin from 10° to 18°S and from 72° to 80°W (Fig. 3.1). Gaps in the SRTM-3 Arc Second dataset were filled using a focal-mean function that interpolates within a square of 9 x 9 pixels. Gaps remaining after five iterations were not processed further and treated as nil data in order to avoid generation of unrealistic values. Topographic cross sections were extracted from the DEM in order to quantitatively identify changes in the topography in relation to the present position of the Nazca Ridge and its dynamics in geological time. Accordingly four ridge-parallel swaths were chosen with a width of 60 km and a length of 300 km each (Fig. 3.2). Within these swaths the minimum, the maximum and the mean values were calculated for every grid column. The minimum values can be viewed as a proxy for the elevation of the major valleys. Dispersal directions of rivers were determined based on topographic grain analysis (Chapman, 1952; Guth, 2001) of three areas covering the coastal region, south, over and north of the current position of the Nazca Ridge. The areas are all of a similar size, between 26000 and 32000 km<sup>2</sup> (Fig. 3.1). Calculations were performed for 6000 m wide squares. The distance between the centres of these individual boxes was 6400 m. Within every box the average slope direction was determined and then plotted as a rose diagram (Fig. 3.3). Slopes with less than 3° were excluded from the plots as their directions are considered to be distributed randomly (Guth, 2001).

## RESULTS

### South

The coastline in the southernmost section lies at 105 km distance from the trench (Fig. 3.1). This area displays an almost uniform taper that dips at 2.8°-3.1°.

The topography rises continuously from the trench at 6500m beneath sea level to almost 5000m above sea level in the Western Cordillera (Fig. 3.2). An exception to this continuous topographic rise is the coastal margin where a narrow plain of less than 20km width is present. The local relief on the Western Cordillera (i.e. the difference between the maximum and minimum elevations) reaches a maximum of 2400 m approximately 70km inland. Onshore the minimum altitude cross section, has a concave-up form. The drainage divide is located approximately 185 km east of the trench.

A simple drainage pattern with one dominant dispersal direction perpendicular to the coast is observed, i.e. from the northeast (Fig. 3.3).

### Centre

The second and third swaths were placed over the leading and the trailing edge of the ridge (centre south, and centre north, respectively) (Fig. 3.1).

In these sections the coast is approximately 100 km east of the trench (Fig. 1B). The depth of the trench decreases from 5200 m (centre south) to 4800 m (centre north). From the trench towards the foothills of the Western Cordillera, the form of the envelope of the topography is convex-up. Over the first 50km distance from the trench the dip of the taper is similar to that in the south (ca. 3°) but over the trailing edge of the ridge approximately 60km from the trench the taper displays a distinct break in slope. The surface of the ocean floor between this feature and the coast is flat, approximately 100 m beneath sea level. Near the leading edge, the Coastal Cordillera rises to 1800 m and in the area of the trailing edge to 900 m. In both sections, the foothills of the Western Cordillera are located at ca. 140 km distance from the trench axis. The local relief of the Western Cordillera over the leading edge of the ridge measures up to 2000 m i.e. 900 m less than in the section over the trailing edge farther north. In the section 'centre north' the drainage divide is at 250 km distance from the trench, hence it is located ca. 40 km farther inland than in the region 'centre south'. The drainage directions reveal a large pattern of dispersion ranging from south to west-southwest (Fig. 3.3).

## North

The northernmost section is located ca. 100 km north of the trailing edge of Nazca ridge (Fig. 3.1). Here the coastal plain is submerged to a maximum depth of ca. 1500 m beneath sea level (Fig. 3.2). In this section the coast is located at ca. 160 km distance from the trench and close to the foothills of the Western Cordillera. The depth of the trench is ca. 5500 m. Offshore the envelope of the submerged topography is gently convex-up over a distance of 160 km. The Coastal Cordillera is not present in this section. Onshore, the local relief of the Western Cordillera is 3300 m. The drainage divide is located at ca. 270 km distance from the trench and the drainage pattern shows more scatter compared to the central area (Fig. 3.3).

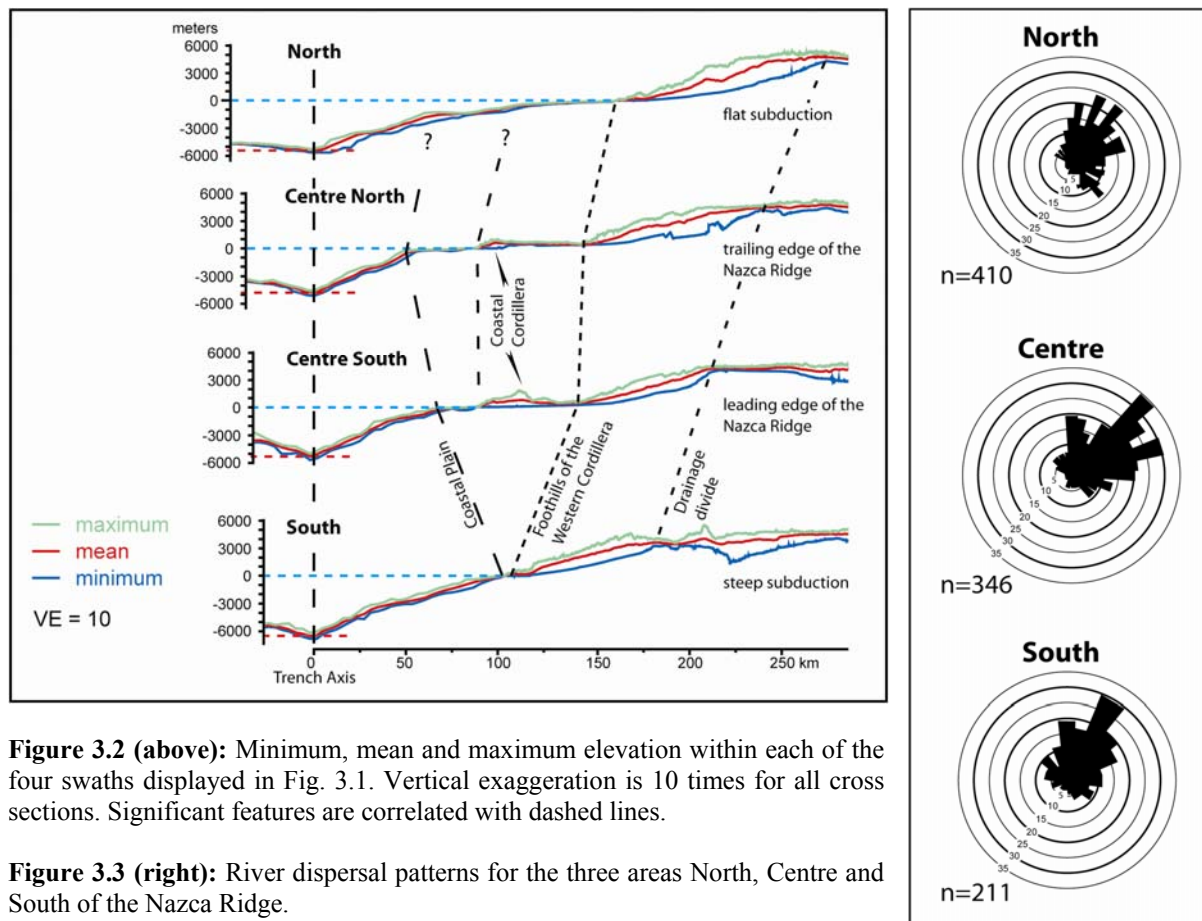


**Figure 3.2 (above):** Minimum, mean and maximum elevation within each of the four swaths displayed in Fig. 3.1. Vertical exaggeration is 10 times for all cross sections. Significant features are correlated with dashed lines.

**Figure 3.3 (right):** River dispersal patterns for the three areas North, Centre and South of the Nazca Ridge.

## DISCUSSION

Assuming that the southern margin of Peru represents the proxy of the “pre ridge subduction” coastline and that the coast was originally equidistant from the trench prior to any impact of the subducting ridge, the changes towards the north of the geomorphic features and the coastline are compared relative to this.

The depth of the trench decreases from 6000 m in the south to 5200 m over the southern section and to 4800 m over the northern section of the ridge. In the very north it drops again to 5500 m. Thus the ridge has uplifted the trench by at least 1200 m. Where the ridge has passed, the trench has begun to readjust to the previous position.

The topography in the south rises from a depth of -6000 m in a uniform manner with a gradient of approximately  $3^\circ$  to almost 4000 m. This slope is broken by a very narrow coastal plain, about 20 km in width. The maximum topographic envelope over the ridge within the first 50-60 km distance from the trench has a similar gradient to the south. A slight bulge which is formed 50km from the trench over the leading edge is interpreted as uplift in response to the underlying Nazca Ridge. Over the trailing edge this bulge evolves to a distinct break in slope 60 km from the trench indicating an increase in width of the coastal plain towards the north. Onshore the Palaeozoic-Precambrian Coastal Cordillera area is up to 1800m high over the leading edge and decreases to 900m over the trailing edge of the ridge presumably due to enhanced surface erosion. Assuming constancy of initial heights and assuming that the timing of the passage of the ridge is 3.5 Ma (Hsu, 1992) then this erosion rate is of the order of 0.26 mm/y. This is in accordance with the estimate of Hsu, (1988) of 0.3 mm/y for the incision rates of the Rio Grande into the Coastal Cordillera.

In the north the dip angle of the taper from the trench to the coast is  $1.8^\circ$  i.e. less than that of the far south and the position of the coastline is further inland than in all other sections. A hint of a break in slope at about 60km from the trench may indicate a remnant of the frontal edge of the subsiding coastal plain.

The ridge induced changes in base level trigger an increase in headward erosion rates. This causes the foothills of the Western Cordillera to shift eastwards and the local relief to increase from approximately 2000 m in the south to 3300 m in the northernmost swath. Furthermore the short term changes of the river dispersal patterns (Fig. 3.3) record these changes and can be directly related to the ridge passage. South of the ridge the drainage is dominantly unidirectional from the northeast. Fission-track ages (Wipf et al., 2005) suggest that this is an old landscape with low erosion rates. The drainage pattern is likely to be old as well. Over the

ridge the drainage has evolved to a more complex system showing a scatter from north to east-northeast. Three directions can tentatively be distinguished (Fig. 3.3). As in the south the rivers flow from the mountains in a preferentially southwest direction. However, where they enter the large coastal plain of the uplifted margin they are diverted southwards before making their way to the coast via the Coastal Cordillera. This is nicely observable in the flow pattern of Rio Ica. North of the ridge adjustment to downwarping is evident in the drainage pattern as it becomes even more scattered. An additional component to the northwest seems to be revealed which might indicate adjustments to the change in the large scale altitude of the topography after down warping.

## **CONCLUSIONS**

Surface uplift caused by the subduction of the Nazca Ridge is followed by subsidence of the coastline as the collision zone moves southward. The absence of major differences in the altitude in the Eastern Cordillera suggests that the impact of the Nazca Ridge decreases from the trench to the drainage divide about 250-275 km inland. Beyond this distance, there is no longer any effect.

The topographic effects of the passage of the Nazca Ridge include changes in depth of the trench uplifted by at least 1200m with renewed increase to greater depths as the ridge passes. The change in the offshore topography is interpreted as a direct influence of the ability of the ridge to uplift the margin. The coastline moves seawards over the ridge indicative of uplift while to the north it retreats eastward, due to drowning of the margin and a landward shift of the foothills by headward erosion (Fig. 3.1). Towards the north the foothills to the Western Cordillera as well as the drainage divide move subsequently to the east while the local relief increases. The unidirectional river dispersal pattern in the south becomes increasingly more complex and scattered northwards. These changes are interpreted to record adjustments to changes in base level caused by uplift and subsequent subsidence.

## **ACKNOWLEDGEMENTS**

We greatly appreciate Darrell Harrison's help to improve this manuscript. This research was supported by the Swiss Sciences Foundation grants 21-63410.00, and is part of PhD thesis of the first author.

**REFERENCES CITED**

- Broggi, J.A., 1946, Las terrazas marina de la Bahia de San Juan en Ica: Boletin de la sociedad Geologica del Peru, v. 19, p. 21-33.
- Clift, P.D., Pecher, I., Kukowski, N., and Hampel, A., 2003, Tectonic erosion of the Peruvian forearc, Lima Basin, by subduction and Nazca Ridge collision: *Tectonics*, v. 22.
- DeVries, T.J., 1988, The geology of late Cenozoic marine terraces (tablazos) in northwestern Peru: *Journal of South American Earth Sciences*, v. 1, p. 121-136.
- , 1998, Oligocene deposition and Cenozoic sequence boundaries in the Pisco Basin (Peru): *Journal of South American Earth Sciences*, v. 11, p. 217-231.
- Dunbar, R.B., Marty, R.C., and Baker, P.A., 1990, Cenozoic Marine Sedimentation in the Sechura and Pisco Basins, Peru: *Palaeogeography Palaeoclimatology Palaeoecology*, v. 77, p. 235-261.
- Goy, J.L., Macharé, J., Ortlieb, L., and Zazo, C., 1990, Neotectonics Plio-Pleistocene sea level records in southern Peru: *Bulletin of the INQUA*, v. Neotectonic Commission, p. 72-73.
- Gregory, W.K.M., 2000, Uplift history of the Central and Northern Andes; a review: *Geological Society of America Bulletin*, v. 112, p. 1091-1105.
- Guth, P.L., 2001, Quantifying terrain fabric in digital elevation models, *in* Ehlen, J., and Harmon, R.S., eds., *The environmental legacy of military operations*, Volume 14, *Geological Society of America Reviews in Engineering Geology*, p. 13-25.
- Gutscher, M.A., Olivet, J.L., Aslanian, D., Eissen, J.P., and Maury, R., 1999, The "lost Inca Plateau": cause of flat subduction beneath Peru?: *Earth and Planetary Science Letters*, v. 171, p. 335-341.
- Hampel, A., 2002, The migration history of the Nazca Ridge along the Peruvian active margin: a re-evaluation: *Earth and Planetary Science Letters*, v. 203, p. 665-679.
- Hampel, A., Kukowski, N., Bialas, J., Huebscher, C., and Heinbockel, R., 2004a, Ridge subduction at an erosive margin: The collision zone of the Nazca Ridge in southern Peru: *Journal of Geophysical Research-Solid Earth*, v. 109, p. B02101, doi: 10.1029/2003JB002593.
- Hampel, A., Adam, J., and Kukowski, N., 2004b, Response of the tectonically erosive south Peruvian forearc to subduction of the Nazca Ridge: Analysis of three-dimensional analogue experiments: *Tectonics*, v. 23, p. TC 5003, doi: 10.1029/2003TC001585.
- Hsu, J.T., 1992, Quaternary uplift of the Peruvian coast related to the subduction of the Nazca Ridge; 13.5 to 15.6 degrees south latitude., *in* Berryman-Kelvin-R, O.-Y.N.-A.-R., ed., *Impacts of tectonics on Quaternary coastal evolution.*, Volume Quaternary International: Oxford, Pergamon, p. 87-97.
- Hsu, J.T., Leonard, E.M., and Wehmiller, J.F., 1989, Aminostratigraphy of Peruvian and Chilean Quaternary Marine Terraces: *Quaternary Science Reviews*, v. 8, p. 255-262.
- Hsu, J.T.J., 1988, Emerged Quaternary marine terraces in southern Peru; sea level changes and continental margin tectonics over the subducting Nazca Ridge [Doctoral thesis]: Ithaca, NY, United States, Cornell University.
- Kulm, L.D.R., J.M.; Thornburg, T.M.; Schrader, H.-J., 1982, Cenozoic structure, stratigraphy and tectonics of the central Peru forearc, *in* Legett, J.K., ed., *Trench.-Forearc Geology*, Volume 10: *Geological Society Special Publication*: London, The Geological Society of London, p. 151-169.
- Machare, J., and Ortlieb, L., 1992, Plioquaternary Vertical Motions and the Subduction of the Nazca Ridge, Central Coast of Peru: *Tectonophysics*, v. 205, p. 97-108.
- Navarez, S., 1964, Boletin Carta Geologico Nacional, 17.

- Ortlieb, L., Ghaleb, B., Hillairemarcel, C., Machare, J., and Pichet, P., 1992, Th/U Disequilibria, Allo Isoleucine Ratios and O-18 Content of Mollusk Shells from Pleistocene Littoral Deposits of Southern Peru - a Basis for Geochronological Assessments: *Comptes Rendus De L Academie Des Sciences Serie Ii*, v. 314, p. 101-107.
- Smith, W.H.F., and Sandwell, D.T., 1997, Global sea floor topography from satellite altimetry and ship depth soundings: *Science*, v. 277, p. 1956-1962.
- Sosson, M., Bourgois, J., and Delepinay, B.M., 1994, Seabeam and Deep-Sea Submersible Nautilic Surveys in the Chiclayo Canyon Off Peru (7-S) - Subsidence and Subduction Erosion of an Andean-Type Convergent Margin since Pliocene Times: *Marine Geology*, v. 118, p. 237-256.
- Spence, W., Mendoza, C., Engdahl, E.R., Choy, G.L., and Norabuena, E., 1999, Seismic subduction of the Nazca Ridge as shown by the 1996-97 Peru earthquakes: *Pure and Applied Geophysics*, v. 154, p. 753-776.
- Turcotte, D.L., and Schubert, G., 2002, *Geodynamics*: Cambridge, New York, Oakleigh, Madrid, Cape Town, Cambridge University Press, 456 p.
- von Huene, R., and Lallemand, S., 1990, Tectonic Erosion Along the Japan and Peru Convergent Margins: *Geological Society of America Bulletin*, v. 102, p. 704-720.
- von Huene, R., Pecher, I.A., and Gutscher, M.A., 1996, Development of the accretionary prism along Peru and material flux after subduction of Nazca Ridge: *Tectonics*, v. 15, p. 19-33.
- von Huene, R., Ranero, C.R., and Vannucchi, P., 2004, Generic model of subduction erosion: *Geology (Boulder)*, v. 32, p. 913-916.
- von Huene, R., and Scholl, D.W., 1991, Observations at Convergent Margins Concerning Sediment Subduction, Subduction Erosion, and the Growth of Continental-Crust: *Reviews of Geophysics*, v. 29, p. 279-316.
- Wipf, M., Seward, D., Stirling, C.H., and Harrison, D., 2005, Constraining the post Jurassic Evolution of Western Peru through Fission Track and (U-Th)/He dating: Vienna 2005, EUG General Assembly, p. EGU05-A-04920.



# Chapter 4

## (U-Th)/He dating on apatite: using laser heating and MC-ICPMS

(to be submitted to the International Journal of Mass Spectrometry)

M. Wipf<sup>1</sup>, C.H. Stirling<sup>2</sup>, D. Harrison<sup>1,2</sup>, D. Seward<sup>1</sup>, R. Wieler<sup>2</sup>, H. Baur<sup>2</sup>

<sup>1</sup> Geological Institute  
ETH-Zentrum, Sonneggstr. 5, 8092 Zürich, Switzerland

<sup>2</sup> Institute for Isotope Geology and Mineral Resources  
ETH-Zentrum, Sonneggstr. 5, 8092 Zürich, Switzerland

### ABSTRACT

The thermal history of the Earth's upper crust can be investigated using temperature-dependant chronometers, such as the (U-Th)/He method. This dating method is based on the accumulation of radiogenic helium as a result of  $\alpha$ -decay from uranium and thorium, and to a smaller extent from samarium, within mineral grains. Measured (U-Th)/He ages are therefore a reflection of the competing effects of in-situ radiogenic He production and also, diffusive loss of He. The effective He-closure temperature in apatite has previously been estimated to be  $68 \pm 5$  °C [1, 2]. This technique is becoming increasingly important in studies of exhumation and erosion complementing apatite fission-track analysis. Helium chronometry requires precise measurements of minute amounts of parent and daughter nuclides making accurate single grain dating difficult. In this article a new technique to determine single grain (U-Th)/He ages is discussed. This new technique relies on helium extraction from apatite through heating with an Nd-YAG laser. The released gas is analysed and quantified with a sector type mass spectrometer. Uranium and thorium contents of the same crystal are subsequently determined by Multiple Collector Inductively Coupled Plasma Mass Spectrometry (MC-ICPMS).

Extraction through laser heating significantly improves procedural blank values making single grain analysis feasible. The analysis of single grains is desirable as grain-to-grain variability in nuclide concentration and age are masked in multigrain aliquots. This additional information potentially offers important insight into the grain's individual crystallisation and cooling history, its provenance and its diffusion behaviour.

Using MC-ICPMS for uranium and thorium analysis offers additional advantages: 1) measuring all required isotopes simultaneously cancels out effects caused by plasma fluctuations and 2) an internally acquired instrumental mass bias fractionation can be applied, eliminating matrix dependent externally determined mass bias corrections.

Combining helium extraction through laser heating with MC-ICPMS for uranium and thorium analysis allows single grain (U-Th)/He determinations with errors equivalent or better than analysis of multigrain aliquots using resistance furnace heating and conventional ICPMS.

## INTRODUCTION

The unique temperature sensitivity of the (U-Th)/He systems in apatite was revealed by Wolf et al. [3] and by Farley [1], and has a “closure temperature” of  $68\pm 5^\circ\text{C}$ . This is one of the lowest known closure temperatures for a radiometric dating system. A number of subsequent applications of the method have illustrated its potential as a powerful tool to reveal the low temperature thermal history of earth’s upper crust [4-6]. The (U-Th)/He analysis of apatite provides an excellent complement to the widely used fission-track analysis of apatite that has a closure temperature of about  $110^\circ\text{C}$  [7].

Until recently, helium extractions were performed through heating with a conventional resistance furnace. While this technology is readily available the associated high He-blank often requires that multigrain aliquots are needed. For many samples it is difficult however to obtain sufficient numbers of suitable crystals. Therefore, and whilst some workers reported initial difficulties [8, 9], more recent studies have attempted single grain analysis using laser heating [10-12]. Isotope-dilution  $\alpha$ -spectrometry was used in some early studies [13-22] to measure uranium and thorium concentrations. However almost all recent studies [1, 2, 6, 8-12, 23-31] have applied conventional single collector quadrupole- or sector type ICPMS. This procedure requires that a spike tracer containing precisely known amounts of uranium and thorium isotopes be added to the sample solutions to determine  $^{238}\text{U}$  and  $^{232}\text{Th}$  concentrations through isotope dilution techniques.

The use of ICPMS has become the technique of choice to analyse uranium and thorium for (U-Th)/He dating. The analytical precision is however limited by instability of the plasma during sequential peak measurement and difficulties in obtaining reliable peak shapes. Corrections for instrumental mass fractionation usually require external standardisation procedures, although internal normalisation has been applied using conventional sector type ICPMS [32]. By applying MC-ICPMS to U-Th isotopic measurement the analytical precision

can be increased significantly as additional advantages become available: 1)  $^{235}\text{U}$ ,  $^{238}\text{U}$ ,  $^{232}\text{Th}$  as well as the spike isotopes  $^{229}\text{Th}$  and  $^{233}\text{U}$  can be measured simultaneously, cancelling out effects caused by plasma fluctuations and allowing for more efficient sample utilisation, 2) an internal instrumental mass bias fractionation can be determined by normalising the measured  $^{235}\text{U}/^{238}\text{U}$  against the assumed natural value of 137.88. Since mass discrimination is effectively independent of the chemical properties of the element the internally measured bias for uranium can be applied to thorium as well [33] thereby eliminating externally acquired mass bias corrections which are matrix dependent. With the exception of Aciego et al. [34] however, nobody has previously used a MC-ICPMS for the analysis of uranium and thorium for the purpose of (U-Th)/He dating.

#### *Historical background*

The accumulation of  $^4\text{He}$  from the  $\alpha$ -decay of uranium and thorium was the first scheme proposed to investigate the ages of rocks [35-37]. However following these initial studies early last century, it was rarely applied successfully as all too often the method yielded ages which seemed unreasonably young. Rutherford [38] recognised in his earliest studies that the most likely reason for these young ages was helium loss from the sample. Thanks to improvements mainly in analytical techniques, (U-Th)/He dating has received renewed interest. Subsequently various accessory minerals such as titanite [39]; non-metamict zircon [13], magnetite [14-16], aragonite [17, 18] pyroxene, and hornblende [19, 20] were analysed and suggested as potential dating techniques. Until the mid 1980's the general assumption was however, that the problem of He "leakage" made (U-Th)/He dating suspect and difficult, if not impossible, to interpret. Damon et al. [15] suggested as early as 1963 that the He dating of apatite represented a viable low-temperature thermochronometer but it was not until 1987 that this was verified by Zeitler et al. [22].

The closure temperature of apatite depends on grain size and cooling rates [28]. Larger grains suffer less diffusive loss than smaller grains and therefore have higher closure temperatures. During rapid cooling there is less time for diffusive loss leading also to higher closure temperatures. For grain sizes and rates of cooling generally observed in nature (i.e. 90-150  $\mu\text{m}$  in diameter) it is thought to be as low as  $68\pm 5^\circ\text{C}$  [1, 2, 6]. Due to the large minimum dimension of up to 4 cm the Durango age-standard apatites have been reported to have closure temperatures as high as  $175^\circ\text{C}$  [23]. Even though the closure temperature can vary, over geologic timescales helium is largely retained within the apatite crystals at low temperatures.

The uniquely low closure temperature as well as its ubiquity and moderately high uranium and thorium contents make apatite the most extensively studied mineral.

### *Technical Background*

The (U-Th)/He chronometer is based on the ingrowth of radiogenic  $^4\text{He}$  ( $\alpha$ -particles) produced by the radioactive decay of  $^{238}\text{U}$ ,  $^{235}\text{U}$  and  $^{232}\text{Th}$ . A generally insignificant amount of  $^4\text{He}$  is also produced by the  $^{147}\text{Sm} \rightarrow ^{143}\text{Nd}$  decay scheme. The complete ingrowth equation is:

$$^4\text{He} = 8^{238}\text{U}[\exp(\lambda_{238}t) - 1] + 7^{235}\text{U}[\exp(\lambda_{235}t) - 1] + 6^{232}\text{Th}[\exp(\lambda_{232}t) - 1] + ^{147}\text{Sm}[\exp(\lambda_{147}t) - 1] \quad [\text{Eq1}]$$

Where  $^4\text{He}$ ,  $^{238}\text{U}$ ,  $^{235}\text{U}$ ,  $^{232}\text{Th}$  and  $^{147}\text{Sm}$  refer to present-day amounts,  $t$  is the accumulation time or He age, and  $\lambda$ 's are the decay constants. Equation 1 assumes secular equilibrium among all daughter products in the decay chain, a condition true for crystals that formed 350,000 years prior to the onset of helium accumulation, with an initial  $^{230}\text{Th}/^{238}\text{U}$  activity ratio of unity. This means that for every decayed  $^{238}\text{U}$ ,  $^{235}\text{U}$  and  $^{232}\text{Th}$  isotope 8, 7 and 6  $\alpha$ -particles are produced respectively, while only one  $\alpha$ -particle is produced from the decay of one  $^{147}\text{Sm}$  isotope. Thus the overwhelming majority of radiogenic  $^4\text{He}$  is produced by  $\alpha$ -decay (i.e. ejection of  $^4\text{He}$  nuclei from the parent nuclide) of the actinides. The term including the decay of samarium is therefore generally neglected. Nonetheless it has been noted that the Sm “age contribution” in apatites may be 0.1-10% and in grains with low actinide concentrations (<10 ppm total) it can be as high as 25 % [40]. In the Durango apatite the total radiogenic  $^4\text{He}$  produced through the decay of  $^{147}\text{Sm}$  is ~0.4% [23], introducing a systematic error to the inferred time since closure of the system. Equation I assumes further that no initial  $^4\text{He}$  is present, a reasonable assumption since the concentration of  $^4\text{He}$  in the atmosphere is so low (5ppm) that contamination by air is unlikely to have a significant effect. However fluid inclusions may carry crustal or mantle helium, these contributions may be high and can therefore affect measured He ages. In order to prevent these potentially problematic effects it is necessary to carefully handpick all analysed apatites under a binocular microscope. Radiogenic helium inherited from the history of the crystal prior to its passing through the closure temperature is unlikely given the very high diffusivity of He in apatite [1, 2, 28]. Effects of secular disequilibrium need to be considered for certain rare occasions, such as dating young volcanic rocks [23, 24, 34].

The (U-Th)/He system shows a series of unusual characteristics, for instance multiple parent nuclides, strongly contrasting physical and chemical behaviour of parent- and daughter nuclides and also energetic recoil that causes long stopping distances of the daughter He-nuclides. Recoil effects result in a spatial separation of the parent- and its daughter nuclide by significant distances and have important implications for the (U-Th)/He technique. The most important is the ejection of  $\alpha$ -particles from the crystals, resulting in apparent ages that are too young. Depending on their initial energy and the elemental composition as well as the density of the mineral these particles can travel a known distance (“stopping distance” [41]) within the lattice (in most minerals approximately 20  $\mu\text{m}$ ). Helium loss therefore takes place primarily when the parent nuclide is located within the first 20  $\mu\text{m}$  (i.e. less than the stopping distance) of the crystal surface. A model to quantitatively correct (U-Th)/He ages for helium loss was developed by Farley et al. [42]. The model assumes that implantation of helium from the surrounding matrix is insignificant and that the uranium and thorium distribution within the crystal is homogenous. If the nature of zoning is known it is possible to calculate an  $\alpha$ -ejection correction for zoned grains [42-44]. Generally however the distribution in the analysed grains is not known and homogeneity is assumed. This assumption represents the biggest uncertainty in applying an  $\alpha$ -ejection correction since zoning of REE and actinides is commonly observed in apatites [45-49]. The correction for  $\alpha$ -ejection can therefore be subject to significant but generally unknown uncertainties.

Closed system evolution is assumed for U and Th isotopes in calculations. This may not necessarily be true but it is generally assumed that the loss of  $\alpha$ -particles (i.e.  $^4\text{He}$  nuclei) through ejection far outweighs the potential loss of U and Th (or their intermediary daughter nuclides).

### **APATITE GRAIN SELECTION AND PREPARATION**

Two different apatite standards were analysed, Durango [23, 50] and Limberg-t3 [51]. The Durango shards originated from an aliquot of the CIT-DUR-A crystal [52], provided by Dr. F. Stuart (SUERC, Scotland). The outer 50 $\mu\text{m}$  of the Durango crystal had been removed prior to its crushing [1]. This eliminates the need of an  $\alpha$ -ejection correction for the Durango shards. The Limberg-t3 crystals were handpicked from an apatite concentrate obtained from Dr. M. Rahn (HSK Villigen, Switzerland).

Handpicking of crystals is a very important process and is necessary to exclude any grains containing mineral/fluid inclusions. In particular, small U and Th rich mineral inclusions such

as zircons (<20 $\mu\text{m}$ ) are known to implant significant amounts of helium into the surrounding apatite, resulting in unreasonably old measured He-ages. All crystals were handpicked under polarised light with a binocular microscope at a magnification of x200. A digital picture of every grain accepted for analysis is taken and the length and width of the crystal is measured. Analysed apatite grains range in width from 70-230  $\mu\text{m}$  and in length from 80-390  $\mu\text{m}$ . Based on these measurements the  $\alpha$ -ejection correction was subsequently calculated according to Farley et al. [42]. It has previously been reported that during He-extraction, heterogeneous coupling of laser light with the crystal may occur, which may lead to some portions of the analyzed grains being heated well over the melting point while others have not been outgassed at all [8, 9]. In order to prevent this, the crystals were wrapped in approximately 1x1 mm squares of pure platinum foil.

### **IR LASER EXTRACTION OF HELIUM AND MEASURING HELIUM VOLUMES**

The major advantage of using a laser line is the small He-blank value, due to the small volume. This blank value does not increase significantly when applying laser heating (Fig. 4. 1). This makes the line ideal for extracting radiogenic helium from small or gas poor apatite grains. The infrared (IR) –laser used to extract the helium is part of a noble gas extraction line, primarily used for extraterrestrial samples. The Nd-YAG IR laser has a wavelength of 1064 nm and can be operated in pulsed or continuous wave (CW) mode. For the heating of the platinum packets containing the apatites the CW mode was most suitable. The output of the laser is variable with a maximum of ~60W. The laser beam can be focused to ~140  $\mu\text{m}$ , ideal for heating samples in the size range common to apatites. The same optical system that serves to focus the laser beam was used to illuminate the sample holder; therefore the IR and the visible light were focused on the same spot. Furthermore, the laser is equipped with a timer allowing precise reproduction of exposure times.

No device to monitor the temperature directly inside the laser chamber was available. In order to reach the required temperatures and power settings a series of experiments was performed. Small pieces of gold foil were wrapped into platinum foil. These packages were then heated with the laser at different settings. Power settings that melted the gold foil and left the platinum untouched were adopted as this indicated that a temperature slightly higher than 1064°C (melting point gold) and significantly lower than 1772°C (melting point platinum) was reached. To prevent volatilisation of U and Th in the apatites it is important that the temperature stayed below 1500°C [10].

The laser light enters the extraction chamber through a glass viewport transmitting light with a wavelength between 320 and 2700 nm (Varian®). The chamber can be moved in the x, y and z direction by micrometer screws. A sample holder made out of aluminium was placed within the laser chamber. In order to avoid significant heating of neighbouring samples the chamber was water-cooled.

Two valves connect the chamber to a pumping system and to the extraction line, where the gas is cleaned. During the actual extraction phase the sample chamber was completely separated from the rest of the extraction line. This was to prevent atmospheric contamination of the system in case of breakage of the glass. A U-shaped cold trap was mounted between the chamber and the extraction line, where an ultra-high-vacuum of  $10^{-8}$  Torr was maintained by a series of turbo molecular and ion-pumps. The trap was cooled with liquid nitrogen ( $-196^{\circ}\text{C}$ ) to freeze out any  $\text{H}_2\text{O}$  and  $\text{CO}_2$  released during the extraction phase. The helium and any remaining active gases were expanded into the extraction line. While the argon was trapped on a cold ( $-196^{\circ}\text{C}$ ) charcoal finger the remaining gas was cleaned for 10 minutes by two Ti/Zr getters (Danielson®) at  $280^{\circ}\text{C}$ . Afterwards the helium was expanded into the mass spectrometer, where an additional Al/Zr getter (SAES®) continuously removed  $\text{H}_2$  and another activated charcoal finger at  $-196^{\circ}\text{C}$  removed any further argon that may be desorbed or any argon released due to ions of the sample gas hitting the walls of the spectrometer. After every measurement the spectrometer was pumped for several minutes before the gas from the following extraction was introduced and analysed.

The “Albatross” mass spectrometer used to measure the extracted helium is a non-commercial mass spectrometer ( $90^{\circ}$ , 21cm radius) designed and built at ETH Zürich to measure low noble gas concentrations. A vacuum of  $10^{-10}$  Torr is maintained within the spectrometer. It is equipped with an electron multiplier operating in pulse-counting mode and a Faraday cup operating with a  $10^{11}$   $\Omega$  resistor for larger beam sizes. The upper limit of the multiplier is set to  $5 \times 10^5$  Hz, which corresponds to  $\sim 1.5 \times 10^{-8}$   $\text{cm}^{-3}$  STP  $^4\text{He}$ . Most samples were analysed on the electron multiplier only; some helium rich grains occasionally released enough helium to be measured on the Faraday cup as well.

Before each analysis run atmospheric gases adsorbed on the samples have to be removed. The chamber with the mounted and loaded sample holder was therefore evacuated for at least 24 hours. For He extraction samples were heated for 3 minutes continuously. Following the measurement of every extraction the sample was heated again to insure complete degassing. Samples which yielded helium amounts significantly above blank values during these re-

extracts were reheated until complete degassing was confirmed. In such cases the amounts of secondary released helium were summed with previous extracts for these samples. The ages determined for these grains should be treated with caution, as they are likely to be compromised by micro-inclusions. A complete analysis run generally lasted several days and included up to 29 samples as well as associated blanks and calibrations.

### *Blanks*

Before running blank measurements and re-extractions of apatite grains the line was pumped down during several minutes to minimise memory effects. Fig. 4.1 shows values for “cold”, “hot” “hot Pt-foil” and “crystal” blanks over a period of 2.5 years. These four different types of blanks were used for corrections and verification of complete degassing. They remained relatively constant especially within single runs. The only exception was the run from September 2004 that shows blank values that were initially about 5 times higher than at the end of the run. These values were decreasing continually with time indicating that in this case the 24 hours of pumping down time prior to the analysis was not sufficient. Therefore the line was pumped down for an additional 72 hours.

Cold blanks which simulate sample extraction without laser heating, were indistinguishable to the hot blanks described below (Fig. 4.1) within the magnitude of their  $2\sigma$  analytical uncertainties.

Hot blanks were analysed by applying the laser to an empty pit in the aluminium sample holder. The irradiation parameters used were identical or higher to those used for samples. The hot blanks were compared to the cold blanks to determine if any helium was released from the aluminium sample holder during heating. Helium released from the sample holder was found to be insignificant.

Platinum blanks were analysed by applying the laser with the same or higher power settings to an empty piece of platinum foil of equal size to those used to wrap the grains. The gas amounts obtained served to decide whether any helium was released from the Pt-foil. Three of the eight analysed pieces of foil were heated above 1772°C and melted. Since the Pt-foil blank values were identical to the hot blank values it was demonstrated that no significant amounts of helium were released from the Pt-foils.

These set of blank measurements confirmed that no helium originated from the sample holder or the Pt-foil allowing for a simple cold-blank correction. In case of the Durango shards and

the Limburg-t3 standard, blanks contributed a maximum of 2‰ and 1.2‰, respectively to the total  $^4\text{He}$  signal.

Crystal blanks were performed by extracting helium from an already degassed grain, in order to confirm complete degassing. With a few exceptions, as noted, the measured helium was identical to the hot blank values verifying that no helium remained within the analysed crystal. An additional extraction was performed if helium amounts above blank were detected.

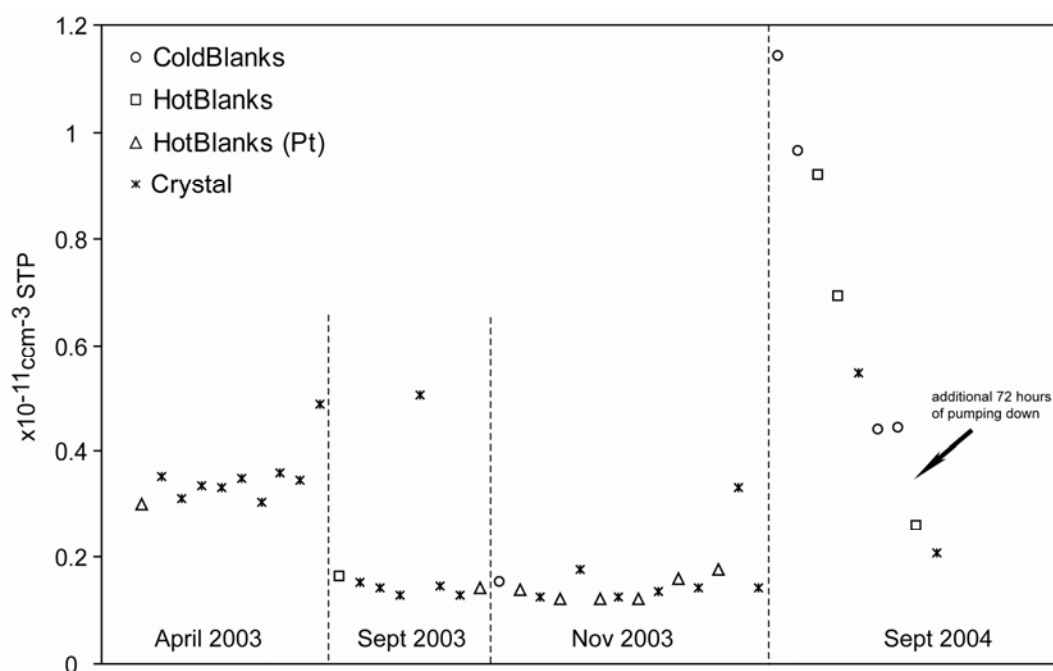


**Figure 4.1:** Evolution of the  $^4\text{He}$  cold-, hot-, Pt- and crystal blanks over 2.5 years. Unusually high values were recorded in Sept. 2004. See text for further explanations.

#### *Calibrations and determination of helium concentration and uncertainties*

Two standards were used as calibrations to determine the sensitivity of the spectrometer (Fig. 4.2). Known pressures of these standard gases were regularly expanded as Fast Calibrations (FC) and Slow Calibrations (SC) into the system. FC's were analysed daily to correct for long-term variation of the mass spectrometer's sensitivity. The SC's were used to determine the peak height of a precisely known amount of  $^4\text{He}$ . Two SC's were measured in the middle and at the end of an analysis run. While the SC calibration gas was only measured on the Faraday cup the FC calibration gas was measured on both detectors in order to determine the Faraday/multiplier-gain ratio. This gain served to scale the Multiplier signal of the samples with the Faraday signal of the SC. Sensitivity of the spectrometer is very stable; the standard deviation of the FC/SC ratios over 2.5 years is less than 9‰ for  $^4\text{He}$ . The filament was

changed in the summer of 2003, explaining the observed jump in sensitivity at this time (Fig. 4.2).

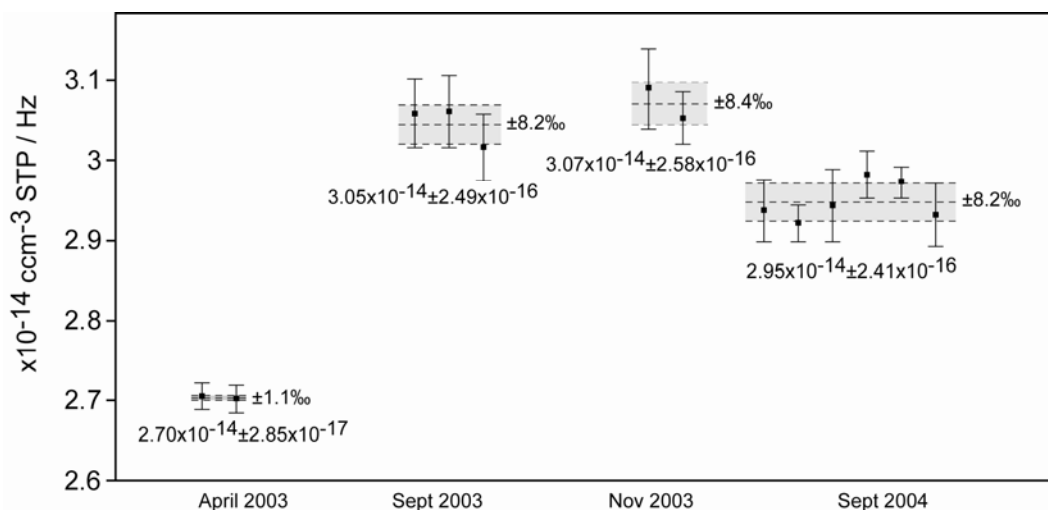


**Figure 4.2:** Evolution of the sensitivity of the noble gas mass spectrometer over 2.5 years. The jump observed in the summer of 2003 is due to the replacement of the filament. Sensitivity of the spectrometer is very stable within one measurement session (<9%).

The reported uncertainties of the measured helium concentrations (Tab. 4.2a) are quoted at the  $2\sigma$  level and include statistical errors, errors of the Faraday/multiplier gain, uncertainties in the measurements of the expansions as well as He-blank contributions. Measurements of identical calibration gases measured in different laboratories revealed a  $\sim 3\%$  uncertainty in the determinations of the absolute gas concentrations [53]. This uncertainty will however not affect the direct comparison among the data, since all samples were measured on the same mass spectrometer with the same calibration reservoirs. Thus this error is not included in the given uncertainties.

## URANIUM AND THORIUM ANALYSIS

### *Sample preparation*

At the end of the helium analysis the sample holder containing the wrapped and degassed crystals was recovered. For uranium and thorium analysis the packages containing the crystals were prepared under clean air conditions (better than class 100). Sample dissolution and chemical preparation was performed using high-purity quartz- and Teflon-distilled reagents. The Pt-packets were partially opened and added to Teflon beakers containing weighted amounts of a mixed  $^{233}\text{U}/^{229}\text{Th}$  spike solution (Tab. 4.1). The apatite crystals were digested overnight on a hot plate held at  $\sim 100^\circ\text{C}$  using 1.5N  $\text{HNO}_3$  and a trace quantity of HF.

	<b>Atomic ratios (spike)</b>	<b>±error (%) (2σ)</b>		<b>Concentration (nmol/g spike)</b>	<b>±error (%) (2σ)</b>
$^{233}\text{U}/^{238}\text{U}$	495.852931	0.0742	$^{233}\text{U}$	0.000356707	0.20314546
$^{235}\text{U}/^{234}\text{U}$	0.337061	0.4404	$^{229}\text{Th}$	0.000138893	0.20330996
$^{236}\text{U}/^{234}\text{U}$	1.087804	0.0980			
$^{233}\text{U}/^{235}\text{U}$	1614.295182	0.4438			
$^{229}\text{Th}/^{232}\text{Th}$	4463.343695	0.2880			
$^{233}\text{U}/^{229}\text{Th}$	2.568210	0.0082			
	<b>Atomic ratios (CRM145)</b>				
$^{238}\text{U}/^{235}\text{U}$	137.8800				
$^{235}\text{U}/^{234}\text{U}$	137.2574				

**Table 4.1:** Isotopic compositions and concentrations of the  $^{229}\text{Th}/^{233}\text{U}$  spike tracer and the isotopic compositions of the CRM145 U metal standard used.

Uranium and thorium were then separated from matrix elements using TRU ion exchange resin (Eichrom) following a chemical protocol modified from Luo et al. [54]. Following chemical separation, the U-Th sample fraction was treated with highly oxidising  $\text{H}_2\text{O}_2$ , in order to break down organic compounds associated with the TRU resin as reported by Andersen et al. [55]. Samples were dissolved in ~1ml 0.3N  $\text{HNO}_3$ -0.1N HF. The total chemistry blank was negligible (<0.2pg of  $^{238}\text{U}$  and  $^{232}\text{Th}$ ) and removed the necessity for a uranium or thorium blank correction.

### *Mass spectrometry*

A Nu Plasma MC-ICPMS was used to analyse the U-Th isotopic composition of the apatites. This instrument is equipped with 12 Faraday collectors and 3 discrete dynode secondary electron multipliers (SEM) operating in pulse counting mode with counting detector systems (Fig. 4.3). More detailed information on the mass spectrometer is available elsewhere [56-58]. Measurements were performed at a normal mass resolution  $\Delta m/m$  of ~400 using an RF power of 1350W. Sample solutions were aspirated into the plasma source through an MCN 6000 Cetac micro-concentric nebuliser and desolvator system (aspiration rate ~100  $\mu\text{l}/\text{min}$ ). Sensitivity of the Nu Plasma MC-ICPMS for U was ~3-4%, and the instrumental mass bias was ~5%  $\text{amu}^{-1}$ . At the start of each measurement session, solutions of the U metal standard

CRM 145 (formerly known as NIST SRM 960) were used to optimise the signal intensity for U and Th and to achieve aligned flat-topped peak shapes across the U-Th mass range.

Washout between measurements was performed using alternate solutions of 0.3N HNO<sub>3</sub> and 0.3N HF-0.1N HCl until the <sup>238</sup>U intensity diminished to the blank value of the machine.

#### *Determination of the ion counters' relative gains*

A multi static routine using a mixed Faraday cup (FC)-multiplier array was used. Faraday collectors with a 10<sup>11</sup>Ω resistor were used for the high-level ion beam of <sup>238</sup>U (~1-3 x 10<sup>-11</sup>A) and multiple ion counters for the low-level ion beams of <sup>233</sup>U (~1 x 10<sup>-14</sup>A), <sup>229</sup>Th (~3 x 10<sup>-15</sup>A).

Calibration of the relative gain between these two detector systems during each session was therefore necessary. Count rates were generally kept below 10<sup>5</sup> cps, in order to extend the lifetime of the multipliers and to minimise uncertainties in the dead time corrections. Count rates for the gain measurements were intensity matched with those for the sample measurements to eliminate non-linearity effects as a potential source of error. Solutions of CRM 145 spiked with a mixed <sup>233</sup>U/<sup>229</sup>Th were used to determine the relative gains of the ion counters (ion counter 0 (IC0) and ion counter 2 (IC2)).

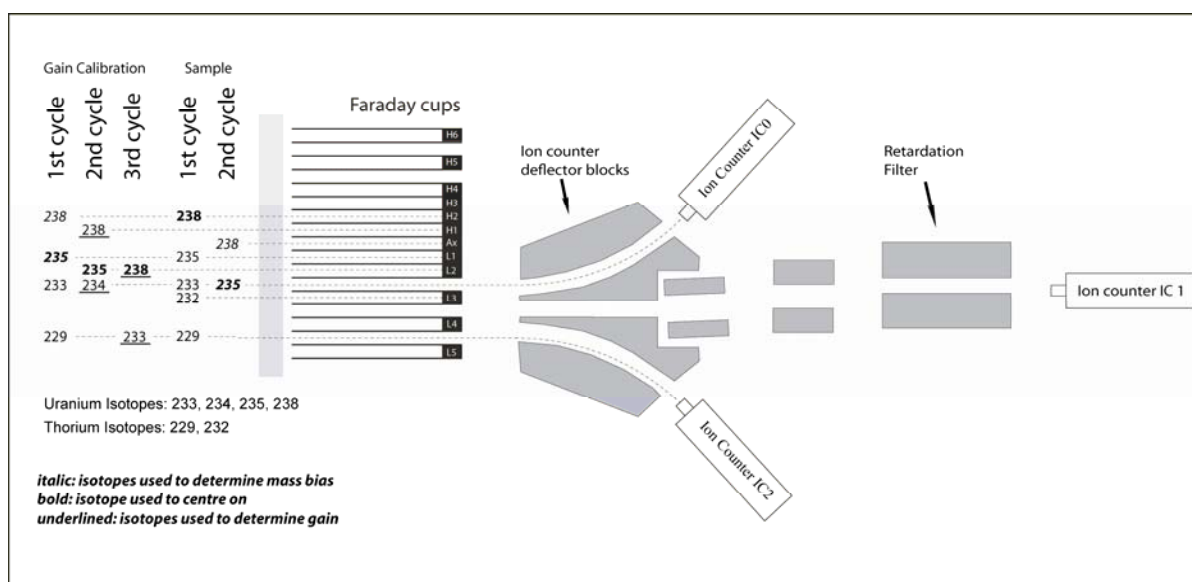


**Figure 4.3:** Schematic overview of the collector array for the Nu Instruments Nu Plasma MC-ICPMS. This instrument is equipped with 12 Faraday collectors fitted with “standard” 10<sup>11</sup>Ω resistors. Low intensity ion beams, such as <sup>229</sup>Th, <sup>233</sup>U and <sup>235</sup>U, can be focused onto three secondary electron multipliers with ion counter detector systems, located behind the Faraday array. See text for further explanations of the multi static routines used.

The following three-cycle measurement routine was employed for the gain calibration of the ion counters (Fig. 4.3):

Cycle 1:  $^{238}\text{U}$  and  $^{235}\text{U}$  were measured on Faraday detectors (H2 and L1, respectively); while  $^{233}\text{U}$  is measured simultaneously on IC0.

Cycle 2:  $^{238}\text{U}$  and  $^{235}\text{U}$  were measured on Faraday detectors (H1 and L2, respectively); while  $^{234}\text{U}$  is measured simultaneously on IC2.

Cycle 3:  $^{238}\text{U}$  and  $^{233}\text{U}$  were measured using the Faraday detector L1 and the IC2 ion counting channel.

All the acquired data was reduced offline. The measured isotopic ratios were corrected iteratively for small contributions of natural isotopes present in the spike tracer (Tab. 4.1), for instrumental mass bias and where necessary for IC-gain. With the data from the first two cycles the  $^{238}\text{U}/^{233}\text{U}$  ratio could be corrected for the combined effects of spike contribution and instrumental mass bias. It was then possible to extract the mass bias correction factor using the assumed natural value of 137.88 for  $^{238}\text{U}/^{235}\text{U}$  and the value of 137.25 for  $^{234}\text{U}/^{238}\text{U}$  (CRM145). Using the spike contribution and the instrumental mass bias corrected  $^{238}\text{U}/^{233}\text{U}$  the relative gain for IC0 could then be derived. The  $^{238}\text{U}/^{233}\text{U}$  determined during cycle 1 could then be corrected for by applying the previously determined IC0-gain correction. The FC-IC gain for IC2 was determined by normalising the mass bias corrected  $^{238}\text{U}/^{233}\text{U}$  from cycle 3 to the gain and mass bias corrected value from cycle 1. FC- IC gains were calculated on a cycle level and then statistically evaluated to determine the average gains with associated errors. Gain calibrations were performed at the start of every measurement session and bracketed every four to five samples. The gain calibration measurements were performed over 30-40-cycles with signal integration times of 5 s. A linear drift between succeeding calibrations was assumed. Therefore a linear interpolation was applied to determine the appropriate gain values necessary to correct the measured ratios in the analysed samples.

### *Determinations of Uranium and Thorium concentrations in apatites*

Samples were analysed according to the following two-cycle multi static routine (Fig. 4.3):

Cycle 1:  $^{238}\text{U}$  and  $^{232}\text{Th}$  were measured in Faraday cups H2 and L1 while  $^{233}\text{U}$  and  $^{229}\text{Th}$  are simultaneously determined in IC0 and IC2 respectively.

Cycle 2:  $^{238}\text{U}$  and  $^{235}\text{U}$  were measured using the axial Faraday detector and IC0 respectively.

Just as previously described for the IC-gain determinations the measured isotopic ratios from the samples need to be corrected offline for the small contributions of natural isotopes present in the spike tracer (Tab. 4.1), for instrumental mass bias and where necessary for IC-gain. A two-cycle routine was necessary in order to be able to measure the sample's small  $^{235}\text{U}$  ion beam ( $<3 \times 10^{-16}\text{A}$ ) reliably on an ion counter. With the data from these two cycles and the previously derived IC-gains the  $^{238}\text{U}/^{233}\text{U}$  ratio could be corrected for the combined effects of spike contribution and instrumental mass bias. The mass bias correction factor could then be extracted using the assumed natural value of 137.88 for  $^{238}\text{U}/^{235}\text{U}$ . The  $^{232}\text{Th}/^{229}\text{Th}$  ratio was then corrected for spike contribution, mass bias and gain by applying the determined factors. The corrected  $^{238}\text{U}/^{233}\text{U}$  and  $^{232}\text{Th}/^{229}\text{Th}$  ratios could then be multiplied by the amount of  $^{233}\text{U}/^{229}\text{Th}$  spike tracer added to give the amount of  $^{238}\text{U}$  and  $^{232}\text{Th}$  present in the solution.  $^{235}\text{U}$  was calculated by dividing  $^{238}\text{U}$  with 137.88 assuming the natural  $^{238}\text{U}/^{235}\text{U}$  ratio.

Measurements were performed over 40-50-cycles with signal integration times of 5 s. Total acquisition time is 8-10 minutes per sample, usually consuming the complete solution.

### *Uncertainties*

All reported uncertainties (Tab. 4.2a) in uranium and thorium isotopic ratios and abundances are at the  $2\sigma$  level. This includes weighing errors of the spike amounts added, errors in the precision of the spike concentration, and errors of the IC-gain calibrations. The  $^{238}\text{U}/^{233}\text{U}$  ratios in the two solutions used to calibrate the relative IC gain values had an external reproducibility of 3.7‰ and 5.1‰ and an averaged internal reproducibility of 1.9‰ and 3.4‰ respectively (Fig. 4.4). The ratio of the external-/internal reproducibility was  $<2$ . The external reproducibility was poorer than the internal reproducibility because the drift of the relative IC gains does not behave linearly. The more conservative error estimates based on the external

reproducibility were taken into account and all reported uncertainties were scaled up by a factor of 2.

Average internal errors of the apatite standards were in most cases  $\sim 8\%$  for  $^{238}\text{U}/^{233}\text{U}$  and  $\sim 7\%$  for  $^{232}\text{Th}/^{229}\text{Th}$  resulting in errors of about  $\sim 1\%$  for the actual uranium and thorium concentrations.

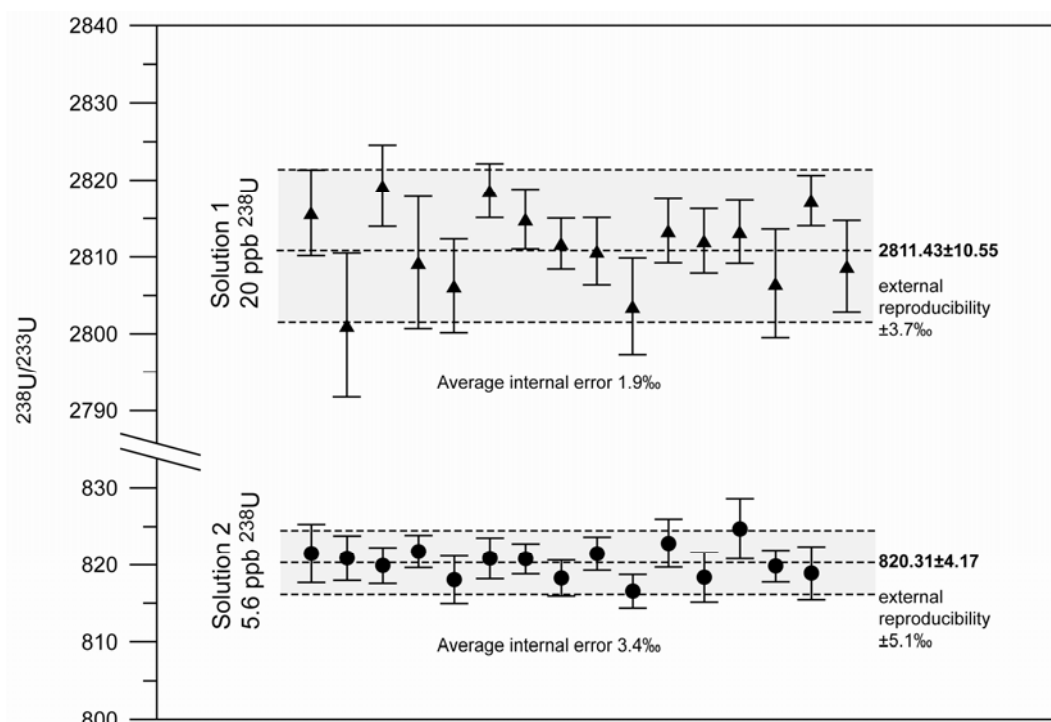


**Figure 4.4:** External reproducibility of the  $^{238}\text{U}/^{233}\text{U}$  ratios in the two solutions used to calibrate the relative IC-gain calibrations. Error bars represent errors on the  $2\sigma$  level for one calibration measurement.

## RESULTS

In total 14 apatite age-standards were dated: nine Durango shards and five Lim t3 (Tab. 4.2b, Fig. 4.5). The  $\alpha$ -ejection correction of Farley et al. [42] was applied to correct the Lim t3 ages while the Durango standards do not require such a correction for reasons explained previously. Errors on the individual ages (Tab. 4.2b) were derived by error propagation of the analytical errors of the He, U and Th measurements. Analysed apatite grains contained between  $1\text{-}6 \times 10^{-9}$  ccm STP  $^4\text{He}$ , 2-20 ppm U, and 50-200 ppm Th equivalent to 0.1-0.6 ng U and 1.3-6.6 ng Th.

### Durango

The nine Durango apatites yielded a weighted mean age of  $30.0 \pm 2.8$  ( $2\sigma$ ) with Th/U ratios ranging from 15.8 to 19.2 (fig. 4.5a). Age uncertainties ( $2\sigma$ ) on individual shards ranged from 0.6 to 1.9 Ma.

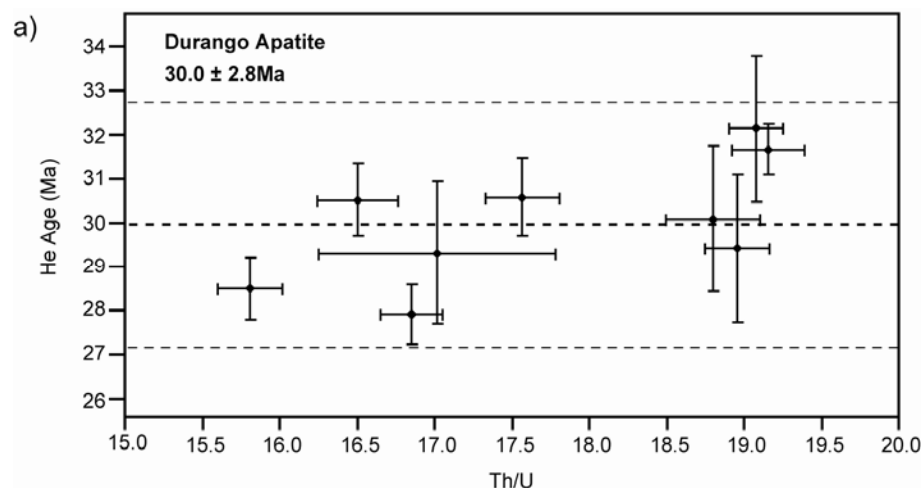


**Figure 4.5a:** (U-Th)/He ages versus Th/U for Durango apatite. Error bars represent analytical uncertainties on the  $2\sigma$  level. Dashed lines show the weighted mean of the analysed single grains for each apatite standard with the associated reproducibility at the  $2\sigma$  level.

### Lim t3

The five Lim t3 apatites yielded a weighted mean age of  $16.3 \pm 3.6$  displaying a broad range in Th/U ratios from 7.6 to 18.5 (Fig. 4.5b). This broad distribution was seen in both uranium and thorium concentrations (Tab. 4.2b). Age uncertainties ( $2\sigma$ ) on individual crystals ranged from 0.8 to 2.7 Ma.

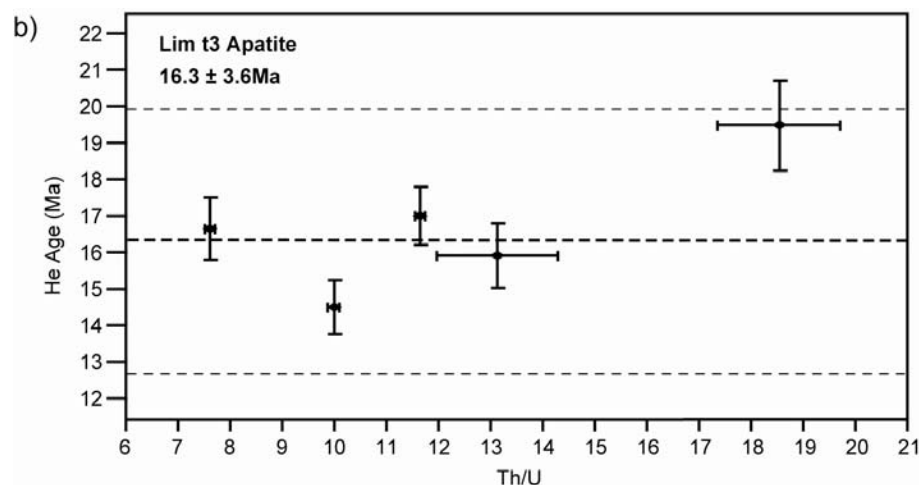


**Figure 4.5b:** (U-Th)/He ages versus Th/U for Lim t3 apatite. Error bars represent analytical uncertainties on the  $2\sigma$  level. Dashed lines show the weighted mean of the analysed single grains for each apatite standard with the associated reproducibility at the  $2\sigma$  level.

<b>SAMPLE</b>	<b>ccm He (STP)</b>	<b>error (%) (2<math>\sigma</math>)</b>	<b>U 238 (ng)</b>	<b>error (%) (2<math>\sigma</math>)</b>	<b>U 235 (ng)</b>	<b>error (%) (2<math>\sigma</math>)</b>	<b>Th 232 (ng)</b>	<b>error (%) (2<math>\sigma</math>)</b>	<b>TH/U</b>	<b>error (2<math>\sigma</math>)</b>
<b>DUR 10</b>	2.58E-09	2.40	0.1518	0.93	0.0011	0.93	2.5763	0.71	16.85	0.20
<b>DUR 7</b>	5.65E-09	2.34	0.3427	0.72	0.0025	0.72	5.4564	1.10	15.81	0.21
<b>DUR 9</b>	1.45E-09	5.22	0.0806	3.17	0.0000	3.17	1.3817	0.65	17.01	0.77
<b>DUR 2</b>	3.23E-09	5.68	0.1650	0.84	0.0012	0.84	3.1277	0.72	18.96	0.21
<b>DUR 27</b>	2.77E-09	5.42	0.1386	1.37	0.0000	1.37	2.6251	0.91	18.80	0.31
<b>DUR 4</b>	4.17E-09	2.52	0.2283	1.04	0.0016	1.04	3.7948	1.19	16.50	0.26
<b>DUR 3/02</b>	3.43E-09	2.81	0.1781	1.22	0.0013	1.22	3.1506	0.65	17.57	0.24
<b>DUR 3/01</b>	3.24E-09	1.71	0.1515	0.69	0.0011	0.69	2.9224	0.64	19.16	0.24
<b>DUR 26</b>	3.33E-09	5.14	0.1539	0.71	0.0011	0.71	2.9561	0.60	19.08	0.18
<b>Lim t3 23</b>	1.09E-09	5.72	0.2093	0.67	0.0015	0.67	2.1063	0.82	9.99	0.05
<b>Lim t3 H</b>	3.12E-09	5.32	0.4503	4.01	0.0032	4.01	5.9508	4.03	13.12	0.59
<b>Lim t3 31</b>	2.75E-09	5.52	0.5292	1.08	0.0038	1.08	4.0528	0.65	7.60	0.05
<b>Lim t3 22</b>	3.94E-09	5.16	0.5601	0.60	0.0040	0.60	6.5685	0.61	11.64	0.05
<b>Lim t3 D</b>	1.39E-09	6.50	0.1199	5.68	0.0009	5.68	2.2391	2.87	18.54	0.59

**Table 4.2a:** Measured He, U and Th amounts for the analysed Durango and Lim t3 apatite crystals with analytical uncertainties quoted at the 2 $\sigma$  level.

SAMPLE	Length ( $\mu\text{m}$ )	Width ( $\mu\text{m}$ )	Ft <sup>+</sup>	weight* (mg)	He* (nmol/g)	U ppm*	Th ppm*	raw age (ma)	Age (ma)	error (2 $\sigma$ )
DUR 10	---	---	1.000	0.01	8.22	10.9	184.0	27.91	<b>27.91</b>	0.69
DUR 7	---	---	1.000	0.03	8.41	11.5	181.9	28.51	<b>28.51</b>	0.71
DUR 9	---	---	1.000	0.01	9.24	11.6	197.4	29.32	<b>29.32</b>	1.55
DUR 2	---	---	1.000	0.02	8.78	10.1	190.7	29.42	<b>29.42</b>	1.68
DUR 27	---	---	1.000	0.02	8.25	9.3	175.0	30.10	<b>30.10</b>	1.65
DUR 4	---	---	1.000	0.02	9.31	11.5	189.7	30.53	<b>30.53</b>	0.82
DUR 3/02	---	---	1.000	0.02	9.56	11.2	196.9	30.59	<b>30.59</b>	0.88
DUR 3/01	---	---	1.000	0.02	9.64	10.2	194.8	31.67	<b>31.67</b>	0.57
DU R26	---	---	1.000	0.02	8.25	8.6	164.2	32.15	<b>32.15</b>	1.66
Lim t3 23	319	190	0.875	0.03	1.71	7.4	74.0	12.70	<b>14.50</b>	0.73
Lim t3 H	474	185	0.869	0.04	3.47	11.3	148.3	13.84	<b>15.92</b>	0.89
Lim t3 31	316	260	0.914	0.05	2.32	10.1	76.7	15.21	<b>16.64</b>	0.84
Lim t3 22	228	239	0.904	0.03	5.46	17.5	204.0	15.37	<b>17.01</b>	0.80
Lim t3 D	312	237	0.908	0.04	1.43	2.8	51.7	17.65	<b>19.43</b>	1.23

**Table 4.2b:** Dimensions of the analysed grains with associated Ft corrections according to Farley et al. [42]. No such correction is required for the Durango shards, see text for explanations. \*Weight and concentrations in ppm is based on crystal sizes and therefore associated with large but unknown errors. (U-Th)/He ages are reported with errors at the 2  $\sigma$  level.

## DISCUSSION

The weighted mean age of the analysed Durango apatites of  $30.0 \pm 2.7$  Ma is in excellent agreement with ages determined in other laboratories for Durango apatite; i.e. California Institute of Technology (single grain):  $31.13 \pm 2.02$  Ma [23], Nancy (multigrain aliquots):  $32.3 \pm 1.4$  Ma [51], CSIRO, Australia, (single grain):  $31.5 \pm 1.6$  Ma [25], SUERC, Glasgow (aliquots of 2 grains):  $30.2 \pm 2.2$  (K. Dobson, personal comm.). The Th/U ratios determined for Durango range from 16.5- 19.2 with an average of  $17.75 \pm 0.9$ . This agrees well with ranges between 15-22 and 17.2-20.4 [10, 23] respectively and with data from earlier studies obtained with various analytical techniques [50, 59]. Because a systematic relationship between Th/U ratios and He-ages is not observed the broad range in Th/U most likely reflects considerable heterogeneity in uranium and thorium within a single grain (all shards originate from the same crystal, CIT-DUR-A). The relatively high error in the uranium determination of DUR 9 can be explained by the very low uranium contents of this sample (Tab. 4.2a).

The Lim t3 apatite yielded a weighted mean age of  $16.3 \pm 3.6$  Ma, that is in agreement with the value of  $16.8 \pm 2.0$  determined on multigrain aliquots [51]. The Th/U ratios range from 7.6 to 18.5 and display a broader spread than the values ranging from 9.5-15.2 reported by Kraml et al. [51]. The data showing the smaller scatter was determined on multigrain samples while ratios reported here are from single grain analysis. The larger scatter in laser single grain data compared to multigrain aliquots have been observed previously [10] and is best explained by the assumption that multi grain aliquots produce average ratios by smoothing out extremes. The grain (Lim t3 D, Tab. 4.2b) yielding the highest age of  $19.4 \pm 1.2$  had the highest Th/U ratio and the lowest concentrations in uranium. Variations in Th/U might indicate loss of parent nuclides during laser heating. Due to the chemically and physically distinct behaviour of these elements, U-Th loss would lead to a shift towards older He-ages [8]. Although this cannot be categorically ruled out the determined age still falls into the  $2\sigma$  range and was therefore not excluded from the calculation of the mean. Excluding the age would result in a weighted mean of  $15.9 \pm 2.2$  that is statistically indistinguishable from the  $16.3 \pm 3.6$  value determined by including this potentially erroneous data point.

The external reproducibility for the Durango apatite is 2.7 Ma and is about 2.5 times higher than the average analytical error of 1.2 Ma. McDowell et al. [23] determined a standard deviation that was 3 times higher than their analytical precision. All these shards originated from the same crystal (CIT-DUR-A). In a laser ablation study also of the Durango apatite, Boyce et al. [60] demonstrated uranium and thorium heterogeneity at a scale of 20-100  $\mu\text{m}$ .

Coupled with the long stopping distances of the  $\alpha$ -particles ( $\sim 20 \mu\text{m}$ ) this heterogeneity could well explain the observed spread in (U-Th)/He ages.

In the case of the Lim t3 apatite the external reproducibility was 3.6 Ma, and was about 3.5 times higher than the average analytical error of 1.1 Ma. No laser ablation data is available for the Lim t3, but uranium and thorium concentrations within individually analysed single crystals show a considerable variation (Tab. 4.2b). This observation is supported by data from Kraml et al. [51] reporting grain size dependent heterogeneity within multigrain aliquots. Zoning of REE and actinides is not unique to the two standards used in this study as it is found in many apatites [45-48, 60]. Most if not all accessory minerals used for (U-Th)/He dating display compositional zoning. Based on these observations it is therefore suggested that several single grains of one sample need to be measured to accurately determine the true spread in ages from one single sample. In light of the recent work done on zircons, titanites and monazites these issues are even more significant since zoning of uranium and thorium in these minerals is even more pronounced [61-64].

Particularly in samples which have remained at temperatures close to the closure temperature for geologically long periods, i.e. several tens of millions of years, and have cooled slowly through the closure temperature, effects of zonation are of significant concern [65]. In crystals that have cooled rapidly through the closure temperature the effect is not believed to produce a large spread in ages. As pointed out by Meesters and Dunai [43] and Hourigan et al. [44] the effects of zonation therefore needs to be incorporated into the calculation of  $\alpha$  ejection corrections.

## CONCLUSIONS

Indirect laser heating of single grains can be applied successfully in combination with MC-ICPMS analysis of uranium and thorium. The obtained He-ages and Th/U ratios of apatite standards (Durango and Limberg t3) are in excellent agreement with published results. Thus single grain dating including small or U-, and Th-poor grains can be performed with an accuracy that is comparable to analyses performed on multigrain aliquots. The very small helium blank associated with laser heating greatly reduces blank issues; nonetheless uncertainties in the helium analysis remain the dominant part of the analytical error associated with the He-age. Applying MC-ICPMS reduces uranium and thorium errors compared to other techniques involving conventional single collector ICPMS [10, 22, 26, 27]. Uranium and thorium errors were mostly  $\sim 1\%$  and have essentially no impact on the error in the He-age. This minimal impact can also be seen for two samples (DUR9, and Lim t3 D) with

higher U and Th errors (Table 2b). The observed errors of the He-ages (2-6%) are therefore completely dominated by the error of the helium measurements. By reducing uncertainties on the uranium and thorium measurements through MC-ICPMS, errors of the He-ages can essentially be limited to the performance of the helium measurements alone.

The errors on individual grains are in most cases smaller than the external reproducibility of the standard ages. This indicates that the spread of single grain ages from one sample (Lim t3) or even within one crystal (Durango) is real. The most likely explanation for this behaviour is the heterogeneity of uranium and thorium within one grain. It may therefore be prudent to date several single grains of one sample in order to reveal the true range of the spread in ages. This is especially important in areas where cooling through the closure temperature and subsequent exhumation was slow (i.e. several tens of millions of years).

Even more desirable, although technically difficult to achieve, would be a direct characterisation of the zoning within the analysed crystal [44]. The geological significance of (U-Th)/He ages could be greatly improved with the knowledge of these additional parameters.

#### **ACKNOWLEDGEMENTS**

The authors wish to thank Dr Meinert Rahn (HSK Villigen, Switzerland) for providing the Limberg t3 apatite and Dr Fin Stuart (SUERC, Scotland) for the CIT-DUR-A Durango crystal shards. Drs Felix Oberli and Heiri Baur are also thanked for their technical support and the rest of the IGMR group at ETH for keeping the clean laboratories and mass spectrometers running. This research was supported by the Swiss Sciences Foundation grants 21-63410.00 and is part of the PhD thesis of the first author.

---

**REFERENCES CITED**

- 1 K.A. Farley, Helium diffusion from apatite; general behavior as illustrated by Durango fluorapatite, *Journal of Geophysical Research, B, Solid Earth and Planets* 105(2), 2903-2914, 2000.
- 2 R.A. Wolf, K.A. Farley and L.T. Silver, Helium diffusion and low-temperature thermochronometry of apatite, *Geochimica et Cosmochimica Acta* 60(21), 4231-4240, 1996.
- 3 R.A. Wolf, K.A. Farley and D.M. Kass, Modeling of the temperature sensitivity of the apatite (U-Th)/ He thermochronometer, *Chemical Geology* 148(1-2), 105-114, 1998.
- 4 M.A. House, B.P. Wernicke and K.A. Farley, Estimation of paleorelief using (U-Th)/ He thermochronology; an example from the Sierra Nevada, California, in: *Geological Society of America, 1997 annual meeting* 29; 6, pp. 478, Geological Society of America (GSA), Boulder, CO, United States, 1997.
- 5 R.A. Wolf, K.A. Farley and L.T. Silver, Assessment of (U-Th)/ He thermochronometry; the low-temperature history of the San Jacinto Mountains, California, *Geology (Boulder)* 25(1), 65-68, 1997.
- 6 A.C. Warnock, P.K. Zeitler, R.A. Wolf and S.C. Bergman, An evaluation of low-temperature apatite U-Th/ He thermochronometry, *Geochimica et Cosmochimica Acta* 61(24), 5371-5377, 1997.
- 7 P.F. Green and I.R. Duddy, Paleotemperature Estimation from Apatite Fission-Track Analysis - Comments, *Journal of Petroleum Geology* 12(1), 111-114, 1989.
- 8 P.W. Reiners and K.A. Farley, Helium diffusion and (U-Th)/ He thermochronometry of titanite, *Geochimica et Cosmochimica Acta* 63(22), 3845-3859, 1999.
- 9 F.M. Stuart and C. Persano, Laser melting of apatite for (U-Th)/ He chronology; progress to date, in: *AGU 1999 fall meeting* 80; 46, Suppl., pp. 1169, American Geophysical Union, Washington, DC, United States, 1999.
- 10 M.A. House, K.A. Farley and D. Stockli, Helium chronometry of apatite and titanite using Nd-YAG laser heating, *Earth and Planetary Science Letters* 183(3-4), 365-368, 2000.
- 11 P.W. Reiners, T.L. Spell, S. Nicolescu and K.A. Zanetti, Zircon (U-Th)/He thermochronometry: He diffusion and comparisons with Ar-40/Ar-39 dating, *Geochimica Et Cosmochimica Acta* 68(8), 1857-1887, 2004.
- 12 D.F. Stockli and K.A. Farley, Empirical constraints on the titanite (U-Th)/He partial retention zone from the KTB drill hole, *Chemical Geology* 207(3-4), 223-236, 2004.
- 13 P.E. Damon and J.L. Kulp, Determination of radiogenic helium in zircon by stable isotope dilution technique, *Transactions - American Geophysical Union* 38(6), 945-953, 1957.
- 14 F.P. Fanale and J.L. Kulp, The helium method and the age of the Cornwall, Pennsylvania magnetite ore, *Economic Geology and the Bulletin of the Society of Economic Geologists* 57, 735-746, 1962.
- 15 P.E. Damon and P.F. Green, Investigations of the helium age dating method by stable isotope dilution technique, in: *Radioactive Dating*, pp. 55-69, IAEA, Vienna, 1963.
- 16 F.P. Fanale and J.L. Kulp, Uranium, Thorium-helium dating of magnetite, *Geological Society of America Special Paper* 76(57), 1964.
- 17 F.P. Fanale and O. Schaeffer, Helium-Uranium Ratios for Pleistocene and Tertiary Fossil Aragonites, *Science* 149(3681), 312-&, 1965.

- 18 M.L. Bender, Helium-Uranium Dating of Corals, *Geochimica Et Cosmochimica Acta* 37(5), 1229-1247, 1973.
- 19 M.P. Ferreira, R. Macedo, V. Costa, J.H. Reynolds, J.E. Riley, Jr. and M.W. Rowe, Rare-gas dating; II, Attempted uranium-helium dating of young volcanic rocks from the Madeira Archipelago, *Earth and Planetary Science Letters* 25(2), 142-150, 1975.
- 20 J.S. Leventhal, An Evaluation of the Uranium-Thorium-Helium Method for Dating Young Basalts, *Journal of Geophysical Research* 80(14), 1911-1914, 1975.
- 21 H.J. Lippolt, M. Leitz, R.S. Wernicke and B. Hagedorn, (Uranium+thorium)/helium dating of apatite; experience with samples from different geochemical environments, *Chemical Geology* 112(1-2), 179-191, 1994.
- 22 P.K. Zeitler, A.L. Herczeg, I. McDougall and M. Honda, U-Th-He dating of apatite; a potential thermochronometer, *Geochimica et Cosmochimica Acta* 51(10), 2865-2868, 1987.
- 23 F.W. McDowell, W.C. McIntosh and K.A. Farley, A precise  $^{40}\text{Ar}/^{39}\text{Ar}$  reference age for the Durango apatite (U-Th)/He and fission-track dating standard, *Chemical Geology* 214(3-4), 249-263, 2005.
- 24 K.A. Farley, B.P. Kohn and B. Pillans, The effects of secular disequilibrium on (U-Th)/He systematics and dating of Quaternary volcanic zircon and apatite, *Earth and Planetary Science Letters* 201(1), 117-125, 2002.
- 25 N.J. Evans, N.S.F. Wilson, J.S. Cline, B.I.A. McInnes and J. Byrne, Fluorite (U-Th)/He thermochronology: Constraints on the low temperature history of Yucca Mountain, Nevada, *Applied Geochemistry* 20(6), 1099-1105, 2005.
- 26 R. Pik, B. Marty, J. Carignan and J. Lave, Stability of the upper Nile drainage network (Ethiopia) deduced from (U-Th)/He thermochronometry; implications for uplift and erosion of the Afar Plume dome, *Earth and Planetary Science Letters* 215(1-2), 73-88, 2003.
- 27 P.W. Reiners, R. Brady, K.A. Farley and B.P. Wernicke, Titanite and apatite (U-Th)/He thermochronometry of the Gold Butte Block, southern Nevada, in: AGU 1999 fall meeting 80; 46, Suppl., pp. 1169, American Geophysical Union, Washington, DC, United States, 1999.
- 28 K.A. Farley, (U-Th)/He dating; techniques, calibrations, and applications, in: Noble gases in geochemistry and cosmochemistry 47, pp. 819-843, Mineralogical Society of America and Geochemical Society, Washington, DC, United States, 2002.
- 29 D.F. Stockli, T.A. Dumitru, M.O. McWilliams and K.A. Farley, Cenozoic tectonic evolution of the White Mountains, California and Nevada, *Geological Society of America Bulletin* 115(7), 788-816, 2003.
- 30 C. Persano, F.M. Stuart, P. Bishop and D.N. Barfod, Apatite (U-Th)/He age constraints on the development of the Great Escarpment on the southeastern Australian passive margin, *Earth and Planetary Science Letters* 200(1-2), 79-90, 2002.
- 31 P.W. Reiners and T.L. Spell, Intercalibration of zircon (U-Th)/He and K-feldspar (super 40) Ar/ (super 39) Ar thermochronometry, in: Abstracts of the 12th annual V M Goldschmidt conference 66; 15A, pp. 631, Pergamon, Oxford, International, 2002.
- 32 C.C. Shen, R.L. Edwards, H. Cheng, J.A. Dorale, R.B. Thomas, S.B. Moran, S.E. Weinstein and H.N. Edmonds, Uranium and thorium isotopic and concentration measurements by magnetic sector inductively coupled plasma mass spectrometry, *Chemical Geology* 185(3-4), 165-178, 2002.
- 33 R.L. Edwards, J.H. Chen and G.J. Wasserburg, U-238 U-234-Th-230-Th-232 Systematics and the Precise Measurement of Time over the Past 500000 Years, *Earth and Planetary Science Letters* 81(2-3), 175-192, 1987.

- 34 S. Aciego, B.M. Kennedy, D.J. DePaolo, N. Christensen John and I. Hutcheon, U-Th/He age of phenocrystic garnet from the 79 AD eruption of Mt. Vesuvius, Earth and Planetary Science Letters 216(1-2), 209-219, 2003.
- 35 E. Rutherford, Present problems in radioactivity, Popular Science Monthly(May), 1-34, 1905.
- 36 E. Rutherford, Die Radioaktivität, 595pp. pp., Springer, Berlin, 1907.
- 37 R.J. Strutt, On The Radioactive Minerals, Proceedings Royal Society(A76), 88 - 101, 1905.
- 38 E. Rutherford, Radioaktive Umwandlungen (Silliman - Vorlesungen), Vieweg, Braunschweig, 1907.
- 39 P.M. Hurley, Alpha Ionization damage as a Cause of Low He Ratios., Transactions of the American Geophysical Union 33, 174 - 183, 1952.
- 40 D.X. Belton, M. Lorencak, T.J. Carter, N. M., B.P. Kohn and A.J.W. Gleadow, Samarium in apatite: contributions to radiogenic helium and the effect on (U-Th)/He thermochronology., in: 10th Fission Track Congress, pp. 40 (DVL-05-P), Amsterdam, 2004.
- 41 J.F. Ziegler, Helium: Stopping Powers and Ranges in all Elementa Matter, 367 pp., Oxford Press, New York, 1977.
- 42 K.A. Farley, R.A. Wolf and L.T. Silver, The effects of long alpha-stopping distances on (U-Th)/ He ages, Geochimica et Cosmochimica Acta 60(21), 4223-4229, 1996.
- 43 A.G.C.A. Meesters and T.J. Dunai, Solving the production-diffusion equation for finite diffusion domains of various shapes; Part II, Application to cases with alpha-ejection and nonhomogeneous distribution of the source, Chemical Geology 186(1-2), 57-73, 2002.
- 44 J.K. Hourigan, P. Reiners and M.T. Brandon, U-Th zonation dependent alpha-ejection in (U-Th)/He chronometry, Geochimica et Cosmochimica Acta 69(13), 3349-3365, 2005.
- 45 J.H. Tepper and S.M. Kuehner, Complex zoning in apatite from the Idaho Batholith; a record of magma mixing and intracrystalline trace element diffusion, American Mineralogist 84(4), 581-595, 1999.
- 46 T.J. Dempster, M. Jolivet, M.N. Tubrett and C.J.R. Braithwaite, Magmatic zoning in apatite; a monitor of porosity and permeability change in granites, Contributions to Mineralogy and Petrology 145(5), 568-577, 2003.
- 47 C. Knutson, D.R. Peacor and W.C. Kelly, Luminescence, color and fission track zoning in apatite crystals of the Panasqueira tin-tungsten deposit, Beira-Baixa, Portugal, American Mineralogist 70(7-8), 829-837, 1985.
- 48 U. Kempe and J. Gotze, Cathodoluminescence (CL) behaviour and crystal chemistry of apatite from rare-metal deposits, Mineralogical Magazine 66(1(434)), 151-172, 2002.
- 49 J.W. Boyce and K.V. Hodges, U and Th zoning in Cerro de Mercado (Durango, Mexico) fluorapatite: Insights regarding the impact of recoil redistribution of radiogenic He-4 on (U-Th)/He thermochronology, Chemical Geology 219(1-4), 261-274, 2005.
- 50 E.J. Young, A.T. Myers, E.L. Munson and N.M. Conklin, Mineralogy and geochemistry of fluorapatite from Cerro de Mercado, Durango, Mexico., U.S. Geol. Surv. Prof. Pap.(650-D), D84-D93, 1969.
- 51 M. Kraml, R. Pik, M.K. Rahn, J. Carignan and J. Keller, A potential single grain  $^{40}\text{Ar}/^{39}\text{Ar}$ , (U-Th)/He and FT age standard: the Limberg t3 tuff, submitted: Geostandards and Geoanalytical Research, 2005.

- 52 K.A. Farley, A.E. Blythe and R.A. Wolf, Apatite helium ages; comparison with fission track ages and track-length-derived thermal models, in: AGU 1996 fall meeting 77; 46, Suppl., pp. 644-645, American Geophysical Union, Washington, DC, United States, 1996.
- 53 R. Wieler, T. Graf, A. Pedroni, P. Signer, P. Pellas, C. Fieni, M. Suter, S. Vogt, R.N. Clayton and J.C. Laul, Exposure history of the regolithic chondrite Fayetteville; II, Solar-gas-free light inclusions, *Geochimica et Cosmochimica Acta* 53(6), 1449-1459, 1989.
- 54 S. Luo, M. Rehkämper, D.C. Lee and A.N. Halliday, High precision  $^{230}\text{Th}/^{232}\text{Th}$  and  $^{234}\text{U}/^{238}\text{U}$  measurements using energy-filtered ICP magnetic sector multiple collector mass spectrometry., *International Journal of Mass Spectrometry*(171), 105-117, 1997.
- 55 M.B. Andersen, C.H. Stirling, E.K. Potter and A.N. Halliday, Toward epsilon levels of measurement precision on U-234/U-238 by using MC-ICPMS, *International Journal of Mass Spectrometry* 237(2-3), 107-118, 2004.
- 56 A.N. Halliday, D.C. Lee, J.N. Christensen, A.J. Walder, P.A. Freedman, C.E. Jones, C.M. Hall, W. Yi and D. Teagle, Recent Developments in Inductively-Coupled Plasma Magnetic-Sector Multiple Collector Mass-Spectrometry, *International Journal of Mass Spectrometry and Ion Processes* 146, 21-33, 1995.
- 57 N.S. Belshaw, P.A. Freedman, R.K. O'Nions, M. Frank and Y. Guo, A new variable dispersion double-focusing plasma mass spectrometer with performance illustrated for Pb isotopes, *International Journal of Mass Spectrometry and Ion Processes* 151, 51-58, 1998.
- 58 S. Turner, P. van Calsteren, N. Vigier and L. Thomas, Determination of thorium and uranium isotope ratios in low-concentration geological materials using a fixed multi-collector-ICP-MS, *Journal of Analytical Atomic Spectrometry* 16(6), 612-615, 2001.
- 59 C.W. Naeser and R.L. Fleischer, Age of the apatite at Cerro de Mercado, Mexico; a problem for fission-track annealing corrections, *Geophysical Research Letters* 2(2), 67-70, 1975.
- 60 J.W. Boyce and K.V. Hodges, U and Th zoning in Cerro de Mercado (Durango Mexico) fluorapatite: Insights regarding the impact of recoil redistribution of radiogenic  $^4\text{He}$  on (U-Th)/He thermochronology, *Chemical Geology* in press, 2005.
- 61 J.N. Aleinikoff, R.P. Wintsch, C.M. Fanning and M.J. Dorais, U-Pb ages from multiple generations of igneous and metamorphic titanite; an integrated SHRIMP, SEM, and EMPA study, in: *Beyond 2000; new frontiers in isotope geoscience (incorporating ACOG 4); abstracts and proceedings*, University of Melbourne, Parkville, Victoria, Australia, 2000.
- 62 G. Foster, H.D. Gibson, R. Parrish, M. Horstwood, J. Fraser and A. Tindle, Textural, chemical and isotopic insights into the nature and behaviour of metamorphic monazite, in: *Chemistry and physics of accessory minerals; crystallisation, transformation and geochronological applications* 191; 1-3, pp. 183-207, Elsevier, Amsterdam, Netherlands, 2002.
- 63 G. Franz, G. Andrehs and D. Rhede, Crystal chemistry of monazite and xenotime from Saxothuringian-Moldanubian metapelites, NE Bavaria, Germany, in: *Fluid inclusions* 8; 5, pp. 1097-1118, Schweizerbart'sche Verlagsbuchhandlung (Naeglele u Obermiller), Stuttgart, Federal Republic of Germany, 1996.
- 64 D.P. Hawkins and S.A. Bowring, U-Pb systematics of monazite and xenotime; case studies from the Paleoproterozoic of the Grand Canyon, Arizona, *Contributions to Mineralogy and Petrology* 127(1-2), 87-103, 1997.

65 P.V. Crowhurst, P.F. Green, K.A. Farley and B.J. Griffin, "Anomalously old" He: ages: what causes them and what can we do about them?, in: 10th Fission Track Congress, pp. 19 (DVL-11-O), Amsterdam, 2004.

# Chapter 5

## Thermochronology of the Coastal Margin of Peru

### 5.1 Introduction

Uncovering the cooling events of the upper crust is often best carried out using low temperature chronometers such as fission-track and (U-Th)/He.

For the fission-track system, there is no discrete "closure" temperature at which the tracks become retained. However, the concept of a partial annealing zone where tracks are unstable has been defined with upper and lower temperature limits. While the apatite partial annealing zone (APAZ) is widely accepted as being between 60 and 110°C, the effective closure temperature is normally taken as 110°C but can vary depending on factors such as chemistry and cooling rates (Corrigan, 1993; Green and Duddy, 1989). Within the APAZ the length of tracks is variable depending on the time taken to pass through the zone. Thus the distribution pattern of confined fission-track lengths is therefore the result of a particular cooling history. The sample age and track-length parameters can be compared to those determined through experimental annealing. This is done using the random Monte Carlo and Genetic Algorithm approach (Gallagher, 1994; Ketcham, 2005; Ketcham et al., 2000) yielding the thermal histories of the chosen sequences.

Research into zircon annealing is not as advanced as that for apatite - from experimental studies extrapolated to the geological time scale, current estimates for the partial annealing zone are 390°C to 170°C (Yamada et al., 1995). The closure temperature considered, in this study is 270°C ± 30°C. The upper limit covers the potentially rapidly cooled Coastal Batholith samples, which according to (Atherton and Petford, 1991; Haederle and Atherton, 2002) were intruded into the crust's upper 2-3 km. The lower limit covers the more slowly cooled zircons from the Precambrian and Palaeozoic suites. Zircon fission-track analysis although not as well constrained as the apatite system can provide important constraints for the Monte Carlo modeling mentioned above.

The (U-Th)/He system displays a comparable behaviour as it also has no discrete closure temperature. Laboratory experiments for apatite show that helium retention is sensitive to very low temperatures (<100°C). It has been shown that the helium diffusion is a function of crystal shape and size, rate of cooling, as well as the distribution of uranium and thorium within the crystal (Farley, 2000; Lippolt et al., 1994; Meesters and Dunai, 2002a, b; Warnock et al., 1997; Wolf et al., 1996). Variations in any of these parameters result in changes of amounts of helium retained within the crystal. The upper boundary of the so called Helium Partial Retention Zone (HePRZ) for an apatite of ~100-150 µm width with a uniform distribution of uranium and thorium is ~68°C for a cooling rate of 10°C/myr. The boundaries of the HePRZ zone are variable however but are considered to lie between 40°C and 85°C (Farley 2000). Just as with fission-track length data the (U-Th)/He data (age, grain size, uranium and thorium distribution) can be modelled applying a Monte Carlo approach (Farley et al., 1996; Ketcham, 2005; Meesters and Dunai, 2002a, b). However as mentioned above, several parameters influence the ages and without a good knowledge of these modelling is not conclusive. In this study the HePRZ is considered to be ~40-85°C with an effective closure temperature of 70±15°C.

By combining the various methodologies including the higher temperature geochronometers, such as U-Pb and Ar/Ar, the long term thermal events, often from crystallisation through the exposure to the surface, can be determined.

Using the methods described above, the primary goal of this study was to gain a better understanding of the low temperature cooling of the Peruvian coastal margin in order to detect thermo-tectonic events. A special emphasis was the attempt to quantify the timing and amount of change induced by the subducting Nazca Ridge. (The regional geology of Peru has been described in chapter 2.)

Very little previous work has been done in the region of the Peruvian coastal margin from a low temperature thermochronological point of view. Laubacher and Naeser (1994) determined fission-track analyses on the granitic rocks of the Eastern Cordillera of northern Peru, where they found evidence for late Jurassic (zircon FT) and Cenozoic (apatite FT) cooling. From southern Peru apatite ages of 30-20 Ma have been reported (Kontak et al., 1990). (Garver et al., 2005) determined late Tertiary ages from the Cordillera Blanca in northern Peru, which suggested rapid uplift since the Tertiary. No (U-Th)/He data has been acquired previously in Peru.

## 5.2 Methods

Zircon and apatite were dated by the fission-track method outlined by (Seward, 1989) using the external detector method (Hurford and Green, 1983). Ages were calculated using the zeta factor approach (Hurford and Green, 1983) with a mean  $\zeta$  value of  $120 \pm 5$  for dosimeter glass CN1/zircon and  $277 \pm 11$  for glass CN5/apatite. The statistical uncertainties on the ages are the standard error as defined by (Green, 1981) and incorporate errors from the induced and spontaneous tracks as well as those of the glass standard. Apatites were dated by the (U-Th)/He method as described in chapter 3 of this thesis. Errors are expressed for both dating techniques in Ma at the  $2\sigma$  level.

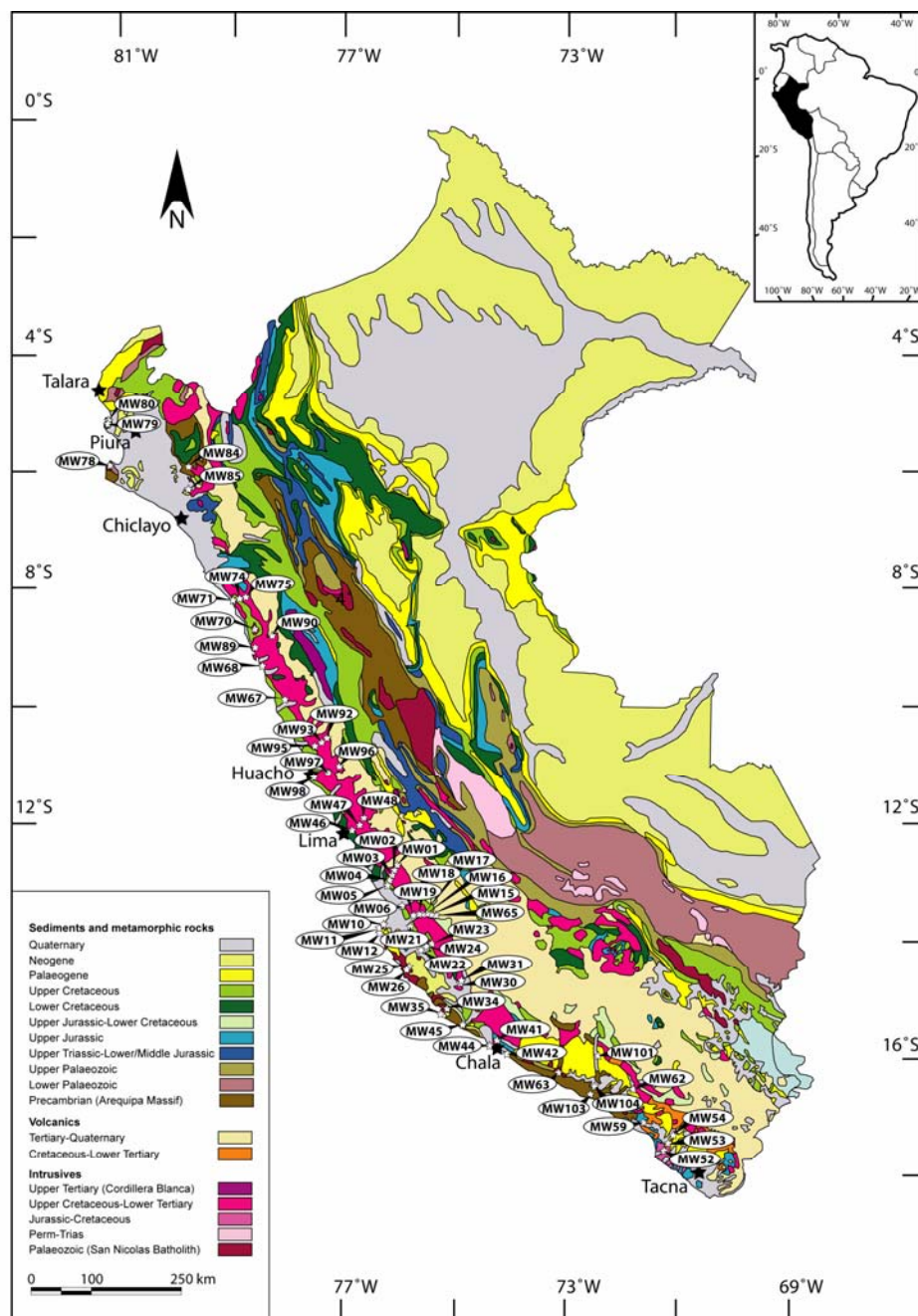


**Figure 5.1:** Location of samples analysed from the Peruvian coastal margin.

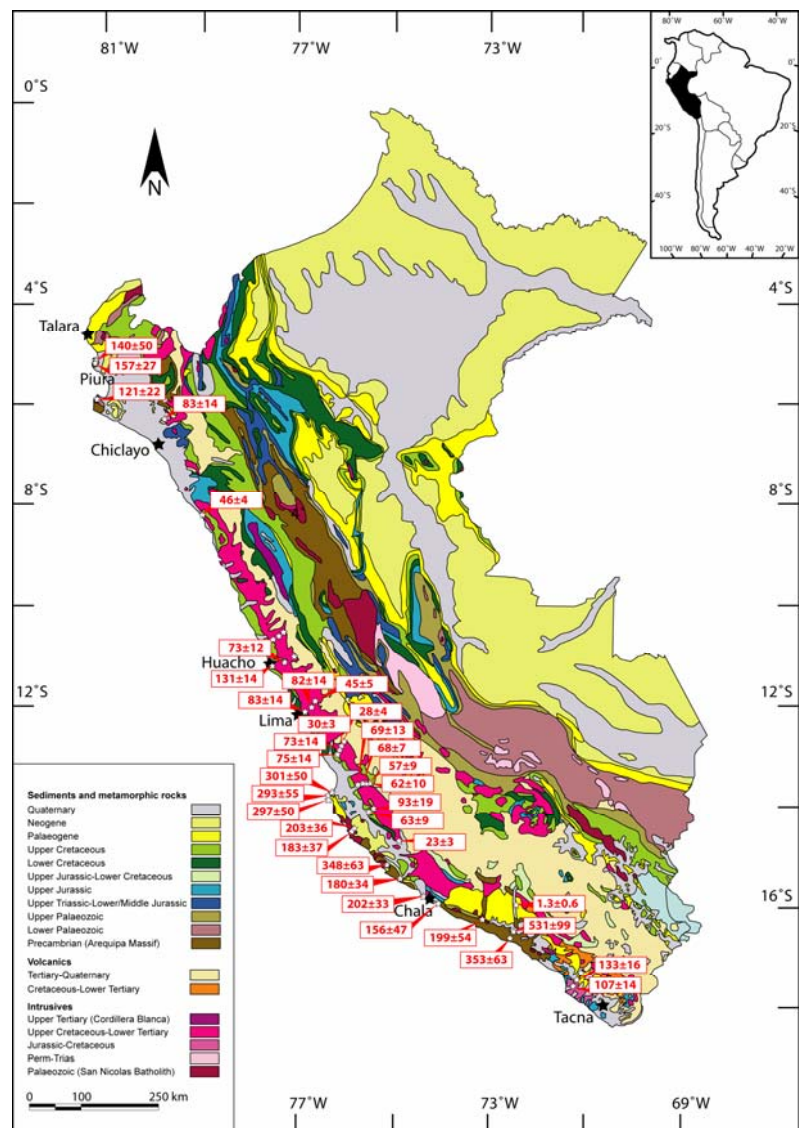
## 5.3 Results

### 5.3.1 Zircon fission track

36 zircon samples from the Precambrian Arequipa Massif and its Palaeozoic intrusive bodies (San Nicolas Batholith), the Coastal Batholith, and Tertiary ignimbrites were dated (Fig. 5.1). While the Precambrian and the Palaeozoic rocks yield zircon fission-track ages from 530-121 Ma, the samples from the Coastal Batholith display much less scatter with ages between 130-45 Ma consistent with their younger origin with a clear cluster of ages between 80-60 Ma (Fig. 5.2, Tab. 5.1). The ignimbrites have Tertiary ages. The  $\chi^2$ -values range from 0 to 99 with a marginal correlation to older ages failing the test (i.e. < 5%). The age-altitude plot excluding the ignimbrites (Fig. 5.3) reveals no immediate correlation.

By plotting all the ages of samples from locations with altitudes of less than 600 m in order to remove any major altitude variability, between Talara in the northwest and Tacna in the southeast (Fig. 5.4a), the difference in the source lithologies is emphasised. The older ages are from the Precambrian and Palaeozoic suites currently outcropping on and south of the Nazca Ridge. The Precambrian outcrops in the far north fall within the age spread of those from the Coastal Batholith. There is no significant variation in Coastal Batholith ages from north to south. Only two ages in the south (MW52, 53) were analysed however and they are slightly older.

**Figure 5.2:** Zircon fission-track ages along the Peruvian coastal margin. Errors reported are  $2\sigma$ .



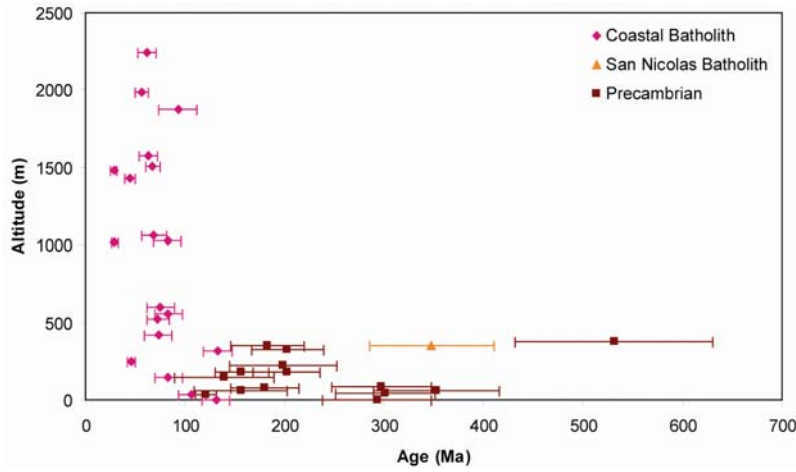
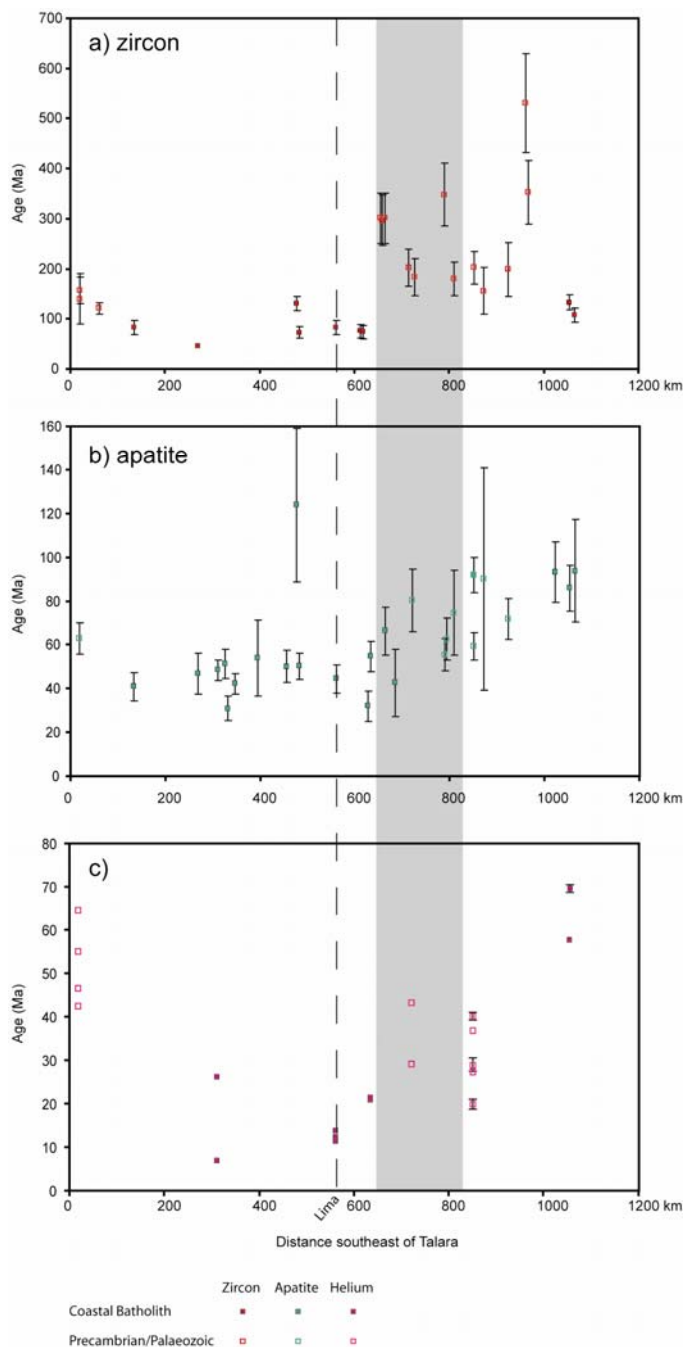


**Figure 5.3:** Zircon fission-track ages versus altitude for all zircon samples except Tertiary ignimbrites. Different lithologies are separated by colours and symbols.

**Figure 5.4:** Fission-track (a, b) and (U-Th)/He (c) ages from altitudes below 600 m. The grey band presents the position of the subducting Nazca Ridge. Note different scales on the age axis for the different geochronometers.



Sample Number	Coordinates (UTM)	Alt. (m)	Irradiation number	Number of grains counted	Standard track $\rho_d \times 10^4 \text{ cm}^{-2}$ (counted)	$\rho_s \times 10^4 \text{ cm}^{-2}$ (counted)	$\rho_i \times 10^4 \text{ cm}^{-2}$ (counted)	U conc (ppm)	P( $\chi^2$ ) (%) (Var)	Age (Ma)	$\pm 2\sigma$ (Ma)
<b>MW01</b>	18 396 776E 85 92 759N	1485	ETH-237-7	10	49.95 (1846)	597 (711)	632 (753)	506	22 (8)	<b>28.4</b>	3.6
<b>MW02</b>	18 398 340E 85 80 143N	1020	ETH-237-8	20	46.47 (1846)	380 (1603)	358 (1511)	308	3 (12)	<b>29.6</b>	3.0
<b>MW03</b>	18 398 340E 85 80 143N	602	ETH-237-10	10	45.32 (1846)	757 (2345)	268 (831)	231	24 (24)	<b>75.4</b>	13.6
<b>MW04</b>	18 373 653 E 85 61 779N	423	ETH-237-7	10	47.10 (1846)	844 (941)	313 (349)	266	1 (21)	<b>73.2</b>	13.8
<b>MW10</b>	18 360 105E 84 73 277N	42	ETH-237-20	10	42.7 (2770)	1645 (2065)	136 (170)	128	90 (0)	<b>301.0</b>	50.0
<b>MW11</b>	18 357 609E 84 61 504N	0	ETH-238-4	10	38.5 (4307)	2057 (1634)	159 (126)	165	75 (1)	<b>293.0</b>	55.0
<b>MW12</b>	18 362 023E 84 65 876N	87	ETH-238-3	17	38.7 (2132)	2009 (2134)	153 (163)	158	49 (2)	<b>297.0</b>	50.0
<b>MW16</b>	18 457 049E 84 95 280N	2245	ETH-238-7	10	35.2 (4307)	535 (738)	180 (249)	204	44 (0)	<b>62.3</b>	9.4
<b>MW17</b>	18 453 600E 84 95 114N	1983	ETH-238-9	20	35.0 (4307)	1073 (2184)	391 (796)	107	0.5 (18)	<b>56.6</b>	6.8
<b>MW18</b>	18 445 590E 84 97 444N	1510	ETH-238-11	20	36.6 (4307)	389 (1446)	126 (467)	137	59 (0)	<b>67.6</b>	7.4

Sample Number	Coordinates (UTM)	Alt. (m)	Irradiation number	Number of grains counted	Standard track $\rho_d \times 10^4 \text{ cm}^{-2}$ (counted)	$\rho_s \times 10^4 \text{ cm}^{-2}$ (counted)	$\rho_i \times 10^4 \text{ cm}^{-2}$ (counted)	U conc (ppm)	P( $\chi^2$ ) (%) (Var)	Age (Ma)	$\pm 2\sigma$ (Ma)
<b>MW19</b>	18 433 929E 84 96 330N	1058	ETH-238-12	10	36.3 (4307)	848 (776)	266 (243)	291	12 (17)	<b>69.0</b>	13.0
<b>MW23</b>	18 462 927E 84 32 859N	1878	ETH-238-17	10	35.0 (4307)	1361 (1760)	298 (385)	339	0 (25)	<b>93.1</b>	18.8
<b>MW24</b>	18 460 131E 84 32 354N	1574	ETH-238-19	9	34.4 (4307)	1467 (778)	479 (254)	554	99 (0)	<b>63.0</b>	9.2
<b>MW25</b>	18 430 480E 84 00 159N	326	ETH-226-12	9	36.4 (2239)	2253 (1363)	238 (144)	255	65 (0)	<b>203.0</b>	36.0
<b>MW26</b>	18 431 239E 84 01 749N	351	ETH-226-20	9	32.2 (2239)	1262 (1232)	130 (127)	161	20 (10)	<b>183.0</b>	37.0
<b>MW31♦</b>	18 529 010E 83 58 942N	2225	ETH-239-25	10	38.3 (2257)	263 (890)	263 (891)	273	7 (11)	<b>23.1</b>	2.8
<b>MW34</b>	18 485 955E 83 08 403N	348	ETH-226-14	10	35.3 (2239)	4284 (2279)	254 (135)	287	73 (0)	<b>348.0</b>	63.0
<b>MW42</b>	18 604 570E 82 30 735N	63	ETH-238-24	5	33.1 (4307)	767 (402)	97 (51)	117	68 (0)	<b>156.0</b>	47.0
<b>MW44</b>	18 575 157E 82 49 915N	176	ETH-239-21	6	41.6 (2257)	1383 (1769)	170 (217)	162	19 (8)	<b>202.0</b>	33.0
<b>MW45</b>	18 530 272E 82 78 088N	75	ETH-226-24	10	30.2 (2239)	1469 (1269)	146 (126)	193	74 (0)	<b>180.0</b>	34.0

Sample Number	Coordinates (UTM)	Alt. (m)	Irradiation number	Number of grains counted	Standard track $\rho_d \times 10^4 \text{ cm}^{-2}$ (counted)	$\rho_s \times 10^4 \text{ cm}^{-2}$ (counted)	$\rho_i \times 10^4 \text{ cm}^{-2}$ (counted)	U conc (ppm)	P( $\chi^2$ ) (%) (Var)	Age (Ma)	$\pm 2\sigma$ (Ma)
<b>MW46</b>	18 302 083E 86 73 987N	559	ETH-226-17	20	33.8 (2239)	765 (2661)	183 (635)	211	0 (29)	<b>83.2</b>	13.6
<b>MW47</b>	18 320 304E 86 80 876N	1026	ETH-239-19	20	43.2 (2257)	248 (2728)	77 (846)	71	0 (32)	<b>82.3</b>	14.2
<b>MW48</b>	18 322 745E 86 90 854N	1427	ETH-239-23	20	39.9 (2257)	726 (1825)	384 (969)	386	6 (14)	<b>44.8</b>	5.0
<b>MW52</b>	19 250 138E 80 45 865N	32	ETH-274-13	16	3.69 (1925)	435 (2440)	89 (502)	97	5 (16)	<b>107.0</b>	14.0
<b>MW53</b>	19 257 500E 80 43 500N	320	ETH-273-6	20	48.5 (2185)	632 (4171)	135 (893)	112	0 (17)	<b>133.0</b>	15.0
<b>MW63</b>	18 700 810E 81 80 574N	220	ETH-272-18	10	36.3 (1865)	1030 (1850)	111 (200)	123	0 (34)	<b>199.0</b>	54.0
<b>MW71</b>	17 724 965E 90 92 210N	250	ETH-273-3	20	46.9 (2185)	519 (3194)	317 (1951)	271	1 (11)	<b>46.0</b>	4.0
<b>MW78</b>	17 496 660E 93 55 337N	35	ETH-273-26	10	32.8 (2185)	718 (1241)	115 (198)	139	15 (14)	<b>121.0</b>	11.0
<b>MW79</b>	17 504 428E 94 29 938N	142	ETH-273-13	7	40.7 (2185)	1932 (1049)	317 (172)	310	0 (41)	<b>140.0</b>	50.0
<b>MW80</b>	17 504 453E 94 29 724N	177	ETH-273-11	10	42.0 (2185)	1292 (1116)	205 (177)	194	21 (6)	<b>156.8</b>	27.0

Sample Number	Coordinates (UTM)	Alt. (m)	Irradiation number	Number of grains counted	Standard track $\rho_d \times 10^4 \text{ cm}^{-2}$ (counted)	$\rho_s \times 10^4 \text{ cm}^{-2}$ (counted)	$\rho_i \times 10^4 \text{ cm}^{-2}$ (counted)	U conc (ppm)	P( $\chi^2$ ) (% (Var))	Age (Ma)	$\pm 2\sigma$ (Ma)
<b>MW85</b>	17 643 724E 93 13 887N	143	ETH-272-11	10	39.4 (1865)	1733 (2122)	492 (602)	500	0 (21)	<b>83.3</b>	<b>14.2</b>
<b>MW97</b>	17 251 912E 87 67 501N	520	ETH-272-29	10	31.4 (1865)	1982 (1582)	504 (402)	642	4 (16)	<b>72.8</b>	11.6
<b>MW98</b>	17 216 758E 87 57 620N	3	ETH-272-27	10	32.3 (1865)	1936 (6350)	282 (926)	350	5 (9)	<b>131.0</b>	14.0
<b>MW101♦</b>	18 200 618E 87 69 247N	3300	ETH-294-21	10	34.20 (2137)	213 (96)	381 (1715)	445	0 (73)	<b>1.3</b>	0.6
<b>MW103</b>	18 743 497E 81 67 952N	64	ETH-294-23	10	32.8 (2315)	1590 (3157)	85 (168)	103	40 (10)	<b>353.0</b>	63.0
<b>MW104</b>	18 772 531E 81 96 684N	380	ETH-294-5	10	41.9 (2315)	2269 (3647)	101 (163)	94	33 (10)	<b>531.0</b>	99.0

**Table 5.1:** Fission-track ages on zircon.  $\rho_d$ ,  $\rho_s$  and  $\rho_i$  represent the dosimeter, sample spontaneous and induced track densities; P( $\chi^2$ ) is the probability of  $\chi^2$  for  $\nu$  degrees of freedom where  $\nu = \text{no. of crystals} - 1$ ; all ages are central ages (Galbraith, 1981).  $\lambda_D = 1.55125 \times 10^{-10}$ .  $\zeta$  (CN1/zircon) = 120.0 $\pm$ 5.0 (Dr. D. Seward). Samples were irradiated at the ANSTO facility, Australia.

♦ Age of Tertiary ignimbrite.

### 5.3.2 Apatite fission track

49 apatite samples from the Precambrian Arequipa Massif and its Palaeozoic intrusive bodies (San Nicolas Batholith), the Coastal Batholith, and Tertiary ignimbrites were dated (Fig. 5.1). Apatite fission-track ages show a wide range from 124 Ma to 7 Ma (Tab. 5.2, Fig. 5.5). The samples from the Precambrian and Palaeozoic rocks as well as those from the Coastal Batholith yield apatite fission-track ages between 124 and 24 Ma. The ignimbrites have Tertiary ages. The age-altitude plot (Fig. 5.6) excluding the Tertiary ignimbrites, does not reveal an immediate correlation. Neither is a correlation between the lithologies and apatite fission-track ages observable (Fig. 5.6) in contrast to the zircon data (Fig. 5.3). The  $\chi^2$ -values range from 1 to 100 with only one sample (MW74) failing the test.

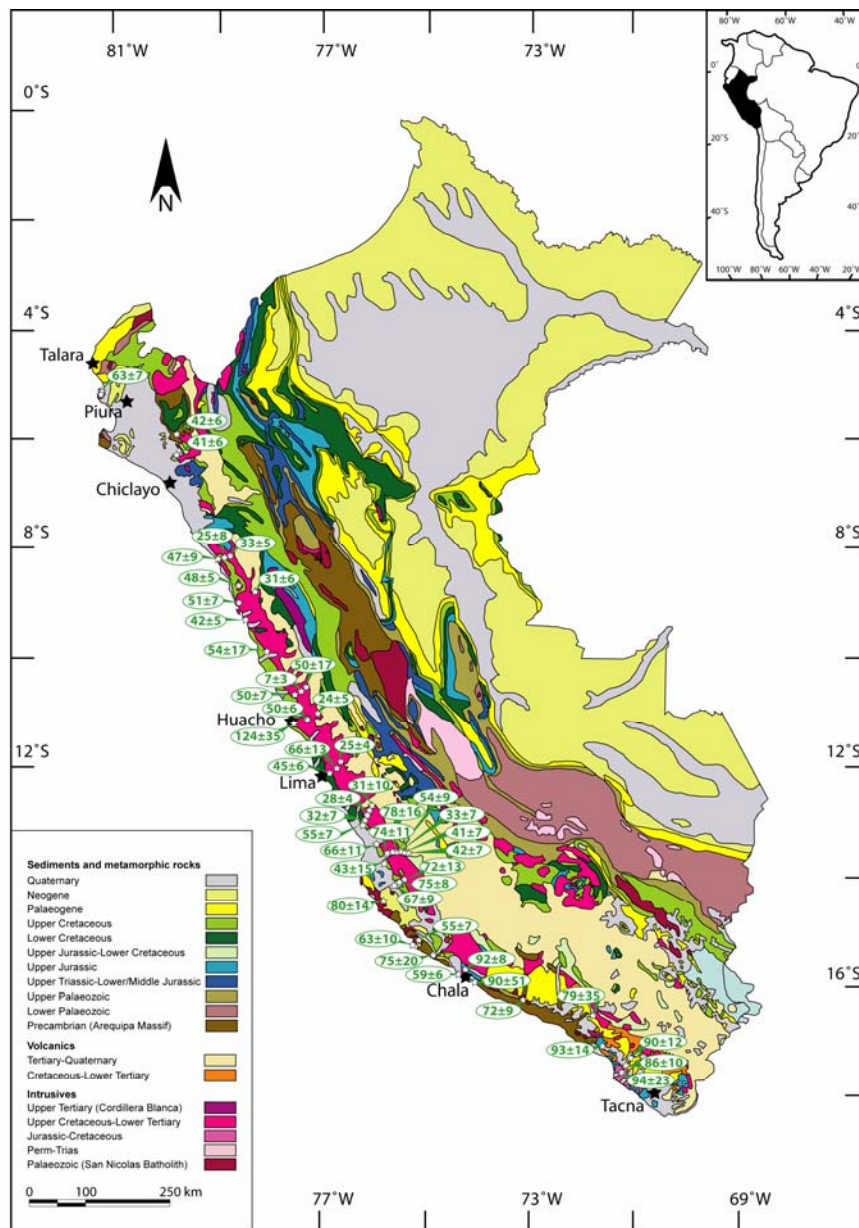


**Figure 5.5:** Apatite fission-track ages along the Peruvian coastal margin. Errors reported are  $2\sigma$ .

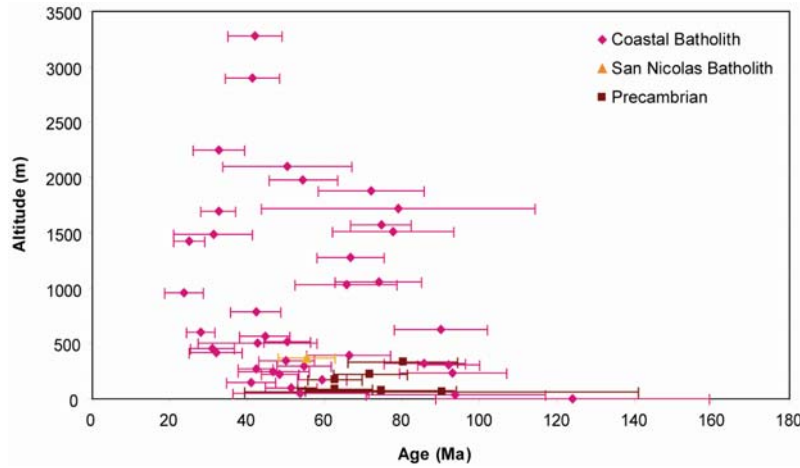


**Figure 5.6:** Apatite fission-track ages versus altitude for all apatite samples except Tertiary ignimbrites. Different lithologies are separated by colours and symbols.

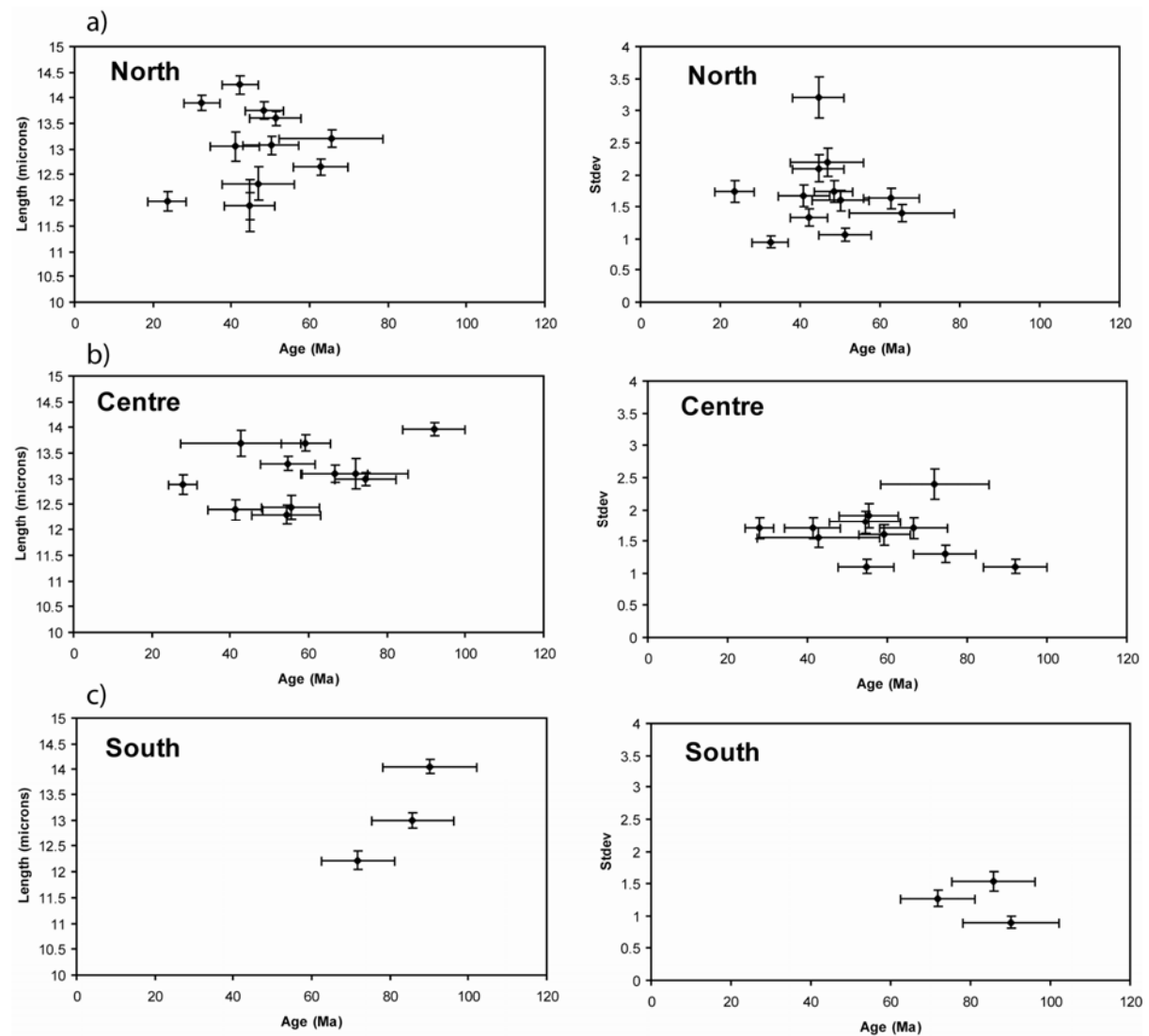


**Figure 5.7:** Boomerang plot (Green 1988) (length vs. age and age vs. standard deviation of the length distribution) for all apatite samples with more than 40 horizontal track lengths and more than 10 dated grains. The data was separated into three regions a) north of, b) above and c) south of the Nazca Ridge. Error bars are  $2\sigma$ .

Sample Number	Coordinates (UTM)	Alt. (m)	Irradiation number	No. of grains counted	Standard track $\rho_d \times 10^4 \text{ cm}^{-2}$ (counted)	$\rho_s \times 10^4 \text{ cm}^{-2}$ (counted)	$\rho_i \times 10^4 \text{ cm}^{-2}$ (counted)	U conc (ppm)	P( $\chi^2$ ) (Var) (%)	Mean track length ( $\mu\text{m}$ )	std dev ( $\mu\text{m}$ ) (No. measured)	Age (Ma)	$\pm 2\sigma$ (Ma)
<b>MW01</b>	18 396 776E 85 92 759N	1485	ETH-233-2/3	8	100.6 (7074)	20.72 (46)	92.34 (205)	16	98 (0)	----	----	<b>31.2</b>	10.2
<b>MW03</b>	18 380 500E 85 71 439N	602	ETH-233-6	20	91.75 (7074)	53.38 (340)	242.07 (1542)	31	99 (0)	12.9 $\pm 0.19$	1.7 (80)	<b>28.0</b>	3.6
<b>MW04</b>	18 373 653E 85 61 779N	423	ETH-233-8/7	19	87.31 (7074)	19.37 (117)	73.34 (443)	12	100 (0)	----	----	<b>31.9</b>	6.8
<b>MW05</b>	18 366 383E 85 55 294N	295	ETH-233-11	20	80.66 (7074)	70.89 (436)	144.23 (887)	22	100 (0)	13.3 $\pm 0.13$	1.1 (76)	<b>54.7</b>	7.0
<b>MW06</b>	18 386 475E 85 17 711N	392	ETH-233-12	20	78.4 (7074)	93.07 (215)	151.95 (351)	23	98 (0)	12.52 $\pm 0.45$	1.42 (10)	<b>66.2</b>	10.8
<b>MW15</b>	18 462 240E 84 95 445N	2895	ETH-233-13	19	76.22 (7074)	68.79 (212)	175.21 (540)	29	96 (0)	12.4 $\pm 0.20$	1.7 (74)	<b>41.3</b>	7.0
<b>MW16</b>	18 457 049E 84 95 280N	2245	ETH-234-2	15	120.6 (3604)	46.18 (127)	235.527 (647)	26	88 (0)	----	----	<b>32.7</b>	6.6
<b>MW17</b>	18 453 600E 84 95 114N	1983	ETH-234-4	16	110.4 (3604)	104.59 (228)	292.66 (638)	30	89 (0)	12.3 $\pm 0.19$	1.8 (88)	<b>54.4</b>	8.8
<b>MW18</b>	18 445 590E 84 97 444N	1510	ETH-234-6	19	103.7 (3604)	47.65 (162)	87.65 (298)	11	99 (0)	----	----	<b>77.6</b>	15.6

Sample Number	Coordinates (UTM)	Alt. (m)	Irradiation number	No. of grains counted	Standard track $\rho_d \times 10^4 \text{ cm}^{-2}$ (counted)	$\rho_s \times 10^4 \text{ cm}^{-2}$ (counted)	$\rho_i \times 10^4 \text{ cm}^{-2}$ (counted)	U conc (ppm)	P( $\chi^2$ ) (Var) (%)	Mean track length ( $\mu\text{m}$ )	std dev ( $\mu\text{m}$ ) (No. measured)	Age (Ma)	$\pm 2\sigma$ (Ma)
<b>MW19</b>	18 433 929E 84 96 330N	1058	ETH-234-8	21	96.9 (3604)	49.92 (310)	90.18 (560)	11	100 (0)	13.3 $\pm 0.35$	1.1 (10)	<b>73.9</b>	11.2
<b>MW21</b>	18 409 469E 84 84 201N	505	ETH-224-3	5	128.42 (6273)	12.19 (39)	50.63 (162)	5	86 (0)	13.69 $\pm 0.25$	1.55 (39)	<b>42.7</b>	15.4
<b>MW22</b>	18 458 613E 84 32 291N	1280	ETH-234-11	20	86.7 (3604)	105.75 (460)	189.66 (825)	26	83 (0)	13.0 $\pm 0.17$	1.7 (105)	<b>66.6</b>	8.6
<b>MW23</b>	18 462 927E 84 32 859N	1878	ETH-234-12	20	83.3 (3604)	71.65 (230)	114.33 (367)	17	94 (0)	13.1 $\pm 0.29$	2.4 (69)	<b>71.9</b>	12.6
<b>MW24</b>	18 460 131E 84 32 354N	1574	ETH-235-2	18	86.44 (3894)	181.53 (806)	290.09 (1288)	39	66 (0.01)	13.0 $\pm 0.13$	1.3 (95)	<b>74.5</b>	7.8
<b>MW25</b>	18 430 480E 84 00 159N	326	ETH-224-5	20	110.5 (6273)	41.70 (211)	79.05 (400)	8	100 (0)	13.14 $\pm 0.21$	1.55 (54)	<b>80.2</b>	14.2
<b>MW34</b>	18 485 955E 83 08 403N	366	ETH-224-12	20	93.8 (6273)	68.59 (369)	160.04 (861)	21	98 (0)	12.44 $\pm 0.23$	1.9 (66)	<b>55.4</b>	7.4
<b>MW35</b>	18 481 742E 83 01 621N	82	ETH-235-5	20	81.77 (3894)	88.72 (299)	159.64 (538)	24	100 (0)	13.88 $\pm 0.20$	1.16 (34)	<b>62.6</b>	9.6
<b>MW41</b>	18 594 897E 82 44 245N	307	ETH-225-3	20	128.4 (4441)	123.45 (1258)	237.1 (2416)	23	56 (0.01)	13.97 $\pm 0.13$	1.1 (77)	<b>91.9</b>	8.0

Sample Number	Coordinates (UTM)	Alt. (m)	Irradiation number	No. of grains counted	Standard track $\rho_d \times 10^4 \text{ cm}^{-2}$ (counted)	$\rho_s \times 10^4 \text{ cm}^{-2}$ (counted)	$\rho_i \times 10^4 \text{ cm}^{-2}$ (counted)	U conc (ppm)	P( $\chi^2$ ) (Var) (%)	Mean track length ( $\mu\text{m}$ )	std dev ( $\mu\text{m}$ ) (No. measured)	Age (Ma)	$\pm 2\sigma$ (Ma)
<b>MW42</b>	18 604 570E 82 30 735N	63	ETH-235-6	7	80.22 (3894)	58.73 (37)	79.37 (50)	11	10 (0.05)	----	----	<b>90.2</b>	50.8
<b>MW44</b>	18 575 157E 82 49 915N	176	ETH-235-8	20	77.1 (3894)	150.74 (609)	270.05 (1091)	39	100 (0)	13.7 $\pm 0.16$	1.6 (103)	<b>59.3</b>	6.4
<b>MW45</b>	18 530 272E 82 78 088N	75	ETH-224-4	20	112.9 (6273)	21.56 (94)	44.95 (196)	5	100 (0)	----	----	<b>74.6</b>	19.5
<b>MW46</b>	18 302 083E 86 73 987N	559	ETH-225-6	20	117.7 (4441)	73.71 (272)	269.11 (993)	29	100 (0)	11.89 $\pm 0.27$	2.1 (64)	<b>44.5</b>	6.4
<b>MW47</b>	18 320 304E 86 80 876N	1026	ETH-235-10	10	73.99 (3894)	59.79 (171)	93.01 (266)	15	73 (0)	11.9 $\pm 0.51$	3.2 (38)	<b>65.5</b>	13.2
<b>MW48</b>	18 322 745E 86 90 854N	1427	ETH-235-12	20	70.87 (3894)	48.96 (211)	192.81 (831)	32	42 (0.06)	13.2 $\pm 0.17$	1.4 (69)	<b>24.9</b>	4.0
<b>MW52</b>	19 250 138E 80 45 865N	32	ETH-255-4	4	100.5 (4589)	259.1 (114)	381.82 (168)	47	52 (0)	13.29 $\pm 0.22$	1.12 (26)	<b>93.8</b>	23.2
<b>MW53</b>	19 257 500E 80 43 500N	320	ETH-255-5	20	98.32 (4589)	147.78 (529)	232.97 (834)	27	100 (0)	13.0 $\pm 0.15$	1.54 (102)	<b>85.8</b>	10.4
<b>MW54</b>	19 265 500E 80 48 500N	630	ETH-255-8	20	91.78 (4589)	51.99 (444)	72.83 (622)	10	99 (0)	14.06 $\pm 0.14$	0.9 (44)	<b>90.1</b>	12.0

Sample Number	Coordinates (UTM)	Alt. (m)	Irradiation number	No. of grains counted	Standard track $\rho_d \times 10^4 \text{ cm}^{-2}$ (counted)	$\rho_s \times 10^4 \text{ cm}^{-2}$ (counted)	$\rho_i \times 10^4 \text{ cm}^{-2}$ (counted)	U conc (ppm)	P( $\chi^2$ ) (Var) (%)	Mean track length ( $\mu\text{m}$ )	std dev ( $\mu\text{m}$ ) (No. measured)	Age (Ma)	$\pm 2\sigma$ (Ma)
<b>MW59</b>	19 242 966E 80 78 927N	230	ETH-255-10	19	87.42 (4589)	166.28 (429)	214.73 (554)	29	65 (0.02)	13.24 $\pm 0.40$	1.38 (12)	<b>93.1</b>	13.8
<b>MW62</b>	19 202 653E 81 70 752N	1714	ETH-255-14	5	78.7 (4589)	10.94 (35)	15 (48)	23	67 (0)	----	----	<b>79.0</b>	35.4
<b>MW63</b>	18 700 810E 81 80 574N	220	ETH-256-3/4	13	82.2 (4432)	178.4 (446)	281.27 (703)	31	51 (0)	12.22 $\pm 0.18$	1.27 (51)	<b>71.8</b>	9.4
<b>MW65</b>	18 465 478E 84 958 864N	3275	ETH-256-5	20	78.8 (4432)	64.18 (215)	165.67 (555)	25	99 (0)	----	----	<b>42.1</b>	7.0
<b>MW67</b>	17 809 530E 88 412 28 N	50	ET-256-8/7	17	73.9 (4432)	29.85 (60)	56.58 (113)	10	98 (0)	----	----	<b>53.8</b>	17.4
<b>MW68</b>	17 800 307E 89 42 895N	265	ETH-256-11	20	68.8 (4432)	115.3 (648)	259.43 (1458)	44	99 (0)	14.26 $\pm 0.13$	1.34 (100)	<b>42.2</b>	4.6
<b>MW68<sup>+</sup></b>	17 800 307E 89 42 895N	265	ETH-256-11	10	91.0 (5340)	72.40 (417)	219.1 (1262)	30	12 (11)	13.91 $\pm 0.13$	1.05 (70)	<b>53.4</b>	7.4
<b>MW70</b>	17 761 816E 90 42 528N	215	ETH-256-12	20	67.1 (4432)	200.7 (859)	383.88 (1643)	68	99 (0)	13.75 $\pm 0.17$	1.74 (102)	<b>48.4</b>	4.8
<b>MW71</b>	17 724 965E 90 92 210N	250	ETH-257-2	15	104.06 (4591)	63.16 (144)	193.86 (442)	25	91 (0)	12.33 $\pm 0.33$	2.19 (44)	<b>46.8</b>	9.2

Sample Number	Coordinates (UTM)	Alt. (m)	Irradiation number	No. of grains counted	Standard track $\rho_d \times 10^4 \text{ cm}^{-2}$ (counted)	$\rho_s \times 10^4 \text{ cm}^{-2}$ (counted)	$\rho_i \times 10^4 \text{ cm}^{-2}$ (counted)	U conc (ppm)	P( $\chi^2$ ) (Var) (%)	Mean track length ( $\mu\text{m}$ )	std dev ( $\mu\text{m}$ ) (No. measured)	Age (Ma)	$\pm 2\sigma$ (Ma)
<b>MW71<sup>+</sup></b>	17 724 965E 90 92 210N	250	ETH-257-2	11	123.9 (2612)	52.31 (163)	262.22 (817)	27	25 (5.9)	----	----	<b>43.9</b>	8.0
<b>MW74<sup>+</sup></b>	17 752 316E 91 13 472N	1050	ETH-257-6	14.0	111.0 (2612)	11.31 (64)	103.40 (585)	12	2.3 (29)	----	----	<b>25.0</b>	8.2
<b>MW75</b>	17 758 067E 91 16 395N	1690	ETH-257-8	20	91.81 (4591)	90.29 (279)	352.75 (1090)	48	95 (0)	13.9 $\pm 0.15$	0.95 (38)	<b>32.5</b>	4.6
<b>MW80</b>	17 504 453E 94 29 724N	177	ETH-257-14 /ETH-258-2	31	79.56 (4591)	82.46 (630)	144.03 (1100)	21	100 (0)	12.65 $\pm 0.16$	1.63 (100)	<b>62.8</b>	7.0
<b>MW84</b>	17 660 136E 93 43 660N	790	ETH-258-5/6	21	102.21 (3812)	79.33 (261)	265.13 (872)	31	100 (0)	12.83 $\pm 0.35$	1.4 (16)	<b>42.2</b>	6.4
<b>MW85</b>	17 643 724E 93 13 887N	143	ETH-258-7	20	97.02 (3812)	63.41 (208)	207.62 (681)	26	100 (0)	13.05 $\pm 0.28$	1.67 (35)	<b>40.9</b>	6.4
<b>MW89</b>	17 766 933E 90 11 705N	95	ETH-258-10	20	89.22 (3812)	89.4 (388)	214.52 (931)	31	100 (0)	13.6 $\pm 0.13$	1.06 (59)	<b>51.3</b>	6.6
<b>MW90</b>	17 798 093E 90 41 344N	455	ETH-258-13	20	81.43 (3812)	51.25 (164)	186.56 (597)	30	99 (0)	13.41 $\pm 0.38$	1.01 (7)	<b>30.9</b>	5.6
<b>MW92</b>	17 228 911E 88 76 405N	2100	ETH-259-2	7	104.8 (4606)	78.89 (71)	226.67 (204)	22	18 (0.18)	15.67 $\pm 0.44$	0.99 (5)	<b>50.3</b>	16.8

Sample Number	Coordinates (UTM)	Alt. (m)	Irradiation number	No. of grains counted	Standard track $\rho_d \times 10^4 \text{ cm}^{-2}$ (counted)	$\rho_s \times 10^4 \text{ cm}^{-2}$ (counted)	$\rho_i \times 10^4 \text{ cm}^{-2}$ (counted)	U conc (ppm)	P( $\chi^2$ ) (Var) (%)	Mean track length ( $\mu\text{m}$ )	std dev ( $\mu\text{m}$ ) (No. measured)	Age (Ma)	$\pm 2\sigma$ (Ma)
<b>MW93♦</b>	17 224 739E 88 77 450N	1850	ETH-259-3	20	102.7 (4606)	4.98 (32)	95.48 (613)	10	89 (0)	----	----	<b>7.4</b>	2.8
<b>MW95</b>	17 202 940E 88 47 193N	340	ETH-259-6	20	96.35 (4606)	121.14 (298)	321.14 (790)	40	72 (0.01)	13.07 $\pm 0.18$	1.6 (81)	<b>50.1</b>	7.2
<b>MW96</b>	17 267 742E 87 77 579N	960	ETH-259-8	20	92.13 (4606)	43.94 (116)	237.12 (626)	30	100 (0)	11.99 $\pm 0.19$	1.74 (83)	<b>23.6</b>	5.0
<b>MW97</b>	17 251 912E 87 67 501N	520	ETH-259-11	21	85.8 (4606)	172.83 (477)	406.52 (1122)	57	85 (0.01)	13.34 $\pm 0.28$	1.33 (22)	<b>50.3</b>	6.0
<b>MW98</b>	17 216 758E 87 57 620	3	ETH-259-12	13	83.67 (4606)	78.68 (107)	72.79 (99)	12	98 (0)	14.31 $\pm 0.29$	0.5 (3)	<b>124.0</b>	35.2

**Table 5.2:** Fission-track ages on apatites.  $\rho_d$ ,  $\rho_s$  and  $\rho_i$  represent the dosimeter, sample spontaneous and induced track densities; P( $\chi^2$ ) is the probability of  $\chi^2$  for  $\nu$  degrees of freedom where  $\nu = \text{no. of crystals} - 1$ ; all ages are central ages (Galbraith, 1981).  $\lambda_D = 1.55125 \times 10^{-10}$ .  $\zeta$  (CN5/apatite) = 277.1 $\pm$ 5.7 (M. Wipf). Samples were irradiated at the ANSTO facility, Australia.

♦ Age of Tertiary ignimbrite.

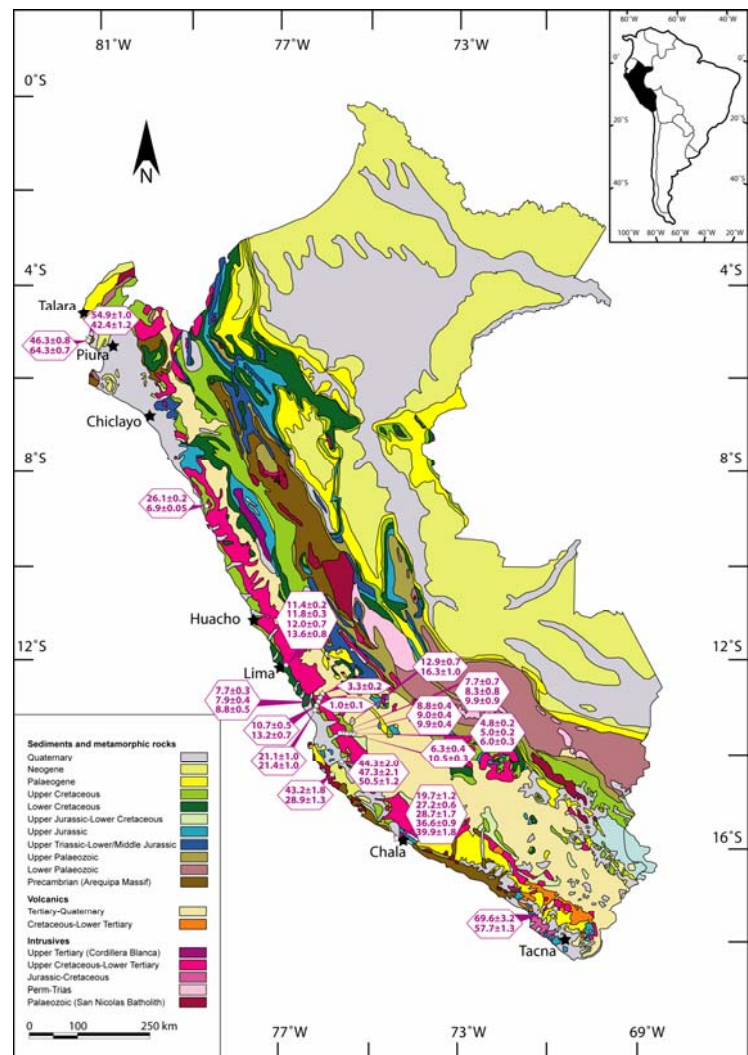
† Age counted by Dr. Diane Seward and calculated with a  $\zeta$  (CN5/apatite) of 355  $\pm$ 5.0.

Boomerang plots (Green, 1988), (i.e. track length vs. age and age vs. standard deviation of the length distribution) were done for samples with more than 40 horizontal track lengths and more than 10 dated grains. The data was separated into three regions north of, on and south of the Nazca Ridge (Fig. 5.7a-c). There is a wide scatter in the data plotted and they do not show a recognisable “boomerang”. Lengths range from 12 to 14.5  $\mu\text{m}$ . Long track lengths ( $> 14.0 \mu\text{m}$ ) possible indicators of rapid cooling are rare but do occur. There are two locations in the centre (MW41) and south (MW54) with apparent ages of approximately 95 Ma as well as two locations in the north (MW68, 75) with apparent ages of 42 and 33 Ma respectively (Fig. 5.5). Figure 5.4b shows the apatite ages of samples from locations with altitudes of less than 600 m between Talara in the northwest and Tacna in the southeast. A gradual change of ages north (i.e. 31 to 66 Ma) to the ages south (i.e. 59 to 93 Ma) of the Nazca Ridge is observed within a relatively narrow swath of approximately 200 km width located directly above the Ridge.

### 5.3.3 Apatite (U-Th)/He

**Figure 5.8:** (U-Th)/He-ages along the Peruvian coastal margin. Ages of all aliquots from every sample are shown. Errors reported are  $2\sigma$ .

(U-Th)/He analysis was performed on carefully picked apatites from 18 samples from the Precambrian Arequipa Massif and the Coastal Batholith. The methodology is described in chapter 4. The (U-Th)/He apatite ages show a wide range from 1 Ma to 70 Ma (Tab. 5.3a, b, Fig. 5.8). With the exception of two samples (MW01, MW02) a minimum of two aliquots were analysed. 35 of 44 analysed aliquots were performed on single grains, while the other nine were done on aliquots with



two or three grains (Tab. 5.3a). The weighted mean ages (Tab. 5.3b) are believed to represent more meaningful results especially in the case of a large spread of ages on the different aliquots. In general the spread in ages between the individual aliquots increases with the age of the sample, this is especially true for the analysed apatite grains from Precambrian rocks. The analytical errors of the ages were in most cases smaller than the reproducibility of the aliquots of one sample. Although figure 5.4c appears to show a similar N-S trend for the (U-Th)/He ages, as is observed for the apatite fission-track ages, the available data are sparse, and must not be overinterpreted.

### 5.3.4 Data breakdown into regions

Age-altitude plots combining the fission-track zircon- and apatite data with the helium ages were analysed on a more regional basis (Figs. 5.9-12).

Figure 5.9 represents the thermochronometric data from the area north of Lima which was further divided into a northern (Chiclayo: MW67, 68, 85, 89, 90, 92, 95, 96, 97, 98) and a southern (Huacho: MW70, 71, 74, 75, 79, 80, 84) section. In both sections a clustering of ages between 60 and 40 Ma is observed in apatite and helium data at altitudes below 500 m. The histogram in the inset in figure 5.9 represents all apatite ages and clearly confirms a concentration of ages between 40 and 60 Ma. One zircon fission-track age falls into this time frame. All He ages in these two sections reproduce poorly. The two samples MW79 and MW80 yielding ages between 42 and 64 Ma (Tab. 5.3a) are from Precambrian rocks. The third He age (MW70) was obtained on apatite from the Coastal Batholith yielded ages of 7 and 26 Ma (Tab. 5.3a).

In Figure 5.10 the low temperature thermochronometric data east of Lima (MW46, 47, 48) and the Lunahuana valley (MW 01, 02, 03, 04, 05, Fig. 5.1) are presented. Both sections are north of the present position of the Nazca Ridge. The zircon ages below 1000 m show a marginal correlation with increasing altitude. Zircon ages above 1000 m are significantly younger than at lower altitudes but no immediate correlation with height is observable. The apatite ages have a wide range (66 Ma –28Ma) and no correlation to altitude is seen. The (U-Th)/He apatite ages reproduce relatively well. Between 400 and 600 m the weighted mean He ages scatter between 12 and 8 Ma, while they are significantly older below 400 m and significantly younger above 1000 m (Tab. 5.3b). A weakly defined knick point in the river profile is observed around 800 m, it is however not as pronounced as in the Pisco section, as described below.

Sample Number	No. Grains	Length (µm)	Width (µm)	No. of terminations <sup>†</sup>	Ft <sup>+</sup>	weight* (mg)	ccm <sup>4</sup> He (ccm STP)	<sup>238</sup> U (ng)	<sup>232</sup> Th (ng)	Th/U	U* (ppm)	Th* (ppm)	<sup>4</sup> He (nmol/g)	Raw age (Ma)	Age (Ma)	± 2σ (Ma)
<b>MW01/1</b>	1	96	125	0	0.792	0.0039	3.15E-11	0.09	0.05	0.62	22	14	0.361	2.64	<b>3.34</b>	0.15
<b>MW2/1</b>	1	126	91	0	0.751	0.0027	1.57E-12	0.01	0.03	3.27	3	11	0.026	0.78	<b>1.04</b>	0.11
<b>MW3/1</b>	1	232	165	1	0.842	0.0164	1.23E-09	1.26	1.28	1.01	78	78	3.349	6.45	<b>7.66</b>	0.34
<b>MW3/3</b>	1	254	167	1	0.845	0.0184	1.00E-09	0.94	0.73	0.77	52	40	2.432	7.41	<b>8.77</b>	0.47
<b>MW3/4</b>	1	253	151	1	0.832	0.0149	8.13E-10	0.84	0.75	0.89	56	50	2.426	6.60	<b>7.94</b>	0.44
<b>MW4/1</b>	1	212	193	0	0.874	0.0205	5.45E-10	0.34	0.23	0.69	16	11	1.188	11.49	<b>13.15</b>	0.71
<b>MW4/4</b>	1	175	192	0	0.874	0.0167	3.14E-10	0.16	0.49	3.01	10	29	0.837	9.31	<b>10.65</b>	0.50
<b>MW5/1</b>	3	132 174 167	163 152 129	1 1 2	0.802	0.0267	1.21E-09	0.43	0.64	1.46	16	24	2.015	16.95	<b>21.12</b>	0.97
<b>MW5/2</b>	1	235	166	2	0.824	0.0168	8.22E-10	0.29	0.40	1.37	17	24	2.186	17.63	<b>21.40</b>	1.05
<b>MW15/2</b>	2	189 301	102 134	1 2	0.779	0.0191	5.43E-10	0.36	0.79	2.18	19	41	1.269	8.18	<b>10.50</b>	0.42
<b>MW15/3</b>	1	218	203	0	0.880	0.0233	2.68E-10	0.34	0.27	0.81	15	12	0.513	5.50	<b>6.25</b>	0.28
<b>MW16/1</b>	1	307	204	0	0.887	0.0331	1.95E-09	2.30	3.00	1.30	70	91	2.625	5.32	<b>6.00</b>	0.29
<b>MW16/2</b>	1	314	231	0	0.899	0.0434	3.72E-10	0.49	0.77	1.54	11	18	0.383	4.53	<b>5.04</b>	0.19
<b>MW16/3</b>	1	335	237	0	0.902	0.0487	1.56E-09	2.33	2.75	1.17	48	56	1.430	4.32	<b>4.79</b>	0.23
<b>MW17/1</b>	1	220	115	0	0.802	0.0075	3.69E-10	0.35	0.32	0.91	47	43	2.183	7.08	<b>8.84</b>	0.36
<b>MW17/2</b>	1	253	146	0	0.843	0.0140	9.59E-10	0.82	0.91	1.10	59	65	3.063	7.62	<b>9.04</b>	0.41
<b>MW17/4</b>	1	317	193	1	0.868	0.0306	8.81E-10	0.69	0.65	0.94	23	21	1.285	8.61	<b>9.92</b>	0.44

Sample Number	No. Grains	Length (µm)	Width (µm)	No. of terminations <sup>†</sup>	Ft <sup>+</sup>	weight* (mg)	ccm <sup>4</sup> He (ccm STP)	<sup>238</sup> U (ng)	<sup>232</sup> Th (ng)	Th/U	U* (ppm)	Th* (ppm)	<sup>4</sup> He (nmol/g)	Raw age (Ma)	Age (Ma)	± 2σ (Ma)
<b>MW18/1</b>	1	208	143	2	0.802	0.0110	9.53E-11	0.05	0.19	3.37	5	17	0.386	7.93	<b>9.89</b>	0.90
<b>MW18/2</b>	1	192	146	2	0.798	0.0106	8.45E-11	0.07	0.14	1.99	7	13	0.356	6.63	<b>8.31</b>	0.75
<b>MW18/3</b>	1	203	199	2	0.841	0.0208	1.38E-10	0.11	0.29	2.68	5	14	0.295	6.51	<b>7.74</b>	0.74
<b>MW19/1</b>	1	192	160	0	0.855	0.0127	2.76E-10	0.13	0.33	2.60	10	26	0.967	11.04	<b>12.92</b>	0.73
<b>MW19/FS1*</b>	2	133 144	153 138	1 0	0.767	0.0151	----	----	----	----	----	----	----	12.50	<b>16.30</b>	0.98
<b>MW22/1</b>	2	203 332	161 151	1 2	0.830	0.0332	4.38E-09	0.74	0.99	1.33	23	30	5.873	36.75	<b>44.27</b>	1.96
<b>MW22/2</b>	1	241	160	1	0.839	0.0160	7.35E-09	1.24	1.20	0.96	78	75	20.512	39.69	<b>47.33</b>	2.10
<b>MW22/3</b>	1	210	155	1	0.835	0.0131	5.25E-09	0.62	1.69	2.69	48	129	17.917	42.17	<b>50.49</b>	1.17
<b>MW25/1</b>	1	175	70	2	0.642	0.0022	3.30E-11	0.01	0.02	4.00	2	9	0.663	27.70	<b>43.17</b>	1.80
<b>MW25/2</b>	1	141	108	1	0.765	0.0043	1.10E-10	0.02	0.08	4.03	5	20	1.148	22.10	<b>28.90</b>	1.27
<b>MW44/1</b>	1	200	164	1	0.835	0.0139	3.32E-09	0.70	0.50	0.72	50	36	10.619	33.37	<b>39.94</b>	1.76
<b>MW44/3</b>	1	276	131	1	0.811	0.0123	1.43E-09	0.45	0.37	0.82	37	30	5.206	22.03	<b>27.16</b>	0.62
<b>MW44/4</b>	2	185 162	185 205	0 0	0.871	0.0340	8.30E-09	1.71	1.81	1.05	51	53	10.881	31.92	<b>36.63</b>	0.90
<b>01W44/FS1<sup>†</sup></b>	1	322	247	0	0.832	0.0509	----	----	----	----	----	----	----	16.40	<b>19.70</b>	1.18
<b>MW44/FS2<sup>◆</sup></b>	2	313 297	181 160	0 0	0.833	0.0462	----	----	----	----	----	----	----	23.90	<b>28.70</b>	1.72
<b>MW46/2</b>	1	300	123	2	0.787	0.0118	1.66E-10	0.12	0.14	1.19	10	12	0.631	9.00	<b>11.43</b>	0.17
<b>MW46/3</b>	1	120	72	0	0.678	0.0016	5.71E-11	0.05	0.04	0.76	31	24	1.582	8.01	<b>11.81</b>	0.26
<b>MW46FS1<sup>◆</sup></b>	2	290 226 226	235 140 138	1 0 2	0.912	0.0530	----	----	----	----	----	----	----	12.40	<b>13.60</b>	0.82
<b>MW46FS2<sup>◆</sup></b>	3	236 228	155 165	2 2	0.717	0.0419	----	----	----	----	----	----	----	8.60	<b>12.00</b>	0.72

Sample Number	No. Grains	Length (µm)	Width (µm)	No. of terminations <sup>†</sup>	Ft <sup>+</sup>	weight* (mg)	ccm <sup>4</sup> He (ccm STP)	<sup>238</sup> U (ng)	<sup>232</sup> Th (ng)	Th/U	U* (ppm)	Th* (ppm)	<sup>4</sup> He (nmol/g)	Raw age (Ma)	Age (Ma)	± 2σ (Ma)
<b>MW53/1</b>	1	166	131	0	0.822	0.0074	2.00E-09	0.20	0.36	1.75	28	48	12.076	57.20	<b>69.60</b>	3.22
<b>MW53/2</b>	1	160	125	0	0.813	0.0065	1.47E-09	0.19	0.30	1.61	29	46	10.108	46.90	<b>57.68</b>	1.30
<b>MW70/1</b>	1	390	150	2	0.830	0.0227	3.29E-10	0.09	0.16	1.84	4	7	0.646	21.71	<b>26.17</b>	0.37
<b>MW70/3</b>	1	196	187	1	0.853	0.0178	9.71E-11	0.10	0.15	1.47	6	8	0.244	5.92	<b>6.94</b>	0.09
<b>MW79/1</b>	2	150 157	67 100	0 2	0.676	0.0058	1.32E-09	0.29	0.03	0.11	49	5	10.162	37.11	<b>54.91</b>	0.50
<b>MW79/2</b>	1	82	100	0	0.739	0.0021	4.06E-10	0.10	0.01	0.12	49	6	8.535	31.34	<b>42.41</b>	0.63
<b>MW80/1</b>	1	235	77	0	0.704	0.0036	4.12E-10	0.10	0.02	0.18	28	5	5.090	32.62	<b>46.30</b>	0.84
<b>MW80/2</b>	1	175	110	2	0.733	0.0055	5.05E-10	0.08	0.02	0.18	15	3	4.111	47.14	<b>64.27</b>	0.70

**Table 5.3a:** (U-Th)/He ages on Apatites.

<sup>†</sup> optically determined number of crystal terminations present in analyzed apatites.

<sup>+</sup> Ft-correction calculated after Farley (1996).

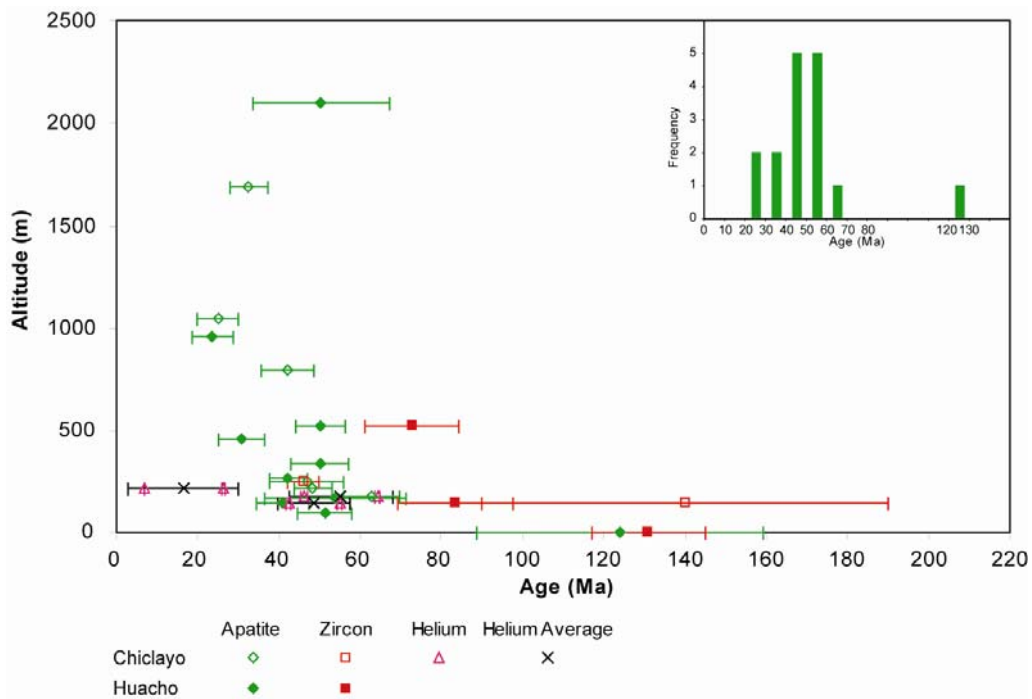
\* Weight is estimated based on length and width of the apatite crystal assuming a cylinder and a density of 3.15 mg/cm<sup>3</sup>, U and Th concentrations in ppm are based on this estimated weight.

FS1<sup>♦</sup>, FS2<sup>♦</sup> aliquots analyzed by Dr. F. Stuart at SUERC, East Kilbride, Scotland.

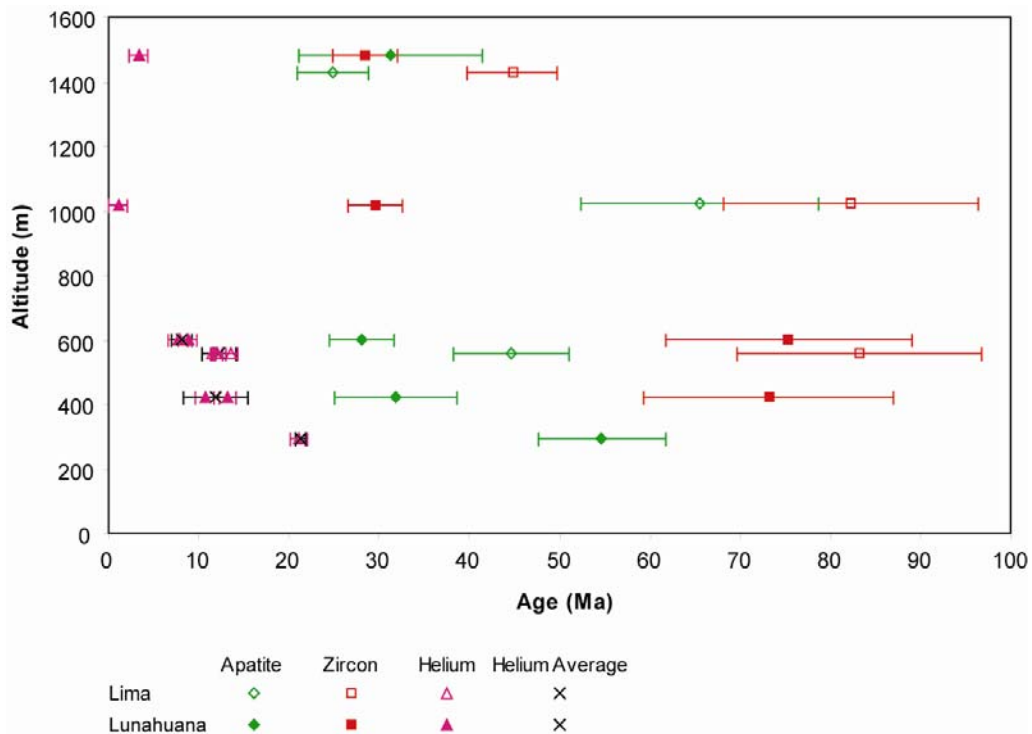
Sample Number	Coordinates (UTM)	Alt. (m)	No. of dated aliquots	Weighted mean Raw age (Ma)	Weighted mean Age (Ma)	$\pm 2\sigma$ (Ma)
<b>MW01</b>	18 396 776E 85 92 759N	1485	1	2.64	<b>3.34</b>	0.15
<b>MW02</b>	18 398 340E 85 80 143N	1020	1	0.78	<b>1.04</b>	0.11
<b>MW03</b>	18 380 500E 85 71 439N	602	3	6.73	<b>8.01</b>	0.66
<b>MW04</b>	18 373 653E 85 61 779N	423	2	10.02	<b>11.46</b>	2.50
<b>MW05</b>	18 366 383E 85 55 294N	295	2	17.26	<b>21.25</b>	0.27
<b>MW15</b>	18 462 240E 84 95 445N	2895	2	6.33	<b>7.57</b>	4.25
<b>MW16</b>	18 457 049E 84 95 280N	2245	3	4.63	<b>5.16</b>	0.74
<b>MW17</b>	18 453 600E 84 95 114N	1983	3	7.68	<b>9.20</b>	0.67
<b>MW18</b>	18 445 590E 84 97 444N	1510	3	6.92	<b>8.50</b>	1.28
<b>MW19</b>	18 433 929E 84 96 330N	1058	2	11.56	<b>14.13</b>	3.38
<b>MW22</b>	18 458 613E 84 32 291N	1280	3	40.55	<b>48.57</b>	3.59
<b>MW25</b>	18 430 480E 84 00 159N	326	2	23.97	<b>33.64</b>	14.27
<b>MW44</b>	18 575 157E 82 49 915N	176	5	24.40	<b>29.25</b>	7.18
<b>MW46</b>	18 302 083E 86 73 987N	559	4	8.91	<b>11.72</b>	1.35
<b>MW53</b>	19 257 500E 80 43 500N	320	2	48.34	<b>59.34</b>	11.92
<b>MW70</b>	17 761 816E 90 42 528N	215	2	6.83	<b>8.05</b>	19.23
<b>MW79</b>	17 504 428E 94 29 938N	142	2	34.90	<b>50.12</b>	12.50
<b>MW80</b>	17 504 453E 94 29 724N	177	2	41.15	<b>56.86</b>	17.97
<b>MW79/80*</b>	-----	-----	4	37.04	<b>52.43</b>	9.72

**Table 3b:** (U-Th)/He weighted mean ages on Apatites.

\* weighted mean age for all four aliquots of MW79 and MW80



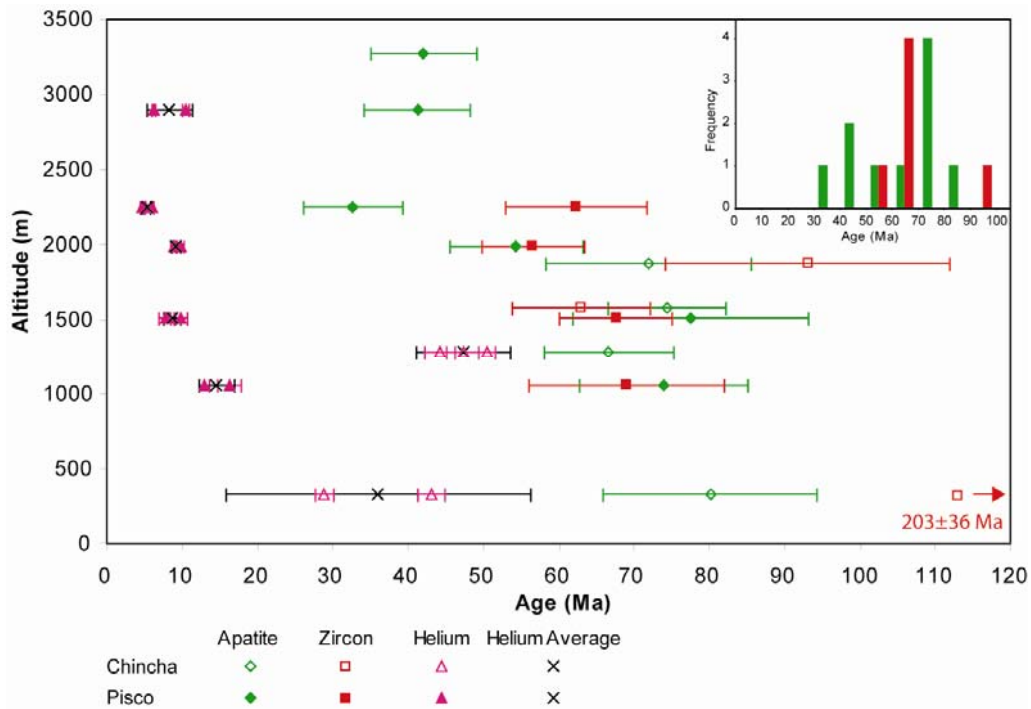
**Figure 5.9:** Age versus altitude for apatite fission-track, zircon fission-track and (U-Th)/He-ages for the area north of Lima along the coastal margin. The data are separated into a northern section (Chiclayo) and a southern section (Huacho). The inset shows a histogram for the frequency of all apatite fission-track ages. Error bars are  $2\sigma$ .



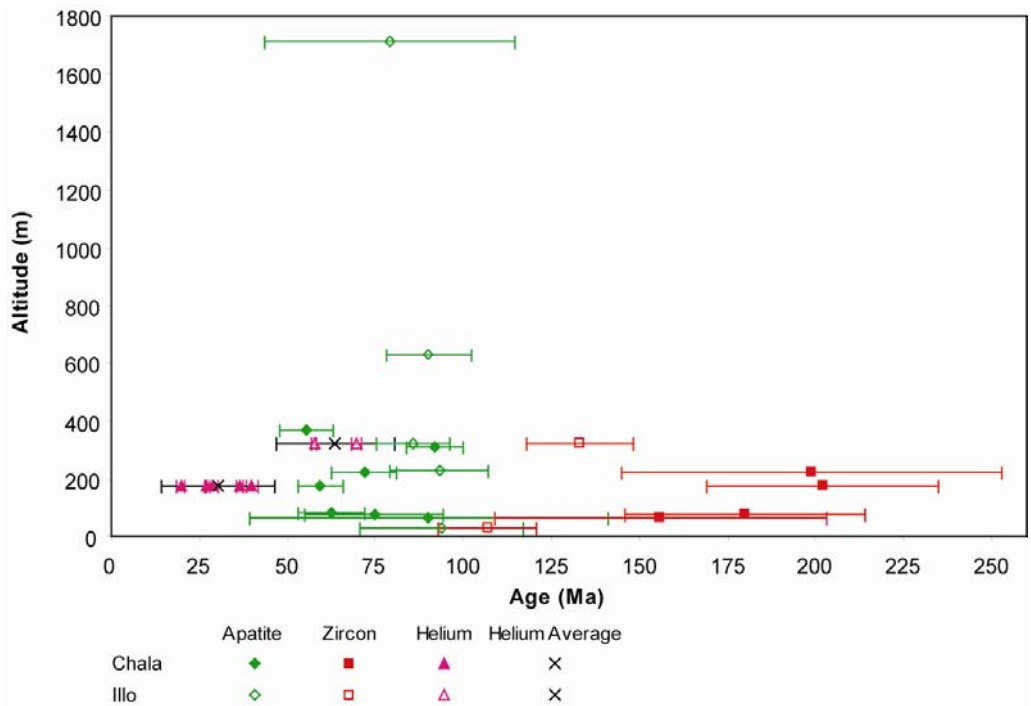
**Figure 5.10:** Age versus altitude for apatite fission-track, zircon fission-track and (U-Th)/He-ages east of Lima and along the Lunahuana valley. Both valleys are north of the subducting Nazca Ridge. Error bars are  $2\sigma$ .

Figure 5.11 represents the low temperature thermochronometric data from the Pisco valley (MW15, 16, 17, 18, 19, 65, Fig. 5.1) and from the area near Chinch Alta (MW22, 23, 24, 25 Fig. 5.1). While the Pisco section is located just above the north-trailing edge of the Nazca Ridge, the Chinch section is above the central part of the Ridge. In both sections below 2000 m neither zircon nor apatite fission-track ages show a significant correlation with altitude. Within-sample apatite- and zircon ages are statistically indistinguishable from each other below 2000 m. In the Pisco valley, apatite ages above 2000 m correlate with increasing altitude. The histogram in the inset in figure 5.11 includes all apatite- and zircon fission-track ages from both sections. It shows a clustering of ages for both apatite and zircon between 60 and 80 Ma. The (U-Th)/He ages for the Chinch section reveal a tentative correlation with increasing altitude (two sites only). It is also important to note here however that sample MW24, a Precambrian gneiss, at an altitude of 326 m reproduces He ages very poorly (Tab. 5.3a) so that a clear conclusion is difficult to make. He ages in the Pisco valley reproduce relatively well. With one exception, the average He ages in the Pisco valley above 1500 m range from 7.6 to 9.2 Ma. The exception is sample MW16 at an altitude of 2245 m with a weighted mean He age of 5.2 Ma. Close to this site a knick point in the Pisco River is developed at an altitude of about 2250 m above sea level.

Figure 5.12 represents the thermochronometric data from the area south of Chala which was further divided into a northern (Chala: MW34, 35, 41, 42, 44, 45, 63) and a southern (Ilo: MW 62, 52, 53, 54, 59) section. While the Chala section is just slightly south of the leading edge of today's position of the Nazca Ridge, the Ilo section is well to the south, hence it has not been influenced in the slightest way by its subduction. In both sections a weak correlation between zircon fission-track ages and increasing altitude is recognised. All zircon-ages in the Chala section are from Palaeozoic or Precambrian rocks, while those from the Ilo section are from intrusives associated with early phases of the Coastal Batholith. Apatite fission-track ages for the two sections show a scatter from 93 to 54 Ma with no recognisable correlation to altitude. Both (U-Th)/He ages reproduce poorly, especially sample MW44 collected from a Precambrian Gneiss which yields ages ranging from 20 to 40 Ma over a total of five aliquots (Tab. 5.3a).



**Figure 5.11:** Age versus altitude for apatite fission-track ages, zircon fission-track ages and (U-Th)/He-ages for the Pisco valley and the area around Chinchá Alta. The inset shows a histogram for the frequency of all apatite- and zircon fission-track ages. Error bars are  $2\sigma$ .



**Figure 5.12:** Age versus altitude for apatite fission-track ages, zircon fission-track ages and (U-Th)/He-ages for the area south of Chala along the coastal margin. The data is separated into a northern section (Chala) and a southern section (Ilo). Error bars are  $2\sigma$ .

### 5.3.5 Low temperature modelling

The apatite fission track-ages and the track-length measurements were used to model the low temperature cooling history. Zircon fission-track ages were used when available to constrain the upper limits of the cooling history assuming a zircon closure temperature of  $270\pm 30^\circ\text{C}$  as explained above. Only samples with more than 40 track length measurements and more than 10 dated crystals were modelled. The algorithm used is the HeFTy beta 2 version (Ketcham, 2005) which is a further development of the AFTA algorithm (Ketcham et al., 2000). HeFTy allows the incorporation of (U-Th)/He data into the modelling attempts. Different attempts with varying number of constraints were tested. For example, sample MW15 was modelled using five constraints (Fig 5.13a), using two constraints (Fig. 5.13b) and including the (U-Th)/He data (Fig. 5.13c).

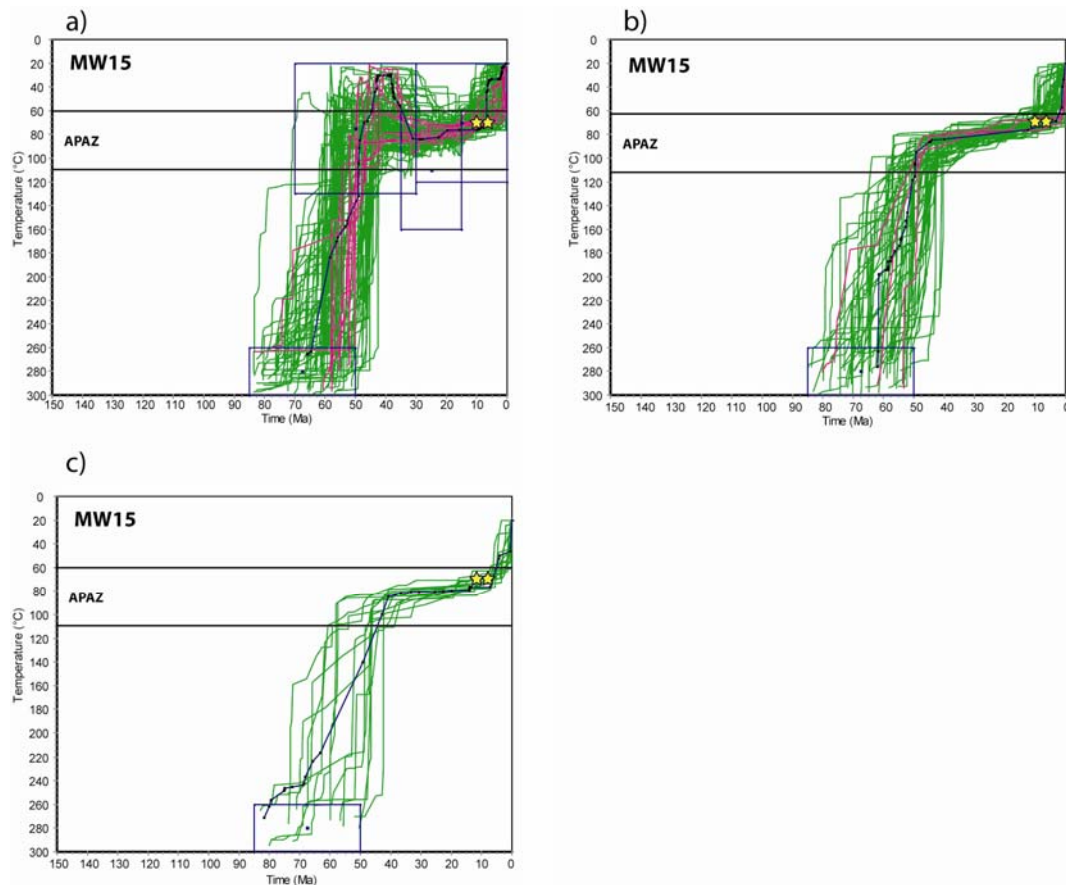


**Figure 5.13:** Modelled T-t paths for sample MW15. Green and pink lines represent possible and likely cooling paths respectively. The black line is the best fit. Yellow stars correspond to (U-Th)/He ages of the two aliquots at  $68^\circ\text{C}$  (closure temperature for (U-Th)/He in apatite). a) with five constraints, b) with two constraints only, c) with two constraints and the (U-Th)/He-age of the sample. APAZ: apatite partial annealing zone.

The five constraints used in the first approach were based on the assumed Cretaceous intrusive age of the Coastal Batholith and by today's temperature of 20°C on the surface. Additionally three boxes were incorporated to include the geological evidence that a palaeosurface existed prior to 40 Ma in the region east of Lima (Noble et al., 1978). These boxes allow reheating through sediment burial with as much freedom as possible. The second model was solely constrained by the fission-track zircon age and by today's temperature of 20°C on the surface. The third model (Fig. 5.13c) used the same constraints as in the second test but additionally included the samples weighted mean (U-Th)/He age. The envelope of the possible fits is somewhat similar for the three models, although a reheating event is seen in the more constrained second model. Although there is strong geological evidence for a palaeosurface, the exact depth of the sampled site at the time of its formation is unknown. It was therefore considered important not to “over-constrain” the model. A second approach to test different constraints was performed with sample MW03 (Fig. 5.14).

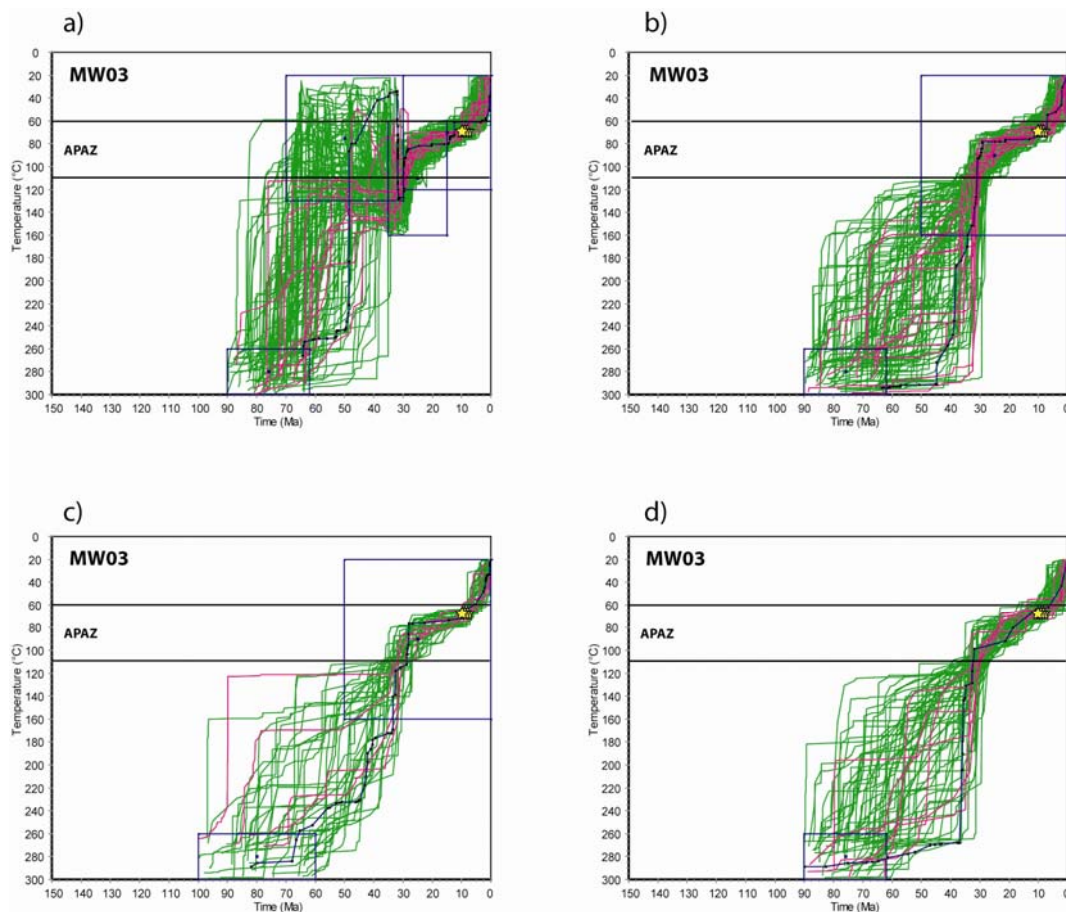


**Figure 5.14:** Modelled T-t paths for sample MW03. Green and pink lines represent possible and likely cooling paths respectively. The black line is the best fit. Yellow stars correspond to (U-Th)/He ages of the three aliquots at 68°C (closure temperature for (U-Th)/He in apatite). a) With 5 constraints, b) with three constraints, c) with three constraints and the (U-Th)/He-age of the sample, d) with two constraints only. APAZ: apatite partial annealing zone.

In a first model (Fig. 5.14a) the same five constraints were used as in MW15 (Fig. 13a). In a second test three constraints were used (Fig. 5.14b), including the zircon fission-track age, a relatively big box to allow the model to come to the surface as early as 50 Ma ago and by today's temperature of 20°C on the surface. The third model (Fig. 5.14c) used the same constraints as in the second test but additionally included the samples weighted mean (U-Th)/He age. In the last test only two constraints were used, the zircon fission-track age and today's temperature of 20°C on the surface (Fig. 5.14d). All four models yield very similar envelopes of good fits and almost identical best fits at < 110°C. Additionally, the He ages fit well all the cooling curves even when not used as constraint. This second approach clearly shows a period of no cooling for all four models. The observed period of quiescence is perfectly consistent an unconformity of Oligocene reported by Noble (1979). Based on these results it was therefore decided to use only the zircon fission-track age if available and today's surface temperature of 20°C to model the cooling paths. (U-Th)/He ages were not included because zoning of uranium and thorium concentrations which affect the diffusion behaviour and hence the He age especially in old and/or slowly cooled samples are unknown.

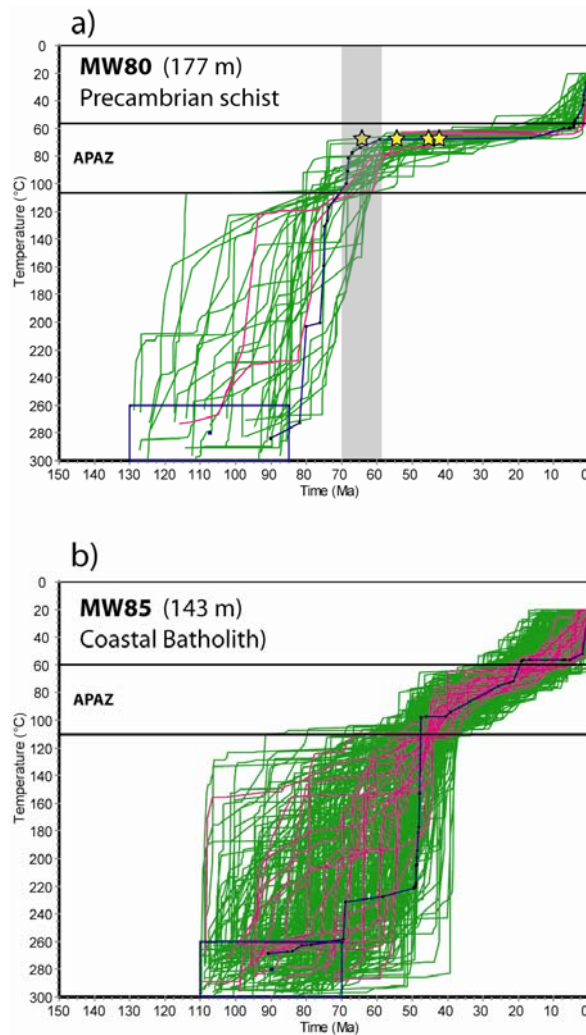
#### 5.3.5.1 Talara-Chiclayo

Figure 5.15 shows the modelled cooling paths for two locations (MW80, 85) in the extreme north of the coastal margin. While MW80 is a Precambrian schist, MW85 is from the Coastal Batholith. MW80 (Fig. 5.15a) shows a rapid cooling (approximately 40 °C/Ma) to about 75°C which it reached by 65±5 Ma. MW85 (Fig. 5.15b) cooled at a similar rate to approximately 80°C by about 45 Ma. Both locations experienced very little or no further cooling after 60 and 45 Ma respectively until renewed rapid cooling (approximately 5°C/Ma) started at 6-3 Ma. Interesting to note is that although the four (U-Th)/He aliquots (including MW79) reproduce very poorly their ages all fall into the beginning of the phase of very slow cooling around 70°C. These two samples from the far north suggest a period of quiescence from ~60-40 Ma to ~5 Ma.

#### 5.3.5.2 Chiclayo-Huacho

The modelled cooling histories for the samples from the area between Chiclayo and Huacho (MW71, 70, 89, 68, 95, 96, 75; Fig. 5.1) are shown in figure 5.16. The locations below 400 m (Fig. 5.16a-e) all cooled rapidly (approximately 15-60 °C) to 100-60°C until 60-50 Ma. The rocks were subjected to very little cooling until 6-3 Ma when a renewed increase is suggested

by the models that is just outside of the APAZ for all best fits and therefore difficult to interpret. Modelled histories for the locations higher up (MW96, 75; Fig. 5.16f, g) suggest a major change in cooling around 35 -25 Ma at 60-80°C. Only in the model of MW96 (Fig. 5.16f) is the renewed period of more rapid cooling (approximately 6°C/Ma) at 6-3 Ma observed within the APAZ. Thus the area between Chiclayo and Huacho at altitudes below 400 m seems to have undergone a period of quiescence from ~55 to at least 10 Ma.



**Figure 5.15:** Modelled T-t paths for samples from the northern part of the coastal margin a) MW80, b) MW85. Green and pink lines represent possible and likely cooling paths respectively. The black line is the best fit. Yellow stars correspond to (U-Th)/He ages of the four aliquots at 68°C (closure temperature for (U-Th)/He in apatite).

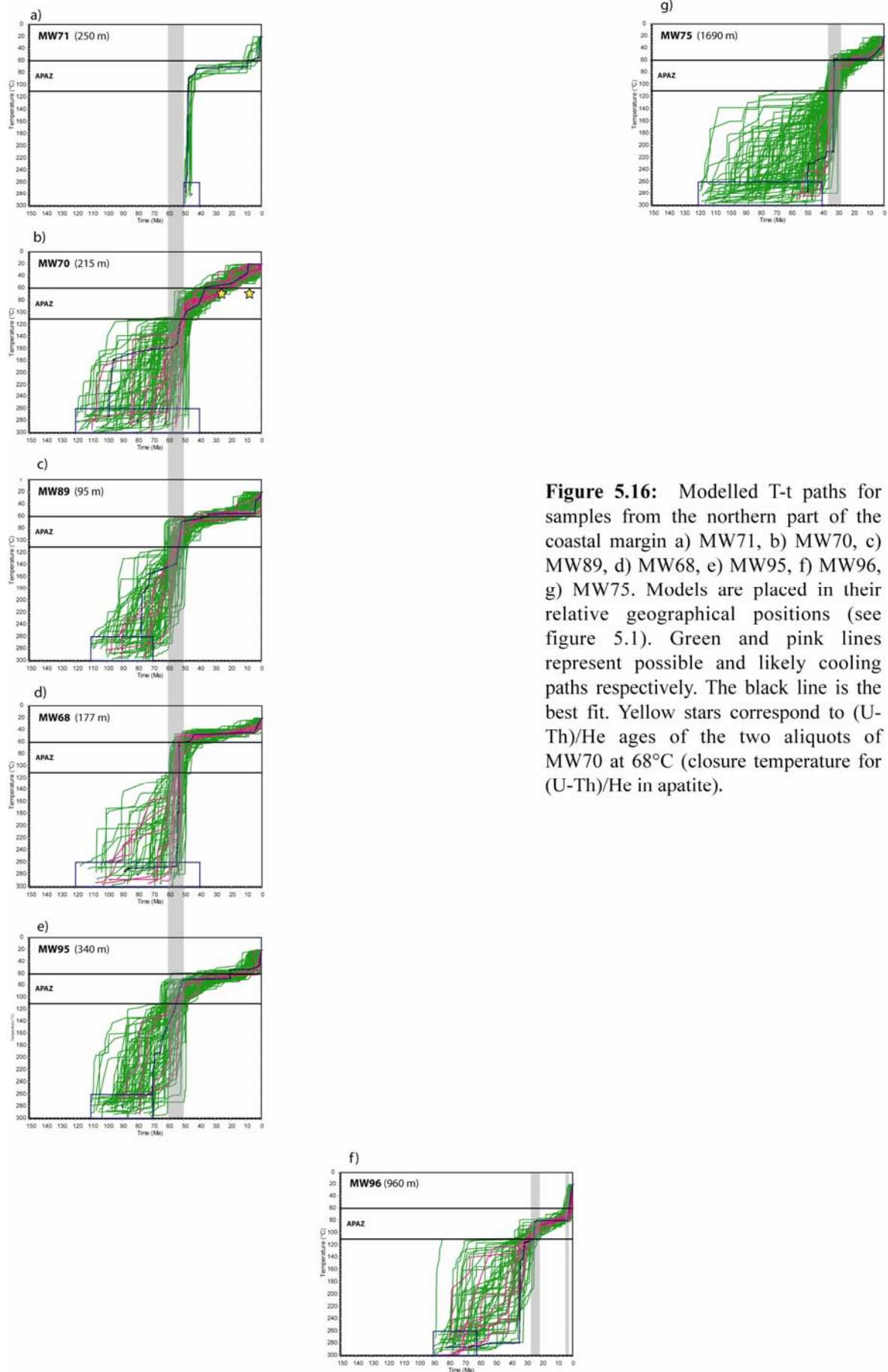


**Figure 5.16:** Modelled T-t paths for samples from the northern part of the coastal margin a) MW71, b) MW70, c) MW89, d) MW68, e) MW95, f) MW96, g) MW75. Models are placed in their relative geographical positions (see figure 5.1). Green and pink lines represent possible and likely cooling paths respectively. The black line is the best fit. Yellow stars correspond to (U-Th)/He ages of the two aliquots of MW70 at 68°C (closure temperature for (U-Th)/He in apatite).

### 5.3.5.3 Lima-Lunahuana

Five samples from the Lima area (MW46, 47, 48, 05, 03) were modelled. While initial rapid cooling (approximately 40°C/Ma) followed by a period of quiescence occurs in all models the exact timing of initiation varies. The cooling slows down at times ranging from ~90 and ~25 Ma between 100 and 60 °C. Modelled histories for MW46 (Fig. 5.17a) and MW03 (Fig. 5.17e) show renewed rapid cooling (approximately 6-8°C) starting at 5-2 Ma which is supported by He ages which range from 13.6 to 11.4 Ma and from 8.7 to 7.6 Ma respectively (Tab. 5.3a). It is also important to note that MW48 (Fig. 5.17c) is a Tertiary intrusive; hence a cooling history does not exist prior to 50 Ma (Tab. 5.1 with zircon age of 44.8 Ma). In all samples the period of quiescence begins after the rapid cooling from the zircon through to the apatite closure temperatures.

### 5.3.5.4 Nazca Ridge area-trailing edge

Modelled samples above the northern end (trailing edge) of today's location of the subducting Nazca Ridge are shown in figure 5.18. With the exception of MW25 that is from the San Nicolas Batholith at an altitude of 326 m (Fig. 5.18f) all other modelled samples from this area of Peru are from the Coastal Batholith at locations above 1200 m. MW15 (Fig 18a), although located at 2895 m and above the Nazca Ridge, shows a similar cooling behaviour than MW03 (Fig 17e) which is located at 602 m and slightly north of the Ridge. The major differences are that the obvious change in the rate of cooling occurred at 50-45 Ma which is roughly 20 Ma earlier than in MW03. The renewed exhumation starts at 2-1 Ma which is slightly younger than for MW03. The observation of a very similar cooling history for the last 40 Ma is further supported by very similar He-ages (Tab. 5.3a, b). Unfortunately the model for MW17 (Fig. 5.18b) did not yield good fits, but the acceptable paths agree well with the good fits for MW 15 (Fig.5.18a).

Models for MW23, 24, 22, 25 (Fig. 5.18c-f) suggest cooling to about 70-80°C by ~80-70 Ma at a rate of approximately 15-30°C/Ma. Unfortunately MW24 does not yield acceptable fits, the best generated fit agrees however with the general cooling behaviour observed for MW23, 22 (Fig. 5.18c-e). Since ~80-70 Ma all four samples have cooled very slowly. It is important to point out here that MW25 from the Palaeozoic San Nicolas Batholith shows a very similar cooling behaviour to the samples from the Coastal Batholith.

In some of these models from the northern Nazca Ridge area, a "Neogene cooling event" is observed. However it is difficult to confirm whether this event is an artefact in the modelling

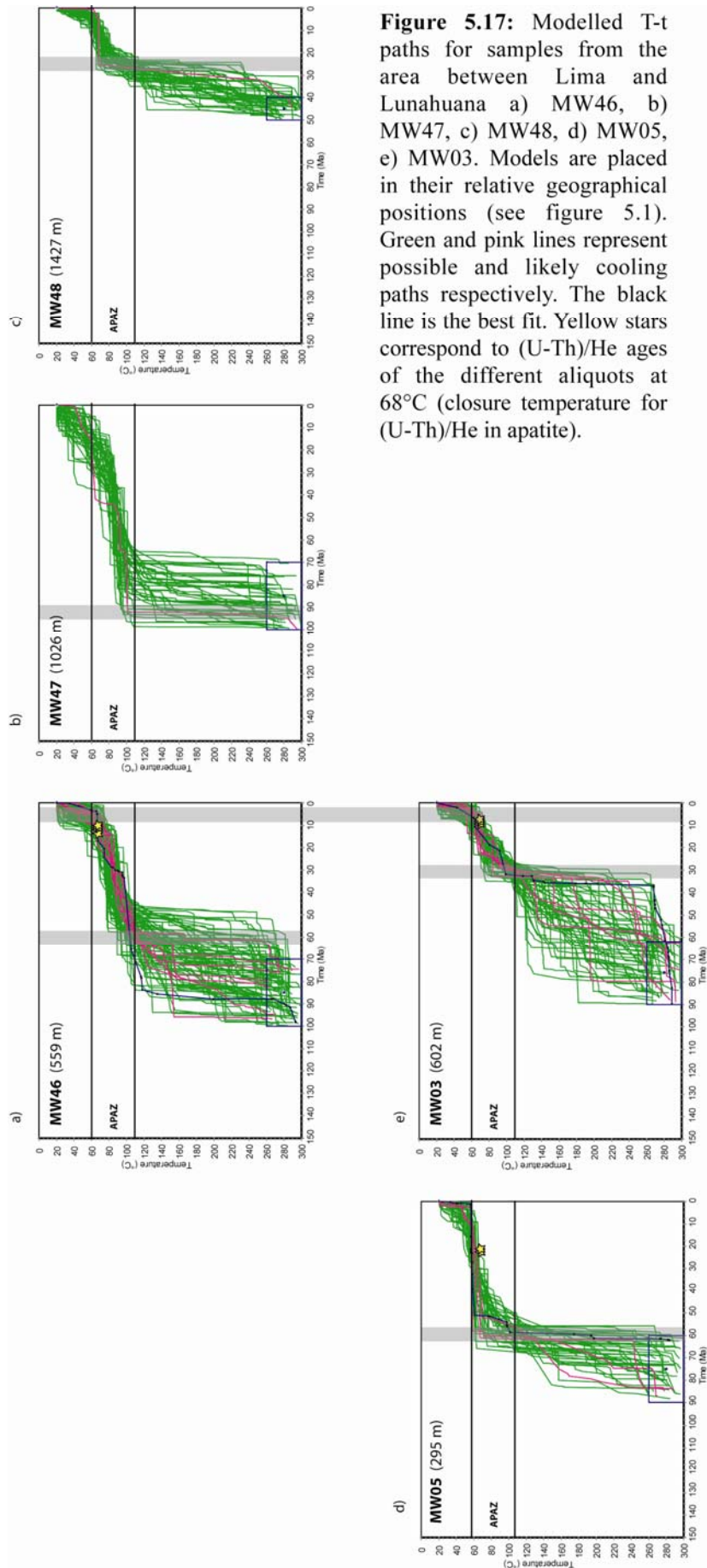


**Figure 5.17:** Modelled T-t paths for samples from the area between Lima and Lunahuana a) MW46, b) MW47, c) MW48, d) MW05, e) MW03. Models are placed in their relative geographical positions (see figure 5.1). Green and pink lines represent possible and likely cooling paths respectively. The black line is the best fit. Yellow stars correspond to (U-Th)/He ages of the different aliquots at 68°C (closure temperature for (U-Th)/He in apatite).

or not. The data are inconsistent. MW15 must have undergone rapid cooling at some time later than 10 Ma as supported by the He ages. On the other hand MW22 and MW25 have much older helium ages with a spread from 50-44 and 43-29 Ma respectively. In both models they fall perfectly onto the modelled fission track history however, and therefore in these samples a change in late Neogene is not supported by He ages.

#### *5.3.5.5 Nazca Ridge area-leading edge*

Modelled cooling histories of the area just over the leading edge of the Nazca Ridge are shown in figure 5.19. MW34, 44 (Fig. 5.19a, b) have zircon-fission track ages of about 200 Ma. They both cooled relatively slowly to 70-80°C by approximately 60-50 Ma at a rate of about 8°C/Ma. A slow cooling through the HePRZ is also suggested by the observed scatter in He ages (Tab. 5.3a). MW41 (Fig. 5.19c) seems to have cooled rapidly through the APAZ by ~100-90 Ma and very slowly since. Further interpretations are not conclusive because the cooling paths are outside the APAZ.

#### *5.3.5.6 Chala-Tacna*

MW63, 53 and 54 (Fig. 5.20a-c) from the very southern end of the Peruvian margin have very similar cooling histories. These three samples are all south of the present position of the Nazca Ridge. They cooled at rates as high as approximately 8°C/Ma to 80-60°C by around 90-80 Myrs ago. Since then, they have cooled slowly to the surface. The modelled cooling histories of MW63 and MW53 (Fig 5.20a, b) suggest a possible increase in the rate of cooling at around 2-10 Ma. The paths suggesting this are on the upper end of the APAZ and an increase is not supported by the He ages which are more in favour of a continuous slow cooling since ~80 Ma.

In general then, the pattern of the modelled cooling histories reveals a period of quiescence for up to 70 Myrs, followed by final exhumation to the surface at about 10-2 Ma. The fission-track zircon age has a relatively big impact on the observed rate of cooling and on the duration of the period of quiescence.

## **5.4 Interpretation and Discussion**

### **5.4.1 Zircon fission track**

The zircon fission track-ages display a large scale regional pattern. Three groups of age ranges related to the of the samples can be distinguished.

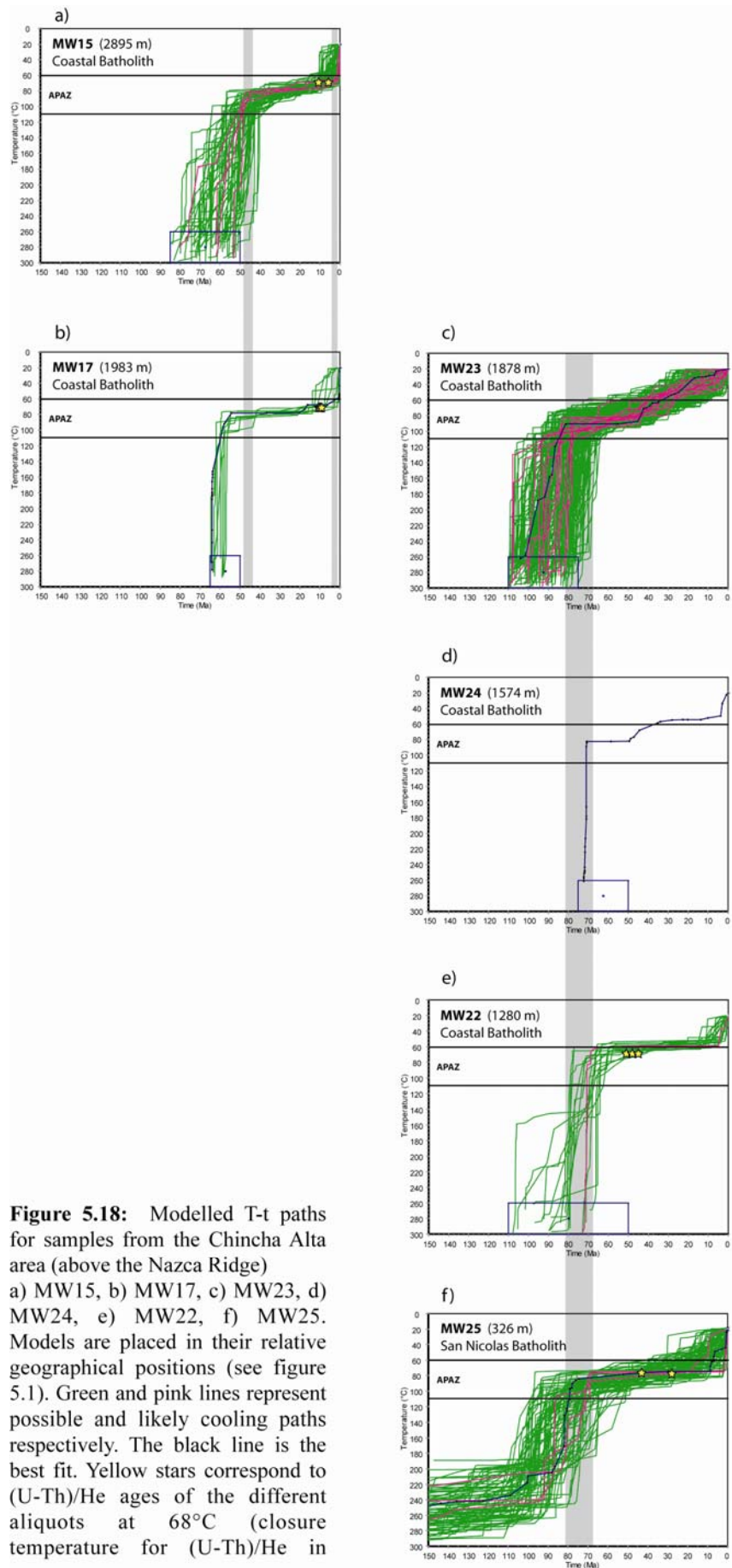


**Figure 5.18:** Modelled T-t paths for samples from the Chincha Alta area (above the Nazca Ridge) a) MW15, b) MW17, c) MW23, d) MW24, e) MW22, f) MW25. Models are placed in their relative geographical positions (see figure 5.1). Green and pink lines represent possible and likely cooling paths respectively. The black line is the best fit. Yellow stars correspond to (U-Th)/He ages of the different aliquots at 68°C (closure temperature for (U-Th)/He in

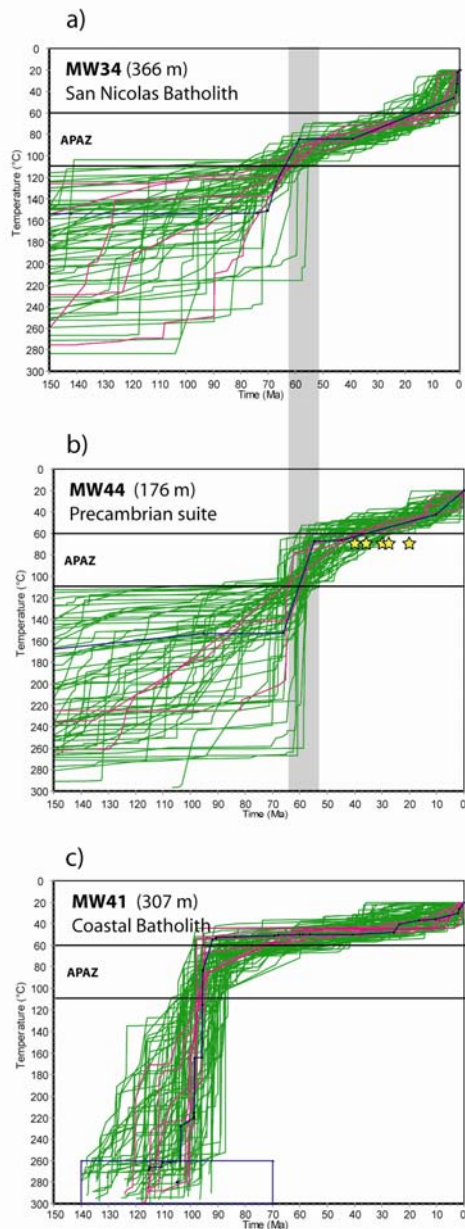


**Figure 5.19:** Modelled T-t paths for samples from the Chala area (above the leading edge of the Nazca Ridge) a) MW34, b) MW44, c) MW41. Models are placed in their relative geographical positions. Green and pink lines represent possible and likely cooling paths respectively. Yellow stars correspond to (U-Th)/He ages of the five aliquots at 68°C for MW44 (closure temperature for (U-Th)/He in apatite).

1: The Palaeozoic and Precambrian rocks have zircon fission-track ages ranging from  $121 \pm 11$  Ma to  $531 \pm 99$  Ma. These metamorphic Precambrian rocks have been reported to have protolith ages as old as 1900 Ma (Dalmayrac et al., 1977; Shackleton et al., 1979; Wasteneys et al., 1995) while the Palaeozoic intrusions are 425–388 Ma old (Mukasa and Henry, 1990; Stewart et al., 1974). The zircon fission-track ages are younger than the stratigraphic or intrusive age of the sampled rock bodies. The ages are interpreted to represent crustal cooling of the protolith aged rocks through to the zircon fission-track ages through exhumation to  $\sim 240\text{--}300$  °C (see page 77)

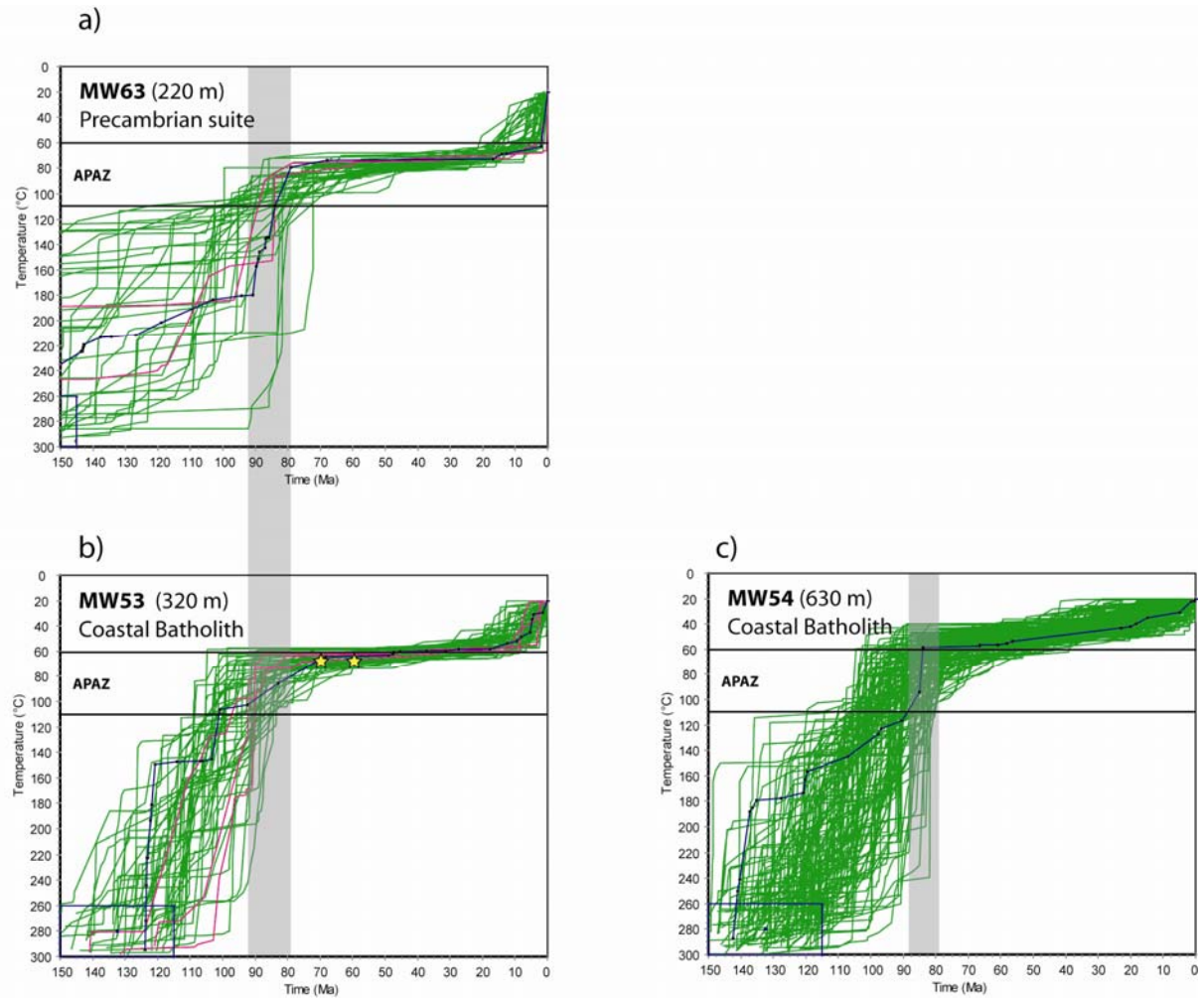


**Figure 5.20:** Modelled T-t paths for samples from the southern part of the coastal margin a) MW63, b) MW53, c) MW54. Models are placed in their geographical positions. Green and pink lines represent possible and likely cooling paths respectively. The black line is the best fit. Yellow stars correspond to (U-Th)/He ages of the two aliquots for MW53 at 68°C (closure temperature for (U-Th)/He in apatite).

2: The Coastal Batholith has crystallisation ages range from 134-28 Ma. According to Atherton and Petford (1991) and Haederle and Atherton (2002) the intrusions ascended to depths of 2-3 km. Assuming a normal geothermal gradient ( $\sim 25\text{-}30^\circ\text{C}/\text{km}$ ) this depth is equivalent to an ambient temperature of  $\sim 50\text{-}100^\circ\text{C}$ . Under these conditions a hot intrusive body will be subject to rapid cooling. The zircon fission-track ages are therefore interpreted to represent rapid cooling through the closure temperature of in this case  $\sim 270\text{-}300^\circ\text{C}$  (see page 77). This interpretation is supported by a comparison between U/Pb- and K/Ar ages by Mukasa (1986). Additionally where possible the fission-track data was compared to published radiometric ages determined with various methods (K/Ar, Ar/Ar, U/Pb, Rb/Sr; for references see chapter 2.3.2). These comparisons will be discussed in section 5.4.4. Unfortunately no radiometric age determinations exist for areas north of  $8^\circ\text{S}$  along the Peruvian coastal margin.

3. The last group is represented by the two dated Tertiary ignimbrites (MW31, 101: Tab. 5.1). Zircon fission-track ages for ignimbrites represent a very close approximation to the actual age of crystallization. MW31 from the Nazca Group yields a zircon-fission track age of  $23.1 \pm 2.8$  which is confirmed by a K-Ar biotite age of  $22.1 \pm 0.6$  Ma. MW101 giving a zircon fission-track age of  $1.3 \pm 0.3$  Ma is most likely from the “Sencca ignimbrites” dated at 3.8-1.4 Ma (Thouret et al., 2005) by the Ar/Ar method.

#### **5.4.2 Apatite fission track**

Apatite fission-track ages do not represent a simple cooling through the closure temperature; they are apparent ages as they are affected by the true integrated cooling history of the sampled rock body. The analysed samples of the Precambrian and Palaeozoic rocks as well as those from the Coastal Batholith yield apatite fission-track ages between 124 and 24 Ma. Although the spread of the apatite-fission track ages is less than the spread of the zircon ages (Fig. 5.6) there is still a considerable variation.

The Tertiary Rio Fortaleza ignimbrite (MW93) has been dated to  $7.4 \pm 2.8$  Ma which is in very good agreement with a K/Ar age measured on biotite of  $6.0 \pm 0.2$  Ma by Myers (1976) indicating that in the case of volcanic extrusives the apatite fission-track age is indistinguishable from the crystallisation age.

#### **5.4.3 (U/Th)/He**

The (U-Th)/He apatite ages also show a wide range from 1 Ma to 70 Ma (Tab. 5.3a, b, Fig. 5.8). The intra-sample spread of ages generally increases between the individual aliquots with the age of the sample, this is especially true for the dated apatite grains from Precambrian rocks. Like apatite fission-track ages the He ages do not represent simple cooling through the closure temperature. The regional spread in ages is interpreted to be the result of various periods of time spent within the HePRZ. Due to the low closure temperature of  $\sim 68^\circ\text{C}$  He ages are sensitive to erosional and geomorphological processes that take place at and close to the surface (i.e.  $< 2\text{km}$ ) thus the regional differences in He ages are therefore thought to mirror the variable evolution of more recent surfaces.

#### **5.4.4 Cooling histories of different regions**

Combining the results from the various methods including the higher temperature geochronometers such as U/Pb, Ar/Ar, K/Ar, Rb/Sr and geomorphological observations,

allows a better understanding of the evolution of the different areas of the Peruvian Coastal margin.

#### *5.4.4.1 Talara-Chiclayo*

Two samples (MW80, MW85) from the extreme north have been modelled to reveal the cooling history. MW80 (Fig. 5.15a) is from a Precambrian schist and is therefore thought to represent the evolution of the “old” crust unaffected by later intrusions. A significant change in the rate of cooling is observed at  $65\pm 5$  Ma. This occurs a little before the time associated with a major unconformity within the early Eocene volcanics generally referred to as the Calipuy Formation or Group in northern Peru (Cobbing et al., 1981). Noble et al. (1990) dated a fresh rhyolite located 500 m above the unconformity at 54.8 Ma using K-Ar on plagioclase, and Benavides (1956) reported from the same area that the lower Santonian rocks were overlain by Eocene sequences in northern Peru supporting a major erosional phase prior to the lower Eocene ( $\sim 55$  Ma). According to Noble et al. (1990; 1985) and McKee et al. (1990) this unconformity was the result of erosion following the compressional Palaeocene Incaic I phase (Fig. 5.6). Interesting to note is that the He ages in MW80 (including MW79 collected from the same schist) show a relatively wide scatter between 42.2 and 64.3 Ma (Fig. 5.15a, Tab. 5.3a), again recording a long period of slow erosion which resulted in the unconformity within the Calipuy Formation.

The scatter in He ages may be the result of zoning of uranium and thorium within the apatite crystals. If such grains are held within the HePRZ for long periods a relatively wide scatter in ages would be expected. The He ages are however significantly older than the  $\sim 8$  Ma suggested by the HeFTy algorithm for the best fit from the fission-track model (Fig. 5.15a). He ages are significantly “too old” in other samples (MW22, 53) as well. The modelled cooling history for all these samples suggests relatively long periods spent within the HePRZ. Although it is possible that some uranium or thorium rich micro-inclusions were overseen while picking the apatite grains this cannot explain the big discrepancies between the suggested and the measured He age. It seems more plausible that the helium diffusion or the annealing of fission tracks behaves differently than generally believed over geologically relevant time periods spent within the HePRZ.

MW85 (Fig. 5.15b) from the Coastal Batholith shows a relatively simple cooling history. While the low temperature history of the Precambrian rocks is interpreted to represent the cooling and exhumation unaffected by intrusives the cooling histories of the shallowly

intruded plutons has to be interpreted differently. As previously noted the batholiths intruded into the crust's upper 2-3 km (Atherton and Petford, 1991; Haederle and Atherton, 2002). This is at a depth lower than the closure temperature of zircon in normal circumstances. Even with an increase in the geotherm, the zircon ages are therefore likely to represent a proxy for the crystallisation age. The intrusions will cause an increase in the geothermal gradient around the shallow intrusive bodies. A more rapid cooling than the normal background cooling due to erosion is therefore expected as geotherms will readjust more rapidly to the ambient temperature. The cooling rate slows down around 45 Ma which is interpreted to represent this adjustment of the geotherms around the hot intrusives to the ambient geotherm. No time of very slow cooling is recorded in this sample. From 48 Ma it simply cools monotonically.

#### 5.4.4.2. Chiclayo-Huacho

All modelled apatites at altitudes below 340 m show very similar envelopes of acceptable cooling paths (Fig. 5.16a-e). A significant reduction in the rate of cooling is observed between 60-50 Ma similar to the one observed in MW85 (Fig. 5.15b). In contrast samples at altitudes above 340 m (MW96, MW75) reached the APAZ at about 30 Ma, this is approximately 25 Ma later than the samples at lower locations.

Assuming that the zircon fission-track ages represent a close approximation of the crystallisation age due to shallow intrusion then the timing of initiation of the phase of very slow cooling depends on the age of the pluton. Many examples can be found where higher temperature chronometers support this notion. For example in sample MW71 that has a zircon fission-track age of 46 Ma and an apatite fission-track age of 46.8 Ma, a K/Ar on biotite (closure temperature:  $\sim 300^{\circ}\text{C}$ ) from the same intrusive complex has been dated at 43 Ma by Stewart et al. (1974; sample no.6). These three ages are statistically indistinguishable and therefore support the interpretation of rapid cooling due to the shallow depth of intrusion. Further support for rapid cooling comes from sample MW74 with an apatite fission-track age of 25.0 Ma from a locality close to where Stewart et al. (1974) collected his sample No. 5 with a K/Ar age of 26 Ma (biotite).

Sample MW95 with an apatite fission-track age of 50.1 Ma is from the same pluton as HS43 (Mukasa, 1986) with a U/Pb age of 64.7 Ma. Cobbing et al. (1981) dated three samples close by (No. 135-137) which gave K/Ar (biotite) ages ranging from 58-64 Ma again fitting the model of rapid cooling (Fig. 5.16e).

Mukasa (1986) reported U/Pb ages of 68.0 and 68.5 for two samples (HS28, HS12) for the same intrusive body from which MW96 was collected. A Rb/Sr isochron derived from 14 whole rock analysis from this area yields an age of 65 Ma (Beckinsale et al., 1985). It is interesting to note here that the apatite ages for MW96 is, at 23.6 Ma, significantly younger than the U/Pb age, but Cobbing et al. (1981; sample 50) reported K/Ar ages of 33.0 and 33.1 measured on biotite and K-feldspar respectively. Stewart et al. (1974) also dated two samples within this rock body (No.20, 21) and determined K/Ar ages on biotite of 33.0 and 32.4 Ma. These data led Cobbing et al. (1981) to speculate that the young ages were a result of a thermal disturbance around this time due to an intrusive body beneath the surface.

Sample MW97 has a zircon fission-track age of 72.8 Ma. This age is within error identical to the U/Pb age of 65.1 Ma (Mukasa, 1986; Sample HS 33), and to a K/Ar age of 66 Ma (Cobbing et al. 1981; sample No.21) derived from biotite from the same rock. This is yet another example of rapid cooling.

The geological evidence for shallow intrusions and the similarities of many ages with higher temperature geochronometers supports the notion that the change in the rate of cooling observed in the modelled cooling histories is not a tectonic event but the result of thermal adjustment of the hot shallow intrusions to the surrounding temperature and minor erosion and exhumation.

A possible renewed acceleration of the rate of cooling as suggested in most models around 5-1 Ma is difficult to verify. Only in MW96 (Fig. 5.16f) located at 960 m is this acceleration within the APAZ. According to Garver et al. (2005) the Cordillera Blanca located 150-200 km northeast of this area (Fig. 5.1) began uplifting at 6 Ma. The cooling in this region may be related to the exhumation of the Cordillera Blanca. Unfortunately the only He ages from this area (MW70; Fig. 5.16b) reproduce poorly with ages of 26.2 and 6.9 Ma (Tab. 5.3a) and do not offer more precise information. The younger age is supportive of renewed cooling at ~7 Ma. According to McNulty and Farber (2002) the exhumation of the Cordillera Blanca coincides with the inferred initiation of flat-slab subduction in this segment of the Nazca subduction zone. The same authors speculated that subduction of the Nazca Ridge may have initiated uplift of the Cordillera Blanca. This interpretation is however inconsistent with Hampel (2002) who proposes that the Nazca Ridge most likely entered the Peruvian Chile Trench at ~11.2 Ma at 11°S, but not north of 10°S, which is still to the south of the Cordillera Blanca (Fig. 5.1).

In summary, a rapid cooling most likely followed granite emplacement and was succeeded by a period of quiescence beginning between 60-50 Ma. This period lasted until  $\sim 7$  Ma when renewed rapid cooling probably associated with the exhumation of the Cordillera Blanca started.

#### 5.4.4.3 Lima-Lunahuana

The evolution of the Lima area is best explained in the same way as the previously discussed Chiclayo-Huacho segment. All samples collected within this area are from the Coastal Batholith. Rapid cooling after intrusion was followed by quiescence. While it cannot be completely excluded that the observed changes in cooling rates between 60 and 25 Ma are the result of tectonic events, the fact that they do not occur at identical times within the area strongly argues against this interpretation. Hence it is more reasonable to conclude that the changes in cooling rates are caused by simple cooling of the intrusive bodies as mentioned above followed by a period of quiescence comparable to the areas north of Lima. Models for MW47 (Fig. 5.17b) and MW48 (Fig. 5.17c) clearly demonstrate that duration of the period of quiescence depends strongly on the zircon fission-track age. This interpretation is also supported by previously published radiometric ages. Mukasa (1986; sample RR7) reports a U/Pb age of 86.4 Ma (coarse zircons) and 84.4 Ma (fine zircons) for the same rock body which is within error identical to the zircon fission-track age of 83.2 Ma determined for MW47. Vidal (1987; sample SRX) determined a K/Ar age on hornblende of 81.8 Ma and on biotite of 65.9 Ma on the same intrusion while Stewart et al. (1974; Sample 29) reported a K/Ar age on biotite from this pluton of 63.1 Ma.

The zircon fission-track age of 44.8 Ma and the modelled cooling history for MW 48 (Fig. 5.17c) indicates that the sampled intrusion is approximately 40 Ma younger than the rest of the plutons analysed within the Lima-Lunahuana region. This interpretation is once more supported by Mukasa (1986; sample RR5) reporting a U/Pb age of 59.1 Ma and by Beckinsale et al. (1985) who reported a Rb/Sr isochron with an age of 62 Ma.

The relatively young zircon and apatite fission-track ages of MW01 and MW02 (28.4 and 29.6 Ma respectively) are also supported by a Rb/Sr isochron of 24 Ma (Beckinsale et al., 1985). MW01, 02 have apatite fission-track-ages which are statistically indistinguishable from their zircon fission-track ages and therefore again support the idea of rapid cooling. In sample locations MW03 and MW46 (Fig. 5.17a, e) a renewed increase in cooling is suggested at 8-4 Ma. In these two samples the He ages also indicate a change in exhumation within this

approximate timeframe (i.e. 7.7-8.7 Ma for MW03 and 11.4 – 13.6 Ma for MW46; Tab. 5.3a). A possible increase in exhumation around 3-8 Ma may be suggested by the modelled cooling history for MW05. This change falls outside of the APAZ and could be an artefact of the modelling as it is not confirmed by the He data. However the consistency of the time of change with the other models suggests that there was a <10 Ma cooling event. The two He ages of MW05 reproduce within  $1\sigma$  of the analytical uncertainty at 21.1 and 21.4 Ma (Tab. 5.3a) and fit directly onto the apatite fission track modelling curve. The He ages of the Lunahuana and Pisco segment display an inverted age–altitude correlation below 1000m (Fig. 5.10). According to (Braun, 2002) inverted age-altitude relationships (AER's) are possible in situations associated with a rapid decrease of relief after the time since the rock passed through the closure temperature. This interpretation is consistent with the observation of a decrease in relief from north of the Nazca Ridge relative to areas located above its present location (see Chapter 3). The youngest of the He ages (MW02: 1.04 Ma) at 1020 m is in the vicinity of a weak river knick point along the Lunahuana River. As river knick points are the site of maximum erosion the exhumation of young ages in their vicinity may be expected. The relief below 1000 m (i.e. below the knick point) has been reduced by erosion in the last 1 myr. At >1000 m, above the actively eroded point, a relatively normal AER is observed (two data points only however), implying significantly less relief change above the knick point.

#### 5.4.4.4 Nazca Ridge area- trailing edge

The area above the trailing area was sampled across two sections.

a) All samples collected in the Pisco valley from the coastal Batholith, have Upper Cretaceous crystallisation ages. A U/Pb age from this part of the Coastal Batholith yields 78.3 Ma (Mukasa, 1986; sample RP-16); Beckinsale et al. (1985) reported a Rb/Sr isochron of 80 Ma and a K/Ar isochron of 80.5 Ma. Stewart et al. (1974; Sample 37) determined a K/Ar age of 65 Ma on biotite while Moore (1984) measured on the same intrusive body in the Ica valley K/Ar ages of 80.9 Ma and 76.9 Ma on hornblende which overlap within error. The zircon fission-track ages range from 93 to 57 Ma and overlap in many cases with the apatite fission-track ages (Fig. 5.11). This close range of ages determined with various methods supports rapid cooling after intrusion also for the Pisco area. A clear clustering of ages between 80 and 60 Ma can be observed for apatites and zircons (Fig. 5.11). Due to the shallow depth of the intrusions all the sampled rock bodies cooled rapidly and therefore no age-altitude correlation is observed. As observed in the Lunahuana valley the He ages show an inverted correlation

with altitude. The youngest He ages (MW16; Tab. 5.3a, b) ranging from 6.0 to 4.8 Ma reproducing well, are observed at 2245 m and coincide with the altitude of an obvious river knick point. As mentioned above such a correlation may indicate an erosion phase causing decrease of relief since cooling through the closure temperature of  $\sim 70^{\circ}\text{C}$  at  $\sim 5.2$  Ma (Tab. 5.3b) (Braun, 2002). This decrease is supported by geomorphological evidence discussed in chapter 3.

b) The samples from the area of Chincha Alta (MW23, 24, 22, 25) show a change in cooling rates around 80-70 Ma, a time which was identified further south as the Peruvian Phase by Steinmann (1929). That this change in cooling rate is the result of the Peruvian phase is difficult to confirm because it may also represent the crystallisation age of the shallow intrusive granitic bodies which are coincident in time. The subsequent phase of very slow cooling could be due to simple erosion after adjustment to the background geotherms as discussed previously. The fact however that MW25 collected from the Palaeozoic San Nicolas Batholith displays an almost identical cooling history indicates that the rapid cooling may be due to a tectonic event in this case. It however also possible that the apatites in the San Nicolas Batholith were reset due to the heating caused by the intrusives of the Coastal Batholith.

In summary subsequent to the rapid cooling, the area was subject to a period of quiescence. Slow cooling seems to have remained the only process affecting the area above the trailing edge of the Nazca Ridge. He ages for MW22 reproduce nicely between 44 and 50 Ma while they spread from 28.9 to 43.2 Ma in MW25 (Tab. 5.3a). Despite the large spread they fit onto the modelled cooling paths (Fig. 5.18f). Based on the best fit from the cooling model of the fission-track data for MW22 and MW25 (Fig. 5.18e, f) He ages of  $\sim 16$  and  $\sim 8$  Ma respectively would be expected. The actually measured He ages are thus significantly older just as seen previously with sample MW80 to the north. Anomalously old He ages and possible explanations have been discussed before (Chapter 4). These explanations however cannot explain the nice reproducibility observed in the case of MW22. This contradiction supports the notion that He diffusion is not fully understood over geologically significant timeframes. In contrast the Pisco area (MW15, 17) has experienced a renewed rapid exhumation around  $\sim 5-2$  Ma. In these models (Fig. 5.18a, b) the renewed increase in the cooling rate falls clearly into the APAZ and is supported by the weighted mean He ages of 7.6 and 5.2 Ma respectively (Tab. 5.3b), although the reproducibility is rather poor for MW15 (Tab. 5.3a).

#### 5.4.4.5 Nazca Ridge area- leading edge

The modelled history for MW41 (Fig. 5.19c) yields a significant change in cooling between 100-90 Ma. This change is generally below the low end of the APAZ and some cooling paths are actually outside which leaves further interpretations inconclusive. Track lengths are relatively long however (13.97  $\mu\text{m}$ ) supporting again rapid cooling due to a shallow depth of intrusion.

The other two models (MW34, 44; Fig. 5.19b, c) show a different behaviour. They are from the San Nicolas Batholith dated at 425-390 Ma (Mukasa and Henry, 1990; Stewart et al., 1974) and the Precambrian basement with a protolith age of 1900 Ma (Dalmayrac et al., 1977; Mukasa and Henry, 1990; Stewart et al., 1974). Rapid cooling is evident in both samples at 60-55 Ma. This can be correlated with the Incaic 1 compressional phase. According to the fission-track model and the helium ages very slow cooling occurred from 55-~20 Ma (MW44; Fig. 5.19b) when renewed more rapid cooling brought the rocks to the surface.

#### 5.4.4.6. Chala-Tacna

MW63 is the only Precambrian rock from the very south for which enough data was available to model the low temperature cooling history (Fig. 5.20a). Rapid cooling at 90-80 Ma is followed by a period of almost no cooling possibly until <10 Ma. MW63 has a zircon fission-track age of 199 Ma and is from the same outcrop where Stewart et al. (1974) sampled their No. 49 with a K/Ar age of 210 Ma measured on muscovite (closure temperature:  $\sim 350^\circ\text{C}$ ) - these ages are identical within error. Several other outcrops from the Precambrian coastal rock suites were dated by Stewart et al. (1974; samples 44, 46-49) resulting in K/Ar ages on various minerals like K-feldspar, biotite, hornblendes and muscovite of 157-210 Ma. Samples slightly further south (MW103, 104) with zircon fission-track ages of 353 and 531 Ma are in the same range as well as the biotite K/Ar ages of 447 and 679 Ma (Stewart et al., 1974; sample 57, 50) from this area.

Sample MW62 a diorite from the Coastal Batholith near Arequipa has an apatite fission-track age of  $79 \pm 35$  ( $2\sigma$ ) Ma. A U/Pb date from this area yields an age of 70.5 Ma (Mukasa, 1986; sample CV-23). It is important to point out the large imprecision of the fission-track age which is due to the fact that only five crystals could be counted. Nonetheless the two ages probably overlap statistically again indicating rapid cooling.

The two ages greater than 100 Ma from the extreme south (i.e. MW52, 53) are from the same group of intrusive bodies which have been dated at 97-113 Ma using the K/Ar- and the Ar/Ar-

method on biotite and hornblende (Beckinsale et al., 1985; Clark et al., 1990a). The modelled cooling paths for the Coastal Batholith (MW53, 54: Fig. 5.20b, c) suggest a similar change in cooling at 90-80 Ma as observed in MW63 (Fig. 5.20a). This takes place near the lower limit of the APAZ however.

In Southern Peru the precise timing of the Peruvian phase is unclear but is believed to postdate Coniacian (~88Ma) marine beds and predate Campanian (~72Ma) red beds (Beckinsale et al., 1985; Clark et al., 1990a; Jaillard, 1994; Vicente et al., 1979). In this scenario the Peruvian tectonic phase is interpreted to have taken place between ~88 and 72 Ma in southern Peru. According to Megard (1984) however a tectonic event during the Santonian represents a major turning point in the evolution of the Andes of Peru because it represents the first widespread episode of deformation. The new low temperature thermochronological data supports the Santonian-cooling phase of Megard (1984).

All models from south Peru (Fig. 5.20a-c) reveal a long period of quiescence subsequent to ~80 Ma. According to the models the coastal margin of south Peru seems to have remained stable since as early as the late Cretaceous.

In the south the models do not record a change which could be correlated with the Palaeocene Incaic I tectonic phase observed in samples further north. According to Clark et al. (1990a; 1990b) the Incaic orogeny was represented by widespread but probably minor uplift, folding and erosion in the Western Cordillera of southern Peru. There are no geomorphic expressions of a post Incaic erosional phase south of 14°S. It is likely however that they are represented by the lower-Moquegua or the internal-Moquegua unconformity (Tosdal et al., 1984). The regional unconformity beneath the lower member of the Moquegua formation is very poorly constrained by a K/Ar age of an eroded pluton of 51 Ma (Laughlin et al., 1968; McBride, 1977). Supergene alunite from the Cerro Verde porphyry Cu-Mo cluster from Arequipa dated by Ar/Ar have maximum ages of 36.1 to 38.8 Ma (Quang et al., 2003), implying that the supergene activity was underway by the latest Eocene. This activity was probably in response to the uplift and erosion resulting from the Incaic II phase. Nonetheless erosion was obviously not strong enough to produce the required cooling/exhumation to bring the deeper levels which recorded the Incaic events in the fission-track data, to the surface.

The wide scatter observed in the He ages of MW53 (i.e. 69.6 and 57.7 Ma; Tab. 5.3) support a long period of quiescence and very slow erosion just as suggested by the fission-track data modelling. As previously noted reproducibility of He ages of Precambrian suites is commonly not very good and usually scatter significantly. In the case of MW53 (Fig. 5.20b) they are

significantly older than an extrapolated ~20 Ma age based on incorporating the best fit into a helium model (Ketcham, 2005). However it must be noted that these ages lie tightly on the modelled fission-track curves. It remains possible that some uranium or thorium rich micro-inclusions were overseen. However other samples (e.g. MW22, 80) also yield relatively long periods spent within the HePRZ, and also have a wide spread of helium ages. As yet the meaning of this is unclear, but the ages match perfectly the fission-track model, which is coincident with the HePRZ over a long period of time.

Additional support for a long period of quiescence in southern Peru is given by cosmogenic dating of palaeosurfaces from northern Chile which yields ages as old as ~37 Ma (Dunai et al., 2005; Evenstar et al., 2005; Kober, 2004). A possible renewed increase in cooling seen in the models for MW53, 63 (Fig. 5.20 a, b) around 3-2 Ma is however on the extreme lower limit of the APAZ and not supported by He ages. It could be simply an artefact created by the modelling algorithm. Interestingly (Evenstar et al., 2005) reports  $^3\text{He}$  exposure ages of 2.96-2.67 for erosional terraces from the very north of Chile, which may also represent the cooling phase seen in these models.

## 5.4.5 Impact of the Nazca Ridge

### 5.4.5.1 Evidence from fission-track and (U/Th)/He ages

The coastal area is the most likely to record an effect of the passing of the Nazca Ridge. Therefore ages below an altitude of 600 m were looked at in more detail (Fig. 5.4a-c). The zircon fission-track ages of samples from the Coastal Batholith show variation across the Ridge but do not follow a recognisable pattern. The apatite fission-track ages on the other hand increase from north to south (Fig. 5.4a, b). The change occurs gradually but is concentrated above the present position of the Nazca Ridge. While the ages north of the ridge scatter from 66 to 31 Ma the ages in the south vary from 59 to 93 Ma. The reason for this apatite fission-track age distribution may be the result of two different effects.

a) The change might be the result of the passing of the subducting Nazca Ridge. Observations supporting this interpretation are that in the northern section the apparent apatite ages tend to get younger towards the Ridge and that the section above the Ridge shows a linear trend towards older ages in the south. The apparent ages *per se* are too old to be the result of exhumation due to the passage of the Ridge, (<12Ma). However, inspection of the thermal modelling, supported by the He ages, hints at a possible increase in cooling (exhumation) at <10Ma, in regions just north and over the Ridge.

Data for the He ages are sparse but they show a similar pattern to the apatite-fission track ages. A jump towards older ages is apparent over the northern edge of the Nazca Ridge, possibly interpreted as enhanced erosion over the ridge but the determination of the exact timing of its passage is also not possible. The He ages from the Lunahuana (MW02, 03, 01; Tab. 5.3) and the Pisco (MW15, 16, 17, 18; Tab. 5.3) valleys are in general significantly younger than further north and south. The increase in erosion as rivers are adjusting to the changes in base level is thought to lead to the exhumation of these young He ages. The young He ages from the Lunahuana valley of 1.0 Ma (MW02) and 3.3 Ma (MW01) are evidence for significant erosion, of the order of 2 km over this period, i.e. at a rate of 0.6-2 mm/yr. The youngest He age from the Pisco valley (MW16; Tab. 5.3) is slightly older but still significantly younger than in areas north and south of the ridge. Additionally the Pisco and the Lunahuana area show a remarkable coincidence of the He ages with the river knickpoint. As knick points are the sites of maximum erosion it is not unexpected that the youngest ages occur in their vicinity.

b) The observed effect could also be the result of simple cooling associated with the crystallisation. As mentioned above many samples have similar zircon and apatite fission-track ages indicating rapid cooling. Hence the trend of older apparent apatite fission-track ages towards the south could be due to increasingly older plutons southwards.

Without a better constraint on the actual time of emplacement of the various plutons sampled the interpretation is inconclusive. The young He ages north and above the trailing edge of the Nazca Ridge as well as the negative age-altitude gradient and its probable correlation to the river knick points most likely are the result of increased exhumation due to the passage of the Ridge. Such an interpretation from the apparent fission-track ages is difficult to confirm however

#### *5.4.5.2 Evidence from thermal modelling*

A renewed increase in cooling rates between 8-1 Ma is observed in various samples (MW80, 71, 89, 68, 95, 75, 96, 46, 03, 15, 17, 63) at altitudes between 95 and 2895 m. Only in samples from central Peru (i.e. MW46, 03, 15, 17) are these changes supported by He data (Tab. 5.3a, b) however. For MW71, 89, 68, 95, 75 from the north these increases are outside the APAZ and therefore inconclusive. It is however plausible that this young event is real as the Cordillera Blanca located east of these sites began uplifting at ~6 Ma (Garver et al., 2005). As previously mentioned, McNulty and Farber (2002) speculated that this exhumation was

triggered by the initiation of flat subduction due to the beginning of Ridge subduction which is however not supported by Hampel (2002). For MW96 an independent confirmation of this renewed increase in the cooling rate is not possible since no He ages were determined. In contrast the He age of MW05 located at 295 m reproduces nicely around 21 Ma and the model suggests nothing but slow cooling. It is important to note that fission-track modelling for MW80 also suggests an increase around 6-4 Ma in the extreme north, which is not confirmed by He ages however. Modelled cooling histories for samples south of the Pisco Valley section (i.e. south of samples MW15, 17) do not indicate the presence of an event around 6-4 Ma. One exception is MW63 where modelled cooling paths hint at an increase in exhumation at 5-3 Ma. Unfortunately no He ages were measured on this sample; the event seems unreal however as it occurs barely within the APAZ and the relatively old He ages from the next sample to the north (MW44) and to the south (MW53) do not favour such an interpretation. Based on these arguments the events seen in MW80 and MW63 are thought to be artefacts from the modelling algorithm. It is therefore tempting to conclude that only samples from central Peru indicate a possible event at 6-4 Ma. According to Hampel (2002) the subduction of the Nazca Ridge started at 11°S at 11 Ma. Hence it seems plausible to correlate this event with the passing of the Nazca Ridge. Areas to the north of 11°S and to the south of today's position of the Nazca Ridge would therefore not record its passage. It is very important to emphasize that this interpretation has to be treated with the utmost care as it takes fission-track analysis to the extreme limit.

## 5.5 Conclusions

A bias in the interpretation of the data caused by the location of the sampling sites seems unlikely for the apatite- and zircon fission-track data. It cannot be excluded however for the He ages.

### 5.5.1 Meaning of the cooling ages

#### 5.5.1.1 *Precambrian and Palaeozoic suites*

Since the protolith ages of the sampled rocks are significantly older than the zircon fission-track ages it is believed that they represent the time of slow cooling through the closure temperature of  $270\pm 30^\circ\text{C}$ .

Apparent apatite fission-track ages of the Precambrian to Palaeozoic rocks range from 90-63 Ma. They tend to be slightly older than the apatite fission-track ages from the Coastal

Batholith at similar altitudes. The ages do overlap however and a statistically valid difference is not observed (Fig. 5.6).

The ages from the slowly cooled Precambrian and Palaeozoic suites with potentially complex cooling histories and extensive periods spent within the HePRZ produce a large scatter. While zoning in uranium and thorium concentrations can explain part of the scatter it cannot account for the entire spread observed. Some of these anomalously old ages are difficult to explain because they are significantly older than expected ages based on modelled fission-track data. It is important however to note that all the ages, in spite of the large spread, fit onto the modelled cooling paths. Based on these observations it is concluded that single grain He ages from such samples are very difficult to interpret. It is likely that the He diffusion is not fully understood yet in geologically relevant time frames. In order to gain a better understanding of the meaning of these ages, it seems necessary to analyse enough grains to gain a statistically relevant distribution of possible ages which should then be presented in the form of radial plots. Additionally a precise determination of uranium and thorium distribution within an individual grain is desirable, although technically difficult to achieve, in order to model the cooling history reliably.

#### *5.5.1.2 Coastal Batholith*

Since the depth of intrusion of the individual plutons of the Coastal Batholith was probably very shallow i.e 2-3 km (Atherton and Petford, 1991; Haederle and Atherton, 2002) the initial cooling was very rapid. As a result the zircon fission-track ages are a very close approximation of the crystallisation ages. In many cases this notion is supported by published radiometric ages determined with other techniques such as U/Pb, Rb/Sr, K/Ar, Ar/Ar that are statistically indistinguishable.

At most sites rapid cooling occurred in the higher temperature region of the APAZ, and for samples where zircon ages are available this rapid cooling extends from  $270\pm 30^{\circ}\text{C}$ . Following this phase, almost all samples rested for extensive periods in the APAZ, before final Neogene exhumation. The helium ages either lie in the HePRZ or coincide with a change in cooling rate in the Neogene as suggested by the fission-track modelling.

### 5.5.2 Identification of tectonic events

Changes in cooling rates derived from modelling based on fission-track data are often associated with possible tectonic events. Two distinctly different types of cooling histories can be seen in the modelled samples.

a) Rocks from Precambrian or Palaeozoic suites show simple slow cooling. Significant changes in the rate of cooling within these models (i.e. MW63, 34, 44, 25, 80; Fig. 20a, 19a, b, 18f, 15a) can be correlated with known major tectonic events such as the Peruvian- (~72-88 Ma) and the Incaic 1 (~60 Ma) Phase. The only model from northern Peru (MW80) shows the Incaic 1- but does not record the Peruvian event. In models from central Peru (MW25, 34, 44) the change in the rate of cooling can be correlated to the Incaic I - (MW34, 44) and to the Peruvian (MW25) phase. In southern Peru only the Peruvian phase is seen (MW63).

b) The modelled cooling histories from the Coastal Batholith show a phase of very rapid cooling, as high as 60 °C/myrs just after intrusion. This cooling slows down and eventually becomes identical to the slow cooling observed in the Precambrian and Palaeozoic rocks. Depending on the variable age of the intrusion, the timing of the change in cooling to the subsequent period of quiescence varies. No tectonic events are believed to be represented by these changes.

Data for a possible late Neogene tectonic event (<10 Ma) recorded by the modelled cooling histories of central Peru is difficult to interpret. A correlation with the passing of the Nazca Ridge is plausible but extremely difficult to verify, through fission-track analysis alone. However increased erosion, seen through the (U-Th)/He system, is observed, but it alone does not identify the exact timing of the Ridge movement (see below).

### 5.5.3 Erosion

The area has been dry since at least 23 Ma, possibly 37 Ma (Dunai et al., 2005) or maybe even since the Jurassic as proposed by Hartley (2005). Assuming a normal geothermal gradient of ~25°-30° C/km <4 km have been removed (i.e. <0.05 mm/yr) over the last 90 Ma south of the Nazca Ridge. On the other hand more erosion has occurred in the coastal areas uplifted by the subducting Nazca Ridge. This can be observed by a south to north reduction of the altitude in the Coastal Cordillera which has taken place during the last 3.5 Myrs (i.e. ~0.3 mm/yr) (see chapter 3). This increase might also have led to the exposure of younger apparent apatite fission-track ages over and to the north of the Nazca Ridge. It is however not big

enough to reveal the timing of the ridge induced uplift itself. There has not been sufficient erosion taking place to exhume the layers further down.

At higher altitudes the enhanced erosion was sufficient to expose very young He ages. The youngest He ages are observed in the vicinity of river knick points, indicating that enough erosion (~1 mm/yr) is occurring in these places to expose rocks which have very recently cooled through 70°C. This is most likely the result of rivers adjusting to changes in base level through surface uplift that is caused by the subducting and passing Nazca Ridge. The inverted age –altitude correlation observed over and immediately north of today's position might also be explained by increased erosion which led to a recent rapid decrease in relief after cooling through the closure temperature as suggested by (Braun, 2002).

## 5.6 References cited

- Atherton, M.P., and Petford, N., 1991, Rifting, insertial volcanism, batholith formation and crustal growth, Peru: *Terra Abstracts*, v. 3, p. 37-38.
- Beckinsale, R.D., Sanchez-Fernandez, A.W., Brook, M., Cobbing, E.J., Taylor, W.P., and Moore, N.D., 1985, Rb-Sr whole-rock isochron and K-Ar age determinations for the Coastal Batholith of Peru, *in* Pitcher, W.S., and Atherton, M.P., eds., *Magmatism at a Plate Edge: The Peruvian Andes*: Glasgow, Blackie, p. 177-202.
- Benavides, V., 1956, Cretaceous system in Northern Peru, *American Journal of Natural History Bulletin*, Volume 108: New York, p. 352-494.
- Braun, J., 2002, Estimating exhumation rate and relief evolution by spectral analysis of age-elevation datasets: *Terra Nova*, v. 14, p. 210-214.
- Clark, A.H., Farrar, E., Kontak, D.J., Langridge, R.J., Arenas, M.J., France, L.J., McBride, S.L., Woodman, P.L., Wasteneys, H.A., Sandeman, H.A., and Archibald, D.A., 1990a, Geologic and Geochronological Constraints on the Metallogenic Evolution of the Andes of Southeastern Peru: *Economic Geology and the Bulletin of the Society of Economic Geologists*, v. 85, p. 1520-1583.
- Clark, A.H., Tosdal, R.M., Farrar, E., and Plazolles, A., 1990b, Geomorphologic Environment and Age of Supergene Enrichment of the Cuajone, Quellaveco, and Toquepala Porphyry Copper-Deposits, Southeastern Peru: *Economic Geology and the Bulletin of the Society of Economic Geologists*, v. 85, p. 1604-1628.
- Cobbing, E.J., Pitcher, W.S., Wilson, J.J., Baldock, J.W., Taylor, W.P., McCourt, W., and Snelling, N.J., 1981, *The geology of the Western Cordillera of northern Peru*: London, Institute of Geological Sciences, 143 p.
- Corrigan, J.D., 1993, Apatite Fission-Track Analysis of Oligocene Strata in South Texas, USA - Testing Annealing Models: *Chemical Geology*, v. 104, p. 227-249.
- Dalmayrac, B., Lancelot, J.R., and Leyreloup, A., 1977, 2-Billion-Year Granulites in Late Precambrian Metamorphic Basement Along Southern Peruvian Coast: *Science*, v. 198, p. 49-51.
- Dunai, T.J., Gonzalez Lopez, G.A., and Juez Larre, J., 2005, Oligocene-Miocene age of aridity in the Atacama Desert revealed by exposure dating of erosion-sensitive

- landforms, Geological Society of America (GSA). Boulder CO United States. 2005., 321-324 p.
- Evenstar, L., Hartley, A.J., Rice, C., Stuart, F., Mather, A., and Chong, G., 2005, Miocene-Pliocene climate change in the Peru-Chile Desert, 6th International Symposium on Andean Geodynamics (ISAG 2005): Barcelona, p. 258-260.
- Farley, K.A., 2000, Helium diffusion from apatite; general behavior as illustrated by Durango fluorapatite: *Journal of Geophysical Research, B, Solid Earth and Planets*, v. 105, p. 2903-2914.
- Farley, K.A., Blythe, A.E., and Wolf, R.A., 1996, Apatite helium ages; comparison with fission track ages and track-length-derived thermal models, AGU 1996 fall meeting, Volume 77; 46, Suppl.: Washington, DC, United States, American Geophysical Union, p. 644-645.
- Gallagher, K., 1994, Genetic algorithms: A powerful new method for modelling fission-track data and thermal histories, *in* Turrin, B.D., ed., *International Conference on Geochronology*, US Geological Survey.
- Garver, J.I., Reiners, P.W., Walker, L.J., Ramage, J.M., and Perry, S.E., 2005, Implications for timing of Andean uplift from thermal resetting of radiation-damaged zircon in the Cordillera Huayhuash, northern Peru: *Journal of Geology*, v. 113, p. 117-138.
- Green, P.F., 1981, A New Look at Statistics in Fission-Track Dating: *Nuclear Tracks and Radiation Measurements*, v. 5, p. 77-86.
- , 1988, The Relationship between Track Shortening and Fission-Track Age Reduction in Apatite - Combined Influences of Inherent Instability, Annealing Anisotropy, Length Bias and System Calibration: *Earth and Planetary Science Letters*, v. 89, p. 335-352.
- Green, P.F., and Duddy, I.R., 1989, Paleotemperature Estimation from Apatite Fission-Track Analysis - Comments: *Journal of Petroleum Geology*, v. 12, p. 111-114.
- Haederle, M., and Atherton, M.P., 2002, Shape and intrusion style of the Coastal Batholith, Peru: *Tectonophysics*, v. 345, p. 17-28.
- Hampel, A., 2002, The migration history of the Nazca Ridge along the Peruvian active margin: a re-evaluation: *Earth and Planetary Science Letters*, v. 203, p. 665-679.
- Hartley, A.J., 2005, What caused Andean uplift, 6th International Symposium on Andean Geodynamics (ISAG 2005): Barcelona, p. 824-827.
- Hurford, A.J., and Green, P.F., 1983, The Zeta-Age Calibration of Fission-Track Dating: *Isotope Geoscience*, v. 1, p. 285-317.
- Jaillard, E., 1994, Kimmeridgian to Paleocene tectonic and Geodynamic evolution of the Peruvian (and Ecuadorian) margin., *in* Salfity, J.A., ed., *Cretaceous Tectonics in the Andes: Braunschweig/Wiesbaden, Earth Evolution sciences*.
- Ketcham, R.A., 2005, Forward and inverse modeling of low-temperature thermochronometry data.: *Reviews in Mineralogy and Geochemistry*, v. 58, p. 275-314.
- Ketcham, R.A., Donelick, R.A., and Donelick, M.B., 2000, AFTSolve: A Program for multi-kinetic modeling of apatite fission-track data: *Geological Materials Research*, v. 2, p. electronic.
- Kober, F., 2004, Quantitative analysis of the topographic evolution of the Andes of Northern Chile using cosmogenic nuclides: Zürich, Switzerland, ETHZ.
- Kontak, D.J., Clark, A.H., Farrar, E., Archibald, D.A., and Baadsgaard, H., 1990, Late Paleozoic Early Mesozoic Magmatism in the Cordillera De Carabaya, Puno, Southeastern Peru - Geochronology and Petrochemistry: *Journal of South American Earth Sciences*, v. 3, p. 213-230.

- Laubacher, G., and Naeser, C.W., 1994, Fission-Track Dating of Granitic-Rocks from the Eastern Cordillera of Peru - Evidence for Late Jurassic and Cenozoic Cooling: *Journal of the Geological Society*, v. 151, p. 473-483.
- Laughlin, A.W., Damon, P.E., and Watson, B.N., 1968, Potassium-Argon Dates from Toquepala and Michiquillay Peru: *Economic Geology*, v. 63, p. 166-&.
- Lippolt, H.J., Leitz, M., Wernicke, R.S., and Hagedorn, B., 1994, (Uranium+thorium)/ helium dating of apatite; experience with samples from different geochemical environments: *Chemical Geology*, v. 112, p. 179-191.
- McBride, S.L., 1977, A K-Ar study of the Cordillera Real Bolivia and its regional setting: Kingston, Canada, Queens University.
- McKee, E.H., Noble, D.C., Erickson, G.E., Pinochet, M.T., and Reinemund, J.A., 1990, Cenozoic tectonic events, magmatic pulses, and base- and precious-metal mineralization in the Central Andes  
In: *Geology of the Andes and its relation to hydrocarbon and mineral resources*, Circum-Pacific Council for Energy and Mineral Resources. Houston TX United States. 1990.
- McNulty, B., and Farber, D., 2002, Active detachment faulting above the Peruvian flat slab: *Geology*, v. 30, p. 567-570.
- Meesters, A.G.C.A., and Dunai, T.J., 2002a, Solving the production-diffusion equation for finite diffusion domains of various shapes; Part I, Implications for low-temperature (U-Th)/ He thermochronology: *Chemical Geology*, v. 186, p. 333-344.
- , 2002b, Solving the production-diffusion equation for finite diffusion domains of various shapes; Part II, Application to cases with alpha -ejection and nonhomogeneous distribution of the source: *Chemical Geology*, v. 186, p. 57-73.
- Megard, F., 1984, The Andean Orogenic Period and Its Major Structures in Central and Northern Peru: *Journal of the Geological Society*, v. 141, p. 893-900.
- Moore, N.D., 1984, Potassium-Argon Ages from the Arequipa Segment of the Coastal Batholith of Peru and Their Correlation with Regional Tectonic Events: *Journal of the Geological Society*, v. 141, p. 511-519.
- Mukasa, S.B., 1986, Zircon U-Pb Ages of Super-Units in the Coastal Batholith, Peru - Implications for Magmatic and Tectonic Processes: *Geological Society of America Bulletin*, v. 97, p. 241-254.
- Mukasa, S.B., and Henry, D.J., 1990, The San-Nicolas Batholith of Coastal Peru - Early Paleozoic Continental Arc or Continental Rift Magmatism: *Journal of the Geological Society*, v. 147, p. 27-39.
- Myers, J.S., 1976, Erosion surfaces and ignimbrite eruption, measures of Andean uplift in northern Peru: *Journal of Geology*, v. 11, p. 29-44.
- Noble, D.C., McKee, E.H., and Megard, F., 1978, Eocene Uplift and Unroofing of Coastal Batholith near Lima, Central Peru: *Journal of Geology*, v. 86, p. 403-405.
- , 1979, Early Tertiary Incaic Tectonism, Uplift, and Volcanic Activity, Andes of Central Peru: *Geological Society of America Bulletin*, v. 90, p. 903-907.
- Noble, D.C., McKee, E.H., Mourier, T., and Megard, F., 1990, Cenozoic Stratigraphy, Magmatic Activity, Compressive Deformation, and Uplift in Northern Peru: *Geological Society of America Bulletin*, v. 102, p. 1105-1113.
- Noble, D.C., Seabrier, M., Megard, F., and McKee, E.H., 1985, Demonstration of 2 Pulses of Paleogene Deformation in the Andes of Peru: *Earth and Planetary Science Letters*, v. 73, p. 345-349.
- Quang, C.X., Clark, A.H., Lee, J.K.W., and Guillen, J.B., 2003, Ar-40-Ar-39 ages of hypogene and supergene mineralization in the Cerro Verde-Santa Rosa porphyry Cu-

- Mo cluster, Arequipa, Peru: *Economic Geology and the Bulletin of the Society of Economic Geologists*, v. 98, p. 1683-1696.
- Seward, D., 1989, Cenozoic Basin Histories Determined by Fission-Track Dating of Basement Granites, South Island, New-Zealand: *Chemical Geology*, v. 79, p. 31-48.
- Shackleton, R.M., Ries, A.C., M.P., C., and Cobbold, P.R., 1979, Structure, metamorphism and geochronology of the Arequipa Massif of coastal Peru: *Geological Society of London*, v. 136, p. 195-214.
- Steinmann, G., 1929, *Geologie von Peru-Heidelberg*, Carl Winters Universitätsbuchhandlung, 448p. p.
- Stewart, J.W., Evernden, J.F., and Snelling, N.J., 1974, Age-Determinations from Andean Peru - Reconnaissance Survey: *Geological Society of America Bulletin*, v. 85, p. 1107-1116.
- Thouret, J.-C., Wörner, G., Singer, B., and Finizola, A., 2005, The Central Andes in Peru: "Old" valleys in a "young" mountain range?, 6th. International Symposium on Andean Geodynamics (ISAG 2005), Volume Extended Abstracts: Barcelona, p. 726-729.
- Tosdal, R.M., Clark, A.H., and Farrar, E., 1984, Cenozoic Polyphase Landscape and Tectonic Evolution of the Cordillera Occidental, Southernmost Peru: *Geological Society of America Bulletin*, v. 95, p. 1318-1332.
- Vicente, J.C., Sequeiros, F., Vladiviva, M.A., and Zavala, J., 1979, El sobre-escurrimientode Cincha-Luta: elemento del accidente mayor andino al NW de Arequipa: *Boletin de la sociedad Geologica del Peru*, v. 61, p. 67-100.
- Warnock, A.C., Zeitler, P.K., Wolf, R.A., and Bergman, S.C., 1997, An evaluation of low-temperature apatite U-Th/ He thermochronometry: *Geochimica et Cosmochimica Acta*, v. 61, p. 5371-5377.
- Wasteneys, H.A., Clark, A.H., Farrar, E., and Langridge, R.J., 1995, Grenvillian Granulite-Facies Metamorphism in the Arequipa Massif, Peru - a Laurentia-Gondwana Link: *Earth and Planetary Science Letters*, v. 132, p. 63-73.
- Wolf, R.A., Farley, K.A., and Silver, L.T., 1996, Helium diffusion and low-temperature thermochronometry of apatite: *Geochimica et Cosmochimica Acta*, v. 60, p. 4231-4240.
- Yamada, R., Tagami, T., Nishimura, S., and Ito, H., 1995, Annealing Kinetics of Fission Tracks in Zircon - an Experimental-Study: *Chemical Geology*, v. 122, p. 249-258.



# Chapter 6

## Summary and outlook

By using an integrated approach combining various radiogenic methods together with geomorphic analysis, details regarding the thermotectonic and geomorphological evolution of the Peruvian coastal margin have been revealed. New fission-track analyses of both zircons and apatites were combined with the published ages from higher temperature chronometers in order to reveal a first order cooling history. In order to bring these cooling histories to lower temperatures, the development of the (U-Th)/He method was undertaken. The resulting (U-Th)/He data offered excellent additional information to the apatite and zircon fission-track data as well as to the geomorphological analysis.

### 6.1 Development of the (U-Th)/He method

A new combination of analytical procedures was successfully applied in order to develop and implement the (U-Th)/He dating technique at the ETH in Zürich. The radiogenic helium was degassed from carefully chosen apatite crystals through laser heating and subsequently analysed on a sector type mass spectrometer. Afterwards the degassed grains were recovered and their uranium and thorium contents were determined on a Multiple-Collector Inductively Coupled Plasma Mass Spectrometer (MC-ICPMS). It was demonstrated, that this approach allowed the determination of very precise (U-Th)/He ages even on small apatite grains (<75µm, diameter).

### 6.2 The Peruvian coastal margin

The Peruvian coastal margin consists mainly of Precambrian to Palaeozoic rocks and Cretaceous intrusives of the Coastal Batholith.

The oldest zircon fission-track ages are from the Precambrian to Palaeozoic rocks, range from 530-121 Ma and are significantly younger than their crystallisation ages. These ages are therefore interpreted as representing slow cooling through the closure temperature of 240-300°C. In contrast to the slowly cooled “old” suites, zircon fission-track ages from the Jurassic to Cretaceous Coastal Batholith overlap in many cases with other previously

published higher temperature radiometric ages acquired with methods such as U/Pb, Rb/Sr, K/Ar, Ar/Ar. The almost identical ages suggest that the intrusives of the Coastal Batholith cooled rapidly. This is supported by the conclusions of petrological studies by Atherton et al. (1985) and Haederle and Atherton (2002) who suggested that the intrusives were emplaced within the upper few kilometres of the crust. Thus the zircon fission-track ages may be considered as a proxy for the crystallisation ages.

Apatite fission-track ages are younger, ranging from 124-23 Ma, consistent with the lower closure temperature. The modelling of the apatite fission-track from the Precambrian to Palaeozoic suites showed that changes in the rate of cooling can be correlated sometimes to previously identified tectonic phases such as the Peruvian (~88-72 Ma) or the Incaic I (~60 Ma) event. On the other hand, for samples from the Coastal Batholith, many apparent apatite fission-track ages are similar or just a little less than the zircon ages. Hence initial rapid cooling from the zircon closure temperature to the lower bounds of the apatite partial annealing zone (60° C) is common and further supports the notion of intrusion of the magmas into the upper levels of the crust.

In most cases a long period of stability in the temperature regime followed before final cooling in the late Neogene. Geologically this period is interpreted as the time associated with the formation of peneplains which have been identified by several workers in different parts of Peru. The length of the period of quiescence is dependant on the timing of the end of the first phase of rapid cooling and in nearly all examples falls generally at approximately 65°C. This is, coincidentally, also at the approximate closure temperature for the helium ages and where there is a long period of quiescence, (>20 my) the helium ages have a broad spread with in general no statistical overlap. The meaning of such ages is open yet to interpretation - as discussed below in “outlook”. However, it is quite remarkable that in all cases the apatite helium ages fall onto the modelled paths of the apatite fission-track data, regardless of their absolute age. Not only in this project but in many others, apatite fission-track cooling models have a tendency to yield a rapid cooling event in the late Neogene often considered to be an artifact of the modelling – however in some cases in this project young helium ages confirm that this event is real. Such young helium ages occur to the north of the trailing margin of the Nazca Ridge, yielding evidence that there has been increased exhumation caused by adjustment to base levels during the passage of the Nazca Ridge. Further the youngest helium ages occur at knick points in the rivers Pisco and Lunahuana and are associated with a

negative age-altitude gradient implying decrease in the relief after the rocks had passed through the closure temperature as suggested by Braun (2002).

On the basis of the thermochronological data there has been very little exhumation along the Peruvian coastal margin. In the south, which has not yet been affected by the subduction of the Nazca Ridge erosion rates are  $< 0.05$  mm/yr. This is very low but is confirmed by the data from the coast of northern Chile which also suggests that no or little erosion has taken place for at least the last 35 myrs (Dunai, 2000; Kober, 2004).

Erosion has not however been sufficient to reveal young apatite fission-track ages. The passage of the Ridge over one spot takes 3.5 Ma (Hsu, 1992). If erosion were to reveal young apatite ages then there must be at least 4 km removed ( $100^{\circ}\text{C}$ ), i.e. erosion has thus been less than 1 mm/yr over the present position of the Ridge. A closer estimate of erosion can be made by comparing the altitudes of the Coastal Cordillera - this yields  $\sim 0.3$  mm/yr. But, over the trailing edge and immediately to the north of the Ridge, as mentioned above are the youngest helium ages of 1 and 3 Ma which attest here to the removal of 2-3 km of overburden. This leads to erosion rates of the order of  $\sim 1$  mm/yr. Thus one may conclude that the subduction of the Nazca Ridge caused surface uplift which generated sufficient erosion to be identified through the apatite (U-Th/He) system. There is as yet insufficient helium age data to reveal the quantitative erosion history.

Thus both the geomorphological analysis and the low temperature thermochronometric data suggest that subduction of the Nazca Ridge has influenced the evolution of the coastal margin of Peru.

## **6.3 Outlook**

The technical aspects of this thesis as well as the field area in Peru offer a wide variety of possibilities for future work.

### **6.3.1 (U-Th)/He**

It has been shown in this thesis that the (U-Th)/He ages of some samples reproduce poorly. In general this is the case in samples with relatively old He ages ( $>40$  Ma) that have rested within the HePRZ for geologically significant times. Nonetheless they fit onto the modelled cooling paths based on apatite fission-track data. The results strongly suggest that more helium ages should be produced per site than is presently accepted. Further, in order to model

the thermal evolution based on (U-Th)/He it is important to understand the meaning of these poorly reproducible ages. It is therefore crucial to address the diffusion behaviour of helium within “old” apatites in more detail in future studies.

Another problem of the (U-Th)/He method that needs to be addressed is the zonation of uranium and thorium within apatites. It has been demonstrated that the effects of zonation need to be incorporated into the calculation of  $\alpha$  ejection corrections (Boyce and Hodges, 2005; Hourigan et al., 2005). Even more desirable, although technically difficult to achieve, would be a direct characterisation of the zoning within the analysed crystal. The geological significance of (U-Th)/He ages could be greatly improved with a better knowledge of these additional parameters.

### **6.3.2 The Peruvian coastal margin**

In spite of the existence of numerous radiometric age determinations for the Precambrian Arequipa massif with the Palaeozoic San Nicolas intrusives and for the Coastal Batholith, the coverage is not sufficient yet to completely understand the evolution of this continental margin. There is ample opportunity to increase the density of the low temperature studies. Because this study has shown that the coastal margin is a region of very low exhumation many more helium ages would aid in the interpretation.

This thesis has shown that the Nazca Ridge influences the evolution of the Peruvian coast. However it is possible that the processes involved in the interaction of the continental crust with the aseismic Ridge could be further improved by concentrating on areas directly above today's position of the Ridge. It would further be desirable if data from the offshore geology such as seismic lines and sedimentological analysis could be included in future studies.

The more distal inland impact of the Ridge should be addressed. This has been approached only in this thesis through geomorphological study. Such analysis could then be extended to the enigmatic “lost Inca Plateau”. Since this feature has been completely subducted it is difficult to quantify its significance. However recent seismicity (Gutscher et al., 1999) clearly suggests its presence and the study of its influence would offer another future project.

The Cordillera Blanca of northern Peru began to exhume at 6 Ma (Garver et al., 2005). U-Th/He ages would add new information to the exhumation as would a detailed geomorphological study of the impact of this growing massif.

## 6.4 References cited

- Atherton, M.P., Warden, V., and Sanderson, L.M., 1985, The Mesozoic marginal basin of Central Peru: A geochemical study of within-plate-edge volcanism, *in* Pitcher, W.S., Cobbing, E.J., and Beckinsale, R.D., eds., *Magmatism at a Plate Edge: The Peruvian Andes*: London, Blackie Halsted Press, p. 47-58.
- Boyce, J.W., and Hodges, K.V., 2005, U and Th zoning in Cerro de Mercado (Durango, Mexico) fluorapatite: Insights regarding the impact of recoil redistribution of radiogenic He-4 on (U-Th)/He thermochronology: *Chemical Geology*, v. 219, p. 261-274.
- Braun, J., 2002, Estimating exhumation rate and relief evolution by spectral analysis of age-elevation datasets: *Terra Nova*, v. 14, p. 210-214.
- Dunai, T.J., 2000, Helium diffusion in apatite revisited; is the previously inferred change in high temperature diffusion mechanism an artifact or a reality?, *Fission track 2000; 9th international conference on fission track dating and thermochronology*, Volume 58;: Sydney, N.S.W., Australia, Geological Society of Australia, p. 73-74.
- Garver, J.I., Reiners, P.W., Walker, L.J., Ramage, J.M., and Perry, S.E., 2005, Implications for timing of Andean uplift from thermal resetting of radiation-damaged zircon in the Cordillera Huayhuash, northern Peru: *Journal of Geology*, v. 113, p. 117-138.
- Gutscher, M.A., Olivet, J.L., Aslanian, D., Eissen, J.P., and Maury, R., 1999, The "lost Inca Plateau": cause of flat subduction beneath Peru?: *Earth and Planetary Science Letters*, v. 171, p. 335-341.
- Haederle, M., and Atherton, M.P., 2002, Shape and intrusion style of the Coastal Batholith, Peru: *Tectonophysics*, v. 345, p. 17-28.
- Hourigan, J.K., Reiners, P., and Brandon, M.T., 2005, U-Th zonation dependent alpha-ejection in (U-Th)/He chronometry: *Geochimica et Cosmochimica Acta*, v. 69, p. 3349-3365.
- Hsu, J.T., 1992, Quaternary uplift of the Peruvian coast related to the subduction of the Nazca Ridge; 13.5 to 15.6 degrees south latitude., *in* Berryman-Kelvin-R, O.-Y.N.-A.-R., ed., *Impacts of tectonics on Quaternary coastal evolution.*, Volume Quaternary International: Oxford, Pergamon, p. 87-97.
- Kober, F., 2004, Quantitative analysis of the topographic evolution of the Andes of Northern Chile using cosmogenic nuclides: Zürich, Switzerland, ETHZ.



# **Chapter 7**

## **Appendix**



## Publications submitted and in preparation

M. Wipf, G. Zeilinger, D. Seward, F. Schlunegger  
**The subducting Nazca Ridge:  
Impact on the geomorphology in South-Central Peru**  
(submitted to *GEOLOGY*)

M. Wipf, C.H. Stirling, D.Harrison, D. Seward,  
**(U-Th)/He age analysis on Apatite:  
Laser Heating and MC-ICPMS - new methodology**  
(planned to be submitted to *International Journal of Mass Spectrometry*)

M. Wipf, D. Seward, C.H. Stirling, D.Harrison,  
**Impact of the subducting Nazca Ridge on the exhumation of the Andean margin of  
South-Central Peru: Evidence from low temperature thermochronology**

M. Wipf, D. Seward, C.H. Stirling, D.Harrison  
**Low temperature thermochronology of the Western Cordillera and Coastal margin of  
Peru: Post Jurassic thermal evolution**

M. Wipf, D. Seward, D.Harrison, C.H. Stirling  
**Evolution of the deep Canyons of southern Peru**

## Abstracts

M. Wipf, G. Zeilinger, D. Seward, F. Schlunegger  
**Geomorphic Effects in Western Peru due to Subduction of the Nazca Ridge**  
*EUG General Assembly, 24-29, April 2005, Vienna, Austria.*

M. Wipf, D. Seward, C. Stirling, D. Harrison  
**Constraining the post Jurassic Evolution of Western Peru through Fission Track and (U-  
Th/He) dating**  
*EUG General Assembly, 24-29, April 2005, Vienna, Austria.*

M. Wipf, D. Harrison, C. Stirling, D. Seward  
**(U-Th)/He How do we measure it?**  
*European He Thermochronology Workshop 2004, 18-19, May 2004, SUERC, East Kilbride,  
Scotland.*

M. Wipf, D. Harrison, C. Stirling, D. Seward, F. Schlunegger  
**The Coastal margin of Peru:  
cooling history through Fission Track and (U-Th/He) dating**  
*10th International Fission Track Dating and Thermochronology Congress 8-13, August 2004,  
Amsterdam, The Netherlands.*

M. Wipf, D. Harrison, C. Stirling, D. Seward, F. Schlunegger

**Entwicklung der Küstenregion zwischen Lima und Chala, Peru**

*Feldkonferenz: Archäologisches Projekt Nasca–Palpa Entwicklung und Adaption archäometrischer Techniken zur Erforschung der Kulturgeschichte, 17-22. September 2004, Palpa, Peru.*

M. Wipf, D. Seward, F. Schlunegger, F. Stuart

**Fission Track and (U-Th/He) thermochronology constraints on the influence of the subduction of the Nazca Ridge on Andean Exhumation in South Central Peru**

*EGS-AGU-EUG Joint Assembly, 6-11, April 2003, Nice France.*

M. Wipf, D. Seward, F. Schlunegger

**Preliminary Fissiontrack Data on the effects of the subducting Nazca Ridge on the Geomorphology in South-Central Peru**

*5<sup>th</sup> International Symposium on Andean Geodynamics, 16-18, September 2003, Toulouse, France.*

M. Wipf, D. Harrison, D. Seward, F. Schlunegger

**Evolution Of The Coastal Margin Of Central Peru Through Fission-Track and (U-Th/He) Analysis**

*AGU Fall Meeting, 8-12, December 2003, San Francisco, USA.*

M. Wipf, D. Seward, F. Schlunegger

**Effects of the subducting Nazca Ridge on Andean Exhumation in South Central Peru.**

*International Workshop on “Fission Track Analysis: Theory and Applications” 4-7, June 2002, El Puerto de Santa Maria, Cadiz, Spain.*

N. Hurley, a. A. Raba, E. Witton, M. Wipf

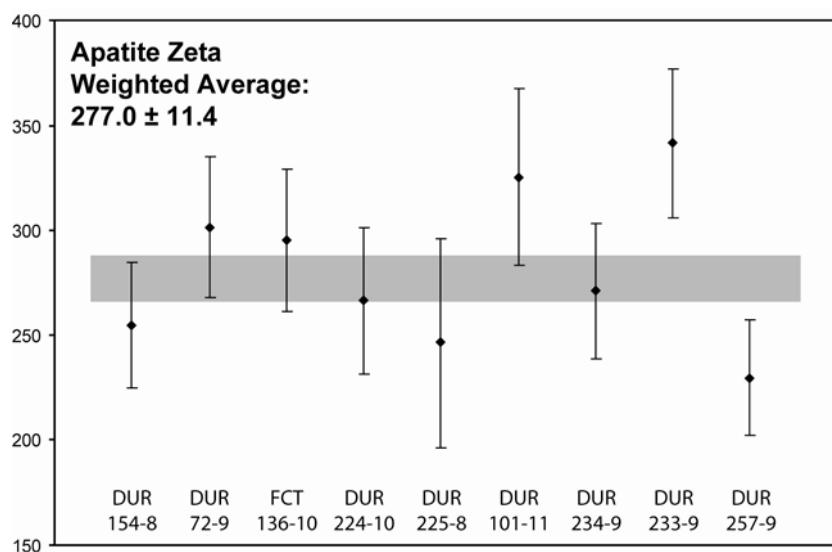
**Outcrop mapping of tear-fault compartments at Rose Dome, Big Horn Basin, Wyoming.**

*American Association of Petroleum Geologists, Annual Meeting 1999, Tulsa, OK, USA.*

## 7. 2 $\zeta$ -calibration factor used for apatite fission-track analysis

Age Standard	Irradiation number	No. grains	Standard track $\rho_d \times 10^4 \text{ cm}^{-2}$ (counted)	$\rho_s \times 10^4 \text{ cm}^{-2}$ (counted)	$\rho_i \times 10^4 \text{ cm}^{-2}$ (counted)	U conc (ppm)	P( $\chi^2$ ) (Var) (%)	$\zeta$	$\pm 2\sigma$
DURANGO	ETH-154-8	20	136.6 (13973)	18.45 (369)	101.4 (2028)	9	99 (0.00)	<b>254.62</b>	15.1
DURANGO	ETH-72-9	23	137.4 (13899)	18.00 (414)	118.7 (2730)	11	99 (0.00)	<b>301.43</b>	8.4
FCT	ETH-136-10	20	103.5 (10633)	20.04 (401)	109.95 (2191)	13	75 (0.01)	<b>295.25</b>	17.1
DURANGO	ETH-224-10	20	98.6 (6273)	15.87 (314)	66.28 (1311)	8	99 (0.00)	<b>266.50</b>	17.6
DURANGO	ETH-225-8	10	110.6 (4441)	16.01 (125)	69.27 (541)	8	99 (0.00)	<b>246.41</b>	25.0
DURANGO	ETH-101-11	21	95.0 (7579)	14.15 (293)	69.52 (1439)	9	99 (0.00)	<b>325.40</b>	21.0
DURANGO	ETH-234-9	24	93.5 (3604)	17.75 (410)	71.47 (1651)	9	33 (0.08)	<b>271.13</b>	16.2
DURANGO	ETH-233-9	35	85.1 (7074)	14.97 (524)	69.11 (2419)	9	33 (0.10)	<b>341.53</b>	17.8
DURANGO	ETH-257-9	20	89.77 (4591)	23.22 (433)	76.03 (1418)	11	99 (0.00)	<b>229.65</b>	13.6
<b>weighted</b>	<b>mean</b>							<b>277.0</b>	<b>11.4</b>

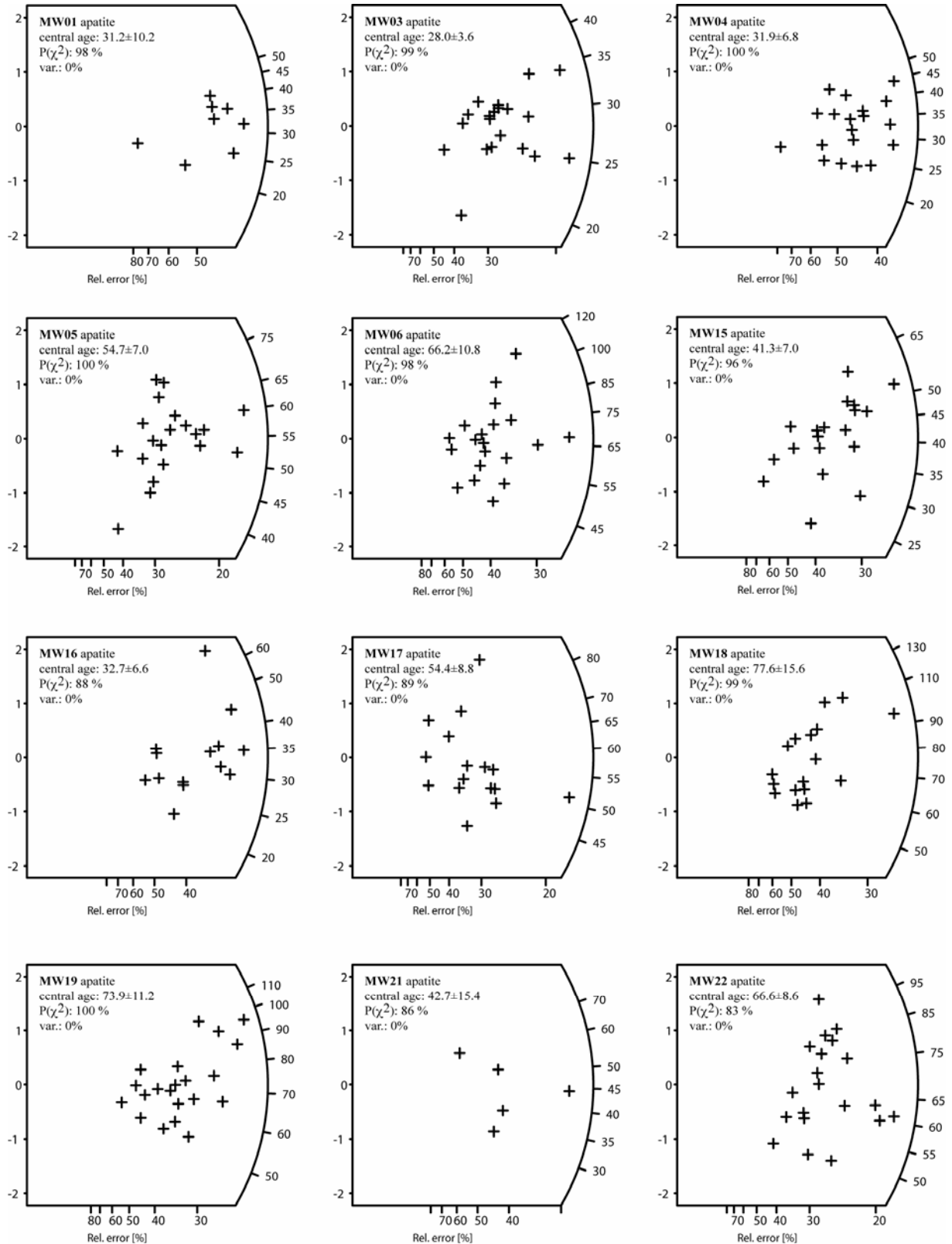
Personal  $\zeta$ -factor calibration. Durango, Fish Canyon Tuff (FCT) apatites and CN5 (12ppm U) were used as age standard and glass dosimeter, respectively.

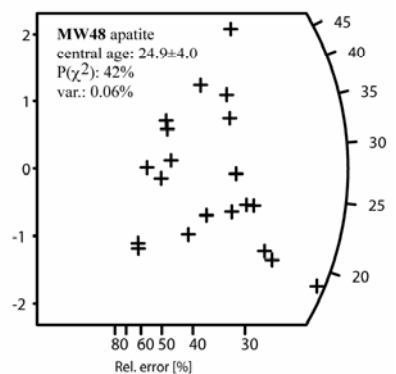
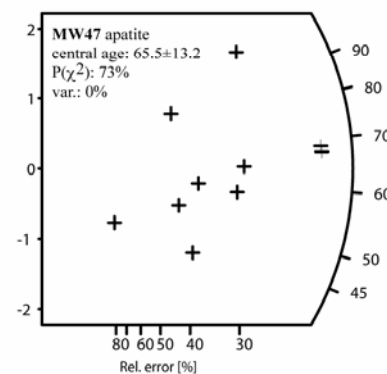
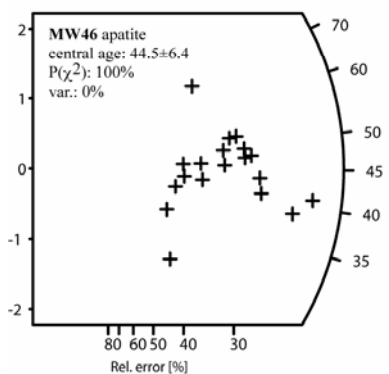
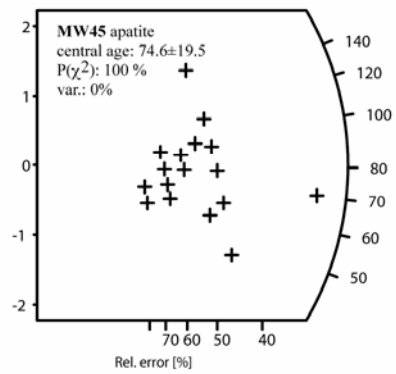
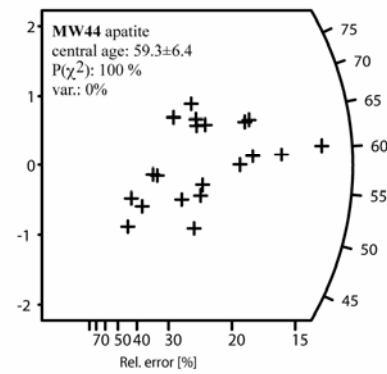
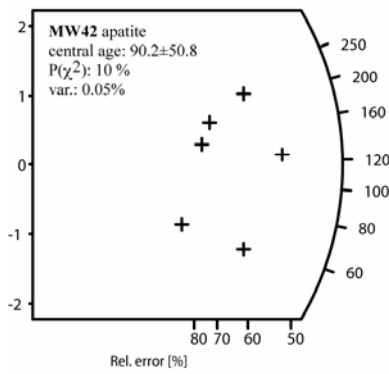
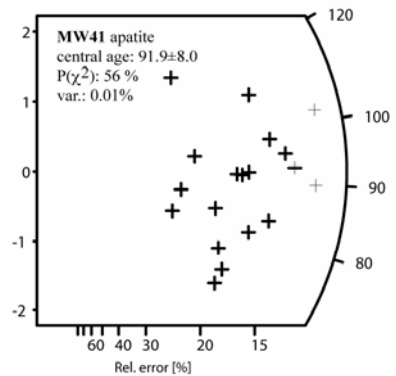
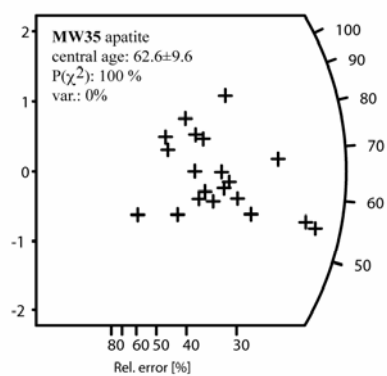
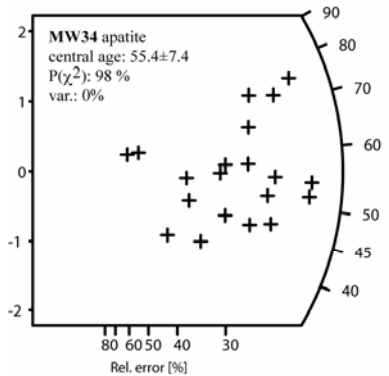
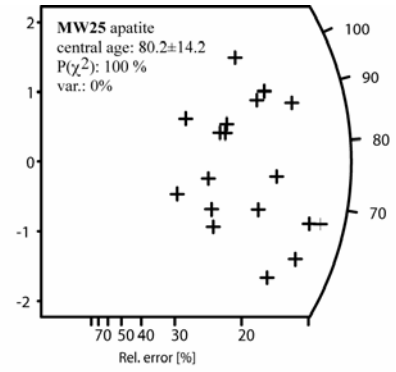
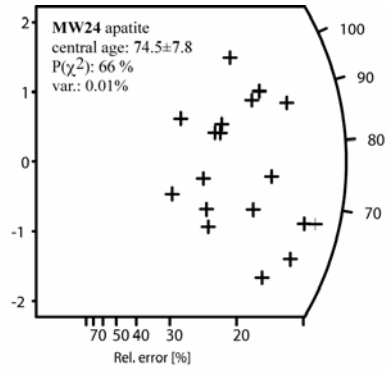
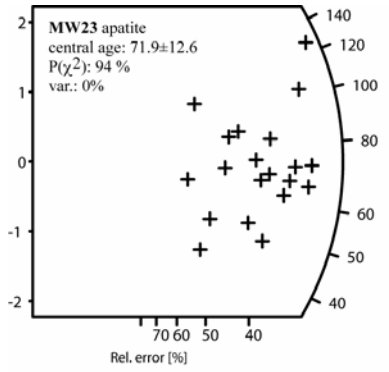


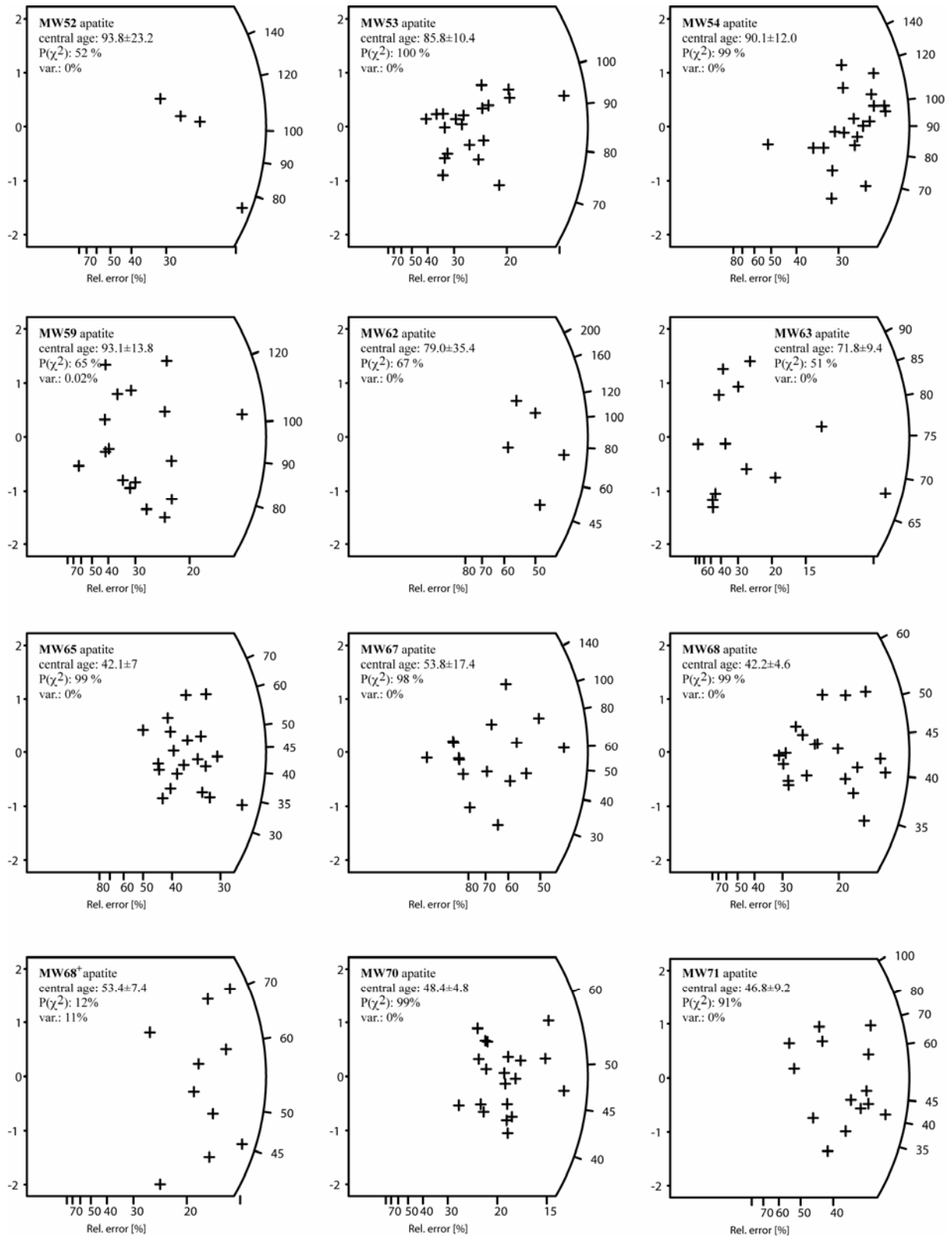
Personal  $\zeta$ -factor values obtained during the time of this study. Durango and Fish Canyon Tuff (FCT) apatites and CN5 (12ppm U) were used as age standard and glass dosimeter, respectively.

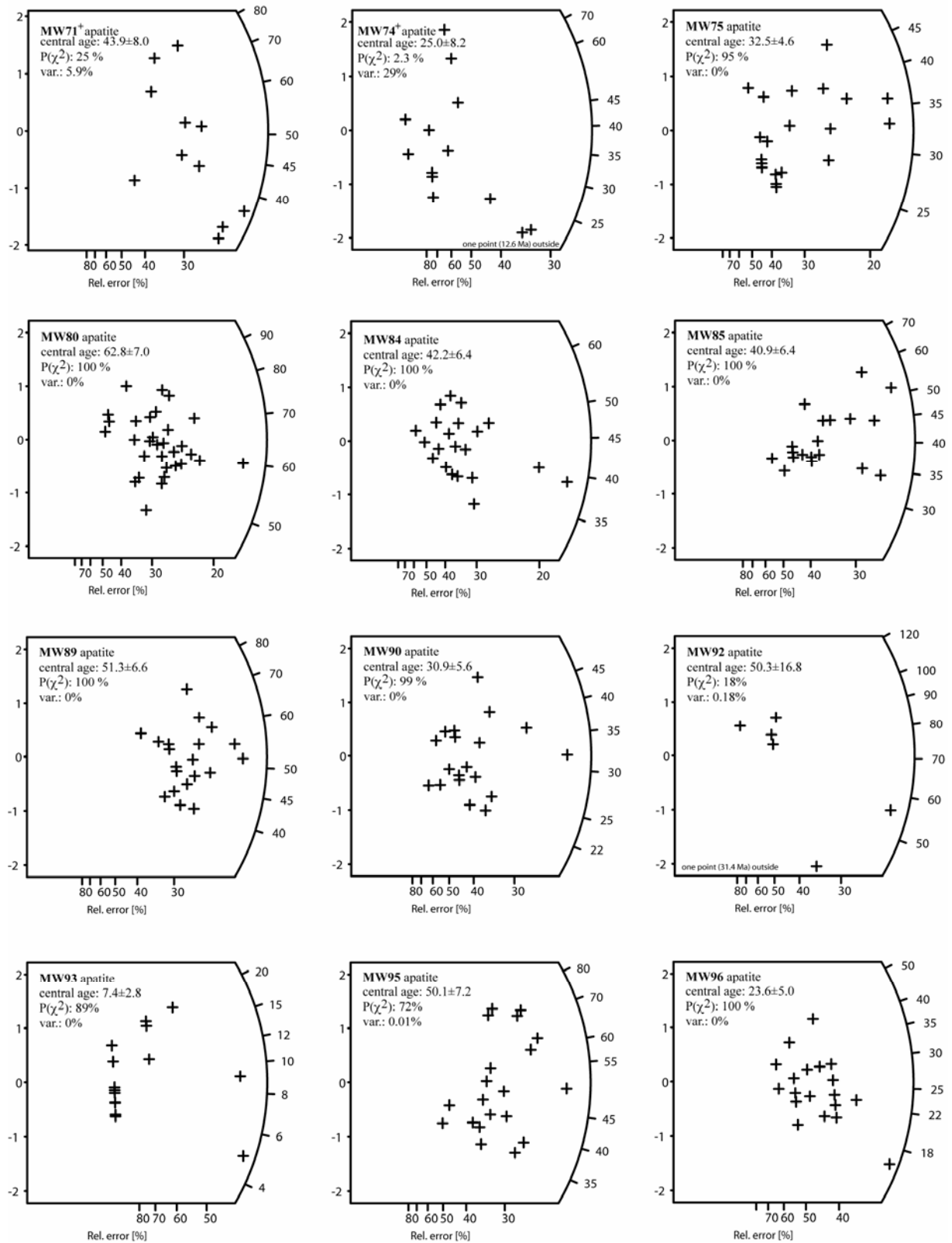
## 7.3 Radial plots

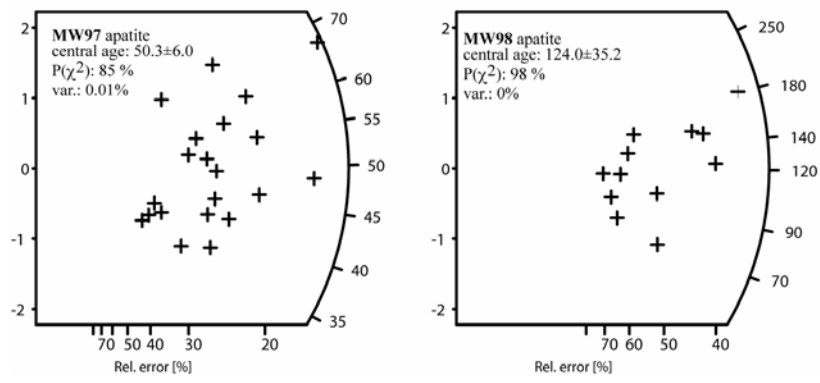
Radial plots for all fission-track age determinations carried out on apatite.











## 7.4 Acknowledgements

Thinking back one realizes how many people in the last four and a half years contributed in some sort to this work. This study was only possible thanks to the advice and support of many people from different fields and I would like to express my gratitude to all those who helped to make this thesis project successful. There are however a number of people who deserve some special thanks.

I am especially grateful to Diane Seward and Claudine Stirling. Diane, thanks for your help, support and guidance either in the field or anywhere else during the last four and a half years. I also thank you for many interesting discussions about various things including the notoriously difficult Swiss society. After all you have also corrected and improved my manuscript and my English knowledge surely benefited thereby. Claudine, thank you too for your endless support and for introducing me to the MC-ICPMS world (or at least parts of it) and to the difficult behaviour of thorium. Morten Andersen (no not the famous NFL kicker) always shared his clean-lab experience and supplies such as TRU spec resin and clean acids. Many thanks also to Rainer Wieler without whom the noble gas part of this thesis never would have happened and to Nadia Vogel and Veronika Heber who introduced me to the “Albatross” noble gas mass spectrometer and its peculiarities. Darrell I greatly appreciated your inputs in countless discussions about the (U-Th)/He method and about all kind of other stuff. Unless you were out snowboarding or skating usually followed by a visit to the emergency room at various hospitals I could always walk into your office with some new crazy ideas. Chapters 3 and 4 greatly improved thanks to your critical reviews.

The help of Fritz Schlunegger and Gerold Zeilinger during the field campaigns in Peru as well as for the geomorphological analysis is also greatly appreciated. Fritz I enjoyed your company in the field very much and learned a lot about the recent and past surface processes that shaped the unique Peruvian coastal margin. Gerold thank you for coming along to the field to Peru twice. I know you still prefer the Chilean Pisco over the Peruvian one, but you have to admit that nothing beats drinking a Pisco Sour in Pisco. It was great having a structural geologist with me in the field and besides that you were always a great and patient driver. Last but not least you introduced me to the magic of DEMs and GIS analyses. I would probably still be drawing cross sections by hand without your help. The other driver which was a great help during our field seasons was Ever Fernandez Porres. Thank you Ever for driving, organising and dealing with the Peruvian Police. Katja and Jörg I will never forget

the night freezing in the broken down Bus in the middle of the Peruvian desert, admiring the Cross of the South. I really appreciated your help in the Tacna and Pisco area.

I would also like to express my gratitude to Jean-Pierre Burg who kindly agreed to take over the task of being my main referee and taking me into his group after Fritz accepted his new professorship in Berne. I know this thesis is not really dealing with structural geology but I enjoyed being part of your group.

The help of many people here at the ETH in Zürich is greatly appreciated. Heiri Baur and Felix Oberli as well as Urs Menet, Donat Niederer and Andreas Suesli always kept the machines and labs operational. In case of an emergency or break down they were always there to help and fix the problems. Then of course there is also Pirovino Frowin, Andreas Jallas and his goldie Winur down in the workshop who helped with polishing the fission-track mounts and many other of my wishes. Regula and Silvia never got tired of dealing with all the administrative stuff and paper work. Many thanks also to Stefan who helped prepare my samples in the hot and sometimes unbearable crushing room.

During the last four and a half years I had the pleasure of sharing office with various fellow Ph. D. students. Lukas, Benno, Alex, Leo, Sonia and Chris thanks for keeping up the good spirit and humour here in our office. There were many other people here at the ETH as well with whom I had a great time be it for lunch, coffee breaks, Friday beer or whatever: Florian, Patrick, Marina, Thomas, Sam, Claudio, Michi, Ruth, Boris, Geoffrey, Richard, Miriam, Stefan, Pauline, Martine, Erwan, Ruben, Nick, Pierre and Marion. Many thanks to all the isotope people downstairs. Ansgar, Tina, Philipp, Marcus, Bastian, Bettina, Veronika, Leo there was always a great spirit on the C-floor.

My friends here at the ETH organised tickets for me to go to the Olympic Winter Games in Torino to see Switzerland play the Czech Republic, thanks a lot for this great idea. Talking about the stunning game I would also like to thank the Olympic Swiss ice-hockey team for winning a historical victory over the Czech Republic. It was a very memorable end to this thesis.

Last but not least very special life-long thanks go to Tamara and my parents Hans-Kaspar and Kathrin Wipf for all their love and unconditional support in my studies and goals with all its ups and downs. I hope I have not missed anybody here and if so it was not done on purpose but simple because I am getting tired of writing up this thesis.



